Design and Application of Polymer Metal–Organic Cage Gels

Julia Zhao

B.S. Chemistry
Rice University, 2015

Submitted to the Department of Chemistry
in Partial Fulfillment of the Requirements for the Degree of
Doctor of Philosophy in Chemistry

Massachusetts Institute of Technology

May 2020

Signature of Author:

_____

Department of Chemistry
May 8, 2020

Certified by:

_____

Jeremiah A. Johnson
Associate Professor of Chemistry
Thesis Supervisor

Accepted by:

_____

Robert W. Field
Haslam and Dewey Professor of Chemistry
Chairman, Departmental Committee on Graduate Students

This doctoral thesis has been examined by a committee of professors from the Departments of Chemistry and Bioengineering as follows:

Professor Timothy M. Swager:

_____

Thesis Committee Chair

Professor Jeremiah A. Johnson:

_____

Thesis Supervisor

Professor Linda G. Griffith:

_____

Thesis Committee Member

Design and Application of Polymer Metal–Organic Cage Gels

By

Julia Zhao

Submitted to the Department of Chemistry on May 8, 2020
in Partial Fulfillment of the Requirements for the Degree of Doctor of Philosophy
in Chemistry at the Massachusetts Institute of Technology

ABSTRACT

Chapter 1. A unifying overview of the fundamentals of polymer network synthesis, structure, and properties is provided, tying together recent trends in the field that are not always associated with classical polymer networks, such as the advent of crystalline "framework" materials. Recent advances in using molecular design and control of topology showcase how a deep understanding of structure-property relationships can lead to advanced networks with exceptional properties.

Chapter 2. A novel bispyridine-based M_6L_{12} coordination cube inspired by related work from Fujita and coworkers is prepared and used to generate a polyMOC gel with intermediate branch functionality compared to previous polyMOC networks. The ligand is able to successfully self-assemble with not only Pd(II) and Pt(II), but also combinations of both metals to form mixed-metal cages. Through adjusting the ratio of palladium and platinum metal salts incorporated into network assembly, we can tune the energy dissipation properties of these materials due to differences in lability of metal–pyridine coordination bonds. Using this strategy, the characteristic relaxation times and loss moduli of these M_6L_{12}-based gels can be tuned over nearly three orders of magnitude while maintaining the general network topology as well as the elastic behavior of the material.

Chapter 3. The $M_{12}L_{24}$-based polyMOC network was optimized for water purification and reuse. A library of ligands was designed and synthesized to target three different chemical families: aromatic, perfluorinated, and alkylated groups. PolyMOC gel purification performance was tested for aromatic compounds and perfluoroalkyl substances (PFAS). These evaluations demonstrated some successes in the absorption of selected model compounds; however, absorption in all cases were accompanied with nonspecific binding of unfunctionalized control gels. Potential absorption mechanisms contributing to this nonspecific binding are discussed. Future work to better determine interaction mechanisms are necessary for improved design and function of polyMOC gels towards water treatment applications.

Thesis Supervisor: Jeremiah A. Johnson
Title: Associate Professor of Chemistry

ACKNOWLEDGEMENTS

I would like to start by thanking my advisor, Prof. Jeremiah Johnson. I first joined his group as a visiting undergraduate student in the summer of 2014, somewhat by accident: my postdoc mentor was jointly advised by Jeremiah and Prof. Brad Olsen. While my formal appointment was in the Olsen Lab, Jeremiah excitedly welcomed me to his group meetings that summer. My first impressions of Jeremiah were of his enthusiasm, geniality, and candor, which led me to return to his group in 2015 and have remained consistent throughout our interactions during my graduate school career. I have always appreciated the ability to speak freely in our relationship, and Jeremiah's ferocious optimism has been an indispensable counterbalance to my chronic pessimism throughout graduate school. Being in the Johnson Group has helped me grow immeasurably as a scientist and as a young professional, and I have Jeremiah to thank for the independence and freedom to explore my research interests, take leadership opportunities, and expand my skills in science illustration.

Other faculty members at MIT have also been important to my growth and success in graduate school. I would like to thank my thesis committee chair Prof. Tim Swager for our annual meetings, where he would show interest not only in my professional development but also my personal wellbeing. Similarly, I would like to thank Prof. Linda Griffith for taking on responsibilities as a member of my thesis committee. The faculty of the Program in Polymers and Soft Matter (PPSM) were also a vital part of my graduate courses and qualifying exams, and in particular I would like to thank Prof. Darrell Irvine and Prof. Alfredo Alexander-Katz, former and current program directors.

So many people throughout the Institute enhanced my graduate school experience and made my research possible. I want to start by thanking Dr. Maryam Khodadoust at MIT Medical for teaching me how to reframe my thinking and advocate for myself. Graduate school has been equally a mental challenge as it has been a scientific one, and Maryam has been a constant cheerleader and a necessary external calibrant to help me put my experiences into perspective. Thank you to the DCIF staff: Dr. Walt Massefski, John Grimes, Dr. Mohan Kumar, and Dr. Bruce Adams. I'm thankful for Walt, who evolved in the past year from a friendly face to a genuine friend in the DCIF. Thanks as well to Mohan for going above and beyond as I desperately collected data before the COVID-19 shutdown. As safety officer, I was also fortunate to work with Scott Ide, the department EHS coordinator, and Brian Pretti, our facilities and operations administrator. Brian is an overworked superstar who still took time to regularly chat with me and check on my wellbeing, which I appreciated immensely. I want to also thank Dr. Jennifer Weisman in the Chemistry Education office for her help and support. Outside of MIT Chemistry, I would also like to thank Prof. Felice Frankel and Christine Daniloff from MIT News for their warm encouragement and support of my interest in science illustration as well as my illustration internship with MIT News. Outside of MIT, I want to thank beamline scientists Dr. Byeongdu Lee and Dr. Xiaobing Zuo for their help and mentorship during my frequent visits to APS. I am also deeply appreciative of my collaborators Dr. Heng Wang and Prof. Xiaopeng Li at University of South Florida, as well as my collaborators Kristen Flynn and Prof. Mo Movassaghi here at MIT.

The people in the Johnson Group have been undoubtedly been one of the best parts of my time at MIT. I want to start by thanking Prof. Mingjiang Zhong, my very first mentor in the Johnson Group. Mingjiang was my postdoc mentor and probably one of my very best friends during my summer UROP at MIT. Mingjiang is a patient and kind mentor in both science and in life, and I truly envy his current and future students at Yale. His unwavering faith in me and long-distance friendship has kept me afloat throughout graduate school. I want to also thank Prof. Alex Zhukhovitskiy, a meticulous mentor who carefully trained me in the material platform he created during my first year. Alex is an incredibly efficient and thoughtful scientist, and his workflow was a source of inspiration. Finally, a heartfelt thanks to Prof. Matt Golder, who very willingly agreed to be my mentor after Mingjiang and Alex left. Matt provided the training wheels I needed to gain independence as a research scientist during my second year, meeting with me on a weekly basis to keep me accountable and ensure I had thought critically about my next experimental steps. He also mentored me through my first and only drug delivery project, which I greatly appreciated.

In addition to good mentors, the Johnson Group has provided me with exceptionally good friends. I want to thank Dr. Deb Ehrlich, who might be the kindest and most generous person I know. I can always count on Deb's special brand of care (mostly baked goods and cat-related trinkets) when things get tough, and I will always be thankful for her mix of friendship and mentorship. I'm also very thankful to be friends with Dr. Michelle MacLeod, who was a huge role model in her advocacy for women and graduate student wellbeing in the department. I am so grateful for all the strong and resilient Johnson Group women: Dr. Jenny Liu, Prof. Jessica Lamb, Wencong Wang, Yasmeen Alfaraj, Dr. Megan Hill, Dr. Sam Kristufek, Leticia Costa, Valerie Lensch, and Hadiqa Zafar. Team #jgw has doubled in size since I joined, and I cherish the warmth of this community. Thanks to Wencong for being a lovely friend always up for boba delivery, to Yasmeen for her eloquent advocacy and empathy, and to Megan for our fulfilling conversations and for her brief stint as my postdoc mentor. I am also thankful for my co-safety officers, past and present—Prof. Alex Zhukhovitskiy, Dr. Deb Ehrlich, Gihan Hewage, Matthew Pearson, Michael Stolberg, and Dr. Chris Brown. I am particularly appreciative of Michael's hard work revitalizing the safety culture in our group. Separately, I should thank Chris for his friendship as well as his recent thesis mentorship. I could tell from the aesthetics of his interview slides that Chris and I would get along well, and I was right: we share a mutual love of fonts, design, and gossip. Many thanks to my fellow graduate students: thanks to Peter Qin, who has always been eager to help with technological and Agilent-based troubles; we have shared four years of Chinese dry pot and cat memes, and I have enjoyed his peculiar sense of humor and his experimentation in 3D printed violins. Thanks to Keith Husted for readily picking up SAXS/WAXS responsibilities and entertaining me with the weirdest memes on the internet. I hope one day he will learn to wear his labcoat. Thanks to David Lundberg for diving right into the polyMOC subgroup and inspiring (and terrifying) the rest of us with his methodical research. Finally, many postdocs in the group enhanced my time at MIT through their friendship—Prof. Jessica Lamb, Dr. Megan Hill, Prof. Bo Qiao, Dr. Wenxu Zhang, and Prof. Nate Oldenhuis. Thanks to Wenxu for coaching me through a half

marathon PR, and thanks to Nate for being a constant source of support, encouragement, and reddit memes. I couldn't have gotten through graduate school without our close friendship, the shared snax™ stash, ambling trips to "the Verds" and A4, and Nate's ridiculous sense of humor.

There are countless alumni who have supported me throughout the past five years: thanks to Dr. Ken Kawamoto, Gihan Hewage, Prof. Ellane Park, Prof. Mingjun Huang, Dr. Hung Nguyen, Prof. Junpeng Wang, Dr. Manuel Hartweg, Shannon Wagner, and Dr. Yuwei Gu. In particular, I want to thank Hung for being the most unexpected source of friendship and emotional support—complete with terrible jokes and enough sarcasm to clog a toilet. Thanks to my former collaborator Prof. Junpeng Wang, who also happens to be a great friend and fellow runner. On that note, thanks to our former lab dogs Buddy and Ellery for never failing to make me smile. Thanks to Manu for his ridiculously loud German enthusiasm for every food and sport on Earth, for bringing whole pineapples to share at lunch, and for normalizing "whole block of cheese" as a meal option. I want to also thank our former administrative assistant Shannon Wagner, who certainly feels like an alum of the group. I am endlessly grateful to Shannon for her continued friendship, quirky sense of humor, general love of cats, and incredible empathy. Finally, I want to thank Yuwei, who was truly one of my best friends in the Johnson Group and in graduate school. While I hated the late nights in graduate school, working the evening shift with Yuwei was a highlight of my time at MIT. Yuwei is truly a rare combination of humble and talented and generous, and I have him to thank for roping me into a series of reviews and kickstarting my career in science illustration.

I have also been fortunate to have a number of friends outside the Johnson Group. The warm welcome of Rice alums Amanda Wicker and Dr. Julian Cooper made my transition to graduate school infinitely easier. Amanda and her cat Linus were great roommates and a wonderful support system my first year, and Julian was kind enough to bear the brunt of my research-related stress and angst. Thanks to my wonderful cohort, particularly Dr. Constantin Voll, Dr. Steve Cohen, Corey Kaminsky, Lindsey Backman, Zach Nelson, Krysta Dummit, Dr. Lilia Xie, and Crystal Chen. I am particularly grateful for weekly dinners with Food Club: Constantin, Steve, Corey, Lindsey, and Zach comprised a very odd but very necessary family during my first year of graduate school. Krysta has been a personal role model in self-advocacy, and I have admired her bravery and strength throughout graduate school. Thanks to my fellow ChemREFS who gave me support: Dr. Kelley Danahy, Dr. Tho Tran, and Erica Tsai. And thanks to the 2018 Organic Retreat Committee for making an arduous responsibility a ton of fun: Dr. Kelley Danahy, Dr. Joey Dennis, Dr. Bryan Ingoglia, Krysta Dummit, Dr. Julian Cooper, and Dr. Saki Ichikawa. I want to also thank the student groups CGSC, CADI, ChemREFS, WIC, and PPSM for offering social events, graduate school support, and student advocacy. I am grateful for the WIC mentorship program, through which I met Cassie Zentner, one of my closest friends. Cassie and I gracefully take turns having emotional meltdowns, and we tend to give each other the same advice that we personally ignore. Somehow it has worked out, and I am quite thankful to both give and take her emotional support. Outside the Chemistry Department, I have been blessed with a number of friendships that have carried me

through graduate school: thanks to Sheryl Wang, Cameron McBride, Hursh Sureka, Andrew Bader, Hao Wu, and Ryan McGillicuddy for our regular dinners, coffee dates, and check ins.

My path to MIT was paved by the academic and emotional support of an army of people. My research experience and career are the credit of my former mentors: Prof. Christy Landes, Dr. Bo Shuang, Dr. Chad Byers, Prof. Lydia Kisley, Prof. Suzie Pun, Prof. Hua Wei, Prof. Junghae Suh, Dr. Chris Dempsey, Dr. Michelle Ho, Prof. Brad Olsen, Prof. Jeremiah Johnson, and Prof. Mingjiang Zhong. The friends I made through those experiences have supported me through my graduate research: Andrea Mansur, Dr. Jessica Heimann, Lachezar Hristov, Rahul Kini, Dr. Sarah Arveson, and Meredith Fields. I am also grateful for the teachers and mentors who have become close friends: I am thankful as ever for my high school orchestra teacher Mrs. Valerie Bell (and “Uncle” John Bell) for her continued support even after I graduated from Park Hill South. I also want to thank Prof. Angel Martí at Rice University, my former inorganic chemistry professor and Lovett College RA. Not only did he guide me through my undergraduate career, graduate school applications, and NSF fellowship applications, Angel remained supportive and faithful in me throughout graduate school, which meant the world.

I thank the friends and loved ones who have been integral to my personal happiness and a limitless source of emotional support. From my high school and college friends Christian Boyd, Daisy Chung, Clare Jensen, Doha Aboul-Fotouh, and Onkur Sen to my cherished MIT friends Julian Cooper, Nate Oldenhuis, Cassie Zentner, Deb Ehrlich, and Sheryl Wang, I have never failed to receive an abundance of love and comfort when I needed it the most. A special thanks to Onkur for his long-distance friendship, remotely absorbing my stresses and celebrating my successes. I especially want to thank Sheryl for being the best roommate, friend, and confidant throughout graduate school, starting from our first year of PPSM courses together. Her silly humor, remarkable empathy, and loyal companionship have eased the toughest parts of graduate school, and I look back fondly at all the times we spent binging good food, followed by over-exercising at the gym. Finally, I am grateful to Mike Coniglione for his overwhelming love, kindness, thoughtfulness, and support. I am thankful for the playfulness, neurotic scheduling, sentiment, culinary adventures, and weekend trips that make up our relationship, which has brought me a happiness I never imagined.

I want to close by thanking my family: Dr. Hui Yu, Dr. Mingyang Zhao, and Beryl Zhao. My PhD was inspired by my parents, and I would not be graduating from MIT without their support throughout my entire life. Their hard work and sacrifices have provided me a life of privilege and opportunities, and I am incredibly grateful for their unconditional love and guidance.

PREFACE

This thesis has been adapted from the following published or submitted articles co-written by the author:

Peer-reviewed: († denotes equal contribution)

Gu, Y.†; **Zhao, J.**†; Johnson, J. A. Polymer networks: from plastics and gels to porous frameworks. *Angew. Chem. Int. Ed.* **2019**, *59* (13), 5022–5049.

Gu. Y.†; **Zhao, J.**†; Johnson, J. A. A (macro)molecular-level understanding of polymer network topology. *Trends Chem.* **2019**, *1* (3), 318-334.

Gu. Y.†; **Zhao, J.**†; Johnson, J. A. Polymer networks. In *Macromolecular engineering: from precise synthesis to macroscopic materials and applications,* 2nd ed.; Wiley. *Accepted.*

In submission/preparation:

Zhao, J.; Oldenhuis, N. J.; Wang, H.; Li, X.; Johnson, J. A. Tuning dynamics of polyMOC gels through mixed-metal systems.

RESPECTIVE CONTRIBUTIONS

Chapter 1: This review was a collaborative effort between Dr. Yuwei Gu and the author.

Chapter 2: The project was conceptualized by the author, Dr. Aleksandr V. Zhukhovitskiy, and Prof. Jeremiah A. Johnson. Dr. Nathan J. Oldenhuis suggested the use of Pt(II) for cage assembly. Molecular optimization was done with the help of Zachary P. Nelson and Prof. Tim Swager at MIT. Soft ionization mass spectrometry methods were performed by Dr. Heng Wang and Prof. Xiaopeng Li at the University of South Florida. The author performed and interpreted all other experimental work and wrote the manuscript.

Chapter 3: The project was conceptualized by the author, Dr. Junpeng Wang, and Prof. Jeremiah A. Johnson. Experimental work was performed by Dr. Junpeng Wang and the author. The author, Dr. Junpeng Wang, and Dr. Nathan J. Oldenhuis contributed to system design optimizations. Dr. Nathan J. Oldenhuis and David Lundberg provided materials for control studies. The author wrote the manuscript.

TABLE OF CONTENTS

Chapter 1. A unifying review of polymer networks: from rubbers and gels to porous frameworks

This chapter is reproduced from the following article with permission:
Gu, Y.†; Zhao, J.†; Johnson, J. A. Polymer networks: from plastics and gels to porous frameworks. *Angew. Chem. Int. Ed.* 2019, *59* (13), 5022–5049.
Text written by Dr. Yuwei Gu and author. Figures produced by author.

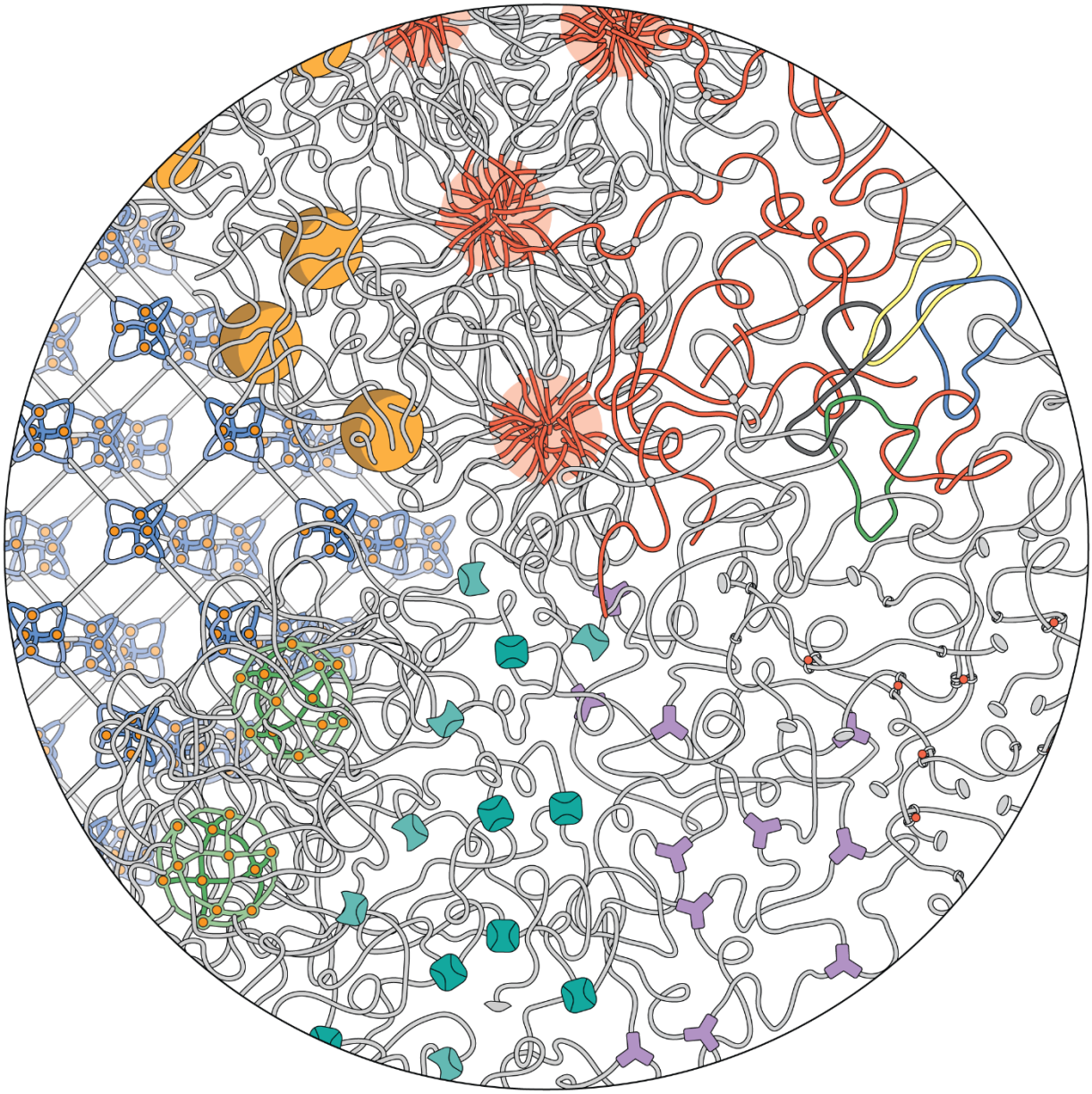

1.1 Introduction

When bifunctional molecules are linked together, linear macromolecules, or "linear polymers," with high molecular weights can form. Analogously, when molecules with functionality greater than two are linked together, three-dimensional (3D) macromolecules, or "polymer networks," with very high (classically referred to as "infinite")[1-2] molecular weights can form. Early organic chemists referred to polymerization, the process used to form linear and 3D polymers, as a "chemical combination involving the operation of primary valence forces," further stating that "the term polymer should not be used (as it frequently is by physical and inorganic chemists) to name loose or vaguely defined molecular aggregates."[1] Similarly, Wallace Carothers defined polymerization as, "any chemical combination of a number of similar molecules to form a single molecule."[1] These notions either implicitly or explicitly defined polymers as being composed of strongly (covalently) bonded constituents. Today, however, it is widely accepted that linear polymers and polymer networks can be constructed from covalent and/or non-covalent bonds; indeed, the full spectrum of bonding interactions, reaction mechanisms, and chemical compositions (*e.g.* organic, inorganic, biological) can be leveraged to design fascinating new polymer networks with exceptional properties.

From a structural perspective, polymer networks are composed of network "junctions" (in some cases, these can also be referred to as "crosslinks", defined as a bond that links one strand to another), which have three or more groups (the exact "branch functionality" we refer to as *f*) emanating from a core, connected together by *f* "strands." Strands can be linear polymer chains, flexible short molecules, rigid struts/linkers, etc. As noted above, junctions and strands in polymer networks can be linked together via physical interactions (*e.g.* van der Waals interactions, hydrophobic interactions, Coulombic interactions, metal-ligand coordination) or covalent bonds. Hence, polymer networks are conventionally classified as "physical" (supramolecular) or "chemical" (covalent) networks. It should be noted that this classification does not always accurately reflect material properties; bond strengths and exchange rates are much more informative. For example, given sufficiently strong and static physical interactions, physical networks can behave identically to chemical networks; alternatively, the incorporation of mechanisms for covalent bond exchange can result in chemical networks that exhibit adaptable mechanical properties regulated by external stimuli. Thus, the properties of polymer networks can vary widely depending on the composition of the junctions and strands as well as the formation and use conditions. With this broad view in mind, nearly all other polymer networks, regardless of their colloquial name (or acronym), structure, properties, etc. can generally be divided into one of four major classes: thermosets, thermoplastics, elastomers, and gels.

Thermosets are polymer networks where the junctions and strands are typically connected via covalent bonds and where the material is used at a temperature well below the glass transition temperature. They are rigid materials (Young's moduli of ~10^9 Pa) that are normally insoluble in all solvents and not processable once formed (unless a mechanism for junction/strand exchange is available, such as in covalent adaptable

networks/vitrimers). Classical thermosets typically degrade rather than become fluid upon heating. Some examples of commercially important thermosets include formaldehyde resins, polyurethanes, and epoxy resins.

Thermoplastics are networks of macromolecules connected together via non-covalent (supramolecular) interactions and where the material is used well below its glass transition temperature. Above a certain temperature, thermoplastics can transition from rigid solids to processable viscoelastic fluids that can, at least in principle, be remolded, healed, and recycled. We note that thermoplastics are conventionally considered as "non-crosslinked" due to the lack of covalent bonding between macromolecular chains; at their operating temperatures, however, the strength of the intermolecular non-covalent interactions within many thermoplastics is very high, resulting in mechanical properties similar to their thermosetting counterparts and justifying their classification as "polymer networks." Examples of thermoplastics are triblock copolymer networks derived from polystyrene-*b*-polybutadiene-*b*-polystyrene (*e.g.* Kraton), poly(methyl methacrylate) acrylics, polycarbonates, and polyamides (*e.g.* Nylon).

Elastomers are polymer networks that are used at temperatures above their glass transition temperature. They are typically composed of covalently bonded macromolecules, though they can also be constructed from non-covalent interactions. As a result, they are soft but non-fluid materials (Young's moduli of ~10^6 Pa or lower) that can be reversibly stretched to high extensions without breaking. Examples of elastomers include vulcanized natural rubber, silicone rubbers, and EPDM (ethylene propylene diene monomer) rubber.

Gels are polymer networks constructed from either covalent or supramolecular bonds that are swollen in liquid media such as water or organic solvents. The network structure ensures that the liquid is held within the material. Gels are usually very soft (Young's moduli of ~10^3-10^4 Pa) but are often capable of undergoing relatively large deformation. Examples of gels include gelatin, fibrin, and polyacrylamide gels.

As perhaps the most important, useful, and broadly studied class of materials from theoretical, academic, and industrial perspectives, polymer networks can have many unique properties, including elasticity, tunable mechanical strength, porosity, and swellability. These properties and others have led to numerous applications of polymer networks in everyday life, such as adhesives, cosmetics, sorbents, membranes, rubber products, coating materials, and food ingredients. Moreover, as recent developments have imparted unconventional properties (*e.g.* malleability, self-healing, conductivity, ultra-high permanent porosity, enhanced crystallinity, and stimuli-responsiveness) into polymer networks, they continue to hold great promise in advanced applications including drug delivery systems,[3] tissue engineering scaffolds,[4] soft actuators,[5] gas storage,[6] catalysis,[6-8] and electronic materials.[9] Thus, though polymer networks have been widely studied for more than a century, there are features of their structure that have only recently been leveraged to impart new properties, and an even deeper understanding is needed to realize the next-generation of functional, and ideally sustainable, polymer networks. In this review, we introduce key concepts related to the

formation, characterization, and properties of polymer networks. Our goal is to provide newcomers to the field with broad and up-to-date knowledge that can serve as a starting point for more detailed investigations of topics of interest. Major focus is devoted to polymer network structure, which includes both chemical and topological aspects. Additionally, several types of recently developed polymer networks with exceptional properties are highlighted.

1.2 Mechanisms for polymer network formation

There are three major mechanisms used for polymer network synthesis: addition/chain-growth polymerization, step-growth polymerization, and vulcanization.

Addition/Chain-growth polymerization occurs by a chain reaction wherein one monomer (typically an unsaturated compound, ***e.g.*** an olefin) at a time adds onto the end of growing polymer strands. In the presence of multifunctional monomers ("crosslinkers," ***e.g.*** divinylbenzene in the case of radical polymerization) that serve as junctions, two or more propagating polymer chains can be linked together ("crosslinked"), inducing the formation of a polymer network.

Step-growth polymerization starts from multifunctional monomers that are capable of reacting with each other to form dimers, then oligomers, and eventually polymers. If one or more of the monomers have a functionality (***f***) greater than two, branched polymers are formed; further reactions between these branched polymers can lead to polymer network formation. One common strategy for forming polymer networks through a step-growth process is referred to as "end-linking," where the chain ends of bifunctional molecules (referred to as "A_2") are linked by multi-functional monomers (referred to as "B_f") in a reaction between functional groups A and B.

Vulcanization is a special case wherein preformed polymers are crosslinked by forming bonds between functional groups present on the polymer backbone or sidechains. A well-known example is sulfur vulcanization of natural rubber, where the alkene groups of polyisoprene strands are crosslinked by reaction with sulfur. Notably, vulcanization can also be viewed as a step-growth polymerization wherein the pre-formed polymer (***e.g.*** polyisoprene) serves as a multifunctional (***e.g.*** B_f) component.[10]

For any polymer network forming process, there is a critical point known as the "gel point," where the reaction phase transitions from liquid to solid. Since many properties of polymer networks change abruptly at the gel point and are only useful beyond the gel point, several theoretical models have been developed to predict the gel point for various network formation processes, such as mean-field theory,[11-12] critical percolation theory,[12-13] and the kinetic gelation model.[14] Here we introduce two classical approaches—the Carothers model[15] and the Flory-Stockmayer model[11, 16]—to predicting the relationship between gelation and the extent of reaction in step-growth polymerization.

Carothers postulated that gelation occurs when the number-average molar mass of the macromolecules in a network forming process approaches infinity. In a step-growth polymerization containing equivalent numbers of A and B groups, Carothers derived that the critical extent of reaction p_c at the gel point is given by:

$$p_c = \frac{2}{f_{avg}} \tag{1}$$

where f_{avg} is defined as

$$f_{avg} = \frac{\sum N_i f_i}{N_i} \tag{2}$$

Here, N_i is the number of molecules of monomer i with functionality f_i. The Carothers model overestimates p_c because it is based upon $\overline{M_n} \to \infty$; practically, gelation occurs when the molar mass of the largest macromolecule(s) approaches infinity.

To better account for this portion of macromolecules with high molar mass, Flory and Stockmayer derived an expression for predicting p_c by calculating the point at which the weight average molar mass approaches infinity, or $\overline{M_w} \to \infty$. The Flory–Stockmayer model is a mean-field approach, where network formation is modeled as percolation on a Bethe lattice. For a step-growth polymerization involving A and B groups, they postulated that

$$p_c = \frac{1}{\left[r\left(f_{w,A} - 1\right)\left(f_{w,B} - 1\right)\right]^{\frac{1}{2}}} \tag{3}$$

Here, r, $f_{w,A}$ and $f_{w,B}$ are defined as below, where $N_{A,i}$ is the number of molecules of monomer i that possesses $f_{A,i}$ as the functionality of the group A, and $N_{B,i}$ is the number of molecules of monomer i that possesses $f_{B,i}$ as the functionality of the group B.

$$r = \frac{\sum f_{A,i} N_{A,i}}{\sum f_{B,i} N_{B,i}} \leq 1 \tag{4}$$

$$f_{w,A} = \frac{\sum {f_{A,i}}^2 N_{A,i}}{\sum f_{A,i} N_{A,i}} \tag{5}$$

$$f_{w,B} = \frac{\sum {f_{B,i}}^2 N_{B,i}}{\sum f_{B,i} N_{B,i}} \tag{6}$$

Because the Flory–Stockmayer model assumes no intramolecular cyclization, it tends to underestimate p_c. Nevertheless, when intramolecular reactions are negligible[17] or the fraction of cyclic defects can be experimentally determined,[18] the Flory–Stockmayer model provides accurate predictions of the gel point. Recently, by accounting for topological defects within the Flory–Stockmayer approach, Olsen and coworkers

developed a theory that quantitatively captures gel point suppression due to intramolecular cyclization.[19]

1.3 Polymer network structure

1.3.1 General features of polymer network topology

Chemical and topological structure together dictate the properties of polymer networks. The chemical structure is described by the chemical composition of network components; as we will discuss later in the review, tuning chemical composition is an effective approach to imparting functions to polymer networks.

Polymer network topology delineates how the junctions and strands of a polymer network are connected. Given that many properties (***e.g.*** elasticity, porosity, and swellability) of polymer networks have topological origins, there is growing interest in understanding and controlling polymer network topology from a molecular perspective. The vast majority of polymer networks are amorphous or semicrystalline (*i.e*. featuring amorphous and crystalline domains) and, thus, are rich in topological features that span across several length scales, ranging from the molecular (~Å) to submicron scale. Fig. 1 depicts these features for amorphous networks.

From ~10–100 nm, polymer network topology is characterized by inhomogeneity in junction/strand density (Fig. 1), which results from concentration fluctuations during network formation.[20] Small-angle scattering techniques provide semi-quantitative information at this length scale.[21-22]

Dangling/unreacted strands and/or junctions, entanglements, and loops of various orders comprise the macromolecular structures that dominate network structure on the length scale ranging from ~1–10 nm (Fig. 1). Dangling functionalities, often referred to as “dangling chains,” occur when a reactive group from the network precursors remains unreacted after network formation. Loops of order *l* are cyclic structures defined by the number of strands and junctions that comprise the cycle. Primary loops, the simplest cyclic topologies, form when both ends of one strand are attached to the same junction. A secondary loop is formed from two strands connected to the same two junctions. Although they contain rich topological information, conventional scattering and spectroscopic methods fail to characterize these macromolecular features.[23]

At the molecular level, network features are primarily dictated by chemistry rather than topology; branch functionality, however, is a critical molecular scale feature that dictates network topology (Fig. 1). While branch functionality is difficult to characterize experimentally, it can typically be predicted based on the functionality of network precursors.

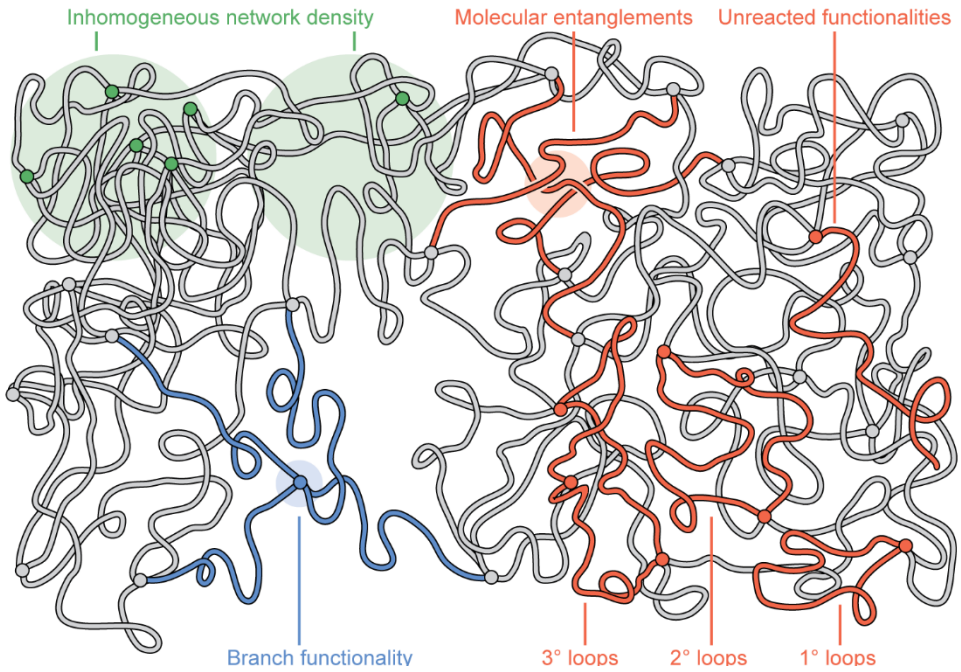

Figure 1. The multi-length scale complexity of polymer network topology. The topological features of amorphous polymer networks can be categorized into at least three different length scales: 10–100 nm (shown in green), 1–10 nm (shown in red), and <1 nm (shown in blue).

Although conventional scattering or spectroscopic techniques provide insights into network topology, these techniques in general lack molecular precision for non-(semi)crystalline networks. To characterize the often chemically indistinguishable (macro)molecular-level topological features in amorphous regions of polymer networks (*e.g.* unreacted functionalities, loops of various orders), theory/simulation, swelling experiments, and mechanical tests are often used. Though broadly applicable and informative, these methods rely upon presumed and often untested relationships between network topology and properties.[24]

Multiple-quantum nuclear magnetic resonance (MQ NMR) spectroscopy and network disassembly spectrometry (NDS) are two recently developed methods for probing macromolecular topological features quantitatively.[23, 25] MQ NMR distinguishes between local network structures through their subtle differences in chain dynamics. Using a multicomponent fitting analysis, fractions of various topological features can be extracted from MQ NMR signals, though it is difficult to distinguish features with similar dynamics such as dangling functionalities and primary loops.[26-27] The use of MQ NMR for characterizing macromolecular-level polymer network topology has been extensively reviewed.[23, 28-29]

NDS, on the other hand, enables quantification of specific topological features of chemically labelled polymer networks via network degradation and analysis of the degradation products.[18] NDS has been used to quantify the dependency of primary and secondary loop fractions in model end-linked networks as well as vulcanized networks on precursor concentration, with excellent agreement between experimental data and simulated results.[10, 30-33]

In recent years, the development of “mechanophores,” which are molecules that are purposefully designed to undergo a specific chemical reaction in response to an applied stress, has provided a novel means to study polymer network structure across a variety of length scales.[34-35] In particular, mechanophores that change color or emit light have been leveraged to image stress buildup in regions of polymer networks,[36-37] while other types of reactive mechanophores that are capable of new bond formation following activation have been used to generate self-strengthening networks.[38] In a related vein, and somewhat reminiscent of photo-induced polymer network strand growth (see Section 1.3.3.4) for network strengthening,[39-41] the random homolytic cleavage of covalent bonds that occurs upon excessively straining polymer networks has been used to induced network healing via the growth of new polymer strands.[42] Moreover, the use of piezoelectric materials such as zinc oxide[43] or even water,[44] which are capable of generating free radicals in response to low-amplitude, high-frequency vibrational forces (e.g. ultrasound), have been used to control polymer growth; this strategy could provide another means to design self-strengthening networks. In the future, novel mechanophore designs coupled with additive manufacturing strategies will enable the development of novel classes of polymer networks ranging from optimized elastomers to advanced metamaterials.[45]

1.3.2 Scattering techniques for probing polymer network structure

A wide variety of scattering techniques are used to characterize structural/topological features of polymer networks. Depending on the type of network (***e.g.*** amorphous, semicrystalline, or crystalline), different methods are more informative than others. Nevertheless, all scattering techniques involve exposure of a sample to incident radiation and measurement of the intensity of scattered radiation as a function of the scattering vector q, where

$$q = \frac{4\pi \sin(\theta)}{\lambda} \tag{7}$$

Here, 2θ is the angle between the incident radiation and the detector measuring the scattered intensity; λ is the wavelength of incident radiation. Small-angle scattering (SAS), which collects and analyzes scattering at small angles ($q < 0.5$ Å^{-1}), is particularly suited for studying materials that possess structural features on the order of 1 to 100 nm.[46] SAS techniques including static light scattering (SLS), small-angle neutron scattering (SANS), and small-angle X-ray scattering (SAXS) are invaluable characterization tools for studying the topology of polymer networks on this length scale (*vide infra*). Other scattering methods such as wide-angle X-ray scattering (WAXS), powder diffraction, electron diffraction, and single-crystal X-ray diffraction are powerful for probing short length scales within ordered samples; these techniques are most applicable for studying (semi)crystalline polymer networks (***e.g.*** semicrystalline polymers, metal-organic frameworks (MOFs), covalent organic frameworks (COFs), etc.; see Section 1.5.2.2).[47-48]

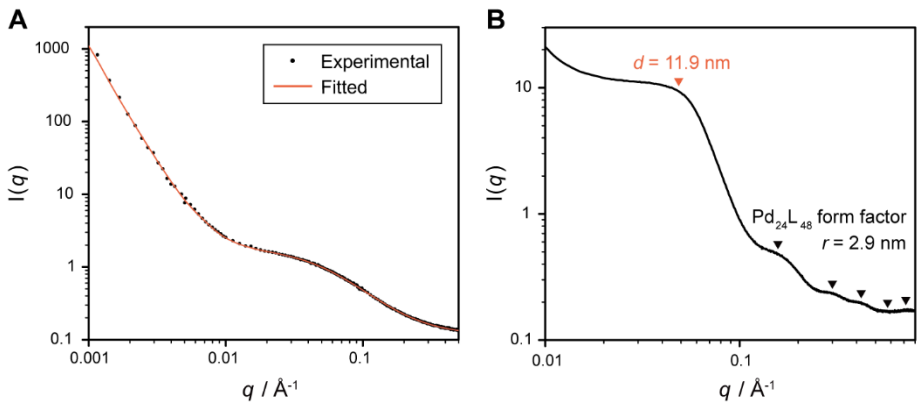

Figure 2. Small angle scattering characterization of polymer network structure. (A) A representative SANS profile of an end-linked PEG network prepared in D_2O. The data are fitted with the correlation length model. (B) A representative SAXS profile of a polyMOC gel where the network junctions are proposed to be discrete $Pd_{24}L_{48}$ supramolecular metal-organic cages (MOCs). The average distance between network junctions and the form factor of the $Pd_{24}L_{48}$ MOCs are determined from the curve.

Given that SANS and SAXS are particularly relevant to studying the most widely used types of polymer networks, *i.e.* those that are amorphous or semicrystalline, we discuss these techniques in further detail here. In either method, sufficient scattering contrast between background and structures of interest is necessary to identify key features in scattering patterns. For example, in gels, scattering contrast between the structural features of interest within the network, the rest of the network, and solvent is needed. While the network composition is intrinsic to its components, the solvent can be readily manipulated. In particular, because hydrogen and deuterium atoms have distinct neutron scattering lengths, SANS contrast can be easily imparted on a gel sample simply by swelling the gel in a deuterated solvent.

Fig. 2A shows a representative SANS pattern obtained for an end-linked poly(ethylene glycol) (PEG) network prepared in D_2O.[49] Correlations between network junctions are rarely observed as scattering peaks in such samples for two reasons: (1) gels derived from polymer end-linking are amorphous, lacking long-range order; (2) there is insufficient scattering contrast between junctions and strands. Hence, such SANS curves are fitted with physical models to extrapolate structural parameters. For gels derived from covalently linked polymers, SANS scattering profiles can be divided into two regions: the high-q region that characterizes polymer chains and the low-q region with features typically attributed to network inhomogeneities. The correlation length model describes features from both high- and low-q regions (Fig. 2A):[50]

$$I(q) = \frac{A}{q^n} + \frac{C}{1 + (q\xi_L)^m} + B \tag{8}$$

The first term describes Porod scattering from larger network features and the second term is a Lorentzian function describing scattering from smaller structures. A and C are constants, B is the incoherent background, n is the Porod exponent that reflects the degree of topological homogeneity at large length scales, m is the Lorentzian exponent

that is dictated by the polymer/solvent interactions, and ξ_L is the correlation length that is empirically related to the mesh size of the network.

SAXS is especially useful when network structural features of interest have distinct electron densities (*e.g.* metal-containing structures) that result in high X-ray scattering contrast. For example, Fig. 2B shows a SAXS pattern obtained for a gel composed of self-assembled metal-organic cage (MOC) junctions and PEG strands. In this sample, the network junctions are discrete $Pd_{24}L_{48}$ MOCs.[51] The scattered intensity I(q) obtained from SAXS can be expressed as P(q)*S(q), where P(q) is the form factor describing the size and shape of the network junctions and S(q) is the structure factor describing the spatial arrangement of the junctions. The five small peaks in the high-q regime in Fig. 2B were assigned to the form factor of a spherical particle with a radius of 2.9 nm, which agrees with the expected $Pd_{24}L_{48}$ cage size. The remainder of the curve was attributed to the structure factor S(q) of the system: the broad peak in the low-q regime corresponds to a d-spacing of 11.9 nm and describes the average distance between MOCs linked by PEG strands.

1.3.3 Structural control of polymer networks

As discussed above, polymer networks can be crystalline, amorphous, or both (semicrystalline). Many thermoplastics (*e.g.* Nylon, Kevlar, linear polyethylene, syndiotactic polystyrene) are semicrystalline or crystalline when processed using slow quenching or uniaxial stretching—conditions that maximize the reversibility of intermolecular interactions (*e.g.* van der Waals or hydrogen bonding interactions) and facilitate packing of polymer chains.[52] Moreover, as described in Section 1.5.2.2, the use of reversible bond formation between conformationally rigid monomers has recently enabled the synthesis of crystalline polymer networks, where the spatial distribution of junctions exhibits long-range order. A common strategy to control the structure of all types of polymers networks incorporates network precursors with preexisting topological features such as a defined branch functionality and/or a unique molecular architecture. Recently, methods that bias polymerization kinetics, such as semibatch monomer addition[32] and templated network synthesis,[49] have also been used to manipulate network topology.

1.3.3.1 Controlling branch functionality of polymer networks

Branch functionality (f) is a theoretical value that describes the number of elastically effective strands connected to a network junction; it is equal to the monomer functionality when there are no unreacted functionalities or loops. In practice, the number of elastically effective strands connected to a junction (effective branch functionality, f_{eff}) could be greatly reduced by the presence of topological defects.

In end-linked networks, the branch functionality can be controlled by changing the functionality of the network precursors: for example,[53] by end-linking an A_2 with B_3, B_4, or B_8 precursors, trifunctional (f = 3, Fig. 3A), tetrafunctional (f = 4), or octafunctional (f = 8) polymer networks can be synthesized. In the context of supramolecular networks, A_2

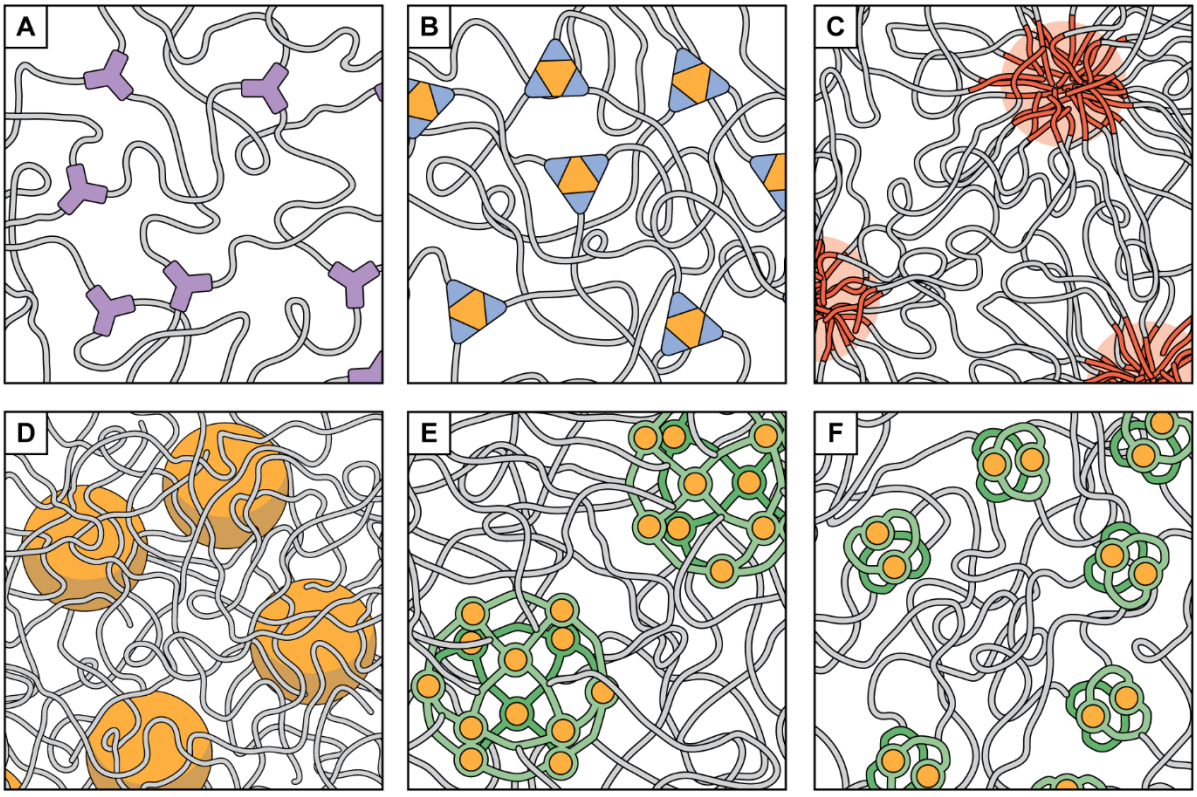

Figure 3. Controlling branch functionality in polymer networks. (A) End-linking A_2 and B_3 precursors forms a trifunctional polymer network. (B) Trifunctional network junctions based on tris-catechol-Fe^{3+} complexes. (C) Multicompartment hydrogels formed from amphiphilic ABA triblock copolymers possess crosslinks induced by the micellar self-assembly of the hydrophobic terminal blocks. (D) Polymer–nanoparticle hydrogel composites are crosslinked through physical adsorption of polymers onto nanoparticles. (E) Pd_2L_4 and (F) $Pd_{12}L_{24}$ polyMOC gels formed through self-assembly of MOCs as network junctions.

strands end-functionalized with coordinating ligands will form polymer networks with branch functionality dictated by the coordination number of a suitable metal ion. An example is the introduction of catechol onto polymer chain ends to form $f = 3$ network junctions upon the addition of Fe^{3+} due to the generation of tris-catechol-Fe^{3+} complexes (Fig. 3B).[54] Similarly, MOFs and COFs have branch functionalities defined by the identity of their metal clusters or multi-functional monomers, respectively (see Section 1.5.2.2).

Constructing high *f* polymer networks often relies on the use of self-assembled structures. For example, styrene-butadiene-styrene thermoplastic elastomers are based on the microphase separation of crystalline polystyrene blocks and amorphous polybutadiene blocks. Similarly, multicompartment hydrogels are formed from the self-assembly of ABA or ABC triblock copolymers (Fig. 3C) with hydrophobic end blocks and hydrophilic midblocks.[55-57] These networks possess micellar crosslinks of branch functionality equivalent to the aggregation number of the micelle,[58] typically $f > 100$. Alternatively, polymer-nanoparticle composite hydrogels obtain their high branch functionality through the physical adsorption of polymers onto the surface of

nanoparticles (Fig. 3D).[59-61] Solution-state studies indicate that hundreds of polymer molecules can adsorb onto a nanoparticle with a diameter of ~100 nm.[62]

PolyMOC networks, which feature network junctions derived from self-assembly of well-defined MOCs,[63] are another class of polymer networks with high yet precise branch functionality. The first reports of polyMOCs used relatively small MOCs and thus had low *f* values.[64-65] In 2016, Johnson and coworkers reported the first examples of polyMOCs with much higher *f*,[66] where $Pd_{12}L_{24}$ junctions (theoretical *f* = 24) were constructed from linear PEG strands end-functionalized with *para*-bispyridyl ligands and Pd^{2+} (Fig. 3E). Compared to an analogous Pd_2L_4 (theoretical *f* = 4) network (Fig. 3F), $Pd_{12}L_{24}$ polyMOC gels have higher storage moduli, longer relaxation times, and high loop densities such that no decrease in storage modulus was observed when 12.5% of polymer ligands were replaced with non-polymer-bound ligands. The defect tolerance of these materials allowed for tuning of their mechanical properties and dynamics by incorporation of different ratios of polymer- and non-polymer-bound ligands.[67]

1.3.3.2 Controlling polymer network strand topology

Many topologically intriguing macromolecular architectures have been realized through the development of advanced synthetic strategies and methods.[68-69] Leveraging these techniques, polymer networks with topologically unique motifs, such as cyclic polymers,[70] polyrotaxanes,[71] and polycatenanes,[72] have been reported.

Cyclic polymer networks are formed from the purposeful use of macrocycles for polymer network formation. An early example of a cyclic polymer network built exclusively from preformed cyclic polymers utilized crosslinking of the double bonds of cyclic poly(5-acetoxy-1-cyclooctene) (Fig. 4A).[73] The resulting gel exhibited a swelling ratio that increased with increasing precursor polymer concentration, an unusual effect proposed to arise from a mesh size reduction at low concentrations due to dominant intra-molecular cross-linking reactions (loop formation). Smaller macrocyclic scaffolds can also be used to generate cyclic polymer networks. For example, Dichtel and coworkers crosslinked the hydroxyl groups of macrocyclic β-cyclodextrin in the presence of tetrafluoroterephthalonitrile to obtain a mesoporous polymer network for the rapid removal of organic micropollutants.[74] Recently, DeForest and coworkers end-linked a macrocyclic A_2 monomer and a B_4 macromer using the strain-promoted azide–alkyne cycloaddition reaction, resulting in one macrocycle per network strand.[75] In each macrocyclic A_2 component, two degradation sites responsive to orthogonal stimuli (*i.e.* an enzymatically degradable oligopeptide sequence that cleaves in the presence of a matrix metalloproteinase and an *ortho*-nitrobenzyl ester that undergoes photocleavage upon ultraviolet light) were incorporated in parallel so that the degradation of the network required application of two inputs (*i.e.* enzyme and light), forming the basis of an “AND” biomaterial logic gate for environmentally triggered therapeutic delivery.

The outstanding mechanical properties of many commonly used polymer networks, e.g. rubbers, are derived from strand entanglements, which are mechanically interlocked, supramolecular topologies. In order to further extend this concept, researchers have

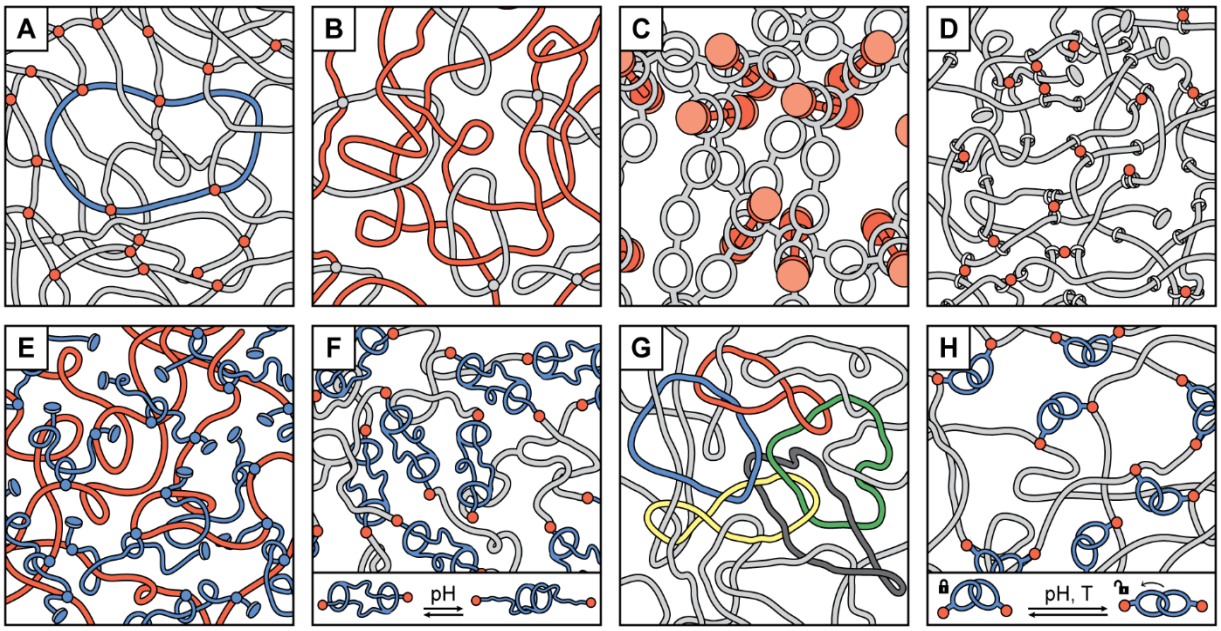

Figure 4. Polymer networks that leverage unique strand topologies. (A) A polymer network based on crosslinking cyclic polymers. (B) Copolymerization of methyl methacrylate (shown in red) and a methacrylate-functionalized cyclic poly(tetrahydrofuran) (shown in blue) results in concomitant threading of cyclic polymers and the formation of a polyrotaxane-based polymer gel. (C) Crosslinking poly(crown ether) strands (shown in black and grey) with bifunctional *sec*-ammonium axles (shown in red) provides a polyrotaxane-based network. (D) Crosslinking α-cyclodextrin groups threaded onto PEG chains results in "slide-ring gels" with movable crosslinks (analogous to entanglements). (E) Polymerization of *n*-butyl acrylate (shown in red) in the presence of polyester rotaxane crosslinker (shown in blue) forms a polyrotaxane-based network. (F) Incorporating bistable [*c*2] daisy chain rotaxanes (shown in blue) into polymer networks results in a network that can contract and expand via pH-triggered actuation of daisy chain units (inset). (G) A hypothetical polymer network formed completely from catenated rings (the "Olympic gel"). (H) Vulcanization of thiol-containing PEG derivatives (shown in grey) using bisvinyl [2]catenane crosslinkers (shown in blue) forms a network that can switch between tough and soft states through pH or temperature regulation of the catenane crosslinker rigidity (inset).

exploited concepts from the field of supramolecular chemistry to purposefully install new mechanically interlocked entanglements into polymer networks. For example, polyrotaxanes are mechanically interlocked molecular architectures that consist of macrocycles threaded onto a molecular axle. The threaded rings of polyrotaxanes can be connected to other rings or axles to form a polyrotaxane-based polymer network with movable crosslinks. These networks can be synthesized using *in situ* macrocyclic threading or rotaxane-first synthesis. *In situ* macrocyclic threading generally relies on the random penetration of growing polymer chains into macrocycle precursors.[76-78] For example, Tezuka and coworkers synthesized a polymer network by copolymerizing methyl methacrylate with a methacrylate-functionalized macrocycle (Fig. 4B).[77] The random threading process renders the exact topology of such polymer networks difficult to predict or to characterize. To address this deficiency, Takata and coworkers synthesized a well-defined polyrotaxane-based network, where dumbbell-shaped axles were introduced to poly(crown ether) strands through reversible thiol-disulfide interchange reactions (Fig. 4C).[79]

In contrast to *in situ* threading, “rotaxane-first” synthesis involves the use of preformed polyrotaxanes as precursors to obtain more well-defined polyrotaxane-based networks. “Slide-ring gels” prepared from crosslinking of α-cyclodextrin groups pre-threaded onto PEG are a remarkable example of networks prepared in this fashion (Fig. 4D).[80] The figure-eight shaped crosslinks are able to move freely and balance tension on threaded polymer chains, resulting in a “pulley effect” that gives this material its flexible, tough, and superabsorbent properties.[81-82] Similarly, enhanced toughness was observed in a slide-ring network developed by Takata and coworkers, where polyester rotaxane crosslinkers with vinyl-functionalized wheels and axles were polymerized with *n*-butyl acrylate (Fig. 4E).[83] More complicated rotaxane-based topologies have also been used in polymer network synthesis. For example, Giuseppone and coworkers incorporated bistable [*c2*] daisy chain rotaxanes, formed from the mutual threading of two rings with pendant axles, into trifunctional polymer networks (Fig. 4F).[84] The pH-triggered actuation (Fig. 4F, inset) of the daisy chain rotaxanes translated to a 50% expansion/contraction of the network volume in response to environmental stimuli.

Catenanes are another class of mechanically interlocked molecular architectures, in this case formed from two or more interlocked macrocycles. While polymer networks formed entirely from interwoven catenanes, so-called “Olympic Gel” polymer networks (Fig. 4G), were conjectured by de Gennes nearly four decades ago,[13] synthetic linear polycatenanes are rare,[85] and polycatenane-based networks are even rarer. Interestingly, networks made entirely from polycatenanes—in the form of over 5000 cyclic, mechanically interlocked DNA strands—were discovered in the organism *Crithidia fasciulata*; such structures, referred to as kinetoplast DNA, provide a beautiful example of how biology regulates the topology of polymer networks to control functions such as gene expression.[86] In synthetic systems, a plausible polycatenane network was reported by Endo and coworkers from the bulk polymerization of 1,2-dithiane,[87] where multiple analytical techniques suggested the presence of cyclic entanglements. Recently, a catenane-based polymer network designed by Huang and coworkers utilized bisvinyl [2]catenanes to crosslink thiol-containing PEG chains (Fig. 4H).[88] The resulting network displayed stimuli-responsive tough and soft mechanical states, resulting from the pH- and temperature-dependent binding between the catenane rings (Fig. 4H, inset).

1.3.3.3 Controlling loops of various orders in polymer networks

Most polymer networks are rich in elastically defective topological structures such as unreacted functionalities and loops of various orders. Unreacted functionalities can be controlled by altering the reaction stoichiometry or through the deliberate doping of monofunctional network precursors.[89] In contrast, controlling the fraction of loops of various orders in amorphous polymer networks is much more challenging.

If two different multifunctional monomers are employed for step-growth polymer network formation, then primary loops can be precluded. For example, Sakai and coworkers used tetrafunctional network precursors to generate A_4 + B_4 networks that cannot form primary loops.[90] Though these “Tetra-PEG” networks feature remarkably high

mechanical strength[91] and a homogeneous topological structure,[92] they are not immune to the formation of loops of higher orders.[26, 93-94] Johnson and coworkers introduced semibatch monomer addition as a method to control loop formation in end-linked polymer networks by biasing network formation kinetics.[32-33] This work demonstrated that slow addition of B_f to A_2 during network formation allows for the capping of each B functionality with excess A groups, resulting in a ~50% reduction in primary loops and significantly enhanced shear storage moduli compared to networks synthesized by conventional batch mixing.

Templation also provides a way to control the topological features of polymer networks. For example, a “traceless topological modification” approach that strategically incorporates self-assembly motifs within the leaving groups of network precursors was recently reported.[49] In this system, A_2 + B_4 PEG networks were synthesized via potassium acyltrifluoroborate (KAT) ligation. Aggregation of network precursors in aqueous solution prior to gelation was controlled by varying the hydrophobicity of the leaving groups of the KAT ligation reaction. Cleavage of these leaving groups from the network during its formation led to “topologically isomeric” polymer networks with identical chemical compositions but different density fluctuations and loop fractions, resulting in distinct mechanical properties.

1.3.3.4 Controlled radical polymerization in polymer network synthesis

Among the various chain-growth polymerization (Section 1.2) techniques (*e.g.* anionic polymerization, cationic polymerization, and radical polymerization), radical polymerization is widely used in polymer network synthesis due to its broad monomer scope and functional group tolerance. Radical polymerization involves four elementary processes: initiation, propagation, chain transfer, and termination. Conventional free radical polymerization suffers from a slow rate of initiation relative to propagation as well as unavoidable termination, together leading to limited control over chain length/topology. In contrast, the concepts of reversible termination and degenerative chain transfer[95-96] enabled to the development of modern reversible deactivation radical polymerization (RDRP) techniques that provide convenient access to polymers with predetermined molecular weights and well-defined microstructures.[97] Three major RDRP techniques are most commonly used for polymer network synthesis: nitroxide mediated polymerization (NMP),[98-100] atom transfer radical polymerization (ATRP),[53, 101-103] and reversible addition-fragmentation chain transfer (RAFT) polymerization.[104-106] All of these methods rely on a reversible equilibrium that effectively lowers the concentration of propagating radicals and thus slows the rate of bimolecular termination reactions. NMP is based on a dormant species (an alkoxyamine) in equilibrium with a propagating radical and a nitroxide (Fig. 5A). ATRP employs alkyl halides as dormant species that are reversibly activated by a lower oxidation state metal complex through an electron transfer process (Fig. 5A). RAFT polymerization makes use of a chain transfer agent (CTA, *e.g.* dithioester, dithiocarbamate, xanthate, and trithiocarbonate) to establish a degenerative chain transfer reaction (Fig. 5A). The CTA-based radical intermediate of the chain transfer process effectively plays the role of the dormant species enabling a RDRP process. Notably, RAFT was originally strictly defined as

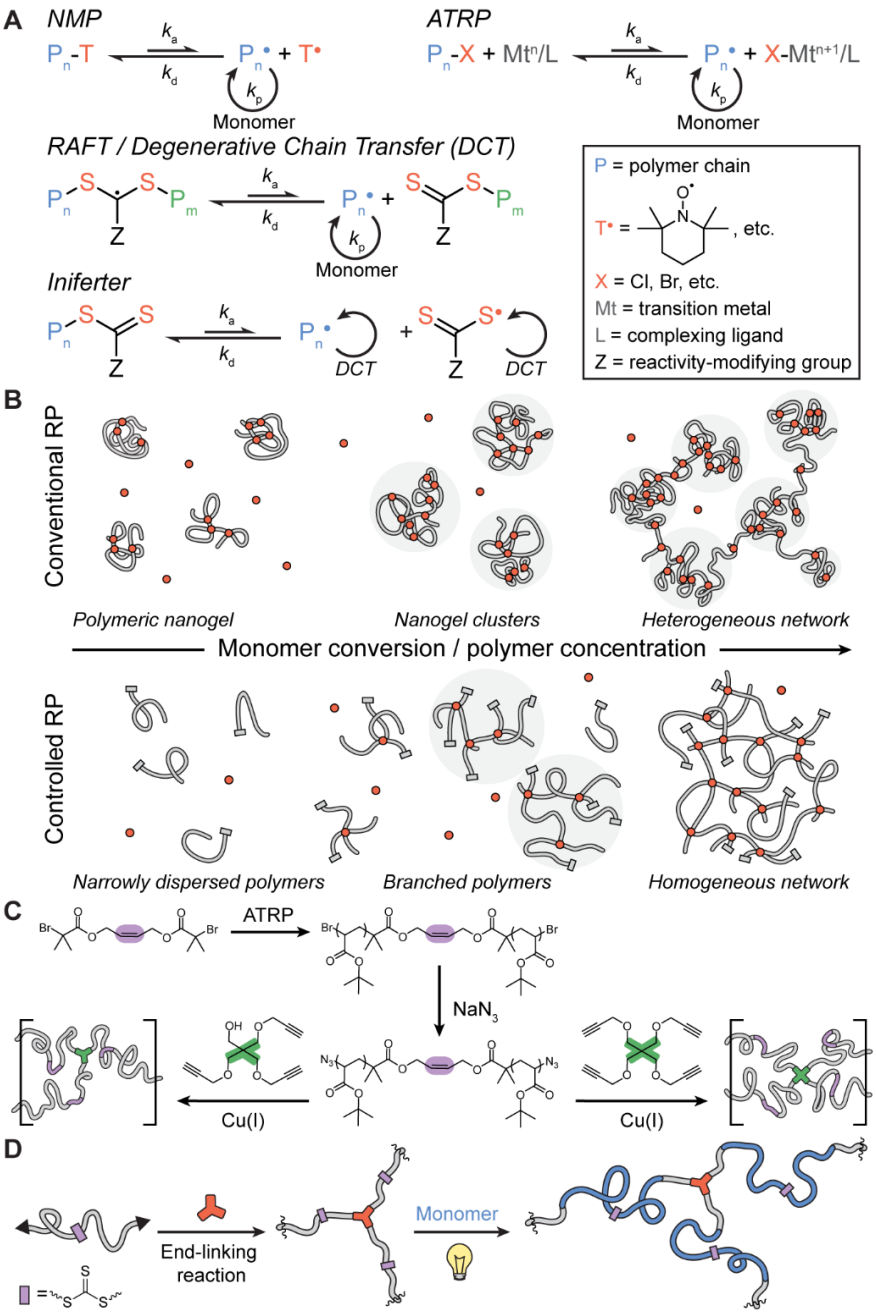

Figure 5. Reversible deactivation radical polymerization (RDRP) processes in polymer network synthesis. (A) Mechanisms of four of the major RDRP techniques used in polymer network synthesis. (B) In contrast to the heterogeneous networks synthesized via conventional radical polymerization, CRP leads to homogeneous networks. (C) Telechelic poly(*tert*-butyl acrylate) was synthesized via ATRP followed by conversion of the terminal bromides to azides. End-linking of this polymer with tris- or tetrakis-acetylene monomers through copper(I)-catalyzed azide-alkyne cycloaddition (CuAAC) formed end-linked organogel networks. The olefins incorporated in the ATRP initiator rendered the networks degradable by ozonolysis. (D) Photo-growth of a polymer network was achieved by incorporating trithiocarbonates into network strands, where the trithiocarbonate simultaneously acts as an initiator, transfer agent, and terminator ("iniferter") to enable controlled network growth in the presence of monomers/crosslinkers and light irradiation.

lacking reversible termination processes,[104] thus distinguishing it from earlier-reported initiation, chain transfer, termination, *i.e.* "iniferter" processes (Fig. 5A), that used similar CTAs.[95] Iniferter-based CRP methods have undergone a renaissance in recent years, particularly with the advent of photoredox catalysis;[107-108] these methods have proven useful for the synthesis of photoactive polymer networks with topologies and compositions that can be spatiotemporally modulated using various wavelengths of light.[39, 41, 109-111]

Though polymer networks can be synthesized using conventional free radical polymerization of vinyl monomers and divinyl crosslinkers, the low rate of initiation compared to propagation along with extensive radical termination inherent to this process lead to large network density fluctuations that negatively impact the mechanical properties of the resulting materials (Fig. 5B). In contrast, the high initiation relative to propagation rates of RDRP processes provide a relatively homogeneous distribution of dormant branched polymers in the early stages of network formation (Fig. 5B); these network fragments can diffuse before they are reactivated, preventing the formation of densely-crosslinked network clusters and producing a more homogenous network overall. This concept was first demonstrated by Fukuda and coworkers using NMP of styrene with 4,4′-divinylbiphenyl in the presence of an oligomeric polystyryl adduct with 2,2,6,6-tetramethylpiperidinyl-1-oxy (TEMPO) as an initiator.[112] The RDRP-based crosslinking led to a homogeneous network as evidenced by gelation consistent with the Flory–Stockmayer model, as well as a remarkable difference in swelling ratio and elastic modulus compared to analogous networks synthesized via conventional free radical polymerization. In addition, ATRP[113-115] and RAFT polymerization[116] have also been exploited for the synthesis of polymer networks with homogeneous structures and enhanced properties compared to their free radical counterparts.

As alluded to above, RDRP processes enable convenient access to complex macromolecules with predetermined molecular weights and topologies that are otherwise difficult to synthesize and may readily serve as precursors for polymer network fabrication. For example, Lodge and coworkers used RAFT polymerization to grow poly(*N*-isopropylacrylamide) (PNIPAm) blocks from a linear PEG macroinitiator, end-functionalized with trithiocarbonate-based CTAs.[57] The obtained triblock copolymer was shown to form a multicompartment hydrogel (Section 1.3.3.1) upon heating. Moreover, because RDRP methods produce polymers with defined chain-end functionality, they offer a powerful strategy for the synthesis of α,ω-end-functional (telechelic) polymers that can subsequently be used to prepare end-linked polymer networks. For example (Fig. 5C),[117] a bifunctional ATRP initiator with an internal alkene was used to synthesize α,ω-bromine terminated poly(*tert*-butyl acrylate) (P*t*BA) via ATRP. After quantitative conversion of the terminal halides to azides, the resulting telechelic polymers were coupled to tris- or tetrakis-acetylene monomers through a step-growth copper(I)-catalyzed azide-alkyne cycloaddition reaction, forming tri- or tetrafunctional polymer networks, respectively. Ozonolysis of the internal alkenes of these networks produced star polymer degradation products with $\overline{M_n}$ values equal to 1.5 (when the tris-acetylene was used) or 2 times (when the tetrakis-acetylene was used) that of the linear telechelic polymer precursor. In addition, degradation products with

half the molecular weight of the telechelic polymer precursor, corresponding to dangling strands within the network, were observed. This approach of using regioselective polymer network degradation to infer parent polymer network structure set the stage for the later development of NDS (Section 1.3.1).

When initiating sites are incorporated into polymer networks, RDRP techniques can enable facile post-synthesis modification to drastically transform the properties of polymer networks. Moreover, recent developments of photocontrolled living radical polymerizations (photo-CRP)[108] provide spatial and temporal control of this post-synthetic network transformation. In 2013, Johnson and coworkers demonstrated that polymer network strands containing trithiocarbonates can grow in the presence of monomers under long-wavelength (~365 nm) UV light irradiation (Fig. 5D).[39] Later, application of photoredox catalysis significantly improved control in this "photo-growth" strategy.[41] Through iniferter mechanisms, photo-growth enables transformation of the shape as well as the physical and mechanical properties of CTA-functionalized polymer networks, converting preformed networks into more advanced, stimuli-responsive materials with complex shapes. This strategy was termed "living additive manufacturing,"[41] as it offers a way to repeatedly modulate the geometry and properties of polymer networks that is distinct from traditional layer-based 3D printing methods. Recently, Matyjaszewski and coworkers reported the preparation of structurally tailored and engineered macromolecular (STEM) gels made possible with RDRP.[118-120] Primary STEM gels were synthesized via RAFT polymerization of (meth)acrylate monomers, di(meth)acrylate crosslinkers, and "inimers" containing latent initiation sites and monomers. Swelling with a second monomer enabled the growth of diverse sidechains from the networks through photocontrolled grafting-from ATRP, facilitating the transformation of primary STEM gels into amphiphilic as well as softer or stiffer materials.

1.3.3.5 Topology-switchable networks

The critical role that topology plays in dictating the properties of materials has inspired a class of polymer networks that can interconvert between two different stable topological states. For example, polyMOC gels formed with photoswitchable, bis-pyridyl dithienylethene (DTE) ligands are able to change between two branch functionalities using light as a stimulus. In this system, the network junctions switch from Pd_3L_6 (f = 6) to $Pd_{24}L_{48}$ (f = 48) upon irradiation with ultraviolet light and back with green light (Fig. 6A).[51] Large changes in the storage modulus are possible upon topology switching; perhaps more interestingly, the different ligand exchange dynamics of the two MOCs are reflected in an order of magnitude difference in the characteristic stress-relaxation times of their corresponding networks, enabling the material to be switched repeatedly between a soft and self-healing state and a stiff dimensionally stable state. For further discussion on the ramifications of network structure/topology on mechanical behaviors, see Section 1.4 below.

Stupp, Luijten, and coworkers recently reported a peptide-based network that experiences topology switching on large length scales in response to added chemical

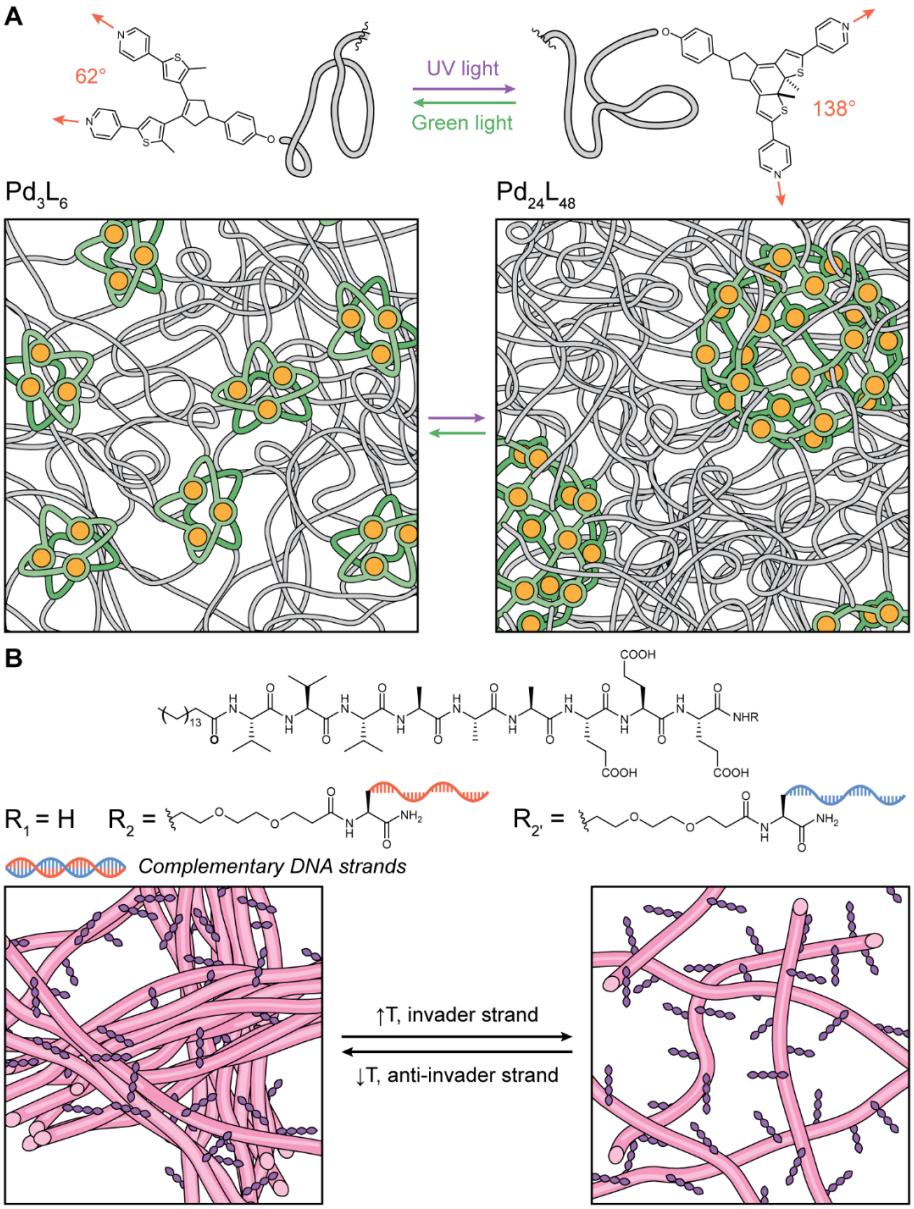

Figure 6. Topology-switchable materials. (A) PolyMOC gels formed with photoswitchable DTE ligands can be modulated between two stable topological states with different branch functionalities, loop contents, and density fluctuations using light as a stimulus. Depending on its topological state, the material has drastically different properties, allowing it to act like two traditional materials in one. (B) Co-assembly of three peptide amphiphiles, two possessing complementary oligonucleotide terminal segments, results in a hydrogel that can interconvert between Topology 1 (twisted bundles and single fibers) and Topology 2 (homogenous fibrillar network) upon changes in temperature or the addition of “invader” or “anti-invader” DNA strands to facilitate strand displacement.

stimuli (Fig. 6B).[121] The co-assembly of three peptide amphiphiles, two possessing complementary oligonucleotide terminal segments, resulted in a hydrogel formed from twisted bundles and single fibers with diameters on the micrometer and nanometer scale, respectively. The peptides with covalently linked nucleotide segments were found primarily in fiber bundles, which could be dissembled to form a homogenous fibrillar

network topology by breaking inter-fiber DNA duplexes through heating or adding "invader" strands. The reversible formation and disassembly of bundles in this network resulted in 15-fold changes in storage moduli. In addition, the two topological states were shown to have divergent effects on neural cell differentiation.

While topology-switchable materials have only emerged recently, they hold potential in various applications, such as soft robotics, adaptable biomaterials, next-generation adhesives, additive manufacturing, and responsive actuation, and they may serve as model polymer networks for fundamental polymer physics studies. We anticipate the development of topology-switchable polymer networks capable of alternating between more than two stable states, achieving unique functions in each state.

1.4 Basic properties of polymer networks

1.4.1 Elasticity

Elasticity is a characteristic feature of many polymer networks such as elastomers and gels. The physical origin of rubber elasticity comes from the loss in conformational entropy that occurs as a strand in a network is stretched; this process is commonly depicted as the unwinding of flexible, random coils. Once the external stretching force is removed, an elastic entropic force restores the strands to their unstretched and higher entropy state. As a result, network strands can be considered as entropic molecular springs. In this section, we introduce the two simplest theories that capture the entropic origin of rubber elasticity for non-entangled polymer networks at the molecular level: the affine and phantom network models.

The affine network model[11] assumes that the relative deformation experienced by each network strand is the same as the macroscopic deformation applied to the entire network. When network strands are treated as Gaussian chains and the polymer network is assumed to be incompressible (*i.e.* Poisson's ratio is 0.5), the stress-deformation behavior of an affine network in response to a uniaxial force is expressed as

$$\sigma = \nu_{eff} RT \left(\lambda - \frac{1}{\lambda^2} \right) \tag{9}$$

where σ is the engineering stress, defined as the applied force divided by the initial cross-sectional area of the material; λ is the ratio of the final length to the initial length of the material along the direction of the applied force (*Note*: when describing material deformation in a tensile test, engineering strain ε is sometimes used in place of λ. ε is defined as the ratio of the total deformation to the initial length of the material along the direction of the applied force. Hence, $\varepsilon = \lambda - 1$); ν_{eff} is the density of elastically effective chains; R is the gas constant; and T is the temperature. The shear modulus, G, which correlates with the Young's modulus E, can be calculated from Eq. 10 (where ν is Poisson's ratio):

$$G = \frac{E}{2(1+\nu)} = \nu_{eff} RT \tag{10}$$

Unlike the affine network model, the phantom network model[122] assumes that network junctions can fluctuate around their average positions. These fluctuations reduce the conformational restrictions experienced by strands, which, in turn, lowers the net free energy of the system relative to the affine network. In the phantom model, the shortest-path tree of network strands connecting each junction to the network surface is simplified as an effective chain that captures the cumulative behavior of the network. This simplification, which takes into consideration the network branch functionality *f*, leads to an expression for the phantom network modulus:[12]

$$G = \nu_{eff} RT \left(1 - \frac{2}{f}\right) \tag{11}$$

As a result, the predicted shear modulus in the phantom network model is lower than that of the affine network model. The equation to calculate the engineering stress for the uniaxial deformation of a phantom network remains the same.

$$\sigma = G\left(\lambda - \frac{1}{\lambda^2}\right) \tag{12}$$

E is often determined from the initial slope of the stress-strain curve under tensile force (Fig. 7A), which is measured using a tensile testing instrument (*e.g.* Instron). On the other hand, *G* is typically determined from oscillatory shear rheology (Section 1.4.3). These methods provide seemingly simple opportunities to experimentally evaluate the affine and phantom models. This approach is complicated, however, by the presence of elastically defective structures in real polymer networks, which preclude an accurate determination of ν_{eff}. Johnson, Olsen, and coworkers developed real elastic network theory (RENT), a modified phantom network model that incorporates the effect of loops of various orders to predict network elasticity.[123-124] Using accurately determined ν_{eff}

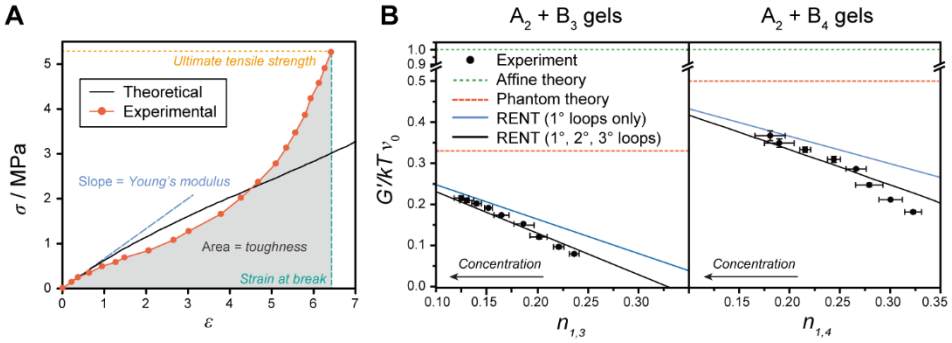

Figure 7. Basic features of non-entangled polymer network elasticity. (A) Experimental stress-strain curve (red) for a crosslinked elastomer under a uniaxial tensile force.[128] The black curve is the classical form (Eq. 11) fit to the small deformation data. (B) Primary loop fractions in trifunctional ($n_{1,3}$) and tetrafunctional ($n_{1,4}$) gels were characterized by NDS and used to simulate higher-order loop fractions. RENT was developed to predict the effects of loops of various orders on network elasticity. The experimentally determined $G'/kT\nu_0$ values (black dots), where ν_0 is the total strand density (including both elastically effective and defective strands), were compared to predictions of affine theory (green dashed line), phantom theory (green dashed line), RENT with only a correction for primary loops (blue line), and RENT accounting for primary and higher-order (2° and 3°) loops (black line).

based on primary loop characterization data obtained through NDS and simulations, RENT precisely predicted the shear elastic moduli G of gels with $f = 3$ or 4 (Fig. 7B). It should be noted that in the original RENT, the predicted impact of larger loops (*i.e.* loops of order three or above) on network elasticity was approximated. Recently, Lang proposed an equivalent resistance method to exactly solve for the impact of finite loops with arbitrary order on elasticity.[125] Inspired by this approach, Olsen and coworkers modified RENT and found that under classical assumptions of phantom network theory, loops with order three or above have zero net impact on the overall elasticity.[126]

Deliberately designed model polymer networks have demonstrated both affine and phantom network behaviors. In 2013, by varying the polymer concentration in $A_4 + B_4$ Tetra-PEG gels, Sakai and coworkers observed a transition between phantom and affine behaviors near the overlapping concentration of the network precursors.[127] Recently, Johnson and coworkers reported a photoswitchable polyMOC gel that demonstrated not only a change in branch functionality ($f = 6$ to 48) but also a concomitant conversion from phantom to affine and back to phantom behavior upon UV and green light radiation, respectively.[51] Taken together, these results suggest that many factors (*e.g.* concentration, branch functionality, loop content, and length of network strands) dictate the extent of junction fluctuation, leading to more phantom- or affine-like behavior. Thus, choosing a model to predict the behavior of a given polymer network requires careful consideration.

One limitation of these classical non-entangled rubber elasticity theories is the Gaussian statistics applied to describe deformed polymer chains, which lead to significant variations from experiment. For example, Fig. 7A shows an experimentally obtained stress-strain curve (red) for an amorphous crosslinked elastomer under uniaxial tension and the corresponding classical fit to these data using Eq. 12 (black).[128] While the classical fit is acceptable for small deformations ($\varepsilon < 0.5$), "strain-softening" at intermediate deformations and "strain-stiffening" at high deformations, both of which are not captured by the classical model, are observed experimentally.[12] The strain-softening behavior is attributed to an increase in strand fluctuations, which reduce the modulus as strands within the network are moved apart. Strain-stiffening at high deformations is attributed to the non-Gaussian statistics of highly deformed chains or, in several cases, stress-induced strand crystallization. In addition to these features, Fig. 7A provides examples of other key parameters that can be obtained from the stress-strain curve, such as the Young's modulus, strain at break, toughness (*i.e.* the area under the stress-strain curve), and ultimate tensile strength (*i.e.* the maximum stress that a material can withstand during a tensile test, often distinct from the stress at fracture).

As noted above, the affine and phantom network models assume no strand entanglements. In polymer networks made of long linear polymers, entanglements effectively serve as additional supramolecular crosslinks to increase the network modulus and toughness. Stress-deformation behaviors of entangled elastomers can be phenomenologically fitted using the Mooney–Rivlin model to empirically obtain the contribution of entanglements towards elasticity.[12, 29] Recently, Matyjaszewski, Sheiko, and coworkers demonstrated the severe reduction of trapped entanglements in

elastomers made of densely grafted bottlebrush polymers.[120, 129-130] In these solvent-free polymer networks, the network strands are effectively swollen by the low T_g grafted sidechains, leading to low moduli comparable to conventional solvent-containing gels. These materials demonstrate stress-strain behaviors resembling a variety of biological tissues[131] and hold great promise for biomaterial applications.[132]

1.4.2 Swelling of polymer networks

Polymer networks constructed from strong (*e.g.* covalent) bonds typically do not dissolve in solvents. Instead, such networks absorb solvent up to an equilibrium concentration and undergo a concomitant increase in volume. The equilibrium degree of swelling is dictated by a balance between the free energy of polymer-solvent mixing and the free energy cost of expanding the network, which is expressed by the Flory–Rehner equation[11, 133] for isotropic swelling of an affine polymer network:

$$\ln(1-\phi_{eq}) + \phi_{eq} + \chi\phi_{eq}^2 = \nu_{eff} V_1 \left(\frac{\phi_{eq}}{2} - \phi_{eq}^{1/3}\right) \quad (13)$$

where ϕ_{eq} is the volume fraction of the polymer network in the equilibrium swollen state, χ is the Flory–Huggins polymer-solvent interaction parameter, ν_{eff} is the density of elastically effective strands in the unswollen elastomer, and V_1 is the molar volume of the solvent.

Although the Flory–Rehner equation shows good agreement with many experiments,[134] it has several limitations. First, it can only be applied to describe the swelling of polymer networks prepared under solvent free conditions, whereas many polymer networks are prepared in solvents. Second, Flory and Rehner's approach estimates the mixing free energy using Flory–Huggins theory, which underestimates correlations between monomers along the same chain.[12] Third, this equation assumes a Gaussian distribution of chain conformations. To address these limitations, several modified theories have been developed to describe the equilibrium swelling behavior of polymer networks.[12-13, 135-136]

As suggested by the Flory–Rehner equation, the equilibrium swelling ratio is readily tunable by varying the solvent quality (χ) or ν_{eff}. In addition to these factors, the use of charged monomers can dramatically increase swelling capability due to the large osmotic pressure contributed by dissociated counterions.[137] In addition, non-swellable hydrogels can be prepared through sophisticated network design. In 2014, Sakai and coworkers synthesized hydrogels from hydrophilic PEG and thermoresponsive poly(ethyl glycidyl ether-co-methyl glycidyl ether), the latter of which displays lower critical solution temperature (LCST) behavior and becomes insoluble in water above 25 °C. Thus, while the hydrogel prepared in this study swelled significantly in water at 10 °C, its volume and mechanical properties remained constant when exposed to water at physiological temperatures due to shrinking of the thermoresponsive polymer component, which counteracted swelling of the hydrophilic polymer component.[138]

The simple ability to control the swelling of polymer networks has recently enabled exciting new applications of these materials. For example, fixing/crosslinking biological tissues onto hydrogels has been exploited to obtain high-resolution optical microscopy images in a technique referred to as CLARITY.[139] Building off of this approach, Boyden and coworkers developed a technique called "expansion microscopy" (ExM) wherein biological specimens are fixed in a polyelectrolyte gel that can swell by almost two orders of magnitude. This swelling leads to physical magnification of the specimen, enabling routine imaging of objects that were closer than the optical diffraction limit prior to swelling.[140] Recently, the same group applied the inverse of this concept to nanofabrication: micron-scale patterns embedded in hydrogels were reduced down to the nanoscale upon dehydration/shrinkage of the hydrogels by up to 10-fold.[141] Moreover, various ways of controlling network swelling have led to recent developments of shape-morphing materials,[142-144] which rely on anisotropic swelling behaviors within polymer networks. Details of these methods can be found in recent reviews.[145-146]

It should be noted that the swelling of networks provides evidence for their porosity (*i.e.* void space in a material that can accommodate guest molecules such as solvent). Porous materials are typically categorized into three classes that have different pore sizes: macroporous (pore diameter larger than 50 nm), mesoporous (pore diameter between 2 nm and 50 nm), and microporous materials (pore diameter smaller than 2 nm). While conventional polymer networks undergo pore collapse upon solvent removal, as polymer strands can adopt many conformations in order to pack space efficiently, recent research efforts have popularized several classes of polymer networks that possess permanent porosity based on the use of rigid components (see Section 1.5.2).

1.4.3 Viscoelasticity of polymer networks

Polymeric materials exhibit both viscous and elastic characteristics upon deformation, meaning that their properties may vary with the time scale or frequency at which measurements are performed. To characterize this viscoelasticity with respect to tensile, compressive, or shear deformation, several types of experimental measurements are commonly applied, such as stress relaxation, creep, and oscillatory shear tests. In this section, we will focus on oscillatory shear rheology of polymer networks. We refer the reader to additional literature for a comprehensive understanding of polymer viscoelasticity.[12, 147-148]

Oscillatory shear measurements are often performed on dynamic mechanical analyzers or rheometers, where a sample is subjected to a sinusoidal shear strain $\gamma(t)$ with small amplitude γ_0 and angular frequency ω:

$$\gamma(t) = \gamma_0 \sin(\omega t) \tag{14}$$

The linear response of a viscoelastic material in terms of stress $\sigma(t)$ is sinusoidal with the same frequency ω, but leads the strain by a phase angle δ:

$$\sigma(t) = \sigma_0 \sin(\omega t + \delta) \quad (15)$$

The stress can be separated into two components that oscillate with the same frequency ω, one in phase with the strain and the other out of phase with the strain by $\pi/2$:

$$\sigma(t) = \gamma_0[G'(\omega)\sin(\omega t) + G''(\omega)\cos(\omega t)] \quad (16)$$

Eq. 16 defines the storage modulus $G'(\omega)$ and the loss modulus $G''(\omega)$, the former of which describes the elastic response of the material while the latter describes the viscous response. At a given frequency ω, if $G'(\omega) > G''(\omega)$, the material response is considered to be solid-like; $G'(\omega) < G''(\omega)$,the material is considered to exhibit fluid-like behavior.

Fig. 8A shows the viscoelastic response of a covalently crosslinked polymer network made by end-linking linear chains with two reactive ends.[49] $G'(\omega)$ for this network is constant over a wide range of frequencies and much higher than $G''(\omega)$. This constant value of $G'(\omega)$ is commonly taken as the shear modulus of the network. The variations in $G''(\omega)$ in the range of 1–100 rad/s are attributed to relaxation of the soluble fraction of the network as well as to network imperfections. In general, networks with large amounts of topological imperfections exhibit higher $G''(\omega)$ than those with more ideal topological structures.[149]

Polymer networks with dynamic bonds can have relatively complicated oscillatory shear rheological behaviors. For example, Fig. 8B shows the viscoelastic response of a polymer gel end-linked with tris-catechol-Fe^{3+} complexes as junctions.[54] Due to the transient nature of catechol-Fe^{3+} coordination bonds, the material dissipates energy rapidly at low frequencies with $G'(\omega) < G''(\omega)$; the material behaves increasingly solid-like, however, as frequency increases, eventually exhibiting a $G'(\omega)$ comparable to covalent polymer networks at frequencies higher than 1 rad/s. The reciprocal of the critical frequency ω_c where $G'(\omega) = G''(\omega)$, which is referred to as the characteristic relaxation time of the network τ_c, provides insight into the network dynamics. In polymer networks based on metal–ligand coordination, τ_c is often associated with molecular-level dynamics such as the kinetics of metal-ligand exchange.[150-151]

Oscillatory shear rheology can be applied to monitor network formation. Fig. 8C shows the evolution of storage moduli and loss moduli at three frequencies during the chemical crosslinking of polybutadiene.[152] As the crosslinking proceeds, the sample transitions from a viscous solution to an elastic solid, resulting in a change in viscoelasticity from $G'(\omega) < G''(\omega)$ to $G'(\omega) > G''(\omega)$. The crossover point at which $G'(\omega) = G''(\omega)$ is commonly used to define the gel point.[153]

Oscillatory shear measurements can also be performed at variable temperatures to study the temperature-dependence of material properties. This technique is especially useful for polymer networks containing dynamic bonds that are sensitive to temperature. Fig. 8D shows the storage and loss moduli (measured at 1 rad/s) as a function of

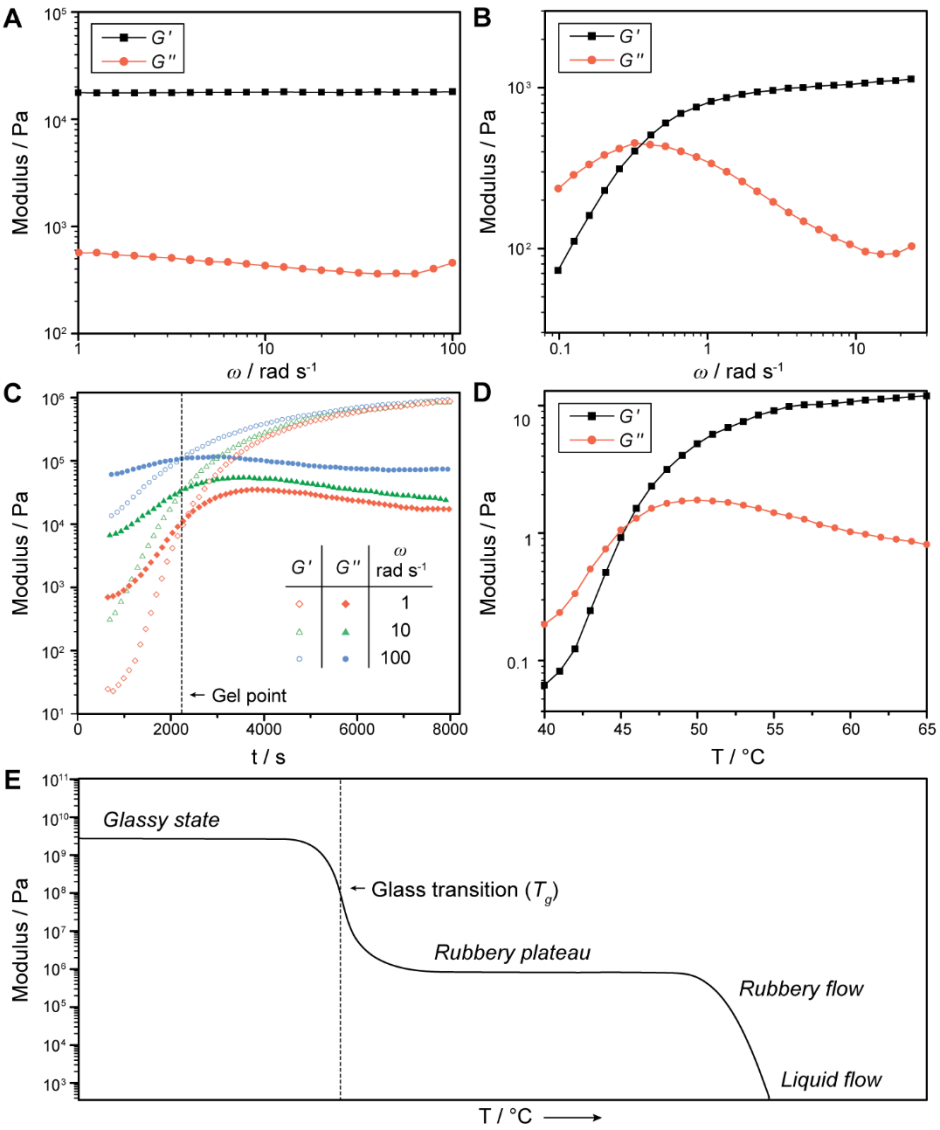

Figure 8. Oscillatory shear rheology of polymer networks. (A) Frequency sweep rheology of a covalently end-linked PEG gel. (B) Frequency sweep rheology of supramolecular end-linked gel with tris-catechol-Fe^{3+} junctions. (C) *G′* and *G″* at three frequencies (ω = 1, 10, and 100 rad/s) during the chemical crosslinking of polybutadiene. (D) The temperature dependence of *G′* and *G″* (measured at ω = 1 rad/s) for a thermoresponsive hydrogel made from PNIPAm-PDMA-PNIPAm.
(E) Temperature dependence of the Young's modulus for an entangled polymer sample. The rubbery plateau represents a temperature regime wherein strand entanglements provide transient network junctions (mechanical crosslinks) that are elastically effective.

temperature for an aqueous solution of a triblock copolymer ABA, where the terminal A blocks are thermoresponsive PNIPAm and the middle block B is hydrophilic poly(*N*,*N*-dimethylacrylamide) (PDMA).[154] Above the LCST of PNIPAm, the terminal A blocks transition from hydrophilic to hydrophobic, inducing the formation of multicompartment hydrogels. Gelation was evidenced by a change of material properties from $G'(\omega) < G''(\omega)$ to $G'(\omega) > G''(\omega)$ around 45 °C.

Entanglements in linear polymers, which can be viewed as dynamic mechanically interlocked bonds, can be experimentally observed through analysis of the modulus as a function of either temperature or time (Fig. 8E). In the classical case of amorphous, entangled polymers that lack covalent crosslinks, at temperatures below T_g a high Young's modulus is observed. At intermediate temperatures above T_g, the modulus decreases, but does not drop to near zero, which occurs for non-entangled polymers. This regime is referred to as the "rubbery plateau"; it represents a temperature or time regime wherein strand entanglements provide transient network junctions (mechanical crosslinks) that are elastically effective. At even higher temperatures or longer times, the modulus drops precipitously, and the material behaves as a liquid.

1.5 Additional examples of polymer networks with unique chemistry/structure-driven properties

1.5.1 Covalent adaptable polymer networks

Due to their strong bonds, covalent polymer networks possess high mechanical strength across a wide range of conditions. While such mechanical stability enables their use in daily life, many emerging applications and environmental sustainability concerns demand unconventional properties of polymer networks, such as reprocessability, repairability upon damage, and adaptability to different environments.

Several strategies have been developed to address these needs. For example, polymer networks with rapid stress relaxation that can heal when damaged ("self-healing") are often constructed from non-covalent network bonds (*e.g.* metal–ligand coordination, host-guest interaction, hydrogen bonding, and hydrophobic interaction) that facilitate energy dissipation and structural reorganization. In addition, stimuli-responsive polymer networks can be made by incorporating stimuli-responsive monomers/polymers. For example, temperature, pH, and light responsiveness were achieved in PNIPAm hydrogels, polyelectrolyte gels, and liquid crystalline elastomers, respectively. Introducing stimuli-responsive bonds (*e.g.* light-cleavable *o*-nitrobenzyl esters, light-isomerizable azobenzenes, mechanoresponsive spiropyrans) provides another approach to imparting stimuli-responsiveness to polymer networks, such as light-regulated reversible sol-gel switching,[155] controlled release of functional molecules,[156] and shear-strengthening properties.[38] Recent reviews discuss these classes of materials in great detail;[157-160] in this section, we focus on covalent adaptable networks (CANs), a recently popularized class of reconfigurable and responsive network systems.

Within the past several decades, the development of dynamic covalent chemistry has exploited various types of covalent bonds that can equilibrate under certain reaction conditions.[161] CANs are produced from incorporating these bonds into covalent polymer networks, which allows for stimulus-induced reconfiguration of networks to reduce stresses or heal damage. As a result, CANs not only exhibit the robust mechanical properties of typical thermosets but they can also possess the processability and relaxation behavior of thermoplastics.

Depending on the exchange mechanism, CANs may be further classified into two groups: dissociative CANs and associative CANs. Dissociative CANs obtain their dynamic properties from dissociative bond exchange, where bonds are first broken and then reformed elsewhere in the network (Fig. 9A, top). A representative reaction used in dissociative CANs is the retro Diels–Alder (D-A) cycloaddition between furan and maleimide. While the formation of D-A adducts is favored at room temperature, the reaction becomes reversible at elevated temperatures. Polymer networks synthesized using furan-maleimide cycloaddition exhibit excellent mechanical properties at room temperature that slowly decay upon heating.[162] At 92 °C (T_{gel}), the equilibrium conversion of the forward D-A reaction drops to 71%, which meets the critical gel point predicted by Flory–Stockmayer theory.[163] Consequently, the material exhibits liquid-like properties at temperatures higher than T_{gel}, as evidenced by an abrupt decrease in modulus and viscosity (Fig. 9B). The reversible nature of this process renders the material thermally remoldable. In addition to this example, dissociative CANs based off a wide range of functional groups including disulfides[110] and isocyanates[164] have been extensively studied.[159, 165]

Using classical substitution and RDRP reactions as analogies, dissociative CANs operate similarly to S_N1 or NMP reactions, respectively, where an equilibrium between a dormant (e.g. alkyl halide or alkoxyamine) state and a reactive state (carbocation or

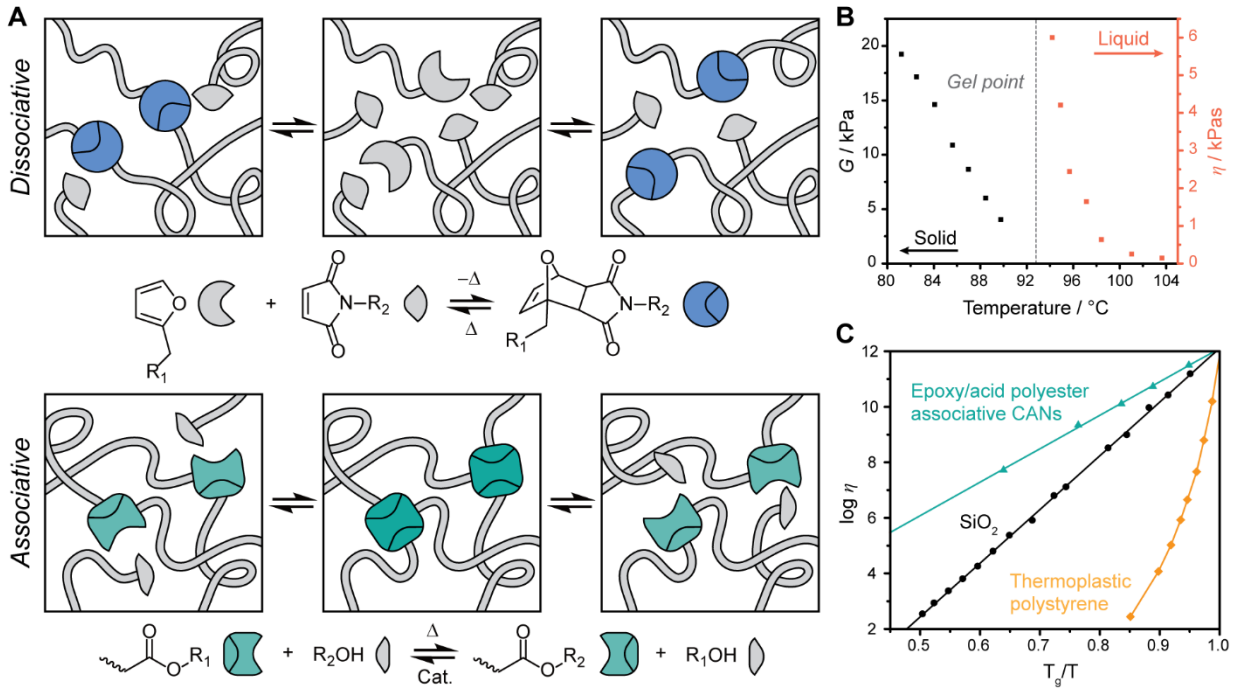

Figure 9. Covalent adaptable polymer networks. (A) Top: Dissociative CANs involve dissociative bond exchange (*e.g.*, retro Diels–Alder cycloaddition between furan and maleimide), where bonds are first broken and then reformed elsewhere in the network. Bottom: Associative CANs involve associative bond exchange (*e.g.*, transesterification), where an original bond is broken only when a new covalent bond has been formed. (B) Dissociative CANs undergoes a reversible gel-to-sol transition near a critical temperature. (C) The viscosity of associative CANs exhibits Arrhenius-like temperature dependency similar to vitreous silica, whereas the viscosity-temperature behaviors of dissociative CANs or thermoplastic polymers follow the WLF model.

propagating radical) exists and the key bond breaking and bond formation events occur in distinct elementary steps. In contrast, associative CANs operate analogously to S_N2 or RAFT reactions where bond breaking and bond formation occur simultaneously (Fig. 9A, bottom). For associative bond exchange, which is often an energetically degenerate process (analogous to chain transfer in RAFT) in associative CANs, changes in temperature or other corresponding stimuli affect the exchange reaction kinetics rather than the chemical equilibrium. As a result, a distinguishing characteristic between dissociative and associative CANs is that associative CANs display a constant crosslinking density with respect to temperature. Since the rate of stress relaxation of these networks depends on the rate of bond rearrangement, the associative bond exchange mechanism is reflected in a viscosity with Arrhenius-like temperature dependency (Fig. 9C). This behavior, typically observed in vitreous silica, led Leibler and coworkers to coin the name “vitrimers” as they studied one of the first purposefully designed associative CANs formed from epoxy/acid polyester-based networks with zinc acetate transesterification catalysts.[166] In contrast, the viscosity-temperature behavior of dissociative CANs or thermoplastic polymers often follows the Williams–Landel–Ferry (WLF) model (Fig. 9C), which best describes the temperature dependence of material properties that undergo an abrupt transition at a critical temperature (*e.g.* changes in viscosity near T_g).

Many reactions have been used to prepare associative CANs,[159-160, 165] including transesterification, transalkylation of triazolium salts, olefin metathesis, and dioxaborolane metathesis. In addition, some CANs rely on exchange mechanisms that combine dissociative and associative aspects (reminiscent of iniferter polymerizations that combine reversible activation with degenerative chain transfer). For example, Bowman and coworkers demonstrated in 2005 that associative allyl sulfide exchange following light-initiated bond homolysis (a dissociative process) enabled photoinduced plasticity in covalent polymer networks.[167] In 2011, Matyjaszewski and coworkers showed that the reshuffling reactions of trithiocarbonates similarly led to photoinduced self-healing of covalent polymer networks.[109] Bowman and coworkers later reported a liquid crystalline polymer network that can undergo programmable yet reversible shape-switching.[168] By incorporating thermotropic mesogens (*i.e.* liquid crystalline structures with alignment that can be controlled by temperature) and allyl sulfide into network strands, the shape of this material could be programmed with light irradiation, where the alignment of mesogens embedded in the network was achieved through photoinduced plasticity enabled by allyl sulfide exchange. The programmed shape was maintained in the absence of light but could be erased using heat and light, conditions that reconfigure the embedded mesogen alignment.

To summarize, CANs, especially those derived from low-cost components, may be easily commercialized in the future to facilitate the recycling of thermosetting plastics. In addition, further developments in the area of dynamic covalent chemistry will help meet the increasing demand for more adaptable and complex CAN-based materials.

1.5.2 Microporous polymer networks

Microporous materials are defined as materials containing interconnected pores of less than 2 nm in diameter on average.[169] Due to their large surface area, many conventional microporous materials (e.g. zeolites, activated carbons) are widely used as catalysts, sorbents, and separation membranes. Recently, the field has evolved rapidly with the development of several novel types of microporous polymer networks. These materials not only benefit fundamental research by introducing modular approaches to accessing numerous sophisticated structures, but also provide new opportunities for various emerging applications.

The central design principle for introducing permanent microporosity into polymer networks involves the use of rigid building blocks. Such rigidity precludes the network strands from behaving effectively as entropic molecular springs and prevents the collapse of microporous structures upon solvent removal; consequently, the mechanical properties of these materials are stiff yet brittle. The rigidity of monomers further prevents small loop formation and, in some cases, allows for establishing long-range order in the presence of self-error-correcting mechanisms (*e.g.* reversible bond formation). Hence, microporous polymer networks can be either amorphous or crystalline. Aside from the general use of very rigid components, the basic concepts of microporous polymer network synthesis are similar to those discussed above for either covalent or physical polymer networks.

1.5.2.1 Amorphous microporous polymer networks

Amorphous microporous polymer networks of different types have been denoted by various names, such as polymers of intrinsic microporosity (PIMs),[6] porous organic polymers (POPs),[170] conjugated microporous polymers (CMPs) [171], and hypercrosslinked polymers (HCPs).[172] We suggest dividing them into two categories, based on whether or not strands are covalently crosslinked.

Covalently crosslinked microporous polymer networks. One straightforward strategy for the synthesis of microporous end-linked polymer networks involves step-growth polymerization of *rigid* monomers where at least one of the monomers has a functionality greater than two. When the polymerization reaction is irreversible, the resulting networks are often amorphous due to accumulated structural defects.

An early example of such a strategy was reported by McKeown and coworkers in 2002, where they prepared a microporous polymer network via nucleophilic aromatic substitution (S_NAr) reactions between *meso*-tetrakis(pentafluorophenyl)porphyrin and a rigid bis(catechol) monomer.[173] The obtained networks exhibited high Brunauer–Emmett–Teller (BET) surface areas in the range of 900–1000 $m^2\ g^{-1}$. Similar approaches were used to synthesize conjugated polymer networks with microporosity. In 2007, Cooper and coworkers synthesized a series of poly(aryleneethynylene) polymer networks using palladium-catalyzed Sonogashira–Hagihara cross-coupling.[174] For example, cross-coupling 1,3,5-triethynylbenzene and 1,4-diiodobenzene yielded a

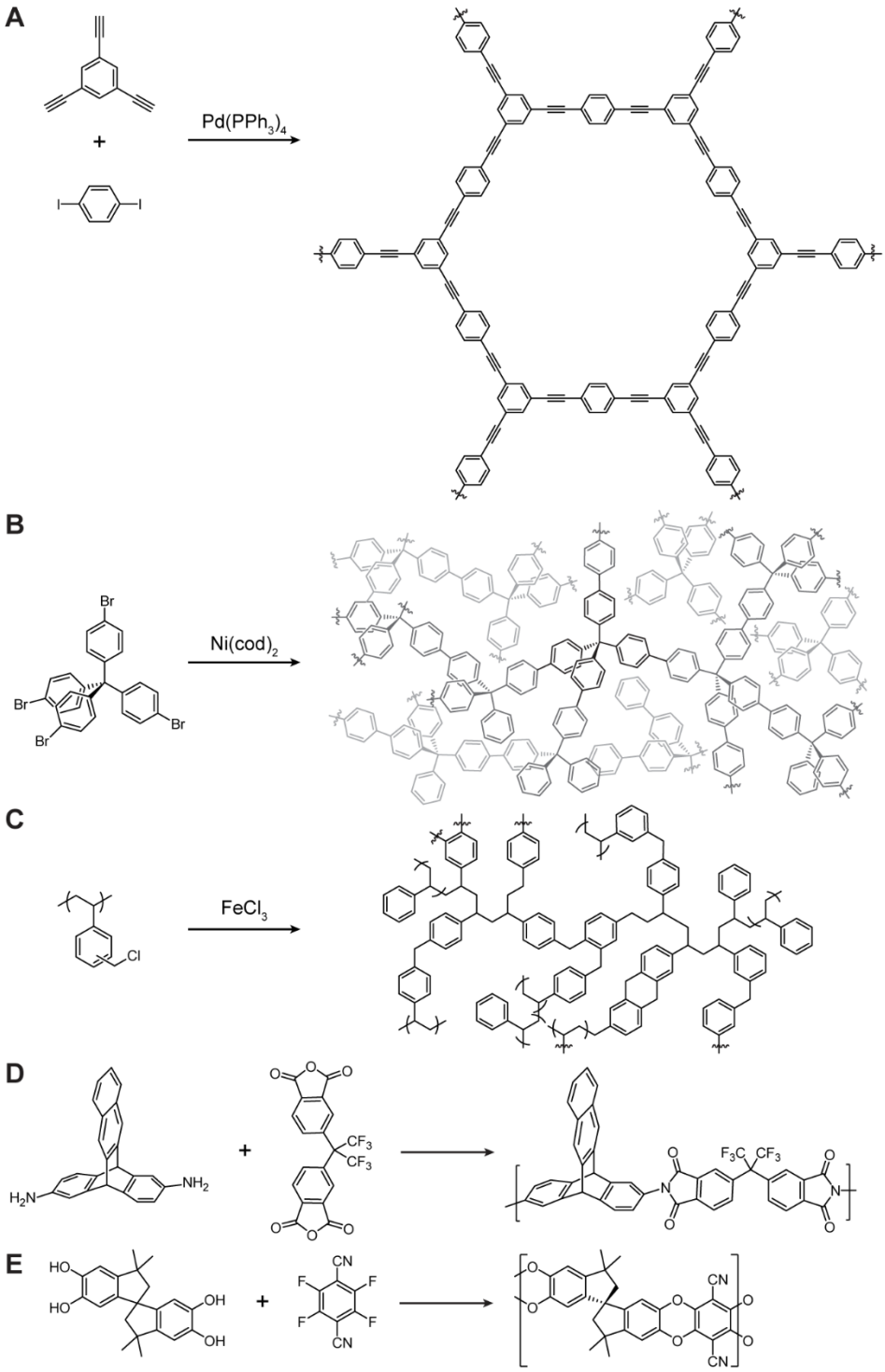

Figure 10. Amorphous microporous polymer networks. (A) An amorphous microporous conjugated polymer network synthesized by palladium-catalyzed Sonogashira–Hagihara cross-coupling. (B) An amorphous polymer network synthesized from crosslinking tetrahedral monomers through Yamamoto coupling. (C) A microporous hypercrosslinked polystyrene network synthesized via vulcanization using a Friedel–Crafts reaction. (D) Microporous triptycene polyimides prepared using rigid and bulky triptycene groups. (E) A ladder-type microporous polymer synthesized from a bis-catechol spirobisindane derivative and tetrafluoroterephthalonitrile.

microporous polymer network possessing a BET surface area of 834 m^2 g^{-1} (Fig. 10A). Recently, Swager and coworkers developed a dynamic self-correcting S_NAr reaction using *ortho*-aryldithiols and *ortho*-aryldifluorides that condense to produce thianthrene units.[175] This approach enabled the synthesis of a microporous ladder polymer network with a BET surface area of 813 m^2 $g^{-1}$from 1,2,4,5-benzenetetrathiol and octafluoronaphthalene.

Tetrahedral monomers are often used to increase the surface area of microporous polymer networks.[176-178] For example, Zhu, Qiu, and coworkers polymerized tetrakis(4-bromo-phenyl)methane using the Yamamoto coupling reaction (Fig. 10B); the resulting amorphous microporous polymer network featured a remarkable BET surface area of 5600 m^2 g^{-1}.[176] Covalently crosslinked microporous polymer networks can also be synthesized via vulcanization. For example, Cooper and coworkers prepared a hypercrosslinked polystyrene material via suspension polymerization of vinylbenzyl chloride followed by a Friedel–Crafts-type post-crosslinking (Fig. 10C).[179] The obtained materials had BET surface areas up to 1466 m^2 g^{-1}.

In terms of applications, covalent microporous polymer networks can outperform conventional porous materials in gas storage, heterogeneous catalysis, and water purification. In addition, they hold great promise in various emerging applications such as light harvesting, selective molecular capture, and organic semiconductors. The details of these applications have been extensively reviewed.[180-181]

Microporous polymer networks without covalent crosslinking. While polymer strands can bend and twist to pack space efficiently, thermoplastics typically possess void space (*i.e.* free volume) as a consequence of non-covalent intermolecular interactions and restricted chain motion below the glass transition temperature. Through appropriate molecular design, polymers with enormous free volume can be synthesized where the voids become interconnected, leading to microporous materials without covalent crosslinking. Similar to ordinary thermoplastics, this class of microporous polymer networks is rigid yet soluble in appropriate solvents, allowing for solution-based processing.

Here again, the key strategy to introduce porosity (free volume) into polymers involves incorporating rigid and/or bulky structural motifs. A particularly interesting example is triptycene.[182-183] In 2003, Swager and coworkers synthesized polymers with pendant triptycene groups, showing that the free volume introduced by triptycene resulted in a BET surface area of approximately 400 m^2 g^{-1}.[182] In 2011, the same group incorporated triptycene into polymer backbones and synthesized triptycene polyimides from 2,6-diaminotriptycene derivatives and aromatic dianhydrides (Fig. 10D).[183] The resulting polymers were soluble in common organic solvents and were processable to form microporous polymer films with high BET surface areas (up to 430 m^2 g^{-1}) and low refractive indices.

In 2004, McKeown and coworkers synthesized rigid ladder-like polymers from a bis-catechol spirobisindane derivative and tetrafluoroterephthalonitrile (Fig. 10E).[184] The

spirocyclic component was crucial in increasing the polymer free volume, resulting in a BET surface area of 850 $m^2 g^{-1}$ and selective gas permeability.[185] Recently, Xia and coworkers synthesized norbornyl benzocyclobutene ladder polymers from norbornadiene and dibromoarenes via catalytic arene-norbornene annulation.[186-187] The microporosity of these polymers was evidenced by BET surface areas of up to 720 $m^2 g^{-1}$.

1.5.2.2 Crystalline microporous polymer networks

Crystalline microporous polymer networks typically possess higher surface areas than their amorphous counterparts. More importantly, their crystallinity leads to a uniform distribution of pore sizes, which facilitates many applications. The key to the formation of crystalline networks is the use of reversible reaction conditions (conceptually analogous to physical/supramolecular networks described above) and highly rigid monomers, which allows for error corrections during network formation and produces thermodynamically stable networks with established long-range order. In this section, we briefly discuss two major types of crystalline microporous polymer networks: MOFs and COFs.

MOFs. MOFs, sometimes referred to as porous coordination polymers (PCPs),[188] are porous polymer networks consisting of metal ions or clusters as junctions coordinated to rigid organic ligands as strands. The reversible nature of metal–ligand coordination enables establishment of long-range order. Notably, when discussing MOFs, most researchers are referring to crystalline materials; metal–ligand coordination does not always produce crystalline materials, even when rigid building blocks are applied. There has been recent interest in the properties of "amorphous MOFs",[189-191] though amorphous supramolecular networks constructed from metal–ligand interactions have been known for decades and are not usually referred to as MOFs. We note that MOFs, whether they are crystalline or not, are coordination polymer networks, and thus the terms "crystalline PCP" or "amorphous PCP" are also applicable. In any case, these materials can be two-dimensional grid structures that further stack on each other through physical (e.g. van der Waals or π-stacking) interactions, or three-dimensional network structures.

The development of MOFs has popularized the concept that crystalline networks with given structures can be assembled from well-defined monomers of simple geometrical shapes (*i.e.* secondary building units (SBUs)) that are organic or metal-containing. This process, referred to as "reticular synthesis" by Yaghi and O'Keeffe, has facilitated the rational design of many novel MOFs and related networks.[192-196] Related concepts have been used in the design classical polymer networks to control topological features such as *f* (see Section 1.3.3). Here, we introduce four representative MOF structures to showcase how the achieved topology is precisely dictated by the SBU structures.

MOF-5 was first synthesized from $Zn(NO_3)_2$ and terephthalic acid.[197] Its SBUs are identified as octahedrally shaped $Zn_4O(CO_2)_6$ (CO_2 = coordinating carboxylate groups) clusters (junctions) connected through bifunctional terephthalate linkers (strands) (Fig.

11A). The structure of MOF-5 is represented in two forms in Fig. 11A: a cartoon form highlighting its network nature reminiscent of many amorphous supramolecular networks based on metal-ligand coordination (*e.g.* polyMOCs), and a crystal structure showing the atomic positions. The clusters form six-coordinated vertices, leading to a simple cubic network. MOF-5 has one type of void space (yellow spheres in Fig. 11A) with a pore diameter of 15 Å.[198] It features BET surface areas as high as ~3800 $m^2\ g^{-1}$.[199]

HKUST-1 was synthesized from $Cu(NO_3)_2$ and trimesic acid.[200] Its SBUs are paddle-wheel $Cu_2(CO_2)_4$ (CO_2 = coordinating carboxylate groups) complexes with four points of extension arranged at the vertices of a square connected through trifunctional trimesate linkers (Fig. 11B). This material features a bimodal pore size distribution, with larger pores of 11~14 Å in diameter and smaller pores of ~5 Å in diameter;[201] its BET surface area was measured to be 692 $m^2\ g^{-1}$.[200]

ZIF-8 represents an important subclass of MOFs—zeolitic imidazolate frameworks (ZIFs)—that have zeolite-like topologies and enhanced thermal/chemical stabilities compared to many other MOFs.[202] ZIF-8 was synthesized from $Zn(NO_3)_2$ and 2-methylimidazole.[203] Its SBUs are ZnN_4-based tetrahedra (N = coordinating nitrogen atoms of imidazolate ligands) connected through bifunctional 2-methylimidazolate linkers (Fig. 11C), where the metal-imidazolate-metal angle is similar to the 145° Si-O-Si angle in zeolites. ZIF-8 possesses a large pore diameter of 11.4 Å yet a small aperture size of 3.4 Å (*i.e.* the limiting size for a molecule to enter the pores),[204] though the aperture of ZIF-8 is flexible and can accommodate guest molecules larger than its size.[205] The BET surface area of ZIF-8 was measured to be 1630 $m^2\ g^{-1}$.[203]

MOF-74 was synthesized from $Zn(NO_3)_2$ and 2,5-dihydroxy-1,4-benzenedicarboxylic acid,[206] featuring an infinite $Zn_3(O)_3(CO_2)_{3\infty}$ (O = coordinating phenoxide groups; CO_2 = coordinating carboxylate groups) rod SBU derived from square pyramids sharing triangular faces (Fig. 11D). Such rod SBUs run along the 001 plane and are linked into a hexagonal, three-dimensional framework. MOF-74 possesses one-dimensional channels of dimensions 10.3 × 5.5 $Å^2$,[206] and a BET surface area of 1000 $m^2\ g^{-1}$.[207]

Combining the basic principle of reticular synthesis and post-synthetic modification,[208-209] numerous MOF structures have been reported with enormous surface areas up to ~7000 $m^2\ g^{-1}$.[210] While many MOFs show limited thermal and chemical/hydrolytic stability due to the instability of metal-ligand coordination, several classes of hydrolytically stable MOFs have been developed,[211] such as UiO-66 formed from $ZrCl_4$ and terephthalic acid.[212] Moreover, creating hybrid materials from flexible polymers and crystalline MOFs has arisen as an intriguing way to increase the stability and processability of these materials.[213-216] As one example, polymer-metal-organic frameworks (polyMOFs)[217-220] can be synthesized from Zn^{2+} and flexible polymer ligands with aromatic dicarboxylic acids in its backbone. PolyMOFs can possess high crystallinity, high porosity, and exceptional water stability.

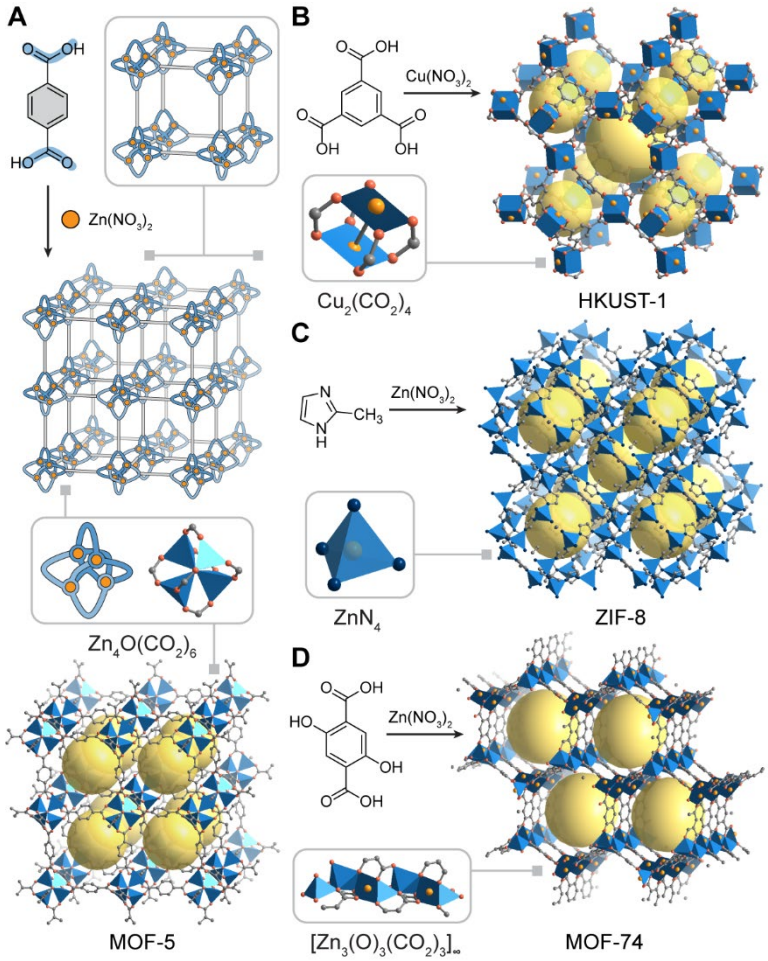

Figure 11. Metal-organic frameworks. (A) Synthesized from $Zn(NO_3)_2$ and terephthalic acid, MOF-5 features octahedrally shaped $Zn_4O(CO_2)_6$ clusters (junctions) connected through bifunctional terephthalate linkers (strands). Here its structure is represented in two forms: a cartoon form (top) highlighting its network nature, and a crystal structure (bottom) showing the atomic positions (red spheres: oxygen; grey spheres: carbon; blue: tetrahedrally coordinated ZnO_4 clusters; yellow spheres: void space). (B) The formation and crystal structure of HKUST-1. Red spheres: oxygen; grey spheres: carbon; orange spheres: copper; yellow spheres: void space. (C) The formation and crystal structure of ZIF-8. Grey spheres: carbon; blue spheres: nitrogen; blue: tetrahedrally coordinated ZnN_4 clusters; yellow spheres: void space. (D) The formation and crystal structure of MOF-74. Red spheres: oxygen; grey spheres: carbon; orange spheres: zinc; blue: tetrahedrally coordinated ZnO_4 clusters; yellow spheres: void space.

The predictable structure-property relationships combined with modular synthesis has popularized MOFs[221-223] as one of the most intensively studied classes of materials for potential applications in areas such as gas storage and separation,[224] catalysis,[225] drug delivery,[226] luminescence and sensors,[227] electrical conduction,[228] and ion transport.[229] Among them, gas separation is perhaps one of the most intriguing areas where MOFs outperform many other porous materials. Here, we provide one example to showcase the effectiveness of MOFs in gas separation.

Gas separation in MOFs relies on both pore sizes and the affinity of MOFs for the targeted molecules. A remarkable example was provided by Long, Krishna, and

coworkers, where they synthesized $Fe_2(BDP)_3$ (BDP^{2-} = 1,4-benzenedipyrazolate), a highly stable MOF with one-dimensional triangular channels, and demonstrated the separation of hexane isomers according to the degree of branching.[230] Monte Carlo simulations suggested that as the degree of branching increased, the hexane isomers became more compact, reducing their van der Waals interactions with the pore wall. Hence, when an equimolar mixture of all five molecules were subjected to a bed packed with $Fe_2(BDP)_3$, the dibranched isomers eluted first, followed by the monobranched isomers, and finally linear *n*-hexane. Moreover, the pore size plays a critical role in the observed separation: narrower channels cannot accommodate all five isomers, whereas wider channels do not maximize the differences in van der Waals interactions.

COFs. Connecting rigid organic building blocks through dynamic covalent chemistry has enabled the development of another class of crystalline polymer networks—COFs. To our knowledge, the first example of COF synthesis using this approach was reported by Yaghi and coworkers in 2005 [231]. Heating diboronic acid and hexahydroxy triphenylene in a Pyrex tube formed a crystalline product (COF-5) through reversible boronate ester formation (Fig. 12A); its structure was determined as stacked two-dimensional COF sheets with pore sizes of 27 $Å^2$. This material exhibited high thermal stability, permanent porosity, and a high BET surface area of 1590 $m^2\ g^{-1}$. This approach was quickly adapted to synthesize three-dimensional COFs, where crystalline COF-102 was synthesized from tetra(4-dihydroxyborylphenyl)methane through reversible boroxine formation (Fig. 12B).[232] COF-102 exhibited a high surface area of 3472 $m^2\ g^{-1}$.

Many other COFs have since been developed using alternative dynamic covalent chemistries such as imine COFs formed through Schiff base reaction,[233] covalent triazine frameworks (CTFs) formed through trimerization of nitriles,[234] and recently a two-dimensional semiconductive sp^2 carbon-conjugated COF formed through the reversible Knoevenagel condensation.[235] The development of COFs has greatly enriched reticular chemistry, providing opportunities to access sophisticated polymer network topologies that are otherwise difficult to achieve.[236] An interesting example was reported by Yaghi, Terasaki, and coworkers in 2016: imine condensation between tetra-aldehyde functionalized copper(I)-bisphenanthroline ($Cu(PDB)_2$) and benzidine formed a three-dimensional COF (COF-505) that featured helical organic threads interlacing to make a weaving crystal structure (Fig. 12C).[237] The copper(I) ions could be reversibly removed from this material and added back without loss of the COF structure. Following a similar approach by replacing benzidine with a rectangular tetratopic linker, another three-dimensional woven COF (COF-500) was recently reported, where one-dimensional organic ribbons of corner-sharing squares were mutually interlocked.[238]

While dynamic covalent bonds facilitate the crystallinity of COFs, the same mechanism results in their low chemical/hydrolytic stability and severely limits their potential applications. Three strategies have been applied to increase COF stability: 1) Using more stable dynamic covalent bonds. For example, hydrazone- or azine-linked COFs were shown to have a higher hydrolytic stability than imine-linked COFs;[239-240]
2) Strengthening the interlayer stacking in two-dimensional COFs.[241-242] For example, Jiang and coworkers reported a stable imine-linked COF by incorporating methoxy

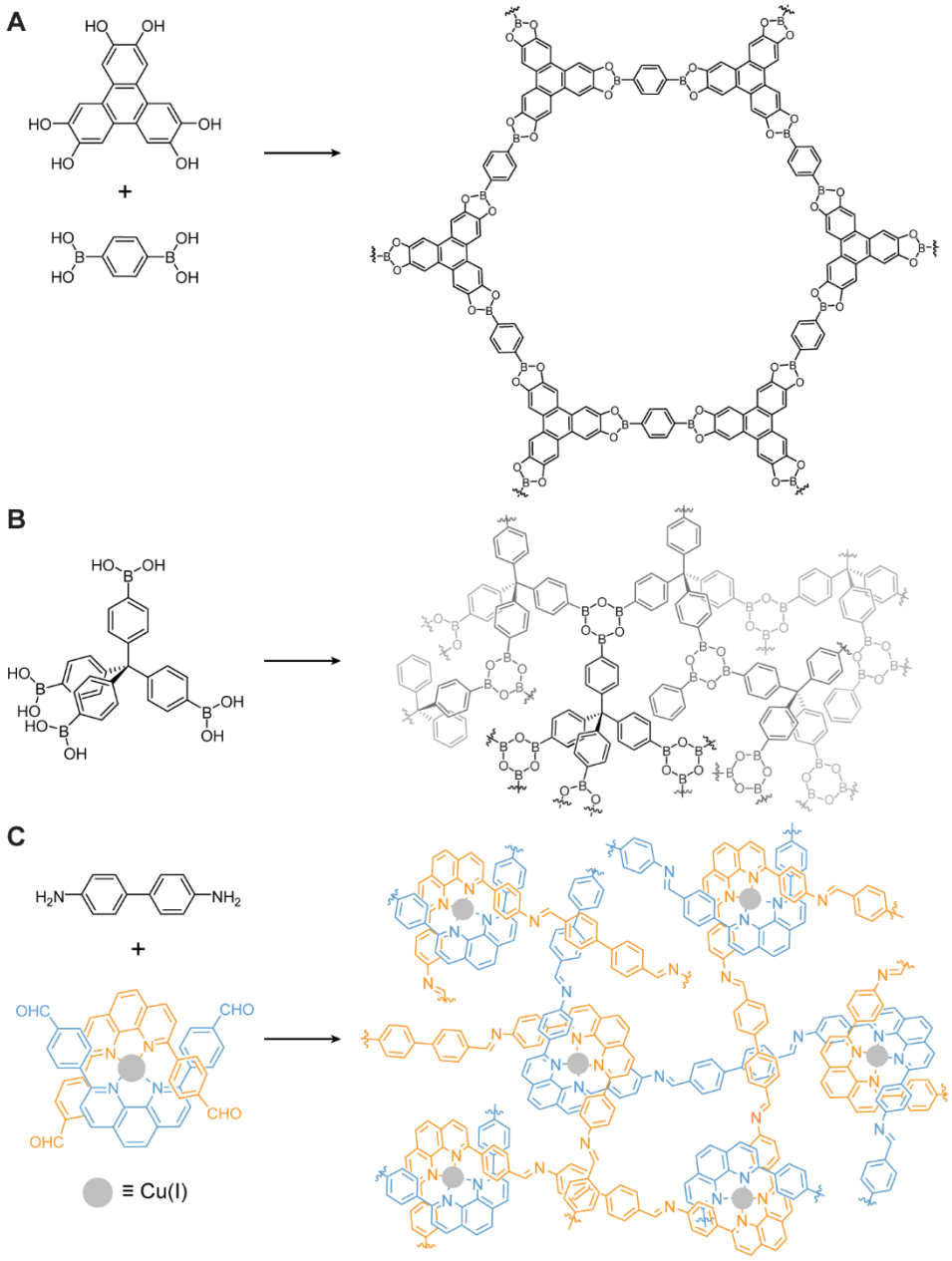

Figure 12. Covalent organic frameworks. (A) A crystalline two-dimensional microporous polymer network, COF-5, was synthesized through the reversible boronate ester formation. (B) A crystalline three-dimensional microporous polymer network, COF-102, was synthesized from tetrahedral monomers through reversible boroxine formation. (C) A woven crystalline polymer network, COF-505, with interlaced helical organic threads templated by copper coordination.

groups into its pore walls,[243] which softened interlayer charge repulsion and reinforced interlayer hydrogen bonding;[244] and 3) Post-synthetic modification that converts reversible bonds to irreversible bonds while maintaining crystallinity. For example, in 2012, Banerjee and coworkers synthesized an enol-imine COF intermediate through reversible Schiff base condensation reaction between 1,3,5-triformylphloroglucinol and aromaticdiamines;[245] subsequently, an irreversible tautomerization occurred, producing a β-ketoenamine linked COF that exhibited extraordinary chemical stability. Recently,

Yaghi and coworkers improved the stability of an imine-linked COF by converting the imines to amides via direct oxidation with retention of crystallinity and permanent porosity.[246]

COFs are generally obtained as polycrystalline powders with crystalline domains smaller than 50 nm. Substantial progress has been made recently to enhance the crystallinity of COFs, of which much focus has been placed on improving the reversibility of COF forming processes. While irreversible reactions lead to amorphous networks, one of the most reversible interactions in nature—the van der Waals interaction—can drive organic molecules into large single crystals, some of which display intrinsic porosity.[247] Indeed, *in situ* polymerization of single crystals of organic monomers represents a facile approach to monocrystalline COFs through single-crystal-to-single-crystal transformations.[248-250] In 2013, Wuest and coworkers constructed a monocrystalline COF by polymerizing tetrakis(4-nitrosophenyl)methane through the formation of azodioxy dimers,[251] which have a low activation barrier of dissociation (20-30 kcal/mol). In 2017, Banerjee and coworkers reported the use of *p*-toluene sulfonic acid as an "external co-agent" to increase the crystallinity of β-ketoenamine linked COFs.[252] They postulated that the reversible proton transfer between the acid and the aromatic diamine monomers enhanced the reversibility of imine formation process.[253] Significant progress was achieved in 2018 towards large COF single crystals. Using a transimination reaction to increase the reversibility of imine bond formation, Yaghi and coworkers obtained a series of three-dimensional monocrystalline imine-linked COFs, with single crystal sizes up to ~100 μm.[254] Around the same time, Dichtel and coworkers synthesized micron sized single crystals of two-dimensional boronate ester COFs by the seeded growth mechanism.[255]

Following the idea that COFs lie in a continuous spectrum between amorphous networks made from irreversible covalent bonds and organic single crystals made of van der Waals interaction, it is not surprising that similar crystalline networks can be synthesized from hydrogen bonding interaction. Such materials, referred to as hydrogen-bonded organic frameworks (HOFs), were pioneered by Wuest in the 1990s and have been popularized recently due to their potential applications in gas separation and storage.[256] One of the earliest HOF examples was an organic diamondoid network formed from a tetraphenylmethane derivative through the N–H···O hydrogen bonds between terminal 2-pyridone groups.[257] The weak hydrogen bonding interactions in HOFs allow the formation of large single crystals yet severely limit their stability.

As summarized in recent reviews,[258-260] COFs have shown great promise in many applications. Chemical instability and poor processability, however, are key challenges that must be addressed to fulfill their full potential. While recent progress has enabled solid state synthesis of COFs,[252, 261] formation of COF thin films,[262] and *in situ* processes of COFs,[252, 263] significant efforts are still needed to realize their real-world applications.

1.5.3 Interpenetrating polymer networks

Interpenetrating polymer networks (IPNs) are typically defined as two (or more) polymer networks that are partially interlaced on a molecular scale but are not covalently bonded.[264] Using any of the above-mentioned network forming compositions/topologies, IPNs can be synthesized in principle using either simultaneous or sequential procedures. While discussions of IPNs are typically focused on either amorphous or crystalline networks depending on the community (polymer chemists or inorganic chemists, respectively), it should be recognized that IPNs can consist of either or both types of networks. Remarkably, MOF IPNs[265] with up to 54-fold interpenetration[266] have been prepared and characterized. IPNs provide a convenient approach to combining the desired properties of two polymer networks. In addition, when appropriately designed, some IPNs exhibit entirely new properties that are not observed in the component networks alone. “Double network” (DN) gels are an example; this special class of IPNs shows superior mechanical properties to either of their component networks.[267]

DN gels possess an IPN structure that combines a brittle first network with a ductile second network. These materials are often synthesized via a two-step sequential free-radical polymerization process. To our knowledge, the first reported DN gel consisted of densely crosslinked poly(2-acrylamido-2-methylpropanesulfonic acid) (PAMPS) as the first network and sparsely crosslinked polyacrylamide (PAAm) as the second network.[268] This DN gel displayed a ~1000-fold increase in toughness (area under the stress-strain curve) compared to PAAm or PAMPS single network gels, which was attributed to internal fracture of the brittle first network under deformation that allowed for efficient energy dissipation.

In these early examples of DN gels, damage accumulated in the brittle first network was not repairable, severely decreasing the mechanical properties after a single exposure to high stresses. To address this deficiency, Suo and coworkers developed analogous gels wherein the brittle first network was a physical network made from alginate crosslinked by ionic interactions with Ca^{2+}.[269] In this case, the reversible physical interactions within the first network enabled recoverable energy dissipation following deformation. Consequently, the material shows high stiffness, high toughness, and recovery of both properties upon cycling. We note that some extent of covalent crosslinking was proposed to occur between the two network components;[269] hence, while the “IPN” definition may or may not fully apply to this material, the concept of embedding a supramolecular network within a covalent network paved the way for the use of reversible interactions as energy dissipation mechanisms to enhance the toughness of polymer networks, removing the necessity of a secondary interpenetrating network.[270-272] For example, Gong and coworkers developed a physical hydrogel composed of polyampholytes bearing randomly dispersed cationic and anionic repeat groups.[270] The randomness within this material generated ionic bonds with a wide distribution of strength; the strong bonds served as more-permanent crosslinks to impart elasticity whereas the weak bonds reversibly exchanged to dissipate energy, resulting in high toughness and high fatigue resistance. In the future, the merger of distinct polymer

network types and formation mechanisms into IPNs of increasing compositional and topological complexity is expected to provide additional synergistic improvements in the functionality and utility of these exciting materials.

1.6 Summary and outlook

Polymer networks are ubiquitous in the modern world. Advances in synthetic chemistry as well as our greater understanding of structure-property relationships have allowed us to design and produce polymer networks with excellent mechanical properties, enhanced crystallinity, self-healing abilities, and environmental adaptability. As discussed in this introductory review, various polymer networks have been developed to meet the needs of performance and function in contemporary materials, including CANs, MOFs, COFs, polyMOCs, DN gels, polymers of intrinsic porosity, topological gels, and polymer-nanoparticle composite hydrogels. Nevertheless, as these materials are developed and studied by researchers from different fields, it is not uncommon that several different colloquial names exist to describe similar materials/structures, which creates barriers for an integrated understanding of polymer networks. Hence, the goal of this review is to provide a unified perspective to the field and stimulate new discoveries. We note that such an interdisciplinary approach represents an ongoing effort and could lead to many exciting new strategies for network synthesis. As just one example, transforming crystalline MOFs to polymer gels was recently suggested as a promising route for creating idealized defect-free polymer networks from flexible precursors.[273]

Looking forward, the field of polymer networks can benefit from further advances in characterization techniques. Despite the developments of MQ NMR and NDS, our methods to probe polymer topology remain limited; we still rely heavily on phenomenological characterization methods such as rheology or swelling tests. In the future, a more general technique is needed to probe sub-10 nm topological features such as entanglements, branch functionality, and loops of various orders, especially in networks synthesized from chain-growth polymerization. Moreover, because polymer networks are often inhomogeneous and amorphous, topological characterization potentially with high spatial resolution[274] is both challenging yet necessary for understanding and improving these materials. New characterization tools, such as the judicious use of mechanophores to observe stress concentration in polymer networks, will facilitate the further development of theories that can provide more thorough structure-property relationship prediction in polymer networks, which is increasingly needed to meet modern needs of functionality and sustainability.

The development of new reaction methodologies and advanced (macro)molecular architectures and topologies will further fuel the design of polymer networks with fascinating behaviors[275-276] and improved mechanical properties. In addition, practical, scalable synthetic strategies are necessary to meet the existential need for recyclable, sustainable polymer networks, next-generation energy storage/harvesting materials, separations membranes, and catalysts. Thus, there is no doubt that this field will continue to witness exciting progress for the foreseeable future.

1.7 References

1. Carothers, W. H. Polymerization. *Chem. Rev.* **1931**, *8* (3), 353.
2. Flory, P. J. Molecular size distribution in three dimensional polymers. I. Gelation. *J. Am. Chem. Soc.* **1941**, *63* (11), 3083.
3. Li, J.; Mooney, D. J. Designing hydrogels for controlled drug delivery. *Nat. Rev. Mater.* **2016,** *1* (12), 16071.
4. Lee, K. Y.; Mooney, D. J. Hydrogels for Tissue Engineering. *Chem. Rev.* **2001,** *101* (7), 1869-1880.
5. Ionov, L. Hydrogel-based actuators: possibilities and limitations. *Mater. Today* **2014,** *17* (10), 494-503.
6. McKeown, N. B.; Budd, P. M. Polymers of intrinsic microporosity (PIMs): organic materials for membrane separations, heterogeneous catalysis and hydrogen storage. *Chem. Soc. Rev.* **2006,** *35* (8), 675-683.
7. Díaz Díaz, D.; Kühbeck, D.; Koopmans, R. J. Stimuli-responsive gels as reaction vessels and reusable catalysts. *Chem. Soc. Rev.* **2011,** *40* (1), 427-448.
8. Zhang, Y.; Riduan, S. N. Functional porous organic polymers for heterogeneous catalysis. *Chem. Soc. Rev.* **2012,** *41* (6), 2083-2094.
9. Rogers, J. A.; Someya, T.; Huang, Y. Materials and Mechanics for Stretchable Electronics. *Science* **2010,** *327* (5973), 1603-1607.
10. Wang, J.; Wang, R.; Sourakov, A.; Olsen, B. D.; Johnson, J. A. Counting loops in sidechain-crosslinked polymers from elastic solids to single-chain nanoparticles. *Chem. Sci.* **2019**, *10* (20), 5332.
11. Flory, P. J. *Principles of Polymer Chemistry*. Cornell University Press: Ithaca, 1953; p 95.
12. Rubinstein, M.; Colby, R. H. *Polymer Physics*. Oxford University Press: Oxford, 2003; p 263.
13. de Gennes, P. G. *Scaling Concepts in Polymer Physics*. Cornell University Press: 1979; p 95.
14. Manneville, P.; de Seze, L. In *Numerical Methods in the Study of Critical Phenomena*, Dora, J. D.; Demongeot, J.; Lacolle, B. Eds. Springer: 1981.
15. Carothers, W. H. Polymers and polyfunctionality. *Trans. Faraday Soc.* **1936,** *32* (0), 39-49.
16. Stockmayer, W. H. Theory of Molecular Size Distribution and Gel Formation in Branched Polymers II. General Cross Linking. *J. Chem. Phys.* **1944,** *12* (4), 125-131.
17. Valles, E. M.; Macosko, C. W. Structure and Viscosity of Poly(dimethylsiloxanes) with Random Branches. *Macromolecules* **1979,** *12* (3), 521-526.
18. Zhou, H.; Woo, J.; Cok, A. M.; Wang, M.; Olsen, B. D.; Johnson, J. A. Counting primary loops in polymer gels. *Proc. Natl. Acad. Sci. USA* **2012,** *109* (47), 19119-19124.
19. Wang, R.; Lin, T.-S.; Johnson, J. A.; Olsen, B. D. Kinetic Monte Carlo Simulation for Quantification of the Gel Point of Polymer Networks. *ACS Macro Lett.* **2017,** *6* (12), 1414-1419.
20. Bastide, J.; Leibler, L. Large-scale heterogeneities in randomly cross-linked networks. *Macromolecules* **1988,** *21* (8), 2647-2649.
21. Shibayama, M. Small-angle neutron scattering on polymer gels: phase behavior, inhomogeneities and deformation mechanisms. *Polym. J.* **2010,** *43* (1), 18-34.
22. Di Lorenzo, F.; Seiffert, S. Nanostructural heterogeneity in polymer networks and gels. *Polym. Chem.* **2015,** *6* (31), 5515-5528.
23. Saalwächter, K.; Seiffert, S. Dynamics-based assessment of nanoscopic polymer-network mesh structures and their defects. *Soft Matter* **2018,** *14* (11), 1976-1991.
24. Olsen, B. D.; Johnson, J. A. Reply to Stadler: combining network disassembly spectrometry with rheology/spectroscopy. *Proc. Natl. Acad. Sci. USA* **2013**, *110* (22), E1973.
25. Gu, Y.; Zhao, J.; Johnson, J. A. A (macro)molecular-level understanding of polymer network topology. *Trends Chem.* **2019**, *1* (3), 318.
26. Lange, F.; Schwenke, K.; Kurakazu, M.; Akagi, Y.; Chung, U.-i.; Lang, M.; Sommer, J.-U.; Sakai, T.; Saalwächter, K. Connectivity and structural defects in model hydrogels: a combined proton NMR and Monte Carlo simulation study. *Macromolecules* **2011,** *44* (24), 9666-9674.
27. Chassé, W.; Lang, M.; Sommer, J.-U.; Saalwächter, K. Cross-link density estimation of PDMS networks with precise consideration of networks defects. *Macromolecules* **2012,** *45* (2), 899-912.
28. Saalwächter, K.; Chassé, W.; Sommer, J.-U. Structure and swelling of polymer networks: insights

from NMR. *Soft Matter* **2013,** *9* (29), 6587-6593.
29. Schlögl, S.; Trutschel, M.-L.; Chassé, W.; Riess, G.; Saalwächter, K. Entanglement Effects in Elastomers: Macroscopic vs Microscopic Properties. *Macromolecules* **2014,** *47* (9), 2759-2773.
30. Zhou, H.; Schön, E.-M.; Wang, M.; Glassman, M. J.; Liu, J.; Zhong, M.; Díaz Díaz, D.; Olsen, B. D.; Johnson, J. A. Crossover Experiments Applied to Network Formation Reactions: Improved Strategies for Counting Elastically Inactive Molecular Defects in PEG Gels and Hyperbranched Polymers. *J. Am. Chem. Soc.* **2014,** *136* (26), 9464-9470.
31. Kawamoto, K.; Zhong, M.; Wang, R.; Olsen, B. D.; Johnson, J. A. Loops versus Branch Functionality in Model Click Hydrogels. *Macromolecules* **2015,** *48* (24), 8980-8988.
32. Gu, Y.; Kawamoto, K.; Zhong, M.; Chen, M.; Hore, M. J. A.; Jordan, A. M.; Korley, L. T. J.; Olsen, B. D.; Johnson, J. A. Semibatch monomer addition as a general method to tune and enhance the mechanics of polymer networks via loop-defect control. *Proc. Natl. Acad. Sci. USA* **2017,** *114* (19), 4875-4880.
33. Wang, J.; Lin, T.-S.; Gu, Y.; Wang, R.; Olsen, B. D.; Johnson, J. A. Counting Secondary Loops Is Required for Accurate Prediction of End-Linked Polymer Network Elasticity. *ACS Macro Lett.* **2018,** *7* (2), 244-249.
34. Li, J. ; Nagamani, C. ; Moore, J. S. Polymer mechanochemistry: from destructive to productive. *Acc. Chem. Res.* **2015**, *48* (8), 2181.
35. *Polymer Mechanochemistry*. Boulatov, R. Ed.; Springer: Berlin 2015.
36. Davis, D. A.; Hamilton, A.; Yang, J.; Cremar, L. D.; Van Gough, D.; Potisek, S. L.; Ong, M. T.; Braun, P. V.; Martínez, T. J.; White, S. R.; Moore, J. S.; Sottos, N. R. Force-induced activation of covalent bonds in mechanoresponsive polymeric materials. *Nature* **2009**, *459* (7243), 68-72.
37. Chen, Y.; Spiering, A. J. H.; S. Karthikeyan, S.; Peters, G. W. M.; Meijer, E. W.; Sijbesma, R. P. Mechanically induced chemiluminescence from polymers incorporating a 1,2-dioxetane unit in the main chain. *Nat. Chem.* **2012**, *4* (7), 559.
38. Ramirez, A. L. B.; Kean, Z. S.; Orlicki, J. A.; Champhekar, M.; Elsakr, S. M.; Krause, W. E.; Craig, S. L. Mechanochemical strengthening of a synthetic polymer in response to typically destructive shear forces. *Nat. Chem.* **2013**, *5* (9), 757.
39. Zhou, H.; Johnson, J. A. Photo-controlled growth of telechelic polymers and end-linked polymer gels. *Angew. Chem. Int. Ed.* **2013,** *52* (8), 2235-2238.
40. Gordon, M. B.; French, J. M.; Wagner, N. J.; Kloxin, C. J. Dynamic bonds in covalently crosslinked polymer networks for photoactivated strengthening and healing. *Adv. Mater.* **2015**, *27* (48), 8007.
41. Chen, M.; Gu, Y.; Singh, A.; Zhong, M.; Jordan, A. M.; Biswas, S.; Korley, L. T. J.; Balazs, A. C.; Johnson, J. A. living additive manufacturing: transformation of parent gels into diversely functionalized daughter gels made possible by visible light photoredox catalysis. *ACS Cent. Sci.* **2017,** *3* (2), 124-134.
42. Matsuda, T.; Kawakami, R.; Namba, R.; Nakajima, T.; Gong, J. P. Mechanoresponsive self-growing hydrogels inspired by muscle training. *Science* **2019**, *363* (6426), 504.
43. Mohapatra, H.; Kleiman, M.; Esser-Kahn, A. P. Mechanically controlled radical polymerization initiated by ultrasound. *Nat. Chem.* **2016**, *9* (35), 135.
44. Wang, Z.; Wang, Z.; Pan, X.; Fu, L.; Lathwal, S.; Olszewski, M.; Yan, J.; Enciso, A. E.; Wang, Z.; Xia, H.; Matyjaszewski, K. Ultrasonication-induced aqueous atom transfer radical polymerization. *ACS Macro Lett.* **2018**, *7* (3), 275.
45. Cao, B.; Boechler, N.; Boydston, A. J. Additive manufacturing with a flex activated mechanophore for nondestructive assessment of mechanochemical reactivity in complex object geometries. *Polymer* **2018**, *152* (12), 4-8.
46. Roe, R. J. *Methods of X-ray and Neutron Scattering in Polymer Science*. Oxford University Press: 2000; p 95.
47. Kasai, N.; Kakudo, M. *X-ray diffraction by macromolecules*, Springer: 2005.
48. Zhang, J.-P.; Liao, P.-Q.; Zhou, H.-L.; Lin, R.-B.; Chen, X.-M. Single-crystal X-ray diffraction studies on structural transformations of porous coordination polymers. *Chem. Soc. Rev.* **2014**, *43* (16), 5789-5814.
49. Gu, Y.; Schauenburg, D.; Bode, J. W.; Johnson, J. A. Leaving Groups as Traceless Topological Modifiers for the Synthesis of Topologically Isomeric Polymer Networks. *J. Am. Chem. Soc.* **2018,** *140* (43), 14033-14037.

50. Hammouda, B.; Ho, D. L.; Kline, S. Insight into Clustering in Poly(ethylene oxide) Solutions. *Macromolecules* **2004,** *37* (18), 6932-6937.
51. Gu, Y.; Alt, E. A.; Wang, H.; Li, X.; Willard, A. P.; Johnson, J. A. Photoswitching topology in polymer networks with metal–organic cages as crosslinks. *Nature* **2018,** *560* (7716), 65-69.
52. Yue, K.; Liu, G.; Feng, X.; Li, L.; Lotz, B.; Cheng, S. Z. D. A few rediscovered and challenging topics in polymer crystals and crystallization. *Polymer Crystallization* **2018,** *1* (4), e10053.
53. Gao, H.; Matyjaszewski, K. Synthesis of functional polymers with controlled architecture by CRP of monomers in the presence of cross-linkers: From stars to gels. *Prog. Polym. Sci.* **2009,** *34* (4), 317-350.
54. Holten-Andersen, N.; Harrington, M. J.; Birkedal, H.; Lee, B. P.; Messersmith, P. B.; Lee, K. Y. C.; Waite, J. H. pH-induced metal-ligand cross-links inspired by mussel yield self-healing polymer networks with near-covalent elastic moduli. *Proc. Natl. Acad. Sci. USA* **2011,** *108* (7), 2651-2655.
55. Ricardo, N. M. P. S.; Honorato, S. B.; Yang, Z.; Castelletto, V.; Hamley, I. W.; Yuan, X.-F.; Attwood, D.; Booth, C. Gelation of Concentrated Micellar Solutions of a Triblock Copolymer of Ethylene Oxide and Styrene Oxide, S5E45S5. *Langmuir* **2004,** *20* (10), 4272-4278.
56. Taribagil, R. R.; Hillmyer, M. A.; Lodge, T. P. Hydrogels from ABA and ABC Triblock Polymers. *Macromolecules* **2010,** *43* (12), 5396-5404.
57. Zhou, C.; Hillmyer, M. A.; Lodge, T. P. Efficient Formation of Multicompartment Hydrogels by Stepwise Self-Assembly of Thermoresponsive ABC Triblock Terpolymers. *J. Am. Chem. Soc.* **2012,** *134* (25), 10365-10368.
58. Hall, C. C.; Zhou, C.; Danielsen, S. P. O.; Lodge, T. P. Formation of Multicompartment Ion Gels by Stepwise Self-Assembly of a Thermoresponsive ABC Triblock Terpolymer in an Ionic Liquid. *Macromolecules* **2016,** *49* (6), 2298-2306.
59. Wang, Q.; Mynar, J. L.; Yoshida, M.; Lee, E.; Lee, M.; Okuro, K.; Kinbara, K.; Aida, T. High-water-content mouldable hydrogels by mixing clay and a dendritic molecular binder. *Nature* **2010,** *463* (7279), 339–343.
60. Appel, E. A.; Tibbitt, M. W.; Webber, M. J.; Mattix, B. A.; Veiseh, O.; Langer, R. Self-assembled hydrogels utilizing polymer–nanoparticle interactions. *Nat. Commun.* **2015,** *6* , 6295.
61. Li, Q.; Barrett, D. G.; Messersmith, P. B.; Holten-Andersen, N. Controlling Hydrogel Mechanics via Bio-Inspired Polymer–Nanoparticle Bond Dynamics. *ACS Nano* **2016,** *10* (1), 1317-1324.
62. Goodwin, D. J.; Sepassi, S.; King, S. M.; Holland, S. J.; Martini, L. G.; Lawrence, M. J. Characterization of Polymer Adsorption onto Drug Nanoparticles Using Depletion Measurements and Small-Angle Neutron Scattering. *Mol. Pharmaceutics* **2013,** *10* (11), 4146-4158.
63. Harris, K.; Fujita, D.; Fujita, M. Giant hollow MnL2n spherical complexes: structure, functionalisation and applications. *Chem. Commun.* **2013,** *49* (60), 6703-6712.
64. Kawamoto, K.; Grindy, S. C.; Liu, J.; Holten-Andersen, N.; Johnson, J. A. Dual Role for 1,2,4,5-Tetrazines in Polymer Networks: Combining Diels–Alder Reactions and Metal Coordination To Generate Functional Supramolecular Gels. *ACS Macro Lett.* **2015,** *4* (4), 458-461.
65. Foster, J. A.; Parker, R. M.; Belenguer, A. M.; Kishi, N.; Sutton, S.; Abell, C.; Nitschke, J. R. Differentially Addressable Cavities within Metal–Organic Cage-Cross-Linked Polymeric Hydrogels. *J. Am. Chem. Soc.* **2015,** *137* (30), 9722-9729.
66. Zhukhovitskiy, A. V.; Zhong, M.; Keeler, E. G.; Michaelis, V. K.; Sun, J. E. P.; Hore, M. J. A.; Pochan, D. J.; Griffin, R. G.; Willard, A. P.; Johnson, J. A. Highly branched and loop-rich gels via formation of metal–organic cages linked by polymers. *Nat. Chem.* **2015,** *8* (1), 33-41.
67. Wang, Y.; Gu, Y.; Keeler, E. G.; Park, J. V.; Griffin, R. G.; Johnson, J. A. Star PolyMOCs with Diverse Structures, Dynamics, and Functions by Three-Component Assembly. *Angew. Chem. Int. Ed.* **2017,** *56* (1), 188-192.
68. Gao, Y.; Newland, B.; Zhou, D.; Matyjaszewski, K.; Wang, W. Controlled Polymerization of Multivinyl Monomers: Formation of Cyclized/Knotted Single-Chain Polymer Architectures. *Angew. Chem. Int. Ed.* **2017,** *56* (2), 450-460.
69. Tezuka, Y. Topological Polymer Chemistry Designing Complex Macromolecular Graph Constructions. *Acc. Chem. Res.* **2017,** *50* (11), 2661-2672.
70. Tu, X.-Y.; Liu, M.-Z.; Wei, H. Recent progress on cyclic polymers: Synthesis, bioproperties, and biomedical applications. *J. Polym. Sci. A* **2016,** *54* (11), 1447-1458.
71. Wenz, G.; Han, B.-H.; Müller, A. Cyclodextrin Rotaxanes and Polyrotaxanes. *Chem. Rev.* **2006,** *106* (3), 782-817.

72. Niu, Z.; Gibson, H. W. Polycatenanes. *Chem. Rev.* **2009,** *109* (11), 6024-6046.
73. Zhang, K.; Lackey, M. A.; Cui, J.; Tew, G. N. Gels Based on Cyclic Polymers. *J. Am. Chem. Soc.* **2011,** *133* (11), 4140-4148.
74. Alsbaiee, A.; Smith, B. J.; Xiao, L.; Ling, Y.; Helbling, D. E.; Dichtel, W. R. Rapid removal of organic micropollutants from water by a porous β-cyclodextrin polymer. *Nature* **2015,** *529* (1), 190-194.
75. Badeau, B. A.; Comerford, M. P.; Arakawa, C. K.; Shadish, J. A.; DeForest, C. A. Engineered modular biomaterial logic gates for environmentally triggered therapeutic delivery. *Nat. Chem.* **2018,** *10* (1), 251–258.
76. Delaviz, Y.; Gibson, H. W. Macrocyclic polymers. 2. Synthesis of poly(amide crown ethers) based on bis(5-carboxy-1,3-phenylene)-32-crown-10. Network formation through threading. *Macromolecules* **1992,** *25* (19), 4859-4862.
77. Oike, H.; Mouri, T.; Tezuka, Y. A Cyclic Macromonomer Designed for a Novel Polymer Network Architecture Having Both Covalent and Physical Linkages. *Macromolecules* **2001,** *34* (18), 6229-6234.
78. Kubo, M.; Hibino, T.; Tamura, M.; Uno, T.; Itoh, T. Synthesis and Copolymerization of Cyclic Macromonomer Based on Cyclic Polystyrene: Gel Formation via Chain Threading. *Macromolecules* **2002,** *35* (15), 5816-5820.
79. Oku, T.; Furusho, Y.; Takata, T. A Concept for Recyclable Cross-Linked Polymers: Topologically Networked Polyrotaxane Capable of Undergoing Reversible Assembly and Disassembly. *Angew. Chem. Int. Ed.* **2004,** *43* (8), 966-969.
80. Okumura, Y.; Ito, K. The Polyrotaxane Gel: A Topological Gel by Figure-of-Eight Cross-links. *Adv. Mater.* **2001,** *13* (7), 485-487.
81. Noda, Y.; Hayashi, Y.; Ito, K. From topological gels to slide-ring materials. *J. Appl. Polym. Sci.* **2014,** *131* (15), 40509.
82. Choi, S.; Kwon, T.-w.; Coskun, A.; Choi, J. W. Highly elastic binders integrating polyrotaxanes for silicon microparticle anodes in lithium ion batteries. *Science* **2017,** *357* (6348), 279-283.
83. Sawada, J.; Aoki, D.; Uchida, S.; Otsuka, H.; Takata, T. Synthesis of Vinylic Macromolecular Rotaxane Cross-Linkers Endowing Network Polymers with Toughness. *ACS Macro Lett.* **2015,** *4* (5), 598-601.
84. Goujon, A.; Lang, T.; Mariani, G.; Moulin, E.; Fuks, G.; Raya, J.; Buhler, E.; Giuseppone, N. Bistable [c2 Daisy Chain Rotaxanes as Reversible Muscle-like Actuators in Mechanically Active Gels. *J. Am. Chem. Soc.* **2017,** *139* (42), 14825-14828.
85. Wu, Q.; Rauscher, P. M.; Lang, X.; Wojtecki, R. J.; de Pablo, J. J.; Hore, M. J. A.; Rowan, S. J. Poly[ncatenanes: Synthesis of molecular interlocked chains. *Science* **2017,** *358* (6369), 1434-1439.
86. Lukeš, J.; Lys Guilbride, D.; Votýpka, J.; Zíková, A.; Benne, R.; Englund, P. T. Kinetoplast DNA Network: Evolution of an Improbable Structure. *Eukaryot. Cell* **2002,** *1* (4), 495-502.
87. Endo, K.; Shiroi, T.; Murata, N.; Kojima, G.; Yamanaka, T. Synthesis and Characterization of Poly(1,2-dithiane). *Macromolecules* **2004,** *37* (9), 3143-3150.
88. Xing, H.; Li, Z.; Wu, Z. L.; Huang, F. Catenane Crosslinked Mechanically Adaptive Polymer Gel. *Macromol. Rapid Commun.* **2018,** *39* (1), 1700361.
89. Chan, D.; Ding, Y.; Dauskardt, R. H.; Appel, E. A. Engineering the Mechanical Properties of Polymer Networks with Precise Doping of Primary Defects. *ACS Appl. Mater. Interfaces* **2017,** *9* (48), 42217-42224.
90. Sakai, T.; Matsunaga, T.; Yamamoto, Y.; Ito, C.; Yoshida, R.; Suzuki, S.; Sasaki, N.; Shibayama, M.; Chung, U.-i. Design and Fabrication of a High-Strength Hydrogel with Ideally Homogeneous Network Structure from Tetrahedron-like Macromonomers. *Macromolecules* **2008,** *41* (14), 5379-5384.
91. Sugimura, A.; Asai, M.; Matsunaga, T.; Akagi, Y.; Sakai, T.; Noguchi, H.; Shibayama, M. Mechanical properties of a polymer network of Tetra-PEG gel. *Polym. J.* **2012,** *45* (3), 300-306.
92. Matsunaga, T.; Sakai, T.; Akagi, Y.; Chung, U.-i.; Shibayama, M. Structure Characterization of Tetra-PEG Gel by Small-Angle Neutron Scattering. *Macromolecules* **2009,** *42* (4), 1344-1351.
93. Akagi, Y.; Matsunaga, T.; Shibayama, M.; Chung, U.-i.; Sakai, T. Evaluation of Topological Defects in Tetra-PEG Gels. *Macromolecules* **2010,** *43* (1), 488-493.
94. Lin, T.-S.; Wang, R.; Johnson, J. A.; Olsen, B. D. Topological Structure of Networks Formed from

Symmetric Four-Arm Precursors. *Macromolecules* **2018,** *51* (3), 1224-1231.
95. Otsu, T. Iniferter concept and living radical polymerization. *J. Polym. Sci. A* **2000**, *38* (12), 2121-2136.
96. Ni, Y.; Zhang, L.; Cheng, Z. ; Zhu, X. Iodine-mediated reversible-deactivation radical polymerization: a powerful strategy for polymer synthesis. *Polym. Chem.* **2019**, *10* (20), 2504-2515.
97. Braunecker, W. A.; Matyjaszewski, K. Controlled/living radical polymerization: Features, developments, and perspectives. *Prog. Polym. Sci.* **2007,** *32* (1), 93-146.
98. Georges, M. K.; Veregin, R. P. N.; Kazmaier, P. M.; Hamer, G. K. Narrow molecular weight resins by a free-radical polymerization process. *Macromolecules* **1993**, *26* (11), 2987-2988.
99. Hawker, C. J. Molecular weight control by a "living" free-radical polymerization process. *J. Am. Chem. Soc.* **1994**, *116* (24), 11185-11186.
100. Nicolas, J.; Guillaneuf, Y.; Lefay, C.; Bertin, D.; Gigmes, D.; Charleux, B. Nitroxide-mediated polymerization. *Prog. Polym. Sci.* **2013,** *38* (1), 63-235.
101. Kato, M.; Kamigaito, M.; Sawamoto, M.; Higashimura, T. Polymerization of methyl methacrylate with the carbon tetrachloride/dichlorotris- (triphenylphosphine)ruthenium(ii)/methylaluminum bis(2,6-di-tert-butylphenoxide) initiating system: possibility of living radical polymerization. *Macromolecules* **1995**, *28* (5), 1721-1723.
102. Wang, J.-S.; Matyjaszewski, K. Controlled/"living" radical polymerization. Atom transfer radical polymerization in the presence of transition-metal complexes. *J. Am. Chem. Soc.* **1995**, *117* (20), 5614-5615.
103. Matyjaszewski, K. Atom transfer radical polymerization (ATRP): current status and future perspectives. *Macromolecules* **2012,** *45* (10), 4015-4039.
104. Chiefari, J.; Chong, Y. K.; Ercole, F.; Krstina, J.; Jeffery, J.; Le, T. P. T.; Mayadunne, R. T. A.; Meijs, G. F.; Moad, C. L.; Moad, G.; Rizzardo, E.; Thang, S. H. Living free-radical polymerization by reversible addition−fragmentation chain transfer: the RAFT process. *Macromolecules* **1998**, *31* (16), 5559-5562.
105. Moad, G.; Rizzardo, E.; Thang, S. H. Radical addition–fragmentation chemistry in polymer synthesis. *Polymer* **2008,** *49* (5), 1079-1131.
106. Perrier, S. 50th Anniversary Perspective: RAFT Polymerization—A User Guide. *Macromolecules* **2017,** *50* (19), 7433-7447.
107. Shanmugam, S.; Xu, J.; Boyer, C. Photoinduced electron transfer–reversible addition–fragmentation chain transfer (PET-RAFT) polymerization of vinyl acetate and N-vinylpyrrolidinone: kinetic and oxygen tolerance study. *Macromolecules* **2014**, *47* (15), 4930-4942.
108. Chen, M.; Zhong, M.; Johnson, J. A. Light-controlled radical polymerization: mechanisms, methods, and applications. *Chem. Rev.* **2016,** *116* (17), 10167-10211.
109. Amamoto, Y.; Kamada, J.; Otsuka, H.; Takahara, A.; Matyjaszewski, K. Repeatable photoinduced self-healing of covalently cross-linked polymers through reshuffling of trithiocarbonate units. *Angew. Chem. Int. Ed.* **2011**, *50* (7), 1660-1663.
110. Amamoto, Y.; Otsuka, H.; Takahara, A.; Matyjaszewski, K. Self-healing of covalently cross-linked polymers by reshuffling thiuram disulfide moieties in air under visible light. *Adv. Mater.* **2012**, *24* (29), 3975-3980.
111. Lampley, M. W.; Harth, E. Photocontrolled growth of cross-linked nanonetworks. *ACS Macro Lett.* **2018**, *7* (6), 745-750.
112. Ide, N.; Fukuda, T. Nitroxide-Controlled Free-Radical Copolymerization of Vinyl and Divinyl Monomers. 2. Gelation. *Macromolecules* **1999,** *32* (1), 95-99.
113. Yu, Q.; Zeng, F.; Zhu, S. Atom Transfer Radical Polymerization of Poly(ethylene glycol) Dimethacrylate. *Macromolecules* **2001,** *34* (6), 1612-1618.
114. Gao, H.; Min, K.; Matyjaszewski, K. Determination of Gel Point during Atom Transfer Radical Copolymerization with Cross-Linker. *Macromolecules* **2007,** *40* (22), 7763-7770.
115. Norioka, C.; Kawamura, A.; Miyata, T. Mechanical and responsive properties of temperature-responsive gels prepared via atom transfer radical polymerization. *Polym. Chem.* **2017,** *8* (39), 6050-6057.
116. Moad, G. RAFT (Reversible addition–fragmentation chain transfer) crosslinking (co)polymerization of multi-olefinic monomers to form polymer networks. *Polym. Int.* **2015,** *64* (1), 15-24.

117. Johnson, J. A.; Lewis, D. R.; Díaz, D. D.; Finn, M. G.; Koberstein, J. T.; Turro, N. J. Synthesis of Degradable Model Networks via ATRP and Click Chemistry. *J. Am. Chem. Soc.* **2006,** *128* (20), 6564-6565.
118. Beziau, A.; Fortney, A.; Fu, L.; Nishiura, C.; Wang, H.; Cuthbert, J.; Gottlieb, E.; Balazs, A. C.; Kowalewski, T.; Matyjaszewski, K. Photoactivated structurally tailored and engineered macromolecular (STEM) gels as precursors for materials with spatially differentiated mechanical properties. *Polymer* **2017,** *126* (22), 224-230.
119. Cuthbert, J.; Beziau, A.; Gottlieb, E.; Fu, L.; Yuan, R.; Balazs, A. C.; Kowalewski, T.; Matyjaszewski, K. Transformable materials: structurally tailored and engineered macromolecular (STEM) gels by controlled radical polymerization. *Macromolecules* **2018,** *51* (10), 3808-3817.
120. Cuthbert, J.; Zhang, T.; Biswas, S.; Olszewski, M.; Shanmugam, S.; Fu, T.; Gottlieb, E.; Kowalewski, T.; Balazs, A. C.; Matyjaszewski, K. structurally tailored and engineered macromolecular (STEM) gels as soft elastomers and hard/soft interfaces. *Macromolecules* **2018,** *51* (22), 9184-9191.
121. Freeman, R.; Han, M.; Álvarez, Z.; Lewis, J. A.; Wester, J. R.; Stephanopoulos, N.; McClendon, M. T.; Lynsky, C.; Godbe, J. M.; Sangji, H.; Luijten, E.; Stupp, S. I. Reversible self-assembly of superstructured networks. *Science* **2018,** *362* (6416), 808-813.
122. James, H. M.; Guth, E. Statistical thermodynamics of rubber elasticity. *J. Chem. Phys.* **1953,** *21* (6), 1039-1049.
123. Zhong, M.; Wang, R.; Kawamoto, K.; Olsen, B. D.; Johnson, J. A. Quantifying the impact of molecular defects on polymer network elasticity. *Science* **2016,** *353* (6305), 1264-1268.
124. Wang, R.; Johnson, J. A.; Olsen, B. D. Odd–even effect of junction functionality on the topology and elasticity of polymer networks. *Macromolecules* **2017,** *50* (6), 2556-2564.
125. Lang, M. Elasticity of phantom model networks with cyclic defects. *ACS Macro Lett.* **2018,** *7* (5), 536-539.
126. Lin, T.-S.; Wang, R.; Johnson, J. A.; Olsen, B. D. Revisiting the elasticity theory for real Gaussian phantom networks. *Macromolecules* **2019**, *52* (4), 1685-1694.
127. Akagi, Y.; Gong, J. P.; Chung, U.-I.; Sakai, T. Transition between phantom and affine network model observed in polymer gels with controlled network structure. *Macromolecules* **2013,** *46* (3), 1035-1040.
128. Treloar, L. R. G. *The physics of rubber elasticity*. Clarendon Press: Oxford, 1975.
129. Mpoukouvalas, A.; Li, W.; Graf, R.; Koynov, K.; Matyjaszewski, K. Soft elastomers via introduction of poly(butyl acrylate) “diluent” to poly(hydroxyethyl acrylate)-based gel networks. *ACS Macro Lett.* **2013,** *2* (1), 23-26.
130. Daniel, W. F. M.; Burdyńska, J.; Vatankhah-Varnoosfaderani, M.; Matyjaszewski, K.; Paturej, J.; Rubinstein, M.; Dobrynin, A. V.; Sheiko, S. S. Solvent-free, supersoft and superelastic bottlebrush melts and networks. *Nat. Mater.* **2015,** *15* (2), 183-189.
131. Vatankhah-Varnosfaderani, M.; Daniel, W. F. M.; Everhart, M. H.; Pandya, A. A.; Liang, H.; Matyjaszewski, K.; Dobrynin, A. V.; Sheiko, S. S. Mimicking biological stress–strain behaviour with synthetic elastomers. *Nature* **2017,** *549* (7673), 497-501.
132. Vatankhah-Varnosfaderani, M.; Keith, A. N.; Cong, Y.; Liang, H.; Rosenthal, M.; Sztucki, M.; Clair, C.; Magonov, S.; Ivanov, D. A.; Dobrynin, A. V.; Sheiko, S. S. Chameleon-like elastomers with molecularly encoded strain-adaptive stiffening and coloration. *Science* **2018,** *359* (6383), 1509-1513.
133. Flory, P. J.; Rehner, J. Statistical Mechanics of Cross-Linked Polymer Networks II. Swelling. *J. Chem. Phys.* **1943,** *11* (11), 521-526.
134. Flory, P. J. Effects of Molecular Structure on Physical Properties of Butyl Rubber. *Ind. Eng. Chem. Res.* **1946,** *38* (4), 417-436.
135. Flory, P. J. Statistical Mechanics of Swelling of Network Structures. *J. Chem. Phys.* **1950,** *18* (1), 108-111.
136. Painter, P. C.; Shenoy, S. L. A simple model for the swelling of polymer networks. *J. Chem. Phys.* **1993,** *99* (2), 1409-1418.
137. Rubinstein, M.; Colby, R. H.; Dobrynin, A. V.; Joanny, J.-F. Elastic Modulus and Equilibrium Swelling of Polyelectrolyte Gels. *Macromolecules* **1996,** *29* (1), 398-406.
138. Kamata, H.; Akagi, Y.; Kayasuga-Kariya, Y.; Chung, U.-i.; Sakai, T. “Nonswellable” Hydrogel Without Mechanical Hysteresis. *Science* **2014,** *343* (6173), 873-875.

139. Chung, K.; Wallace, J.; Kim, S.-Y.; Kalyanasundaram, S.; Andalman, A. S.; Davidson, T. J.; Mirzabekov, J. J.; Zalocusky, K. A.; Mattis, J.; Denisin, A. K.; Pak, S.; Bernstein, H.; Ramakrishnan, C.; Grosenick, L.; Gradinaru, V.; Deisseroth, K. Structural and molecular interrogation of intact biological systems. *Nature* **2013,** *497* (7449), 332-337.
140. Chen, F.; Tillberg, P. W.; Boyden, E. S. Expansion microscopy. *Science* **2015,** *347* (6221), 543-548.
141. Oran, D.; Rodriques, S. G.; Gao, R.; Asano, S.; Skylar-Scott, M. A.; Chen, F.; Tillberg, P. W.; Marblestone, A. H.; Boyden, E. S. 3D nanofabrication by volumetric deposition and controlled shrinkage of patterned scaffolds. *Science* **2018,** *362* (6420), 1281-1285.
142. Kim, J.; Hanna, J. A.; Byun, M.; Santangelo, C. D.; Hayward, R. C. Designing Responsive Buckled Surfaces by Halftone Gel Lithography. *Science* **2012,** *335* (6073), 1201-1205.
143. Sydney Gladman, A.; Matsumoto, E. A.; Nuzzo, R. G.; Mahadevan, L.; Lewis, J. A. Biomimetic 4D printing. *Nat. Mater.* **2016,** *15* (4), 413-418.
144. Cangialosi, A.; Yoon, C.; Liu, J.; Huang, Q.; Guo, J.; Nguyen, T. D.; Gracias, D. H.; Schulman, R. DNA sequence–directed shape change of photopatterned hydrogels via high-degree swelling. *Science* **2017,** *357* (6356), 1126-1130.
145. Zarzar, L. D.; Aizenberg, J. Stimuli-Responsive Chemomechanical Actuation: A Hybrid Materials Approach. *Acc. Chem. Res.* **2014,** *47* (2), 530-539.
146. Jeon, S.-J.; Hauser, A. W.; Hayward, R. C. Shape-Morphing Materials from Stimuli-Responsive Hydrogel Hybrids. *Acc. Chem. Res.* **2017,** *50* (2), 161-169.
147. Ferry, J. D. *Viscoelastic Properties of Polymers*. 3rd ed.; John Wiley & Sons: 1980.
148. Shaw, M. T. *Introduction to Polymer Rheology*. John Wiley & Sons: 2012.
149. Patel, S. K.; Malone, S.; Cohen, C.; Gillmor, J. R.; Colby, R. H. Elastic modulus and equilibrium swelling of poly(dimethylsiloxane) networks. *Macromolecules* **1992,** *25* (20), 5241-5251.
150. Yount, W. C.; Loveless, D. M.; Craig, S. L. Small-Molecule Dynamics and Mechanisms Underlying the Macroscopic Mechanical Properties of Coordinatively Cross-Linked Polymer Networks. *J. Am. Chem. Soc.* **2005,** *127* (41), 14488-14496.
151. Grindy, S. C.; Learsch, R.; Mozhdehi, D.; Cheng, J.; Barrett, D. G.; Guan, Z.; Messersmith, P. B.; Holten-Andersen, N. Control of hierarchical polymer mechanics with bioinspired metal-coordination dynamics. *Nat. Mater.* **2015,** *14* (12), 1210-1216.
152. Mours, M.; Winter, H. H. Relaxation Patterns of Nearly Critical Gels. *Macromolecules* **1996,** *29* (22), 7221-7229.
153. Winter, H. H. Can the gel point of a cross-linking polymer be detected by the G′ – G″ crossover? *Polym. Eng. Sci.* **1987,** *27* (22), 1698-1702.
154. Despax, L.; Fitremann, J.; Destarac, M.; Harrisson, S. Low concentration thermoresponsive hydrogels from readily accessible triblock copolymers. *Polym. Chem.* **2016,** *7* (20), 3375-3377.
155. Zhao, Y.-L.; Stoddart, J. F. Azobenzene-Based Light-Responsive Hydrogel System. *Langmuir* **2009,** *25* (15), 8442-8446.
156. Kloxin, A. M.; Kasko, A. M.; Salinas, C. N.; Anseth, K. S. Photodegradable Hydrogels for Dynamic Tuning of Physical and Chemical Properties. *Science* **2009,** *324* (5923), 59-63.
157. Ahn, S.-k.; Kasi, R. M.; Kim, S.-C.; Sharma, N.; Zhou, Y. Stimuli-responsive polymer gels. *Soft Matter* **2008,** *4* (6), 1151-1157.
158. Yang, Y.; Urban, M. W. Self-healing polymeric materials. *Chem. Soc. Rev.* **2013,** *42* (17), 7446-7467.
159. Kloxin, C. J.; Bowman, C. N. Covalent adaptable networks: smart, reconfigurable and responsive network systems. *Chem. Soc. Rev.* **2013,** *42* (17), 7161-7173.
160. Denissen, W.; Winne, J. M.; Du Prez, F. E. Vitrimers: permanent organic networks with glass-like fluidity. *Chem. Sci.* **2016,** *7* (1), 30-38.
161. Jin, Y.; Yu, C.; Denman, R. J.; Zhang, W. Recent advances in dynamic covalent chemistry. *Chem. Soc. Rev.* **2013,** *42* (16), 6634-6654.
162. Chen, X.; Dam, M. A.; Ono, K.; Mal, A.; Shen, H.; Nutt, S. R.; Sheran, K.; Wudl, F. A Thermally Re-mendable Cross-Linked Polymeric Material. *Science* **2002,** *295* (5560), 1698-1702.
163. Adzima, B. J.; Aguirre, H. A.; Kloxin, C. J.; Scott, T. F.; Bowman, C. N. Rheological and chemical analysis of reverse gelation in a covalently cross-linked diels−alder polymer network. *Macromolecules* **2008,** *41* (23), 9112-9117.
164. Amamoto, Y.; Otsuka, H.; Takahara, A.; Matyjaszewski, K. Self-healing of covalently cross-linked

polymers by reshuffling thiuram disulfide moieties in air under visible light. *Adv. Mater.* **2012,** *24* (29), 3975-3980.
165. Montarnal, D.; Capelot, M.; Tournilhac, F.; Leibler, L. Silica-like malleable materials from permanent organic networks. *Science* **2011,** *334* (6058), 965-968.
166. Scott, T. F.; Schneider, A. D.; Cook, W. D.; Bowman, C. N. Photoinduced plasticity in cross-linked polymers. *Science* **2005,** *308* (5728), 1615-1617.
167. Amamoto, Y.; Kamada, J.; Otsuka, H.; Takahara, A.; Matyjaszewski, K. Repeatable photoinduced self-healing of covalently cross-linked polymers through reshuffling of trithiocarbonate units. *Angew. Chem. Int. Ed.* **2011,** *50* (7), 1660-1663.
168. McBride, M. K.; Martinez, A. M.; Cox, L.; Alim, M.; Childress, K.; Beiswinger, M.; Podgorski, M.; Worrell, B. T.; Killgore, J.; Bowman, C. N. A readily programmable, fully reversible shape-switching material. *Sci. Adv.* **2018,** *4* (8), eaat4634.
169. Slater, A. G.; Cooper, A. I. Function-led design of new porous materials. *Science* **2015,** *348* (6238), aaa8075.
170. Kaur, P.; Hupp, J. T.; Nguyen, S. T. Porous organic polymers in catalysis: opportunities and challenges. *ACS Catal.* **2011,** *1* (7), 819-835.
171. Xu, Y.; Jin, S.; Xu, H.; Nagai, A.; Jiang, D. Conjugated microporous polymers: design, synthesis and application. *Chem. Soc. Rev.* **2013,** *42* (20), 8012-8031.
172. Tan, L.; Tan, B. Hypercrosslinked porous polymer materials: design, synthesis, and applications. *Chem. Soc. Rev.* **2017,** *46* (11), 3322-3356.
173. McKeown, N. B.; Hanif, S.; Msayib, K.; Tattershall, C. E.; Budd, P. M. Porphyrin-based nanoporous network polymers. *Chem. Commun.* **2002,** *0* (23), 2782-2783.
174. Jiang, J.-X.; Su, F.; Trewin, A.; Wood, C. D.; Campbell, N. L.; Niu, H.; Dickinson, C.; Ganin, A. Y.; Rosseinsky, M. J.; Khimyak, Y. Z.; Cooper, A. I. Conjugated microporous poly(aryleneethynylene) networks. *Angew. Chem. Int. Ed.* **2007,** *46* (45), 8574-8578.
175. Ong, W. J.; Swager, T. M. Dynamic self-correcting nucleophilic aromatic substitution. *Nat. Chem.* **2018,** *10* (10), 1023-1030.
176. Ben, T.; Ren, H.; Ma, S.; Cao, D.; Lan, J.; Jing, X.; Wang, W.; Xu, J.; Deng, F.; Simmons, J. M.; Qiu, S.; Zhu, G. Targeted synthesis of a porous aromatic framework with high stability and exceptionally high surface area. *Angew. Chem. Int. Ed.* **2009,** *48* (50), 9457-9460.
177. Pandey, P.; Farha, O. K.; Spokoyny, A. M.; Mirkin, C. A.; Kanatzidis, M. G.; Hupp, J. T.; Nguyen, S. T. A "click-based" porous organic polymer from tetrahedral building blocks. *J. Mater. Chem.* **2011,** *21* (6), 1700-1703.
178. Lu, W.; Yuan, D.; Zhao, D.; Schilling, C. I.; Plietzsch, O.; Muller, T.; Bräse, S.; Guenther, J.; Blümel, J.; Krishna, R.; Li, Z.; Zhou, H.-C. Porous polymer networks: synthesis, porosity, and applications in gas storage/separation. *Chem. Mater.* **2010,** *22* (21), 5964-5972.
179. Lee, J.-Y.; Wood, C. D.; Bradshaw, D.; Rosseinsky, M. J.; Cooper, A. I. Hydrogen adsorption in microporous hypercrosslinked polymers. *Chem. Commun.* **2006,** *0* (25), 2670-2672.
180. Dawson, R.; Cooper, A. I.; Adams, D. J. Nanoporous organic polymer networks. *Prog. Polym. Sci.* **2012,** *37* (4), 530-563.
181. Das, S.; Heasman, P.; Ben, T.; Qiu, S. Porous organic materials: strategic design and structure–function correlation. *Chem. Rev.* **2017,** *117* (3), 1515-1563.
182. Long, T. M.; Swager, T. M. Molecular Design of Free Volume as a Route to Low-κ Dielectric Materials. *J. Am. Chem. Soc.* **2003,** *125* (46), 14113-14119.
183. Sydlik, S. A.; Chen, Z.; Swager, T. M. Triptycene polyimides: soluble polymers with high thermal stability and low refractive indices. *Macromolecules* **2011,** *44* (4), 976-980.
184. Budd, P. M.; Ghanem, B. S.; Makhseed, S.; McKeown, N. B.; Msayib, K. J.; Tattershall, C. E. Polymers of intrinsic microporosity (PIMs): robust, solution-processable, organic nanoporous materials. *Chem. Commun.* **2004,** *0* (2), 230-231.
185. Carta, M.; Malpass-Evans, R.; Croad, M.; Rogan, Y.; Jansen, J. C.; Bernardo, P.; Bazzarelli, F.; McKeown, N. B. An efficient polymer molecular sieve for membrane gas separations. *Science* **2013,** *339* (6117), 303-307.
186. Liu, S.; Jin, Z.; Teo, Y. C.; Xia, Y. Efficient synthesis of rigid ladder polymers via palladium catalyzed annulation. *J. Am. Chem. Soc.* **2014,** *136* (50), 17434-17437.
187. Lai, H. W. H.; Liu, S.; Xia, Y. Norbornyl benzocyclobutene ladder polymers: Conformation and microporosity. *J. Polym. Sci. A* **2017,** *55* (18), 3075-3081.

188. Kitagawa, S.; Kitaura, R.; Noro, S.-i. Functional porous coordination polymers. *Angew. Chem. Int. Ed.* **2004,** *43* (18), 2334-2375.
189. Hosono, N.; Kitagawa, S. Modular Design of Porous Soft Materials via Self-Organization of Metal–Organic Cages. *Acc. Chem. Res.* **2018,** *51* (10), 2437-2446.
190. Zhou, C.; Longley, L.; Krajnc, A.; Smales, G. J.; Qiao, A.; Erucar, I.; Doherty, C. M.; Thornton, A. W.; Hill, A. J.; Ashling, C. W.; Qazvini, O. T.; Lee, S. J.; Chater, P. A.; Terrill, N. J.; Smith, A. J.; Yue, Y.; Mali, G.; Keen, D. A.; Telfer, S. G.; Bennett, T. D. Metal-organic framework glasses with permanent accessible porosity. *Nat. Commun.* **2018,** *9* (1), 5042.
191. Lal, G.; Derakhshandeh, M.; Akhtar, F.; Spasyuk, D. M.; Lin, J.-B.; Trifkovic, M.; Shimizu, G. K. H. Mechanical properties of a metal–organic framework formed by covalent cross-linking of metal–organic polyhedra. *J. Am. Chem. Soc.* **2018**, *141* (2), 1045-1053.
192. Yaghi, O. M.; O'Keeffe, M.; Ockwig, N. W.; Chae, H. K.; Eddaoudi, M.; Kim, J. Reticular synthesis and the design of new materials. *Nature* **2003,** *423* (6941), 705-714.
193. O'Keeffe, M.; Yaghi, O. M. Deconstructing the crystal structures of metal–organic frameworks and related materials into their underlying nets. *Chem. Rev.* **2012,** *112* (2), 675-702.
194. Li, M.; Li, D.; O'Keeffe, M.; Yaghi, O. M. Topological analysis of metal–organic frameworks with polytopic linkers and/or multiple building units and the minimal transitivity principle. *Chem. Rev.* **2014,** *114* (2), 1343-1370.
195. Schoedel, A.; Li, M.; Li, D.; O'Keeffe, M.; Yaghi, O. M. structures of metal–organic frameworks with rod secondary building units. *Chem. Rev.* **2016,** *116* (19), 12466-12535.
196. Kalmutzki, M. J.; Hanikel, N.; Yaghi, O. M. Secondary building units as the turning point in the development of the reticular chemistry of MOFs. *Sci. Adv.* **2018,** *4* (10), eaat9180.
197. Li, H.; Eddaoudi, M.; O'Keeffe, M.; Yaghi, O. M. Design and synthesis of an exceptionally stable and highly porous metal-organic framework. *Nature* **1999,** *402*, 276-279.
198. Furukawa, H.; Cordova, K. E.; O'Keeffe, M.; Yaghi, O. M. the chemistry and applications of metal-organic frameworks. *Science* **2013,** *341* (6149), 1230444.
199. Kaye, S. S.; Dailly, A.; Yaghi, O. M.; Long, J. R. Impact of preparation and handling on the hydrogen storage properties of Zn4O(1,4-benzenedicarboxylate)3 (MOF-5). *J. Am. Chem. Soc.* **2007,** *129* (46), 14176-14177.
200. Chui, S. S.-Y.; Lo, S. M.-F.; Charmant, J. P. H.; Orpen, A. G.; Williams, I. D. A chemically functionalizable nanoporous material $[Cu_3(TMA)_2(H_2O)_{3n}$. *Science* **1999,** *283* (5405), 1148-1150.
201. Worrall, S. D.; Bissett, M. A.; Hill, P. I.; Rooney, A. P.; Haigh, S. J.; Attfield, M. P.; Dryfe, R. A. W. Metal-organic framework templated electrodeposition of functional gold nanostructures. *Electrochim. Acta* **2016,** *222* (20), 361-369.
202. Chen, B.; Yang, Z.; Zhu, Y.; Xia, Y . Zeolitic imidazolate framework materials: recent progress in synthesis and applications. *J. Mater. Chem. A* **2014,** *2* (40), 16811-16831.
203. Park, K. S.; Ni, Z.; Côté, A. P.; Choi, J. Y.; Huang, R.; Uribe-Romo, F. J.; Chae, H. K.; O'Keeffe, M.; Yaghi, O. M . Exceptional chemical and thermal stability of zeolitic imidazolate frameworks. *Proc. Natl. Acad. Sci. USA* **2006,** *103* (27), 10186-10191.
204. Liang, W.; Ricco, R.; Maddigan, N. K.; Dickinson, R. P.; Xu, H.; Li, Q.; Sumby, C. J.; Bell, S. G.; Falcaro, P.; Doonan, C. J. Control of structure topology and spatial distribution of biomacromolecules in protein@ZIF-8 biocomposites. *Chem. Mater.* **2018,** *30* (3), 1069-1077.
205. Fairen-Jimenez, D.; Moggach, S. A.; Wharmby, M. T.; Wright, P. A.; Parsons, S.; Düren, T. Opening the gate: framework flexibility in zif-8 explored by experiments and simulations. *J. Am. Chem. Soc.* **2011,** *133* (23), 8900-8902.
206. Rosi, N. L.; Kim, J.; Eddaoudi, M.; Chen, B.; O'Keeffe, M.; Yaghi, O. M. Rod packings and metal−organic frameworks constructed from rod-shaped secondary building units. *J. Am. Chem. Soc.* **2005,** *127* (5), 1504-1518.
207. Srinivas, G.; Krungleviciute, V.; Guo, Z.-X.; Yildirim, T. Exceptional CO_2 capture in a hierarchically porous carbon with simultaneous high surface area and pore volume. *Energy Environ. Sci.* **2014,** *7* (1), 335-342.
208. Tanabe, K. K.; Cohen, S. M. Postsynthetic modification of metal–organic frameworks—a progress report. *Chem. Soc. Rev.* **2011,** *40* (2), 498-519.
209. Islamoglu, T.; Goswami, S.; Li, Z.; Howarth, A. J.; Farha, O. K.; Hupp, J. T. Postsynthetic tuning of metal–organic frameworks for targeted applications. *Acc. Chem. Res.* **2017,** *50* (4), 805-813.
210. Farha, O. K.; Eryazici, I.; Jeong, N. C.; Hauser, B. G.; Wilmer, C. E.; Sarjeant, A. A.; Snurr, R. Q.;

Nguyen, S. T.; Yazaydın, A. Ö.; Hupp, J. T. Metal–organic framework materials with ultrahigh surface areas: is the sky the limit? *J. Am. Chem. Soc.* **2012,** *134* (36), 15016-15021.
211. Yuan, S.; Feng, L.; Wang, K.; Pang, J.; Bosch, M.; Lollar, C.; Sun, Y.; Qin, J.; Yang, X.; Zhang, P.; Wang, Q.; Zou, L.; Zhang, Y.; Zhang, L.; Fang, Y.; Li, J.; Zhou, H.-C. Stable metal–organic frameworks: design, synthesis, and applications. *Adv. Mater.* **2018,** *30* (37), 1704303.
212. Cavka, J. H.; Jakobsen, S.; Olsbye, U.; Guillou, N.; Lamberti, C.; Bordiga, S.; Lillerud, K. P. A new zirconium inorganic building brick forming metal organic frameworks with exceptional stability. *J. Am. Chem. Soc.* **2008,** *130* (42), 13850-13851.
213. Zhang, Y.; Feng, X.; Yuan, S.; Zhou, J.; Wang, B. Challenges and recent advances in MOF–polymer composite membranes for gas separation. *Inorg. Chem. Front.* **2016,** *3* (7), 896-909.
214. Pastore, V. J.; Cook, T. R.; Rzayev, J. Polymer–MOF hybrid composites with high porosity and stability through surface-selective ligand exchange. *Chem. Mater.* **2018,** *30* (23), 8639-8649.
215. Qiao, Z.; Zhao, S.; Sheng, M.; Wang, J.; Wang, S.; Wang, Z.; Zhong, C.; Guiver, M. D. Metal-induced ordered microporous polymers for fabricating large-area gas separation membranes. *Nat. Mater.* **2019,** *18* (2), 163-168.
216. Kalaj, M.; Denny Jr, M. S.; Bentz, K. C.; Palomba, J. M.; Cohen, S. M. Nylon–MOF composites through postsynthetic polymerization. *Angew. Chem. Int. Ed.* **2019,** *58* (8), 2336-2340.
217. Zhang, Z.; Nguyen, H. T. H.; Miller, S. A.; Cohen, S. M. PolyMOFs: a class of interconvertible polymer-metal-organic-framework hybrid materials. *Angew. Chem. Int. Ed.* **2015,** *54* (21), 6152-6157.
218. Zhang, Z.; Nguyen, H. T. H.; Miller, S. A.; Ploskonka, A. M.; DeCoste, J. B.; Cohen, S. M. Polymer–metal–organic frameworks (polyMOFs) as water tolerant materials for selective carbon dioxide separations. *J. Am. Chem. Soc.* **2016,** *138* (3), 920-925.
219. MacLeod, M. J.; Johnson, J. A. Block co-polyMOFs: assembly of polymer–polyMOF hybrids via iterative exponential growth and “click” chemistry. *Polym. Chem.* **2017,** *8* (31), 4488-4493.
220. Bentz, K. C.; Cohen, S. M. Supramolecular metallopolymers: from linear materials to infinite networks. *Angew. Chem. Int. Ed.* **2018,** *57* (46), 14992-15001.
221. Stock, N.; Biswas, S. Synthesis of metal-organic frameworks (MOFs): routes to various MOF topologies, morphologies, and composites. *Chem. Rev.* **2012,** *112* (2), 933-969.
222. Zhao, M.; Huang, Y.; Peng, Y.; Huang, Z.; Ma, Q.; Zhang, H. Two-dimensional metal–organic framework nanosheets: synthesis and applications. *Chem. Soc. Rev.* **2018,** *47* (16), 6267-6295.
223. Wang, S.; McGuirk, C. M.; d'Aquino, A.; Mason, J. A.; Mirkin, C. A. Metal–organic framework nanoparticles. *Adv. Mater.* **2018,** *30* (37), 1800202.
224. Li, J.-R.; Sculley, J.; Zhou, H.-C. Metal–organic frameworks for separations. *Chem. Rev.* **2012,** *112* (2), 869-932.
225. Jiao, L.; Wang, Y.; Jiang, H.-L.; Xu, Q. Metal–organic frameworks as platforms for catalytic applications. *Adv. Mater.* **2018,** *30* (37), 1703663.
226. Wu, M.-X.; Yang, Y.-W. Metal–organic framework (MOF)-based drug/cargo delivery and cancer therapy. *Adv. Mater.* **2017,** *29* (23), 1606134.
227. Lustig, W. P.; Mukherjee, S.; Rudd, N. D.; Desai, A. V.; Li, J.; Ghosh, S. K. Metal–organic frameworks: functional luminescent and photonic materials for sensing applications. *Chem. Soc. Rev.* **2017,** *46* (11), 3242-3285.
228. Sun, L.; Campbell, M. G.; Dincă, M. Electrically conductive porous metal–organic frameworks. *Angew. Chem. Int. Ed.* **2016,** *55* (11), 3566-3579.
229. Horike, S.; Umeyama, D.; Kitagawa, S. Ion conductivity and transport by porous coordination polymers and metal–organic frameworks. *Acc. Chem. Res.* **2013,** *46* (11), 2376-2384.
230. Herm, Z. R.; Wiers, B. M.; Mason, J. A.; van Baten, J. M.; Hudson, M. R.; Zajdel, P.; Brown, C. M.; Masciocchi, N.; Krishna, R.; Long, J. R. separation of hexane isomers in a metal-organic framework with triangular channels. *Science* **2013,** *340* (6135), 960-964.
231. Côté, A. P.; Benin, A. I.; Ockwig, N. W.; O'Keeffe, M.; Matzger, A. J.; Yaghi, O. M. Porous, crystalline, covalent organic frameworks. *Science* **2005,** *310* (5751), 1166-1170.
232. El-Kaderi, H. M.; Hunt, J. R.; Mendoza-Cortés, J. L.; Côté, A. P.; Taylor, R. E.; O'Keeffe, M.; Yaghi, O. M. Designed synthesis of 3D covalent organic frameworks. *Science* **2007,** *316* (5822), 268-272.
233. Uribe-Romo, F. J.; Hunt, J. R.; Furukawa, H.; Klöck, C.; O’Keeffe, M.; Yaghi, O. M. A crystalline imine-linked 3-D porous covalent organic framework. *J. Am. Chem. Soc.* **2009,** *131* (13), 4570-

4571.
234. Kuhn, P.; Antonietti, M.; Thomas, A. Porous, covalent triazine-based frameworks prepared by ionothermal synthesis. *Angew. Chem. Int. Ed.* **2008,** *47* (18), 3450-3453.
235. Jin, E.; Asada, M.; Xu, Q.; Dalapati, S.; Addicoat, M. A.; Brady, M. A.; Xu, H.; Nakamura, T.; Heine, T.; Chen, Q.; Jiang, D. Two-dimensional sp^2 carbon–conjugated covalent organic frameworks. *Science* **2017,** *357* (6352), 673-676.
236. Liu, Y.; O'Keeffe, M.; Treacy, M. M. J.; Yaghi, O. M. The geometry of periodic knots, polycatenanes and weaving from a chemical perspective: a library for reticular chemistry. *Chem. Soc. Rev.* **2018,** *47* (12), 4642-4664.
237. Liu, Y.; Ma, Y.; Zhao, Y.; Sun, X.; Gándara, F.; Furukawa, H.; Liu, Z.; Zhu, H.; Zhu, C.; Suenaga, K.; Oleynikov, P.; Alshammari, A. S.; Zhang, X.; Terasaki, O.; Yaghi, O. M. Weaving of organic threads into a crystalline covalent organic framework. *Science* **2016,** *351* (6271), 365-369.
238. Liu, Y.; Diercks, C. S.; Ma, Y.; Lyu, H.; Zhu, C.; Alshmimri, S. A.; Alshihri, S.; Yaghi, O. M. 3D covalent organic frameworks of interlocking 1D square ribbons. *J. Am. Chem. Soc.* **2019,** *141* (1), 677-683.
239. Uribe-Romo, F. J.; Doonan, C. J.; Furukawa, H.; Oisaki, K.; Yaghi, O. M. Crystalline covalent organic frameworks with hydrazone linkages. *J. Am. Chem. Soc.* **2011,** *133* (30), 11478-11481.
240. Dalapati, S.; Jin, S.; Gao, J.; Xu, Y.; Nagai, A.; Jiang, D. An azine-linked covalent organic framework. *J. Am. Chem. Soc.* **2013,** *135* (46), 17310-17313.
241. Ascherl, L.; Sick, T.; Margraf, J. T.; Lapidus, S. H.; Calik, M.; Hettstedt, C.; Karaghiosoff, K.; Döblinger, M.; Clark, T.; Chapman, K. W.; Auras, F.; Bein, T. Molecular docking sites designed for the generation of highly crystalline covalent organic frameworks. *Nat. Chem.* **2016,** *8* (4), 310-316.
242. Kandambeth, S.; Shinde, D. B.; Panda, M. K.; Lukose, B.; Heine, T.; Banerjee, R. Enhancement of chemical stability and crystallinity in porphyrin-containing covalent organic frameworks by intramolecular hydrogen bonds. *Angew. Chem. Int. Ed.* **2013,** *52* (49), 13052-13056.
243. Xu, H.; Gao, J.; Jiang, D. Stable, crystalline, porous, covalent organic frameworks as a platform for chiral organocatalysts. *Nat. Chem.* **2015,** *7*, 905-912.
244. Halder, A.; Karak, S.; Addicoat, M.; Bera, S.; Chakraborty, A.; Kunjattu, S. H.; Pachfule, P.; Heine, T.; Banerjee, R. Ultrastable imine-based covalent organic frameworks for sulfuric acid recovery: an effect of interlayer hydrogen bonding. *Angew. Chem. Int. Ed.* **2018,** *57* (20), 5797-5802.
245. Kandambeth, S.; Mallick, A.; Lukose, B.; Mane, M. V.; Heine, T.; Banerjee, R. Construction of crystalline 2D covalent organic frameworks with remarkable chemical (acid/base) stability via a combined reversible and irreversible route. *J. Am. Chem. Soc.* **2012,** *134* (48), 19524-19527.
246. Waller, P. J.; Lyle, S. J.; Osborn Popp, T. M.; Diercks, C. S.; Reimer, J. A.; Yaghi, O. M. Chemical conversion of linkages in covalent organic frameworks. *J. Am. Chem. Soc.* **2016,** *138* (48), 15519-15522.
247. Yamagishi, H.; Sato, H.; Hori, A.; Sato, Y.; Matsuda, R.; Kato, K.; Aida, T. Self-assembly of lattices with high structural complexity from a geometrically simple molecule. *Science* **2018,** *361* (6408), 1242-1246.
248. Kissel, P.; Erni, R.; Schweizer, W. B.; Rossell, M. D.; King, B. T.; Bauer, T.; Götzinger, S.; Schlüter, A. D.; Sakamoto, J. A two-dimensional polymer prepared by organic synthesis. *Nat. Chem.* **2012,** *4* (4), 287-291.
249. Kissel, P.; Murray, D. J.; Wulftange, W. J.; Catalano, V. J.; King, B. T. A nanoporous two-dimensional polymer by single-crystal-to-single-crystal photopolymerization. *Nat. Chem.* **2014,** *6* (9), 774-778.
250. Kory, M. J.; Wörle, M.; Weber, T.; Payamyar, P.; van de Poll, S. W.; Dshemuchadse, J.; Trapp, N.; Schlüter, A. D. Gram-scale synthesis of two-dimensional polymer crystals and their structure analysis by X-ray diffraction. *Nat. Chem.* **2014,** *6* (9), 779-784.
251. Beaudoin, D.; Maris, T.; Wuest, J. D. Constructing monocrystalline covalent organic networks by polymerization. *Nat. Chem.* **2013,** *5* (10), 830-834.
252. Karak, S.; Kandambeth, S.; Biswal, B. P.; Sasmal, H. S.; Kumar, S.; Pachfule, P.; Banerjee, R. Constructing ultraporous covalent organic frameworks in seconds via an organic terracotta process. *J. Am. Chem. Soc.* **2017,** *139* (5), 1856-1862.
253. Karak, S.; Kumar, S.; Pachfule, P.; Banerjee, R. Porosity Prediction through hydrogen bonding in covalent organic frameworks. *J. Am. Chem. Soc.* **2018,** *140* (15), 5138-5145.

254. Ma, T.; Kapustin, E. A.; Yin, S. X.; Liang, L.; Zhou, Z.; Niu, J.; Li, L.-H.; Wang, Y.; Su, J.; Li, J.; Wang, X.; Wang, W. D.; Wang, W.; Sun, J.; Yaghi, O. M. Single-crystal x-ray diffraction structures of covalent organic frameworks. *Science* **2018,** *361* (6397), 48-52.
255. Evans, A. M.; Parent, L. R.; Flanders, N. C.; Bisbey, R. P.; Vitaku, E.; Kirschner, M. S.; Schaller, R. D.; Chen, L. X.; Gianneschi, N. C.; Dichtel, W. R. Seeded growth of single-crystal two-dimensional covalent organic frameworks. *Science* **2018,** *361* (6397), 52-57.
256. Luo, J.; Wang, J.-W.; Zhang, J.-H.; Lai, S.; Zhong, D.-C. Hydrogen-bonded organic frameworks: design, structures and potential applications. *CrystEngComm* **2018,** *20* (39), 5884-5898.
257. Simard, M.; Su, D.; Wuest, J. D. Use of hydrogen bonds to control molecular aggregation. Self-assembly of three-dimensional networks with large chambers. *J. Am. Chem. Soc.* **1991,** *113* (12), 4696-4698.
258. Ding, S.-Y.; Wang, W. Covalent organic frameworks (COFs): from design to applications. *Chem. Soc. Rev.* **2013,** *42* (2), 548-568.
259. Huang, N.; Wang, P.; Jiang, D. Covalent organic frameworks: a materials platform for structural and functional designs. *Nat. Rev. Mater.* **2016,** *1* (10), 16068.
260. Diercks, C. S.; Yaghi, O. M. The atom, the molecule, and the covalent organic framework. *Science* **2017,** *355* (6328), eaal1585.
261. Biswal, B. P.; Chandra, S.; Kandambeth, S.; Lukose, B.; Heine, T.; Banerjee, R. Mechanochemical synthesis of chemically stable isoreticular covalent organic frameworks. *J. Am. Chem. Soc.* **2013,** *135* (14), 5328-5331.
262. Colson, J. W.; Woll, A. R.; Mukherjee, A.; Levendorf, M. P.; Spitler, E. L.; Shields, V. B.; Spencer, M. G.; Park, J.; Dichtel, W. R. Oriented 2D covalent organic framework thin films on single-layer graphene. *Science* **2011,** *332* (6026), 228-231.
263. Zhang, M.; Li, L.; Lin, Q.; Tang, M.; Wu, Y.; Ke, C. Hierarchical-coassembly-enabled 3D-printing of homogeneous and heterogeneous covalent organic frameworks. *J. Am. Chem. Soc.* **2019**, *141*, 5154-5158.
264. Dragan, E. S. Design and applications of interpenetrating polymer network hydrogels. A review. *Chem. Eng. J.* **2014,** *243* (1), 572-590.
265. Gong, Y.-N.; Zhong, D.-C.; Lu, T.-B. Interpenetrating metal–organic frameworks. *CrystEngComm* **2016,** *18* (15), 2596-2606.
266. Wu, H.; Yang, J.; Su, Z.-M.; Batten, S. R.; Ma, J.-F. An Exceptional 54-fold interpenetrated coordination polymer with 103-srs network topology. *J. Am. Chem. Soc.* **2011,** *133* (30), 11406-11409.
267. Haque, M. A.; Kurokawa, T.; Gong, J. P. Super tough double network hydrogels and their application as biomaterials. *Polymer* **2012,** *53* (9), 1805-1822.
268. Gong, J. P.; Katsuyama, Y.; Kurokawa, T.; Osada, Y. Double-network hydrogels with extremely high mechanical strength. *Adv. Mater.* **2003,** *15* (14), 1155-1158.
269. Sun, J.-Y.; Zhao, X.; Illeperuma, W. R. K.; Chaudhuri, O.; Oh, K. H.; Mooney, D. J.; Vlassak, J. J.; Suo, Z. Highly stretchable and tough hydrogels. *Nature* **2012,** *489* (7414), 133-136.
270. Sun, T. L.; Kurokawa, T.; Kuroda, S.; Ihsan, A. B.; Akasaki, T.; Sato, K.; Haque, M. A.; Nakajima, T.; Gong, J. P. Physical hydrogels composed of polyampholytes demonstrate high toughness and viscoelasticity. *Nat. Mater.* **2013,** *12* (10), 932-937.
271. Neal, J. A.; Mozhdehi, D.; Guan, Z. Enhancing mechanical performance of a covalent self-healing material by sacrificial noncovalent bonds. *J. Am. Chem. Soc.* **2015,** *137* (14), 4846-4850.
272. Filippidi, E.; Cristiani, T. R.; Eisenbach, C. D.; Waite, J. H.; Israelachvili, J. N.; Ahn, B. K.; Valentine, M. T. Toughening elastomers using mussel-inspired iron-catechol complexes. *Science* **2017,** *358* (6362), 502-505.
273. Ishiwata, T.; Furukawa, Y.; Sugikawa, K.; Kokado, K.; Sada, K. Transformation of metal–organic framework to polymer gel by cross-linking the organic ligands preorganized in metal–organic framework. *J. Am. Chem. Soc.* **2013,** *135* (14), 5427-5432.
274. Siemes, E.; Nevskyi, O.; Sysoiev, D.; Turnhoff, S. K.; Oppermann, A.; Huhn, T.; Richtering, W.; Wöll, D. Nanoscopic visualization of cross-linking density in polymer networks with diarylethene photoswitches. *Angew. Chem. Int. Ed.* **2018,** *57* (38), 12280-12284.
275. Li, Q.; Fuks, G.; Moulin, E.; Maaloum, M.; Rawiso, M.; Kulic, I.; Foy, J. T.; Giuseppone, N. Macroscopic contraction of a gel induced by the integrated motion of light-driven molecular motors. *Nat. Nanotechnol.* **2015,** *10* (2), 161-165.

276. Foy, J. T.; Li, Q.; Goujon, A.; Colard-Itté, J.-R.; Fuks, G.; Moulin, E.; Schiffmann, O.; Dattler, D.; Funeriu, D. P.; Giuseppone, N. Dual-light control of nanomachines that integrate motor and modulator subunits. *Nat. Nanotechnol.* **2017,** *12* (6), 540-545.

Chapter 2. Tuning dynamics of polyMOC gels through mixed-metal systems

2.1 Introduction

2.1.1 Dynamic mechanical properties of polymer networks

As discussed in Section 1.4.3, polymer networks are viscoelastic materials that display both viscous and elastic characteristics when deformed. These properties are quantitatively described by the loss and storage moduli: the loss modulus (*G″*) measures the viscous response, or the energy dissipation by heat upon the application of stress; meanwhile, the storage modulus (*G′*) measures stored energy and the material's elastic response. Both are obvious considerations in improving and tailoring the mechanical properties of polymer networks towards different applications.

The storage (or elastic) modulus of any polymer network relies upon a few key features that can be manipulated through network design. Storage modulus increases with increasing crosslink density, which can be tuned by changing the molecular weight or chain length of polymers between crosslinks.[1] Naturally arising network defects can enhance or reduce the modulus: polymer entanglements behave as physical crosslinks and increase *G′*, while loops and chain ends lower the number of effective crosslinks in the material, lowering *G′* (Section 1.3.1). Gels, essentially solvated polymer networks, experience an equilibrium level of swelling that reduces the modulus as well (Section 1.4.2).

The ability to resist deformation is a vital mechanical property of polymer networks; however, the ability to dissipate energy and dampen applied forces is equally important in both designing ductile materials and preventing premature material failure. While damping mechanisms in covalently crosslinked polymer networks are limited to polymer chain reptation and segmental motion, physical networks and covalent adaptable networks provide an additional mode of energy dissipation through their crosslinks, which can break and reform.[2,3] A great example of leveraging physical networks to improve material properties is the double network of covalently crosslinked polyacrylamide mixed with ionically crosslinked alginate developed by Suo and coworkers.[4] The high toughness and fracture energy of this hybrid gel results from the "unzipping" of ionic crosslinks in the alginate gel, which are then able to reform and heal internal damage. Introducing unique topological features into networks is another method of incorporating new stress relaxation mechanisms into a network: for example, the slide-ring gels discussed in Section 1.3.3.2 demonstrate high toughness due to the relative sliding movement of polymer chains and crosslinks.[5,6]

Polymer networks formed from these dynamic and transient crosslinks, such as hydrogen bonding, ionic interactions, metal–ligand coordination, and π-π stacking interactions, are categorized as supramolecular networks.[7] The viscoelastic response of these networks is largely influenced by the dynamics of network crosslinks.[8] As a result, these materials respond differently to deformation on various timescales and strain

rates, behavior best quantified by the characteristic relaxation time (τ). When a constant strain is applied, a material displays a stress response that decays exponentially relative to its characteristic relaxation time. This stress response is typically measured as the stress relaxation modulus (G), which is equal to the stress over applied strain. As Eq. 1 indicates, G demonstrates an exponential decay over time (t) that is dictated by τ, where G_0 represents the plateau elastic modulus.

$$G(t) = G_0 \exp\left(\frac{-t}{\tau}\right) \quad (1)$$

More intuitively defined, the characteristic relaxation time marks a boundary in viscoelastic behavior, where materials respond like solids at time scales shorter than τ and flow like liquids on time scales longer than τ.

2.1.2 Tuning stress relaxation in polymer networks

Dynamic mechanical properties are important elements to consider in designing viscoelastic materials, particularly in biomimetic materials.[9,10] However, these properties are difficult to adjust independently: the stress relaxation character of polymer networks is inherently coupled to structural design, which dictates elastic behavior. For physical gels in particular, dynamic behavior depends largely on the position and density of crosslinks as well as the thermodynamics and kinetics of the crosslink.[11] Adjusting the density of non-covalent bonds naturally changes the elastic modulus; changing the binding kinetics frequently requires switching between crosslinks, which often introduces a change in branch functionality f, which also alters the elastic character of the material. As a result, tuning the characteristic relaxation time of a material while maintaining static mechanical properties remains challenging.

Changing network topology and design is a common strategy in materials research where dynamic behavior is an important independent variable.[12–15] Mooney and coworkers tuned the stress relaxation behavior of alginate hydrogels while maintaining their elastic moduli through a combination of changing polymer molecular weight, covalently attaching PEG “spacers” to reduce crosslinking, and adjusting calcium–alginate ionic crosslinking density.[13] By controlling dynamic behavior in these biomimetic materials, the authors were able to observe the positive effects of faster relaxation on the spreading, proliferation, and differentiation of mammalian stem cells.[13,16]

Other literature examples have tuned relaxation time by mixing similar network junctions with unique dynamic behaviors while maintaining nanoscale architectures. Anseth and coworkers were able to use environmental changes to tune the viscoelastic properties of covalent adaptable hydrogels based on thioester exchange: the exchange reaction between thioester crosslinks with pendant network thiols was hastened using higher solution pH or the addition of exchange catalyst.[17] Elevated pH levels resulted in faster exchange through decreased network connectivity, while catalyzed exchange was able to accelerate stress relaxation of these hydrogels without affecting the storage modulus. Dooling and Tirrell altered binding interactions between coiled-coil domains of a protein

network by introducing single-site mutations, which translated into macroscopic changes in dynamic behavior.[18] The orthogonal crosslinking of two mutants resulted in a material with two distinct relaxation times and processes, while mixed-mutant crosslinking produced a material with a broad distribution of relaxation times. Similarly, Holten-Andersen and coworkers controlled macroscale relaxation behavior of a PEG-based hydrogel by incorporating multiple metal–histidine crosslinks with distinct kinetics within the same network.[3] Double metal coordinated networks with both fast and slow stress dissipation modes were obtained by combining Ni(II) (slow exchange kinetics) with Cu(II) or Zn(II) metals (fast exchange kinetics). Changing the ratio of Ni(II) to Zn(II)/Cu(II) modulated the relative contributions of slow and fast dissipation modes in a nonlinear fashion that differed between Zn(II) and Cu(II). In both these examples of coiled-coil protein[2] and metal–histidine[3] networks, the polymer network was preserved while crosslinkers were altered to tune stress relaxation behavior; however, relaxation dynamics were controlled at the cost of the elastic modulus, which remained dependent on the network crosslinker identity.

2.1.3 Tuning stress relaxation in polyMOC gels

In this work, we decouple stress relaxation behavior from elastic modulus by incorporating mixed metals into a novel polymer metal–organic cage (polyMOC) gel. Briefly described in 1.3.3.1, polyMOC gels are solvated polymer networks crosslinked through the self-assembly of intricate metal–organic cages/polyhedra, discrete assemblies formed from multiple metal atoms (M) and organic ligands (L) (Fig. 1A). PolyMOC network branch functionality is dictated by the ligand bite angle, which determines the MOC polyhedral architecture.[19] The Johnson Group reported examples of polyMOC gels with high *f* through the use of $Pd_{12}L_{24}$ cuboctahedron junctions, which are assembled from Pd(II) and *para*-bispyridyl ligands attached to linear poly(ethylene glycol) (PEG) chain ends (Fig. 1B).[20] The augmented stoichiometry provided by MOCs is the largest structural differentiator between these materials and classical metallogels, which rely on single metal atom-based network junctions.[21]

Similar to other physical gels, the viscoelastic properties of polyMOC networks depend upon the dynamic behaviors of their supramolecular crosslinks. For the bispyridine ligand-based family of M_nL_{2n} cage assemblies, the kinetics of ligand exchange are well studied.[22–26] Large cage assemblies such as $Pd_{12}L_{24}$ have covalent-like stabilities at room temperature once formed, relying upon the cooperative effect of many labile Pd(II)–pyridine bonds.[22] Smaller cages with lower cooperativity are more dynamic; accordingly, strain and swelling studies of $Pd_{12}L_{24}$- and Pd_2L_4-based polyMOC networks indicated that lower stoichiometry polyMOC gels are also more dynamic.[20] The half-life of ligand exchange for large $M_{12}L_{24}$ cages takes 20 days but hastens at higher temperatures.[22,27] As expected, stress relaxation experiments demonstrated faster relaxation time with increasing temperature on star polyMOC gels formed from tetra-arm polymers and $Pd_{12}L_{24}$ crosslinks, which behave as elastic solids at room temperature.[28] The characteristic relaxation time of this particular polyMOC system can be tuned by the partial substitution of polymer ligand with free ligand, or ligand unattached to a polymer chain. A 5:1 ratio of free ligand to polymer ligand incorporation produced the longest characteristic relaxation time as well as the highest elastic modulus.

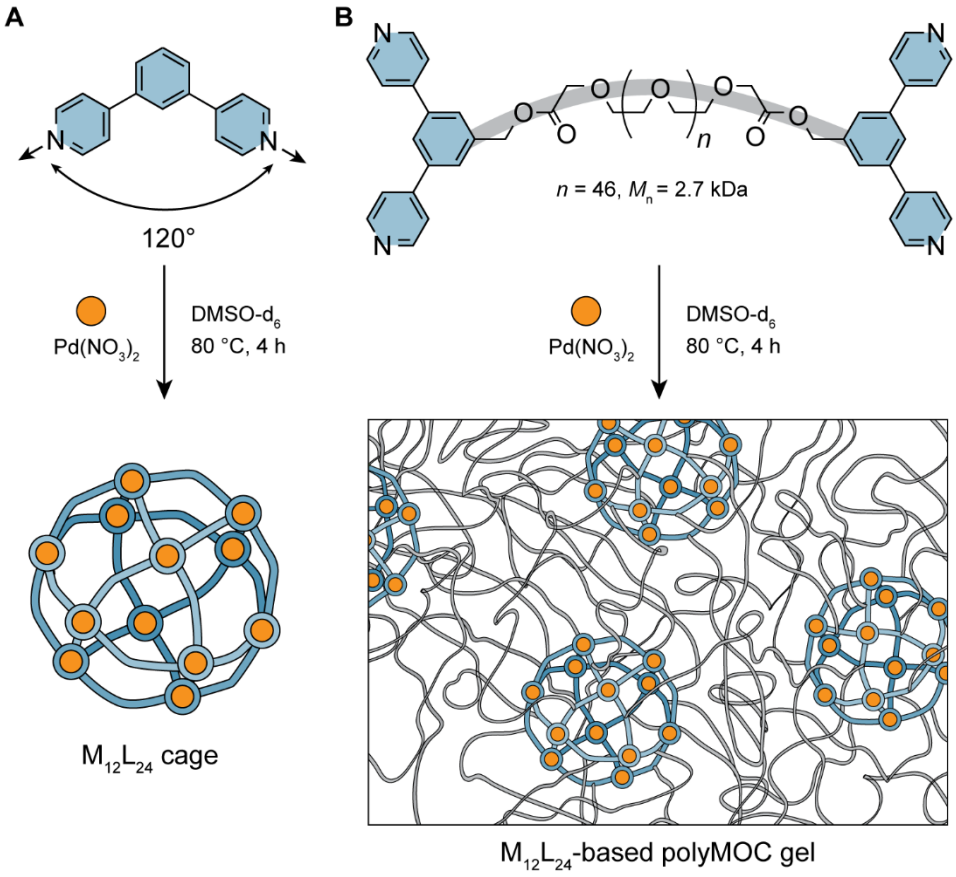

Figure 1. (A) MOCs such as $M_{12}L_{24}$ are self-assembled from multiple metal atoms (M) and multiple organic ligands (L). Here, M = Pd(II) and L = 1,3-di(pyridine-4-yl)benzene. (B) An $M_{12}L_{24}$-based polyMOC gel is formed from the self-assembly of Pd(II) with 1,3-di(pyridine-4-yl)benzene, attached to the chain ends of linear PEG.

To tune the stress relaxation behavior in polyMOC gels without altering their elastic character, we capitalized on previously demonstrated substitutions of Pd(II) with Pt(II) that successfully formed identical MOC architectures with very different metal–ligand dynamics.[24,26,29,30] Similar to Pd(II), Pt(II) also binds in a square planar coordination geometry; because both metals produce near-identical cage assemblies, the polyMOC branch functionality and elastic modulus should remain consistent. However, Pt(II) coordination bonds are stronger and significantly less labile than those of Pd(II), a result of the relativistic expansion of platinum's 5d atomic orbitals.[31–34] This difference results in much slower substitution reactions of coordination complexes and slower ligand exchange in supramolecular assemblies of Pt(II) compared to Pd(II). Pt(II) cage assemblies typically require higher temperatures or longer annealing times to form than their Pd(II) equivalents;[27] frequently, labilizing agents are needed to "unlock" the inert Pt(II)–pyridine bond to form stable cage assemblies from kinetically-trapped intermediates.[29,35,36] Pd(II)-based assemblies demonstrate faster ligand exchange and decompose at much lower temperatures compared to those formed from Pt(II).[8,25,26] Due to the cooperative effect of multiple metal–ligand interactions, Pt_nL_{2n} assemblies are considerably more robust and static than Pd_nL_{2n} counterparts. Embedded within a

network, Pd(II)-based and Pt(II)-based cage analogues should produce very similar elastic properties with extremely different dynamic behaviors.

In this work, a novel bispyridine-based M_6L_{12} coordination cube inspired by related work from Fujita and coworkers[37] is prepared and used to generate a polyMOC gel with intermediate branch functionality compared to previous polyMOC networks. The ligand is able to successfully self-assemble with not only Pd(II) and Pt(II), but also combinations of both metals to form mixed-metal cages. Through adjusting the ratio of palladium and platinum metal salts incorporated into network assembly, we can tune the energy dissipation properties of these materials due to differences in lability of metal–pyridine coordination bonds. Using this strategy, the characteristic relaxation times and loss moduli of these M_6L_{12}-based gels can be tuned over nearly three orders of magnitude while maintaining the general network topology as well as the elastic behavior of the material.

2.2 Results and discussion

2.2.1 Novel bispyridine ligand maintains M_6L_{12} self-assembly behavior

$M_{12}L_{24}$- and M_2L_4-based polyMOC gels have been developed and studied extensively.[20,28,38,39] The slow ligand exchange kinetics of $M_{12}L_{24}$ cuboctahedral cages[22,29] would make it difficult to measure the dynamic behavior of $Pt_{12}L_{24}$-based polyMOCs on a reasonable timescale; at the other extreme, M_2L_4-based polyMOC gels are very dynamic but assemble with an estimated f of 2.13, barely above the limit of gelation.[20] As a result, we chose to design a novel polyMOC gel with intermediate branch functionality. A bispyridine-based Pd_6L_{12} coordination cube[37] was an ideal candidate to adapt as a novel polyMOC network junction with $f = 6$, which might avoid the anticipated obstacles in tuning dynamics of higher and lower f polyMOC gels.

To serve as a network crosslink, a carbazole analogue of the Pd_6L_{12}-forming dibenzofuran bispyridyl ligand reported by Fujita and coworkers[37] was designed to allow for polymer end functionalization (Fig. 2A). Because the self-assembled MOC architecture depends greatly on the ligand bite angle between coordinating groups, we sought confirmation that exchange of an O atom for an N atom would maintain the geometry of the original dibenzofuran ligand. Through DFT molecular geometry optimizations, it was shown that the carbazole ligand maintains the critical 90° bite angle required to form M_6L_{12} coordination cubes (calculated with the aid of Zachary P. Nelson and Prof. Timothy M. Swager at MIT). Ligand [2] was synthesized through the methylation of diiodocarbazole, followed by a Sonogashira coupling reaction (Scheme S1); alkylation of the carbazole nitrogen was performed to avoid any possible reactivity or intermolecular hydrogen bonding, which was demonstrated in previous work using the nonmethylated carbazole bispyridine ligand.[40]

To form Pd_6L_{12} assemblies, [2] was combined with $Pd(MeCN)_4(OTf)_2$ at a 2:1.1 ratio in DMSO-d_6 and heated at 50 °C for 10 h. Following heating, ^{1}H NMR characterization of the mixture demonstrated characteristic downfield shifts of the pyridyl protons expected

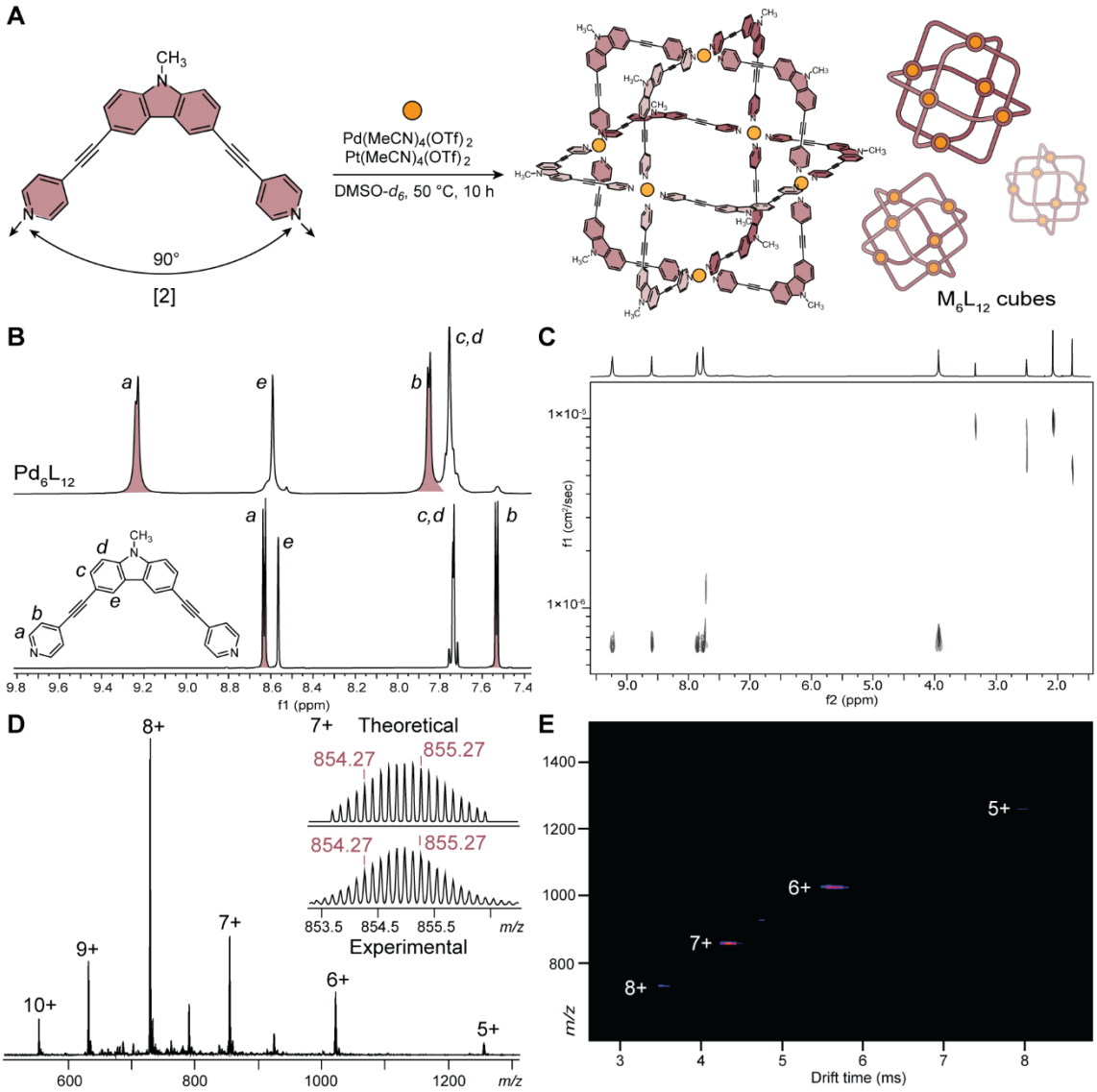

Figure 2. Modified carbazole-based ligand demonstrates successful M_6L_{12} assembly. (A) Schematic of self-assembly of modified carbazole-based ligand [2] with Pd(II) or Pt(II) metal salts to form M_6L_{12} coordination cubes. (B) ^{1}H NMR spectra of [2] (bottom) and assembled cube (top). Highlighted are the downfield shifts of pyridyl protons, characteristic of successful self-assembly. (C) ^{1}H DOSY NMR (DMSO-d_6, 500 MHz, 25 °C) spectrum of Pd_6L_{12} indicates slower diffusion of a large, single product with a hydrodynamic radius of 1.5 nm. (D) ESI-MS and (E) TWIM-MS plots (*m/z* vs. drift time) of Pd_6L_{12} assembly.

for uniform and symmetric cage assemblies (Fig. 2B), very similar to that of the referenced MOC.[37] Further support for successful Pd_6L_{12} cube assembly using the carbazole ligand was provided by diffusion ordered spectroscopy (DOSY) ^{1}H NMR, which indicated structural convergence into a single, slowly diffusing product (Fig. 2C, S18). The diffusion coefficient of the Pd_6L_{12} cage was calculated to be $D = 6.78 \times 10^{-7}$ cm^2/s; analysis using the Stokes–Einstein equation, which assumes a spherical particle in solution, estimates a particle radius of 1.5 nm (see Experimental for calculations). This size corresponds well to crystallographic data of Fujita's dibenzofuran-based coordination cube, which has edge dimensions of 3 nm and a main diagonal measuring

4 nm.[37] Finally, Pd_6L_{12} assembly and composition were confirmed through electrospray ionization-mass spectrometry (ESI-MS) and traveling-wave ion mobility-mass spectrometry (TWIM-MS), which relies on gas phase ion separation using a traveling voltage wave produced by a stacked-ring ion guide[41,42] (experiments conducted by Dr. Heng Wang and Prof. Xiaopeng Li at the University of South Florida). Using these methods, a series of $[M - n(OTf^-)]^{n+}$ peaks (n = 5–8) with isotopic distribution patterns consistent with theoretical simulations were observed (Fig. 2D–E, S20).

Pt_6L_{12} cubes were synthesized using $Pt(MeCN)_4(OTf)_2$ following the same assembly procedure. ^{1}H NMR characterization of the [2]/Pt mixture supported successful platinum MOC assembly through downfield shifts of broadened pyridyl proton peaks (Fig. S16); the broadness of ^{1}H NMR peaks for large cage assemblies has been attributed to slow local motions of assembled ligands, caused by stronger binding of Pt(II).[25,29] Through ^{1}H DOSY (Fig. S19), Pt_6L_{12} cages demonstrated a slower diffusion coefficient of D = 3.92 x 10^{-7} cm^2/s, resulting in an estimated Stokes–Einstein radius of 2.5 nm. Although this value is also within the expected range for these assemblies, it is unclear why a Pt(II) assembly would diffuse slower than its Pd(II) counterpart, as the cage assemblies should be relatively similar in size: crystal structures of analogous Pd(II)– and Pt(II)–bispyridine complexes demonstrate exceptionally small deviations in Pd(II)–N and Pt(II)–N bond length.[24] Previous studies, however, have observed dissimilar diffusion rates of Pd(II) and Pt(II) cage analogues.[25,29,43] Fortunately, the successful formation of Pt_6L_{12} cages was verified unambiguously through ESI-MS (Fig. S21–23).

Mixed-metal cages were formed by combining [2] with the same palladium and platinum metal salts at Pd(II)/Pt(II) ratios of 100:0, 75:25, 50:50, 25:75, and 0:100. Cage assembly was once again characterized with ^{1}H NMR (Fig. S17) and confirmed using ESI-MS (Fig. S21–23), which evidenced a range of mixed-metal M_6L_{12} cage assemblies rather than the self-segregation and assembly of single-metal cages only.

2.2.2 Polymer ligand demonstrates successful cage formation in gels

A carboxylic acid group was installed onto the carbazole bispyridine ligand, which was end-functionalized onto bis-amine-terminated linear poly(ethylene glycol) (PEG) through amide coupling (Fig. 3A, Scheme S2). The resulting polymer ligand (pL) was mixed with Pd(II) and Pt(II) metal salts at ratios of 100:0, 75:25, 50:50, 25:75, and 0:100 in DMSO-d_6 at 5–6 wt% and annealed for two days at 50 °C under air- and moisture-free conditions to obtain free-standing gels. Successful cage formation within these gels was supported by magic angle spinning (MAS) solid-state ^{1}H NMR characterization, yielding broad pyridyl peaks similar to those of the solution-state assembly (Fig. 2B, S24).

PolyMOC gel structure was probed with small- and wide-angle X-ray scattering (SAXS/WAXS) experiments, where the presence of scattering peaks indicates microphase separation in polymer gels. The scattering peak maximum occurs at a scattering vector q, which can be related to short-range order within the sample through the equation

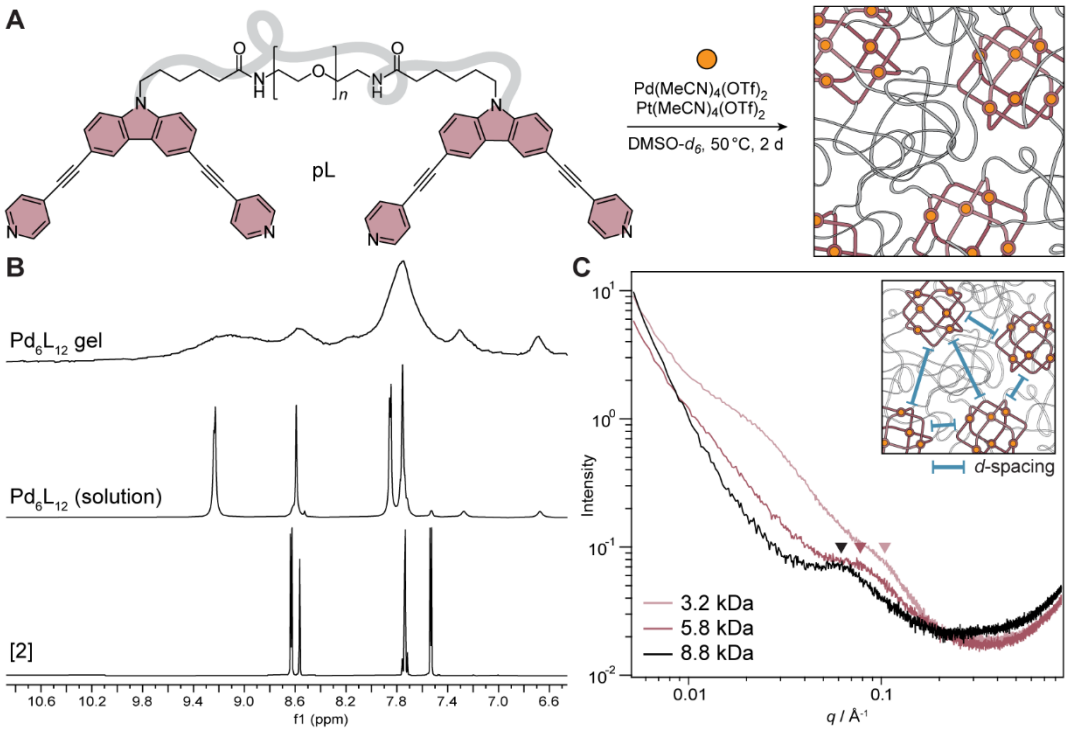

Figure 3. Successful self-assembly of M_6L_{12}-based polyMOC gels. (A) Schematic of polymer ligand (pL) self-assembly with Pd(II) and Pt(II) metal salts to form an M_6L_{12}-based network. (B) MAS ^{1}H solid-state NMR (500 MHz, 25 °C, 5 kHz spin rate) characterization of cube-based gel formed with pL (5.2 kDa) and Pd(II). Compared with solution Pd_6L_{12} cage (500 MHz, DMSO-d_6, 25 °C) and [2] (600 MHz, DMSO-d_6, 25 °C). (C) SAXS characterization of M_6L_{12}-based polyMOC gels formed from Pd(II) with pL of increasing molecular weight (3.2, 5.8, 8.8 kDa).

$$d = \frac{2\pi}{q} \tag{2}$$

where d is the repeat distance of concentration fluctuations causing microphase separation within the sample.[44] Scattering of Pd_6L_{12}-based polyMOC gels demonstrated anticipated broad peaks with peak maximums at scattering vector q = 0.6–0.9 Å^{-1} (Fig. 2C), a feature attributed in previous studies to the d-spacing between cage junctions in polyMOC gels.[45] This peak shifted to correspondingly smaller q values with increasing pL molecular weight (Table 1). Experimental d-spacings were calculated from q values using Eq. 2.

As the distance between network junctions, this d-spacing should equal the sum of the polymer end-to-end distance and the cage diameter; comparing experimental end-to-end distances (R_{exp}) with theoretical minimums and maximums might tell us more about the network topology or environment. Theoretical root-mean square polymer end-to-end distances (R_0) can be calculated by treating the pL as a PEG chain and using the equation:[1,46]

$$R_0 = b(N^{\alpha}) \tag{3}$$

Table 1. Tabulated *q* values, *d*-spacing, and R_{exp} from SAXS/WAXS characterization with theoretical d_{FCC}, $R_{0,min}$ and $R_{0,max}$ of Pd_6L_{12}-based polyMOC gels with different molecular weights.

M_n (kDa)	*q* (Å^{-1})	*d* (Å)	d_{FCC} (Å)	R_{exp} (Å)	$R_{0,min}$ (Å)	$R_{0,max}$ (Å)
3.2	0.098	64	89	34	47	59
5.8	0.078	80	109	50	60	84
8.8	0.061	103	125	73	74	106

In Eq. 3, *b* and *N* are the Kuhn length and the number of Kuhn segments, respectively, and dictated by the number average molecular weight M_n as well as the polymer composition. The scaling exponent α is 0.58 for a polymer in a good solvent,[47] which produces a maximum end-to-end distance $R_{0,max}$. The value of α = 0.50 expected for real chains in a polymer melt[1] is used to calculate $R_{0,min}$.

Calculated R_{exp} generally fell below or close to $R_{0,min}$ (Table 1), a trend seen in previous polyMOC studies. Furthermore, R_{exp} were smaller than theoretical *d*-spacings calculated for cages distributed homogeneously on an FCC lattice (d_{FCC}, Table 1; see Experimental for calculations). Together, these data are indicative of MOC clustering and phase separation, which has previously been reported.[38]

2.2.3 M_6L_{12}-based polyMOC gels maintain shear storage moduli with tunable dynamic behavior across Pd(II)/Pt(II) ratios

To evaluate the mechanical properties of these materials, shear rheology was performed on M_6L_{12}-based polyMOC gels formed with 5.2 kDa pL and Pd(II)/Pt(II) ratios of 100:0, 75:25, 50:50 25:75, and 0:100. The shear storage (*G′*) and loss (*G″*) moduli of M_6L_{12}-based polyMOC gels were measured at 5 rad/s through oscillatory rheometry frequency sweeps. From averaged values of *G′*, the experimental branch functionality *f* was calculated using the phantom network theory of rubber elasticity (see Experimental for calculations).

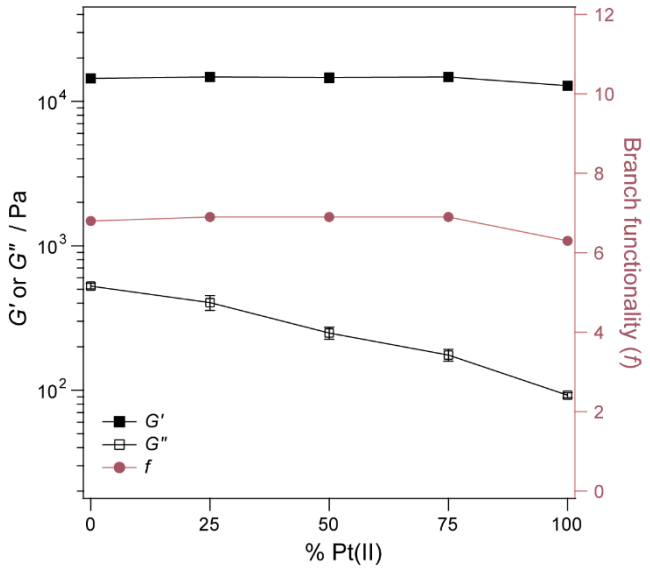

Figure 4. Average elastic (*G′*) and storage (*G″*) moduli and calculated branch functionality *f* of M_6L_{12}-based polyMOC gels at increasing Pt(II)/Pt(II) ratios.

The elastic moduli of all M_6L_{12}-based gels remained close to 14.5 kPa with *f* = 6.9 across most Pd(II)/Pt(II) ratios (Fig. 4; Tables 2, S1). Pt_6L_{12}-based gels were a notable exception, with a lower average *G′* value of 12.9 kPa and *f* = 6.3. This result suggested that, through weaker bonding with pyridyl groups and faster ligand exchange, incorporated Pd(II) might be acting as a labilizing agent towards the more inert Pt(II)–pyridyl coordination bond, allowing the successful formation of stable M_6L_{12} cages from kinetically trapped structures. Pt(II)–pyridyl assemblies

Table 2. Averaged storage moduli (*G′*), averaged loss moduli (*G″*), and calculated branch functionality (*f*) of M_6L_{12}-based gels (5.2 kDa pL)

Pd(II)/Pt(II)	*G′* (Pa)*	*G″* (Pa)*	*f*
100:0	14443.8 ± 267.7	525.0 ± 23.1	6.8
75:25	14772.8 ± 457.2	404.2 ± 47.1	6.9
50:50	14631.7 ± 1104.7	248.5 ± 23.5	6.9
25:75	14773.2 ± 258.8	174.8 ± 16.6	6.9
0:100	12851.8 ± 392.8	92.4 ± 3.8	6.3

* Measured at 5 rad/s

have previously been shown to "unlock" through salt-mediated,[35] photochemical,[36] and solvent[29] labilization. Without the presence of Pd(II), a mixture of local-minimum assemblies with lower coordination stoichiometries may form in the 100% Pt(II) polymer network rather than the desired Pt_6L_{12} network junction; a lower *f* could certainly explain the reduced elastic modulus.

To test this hypothesis, both Pt_6L_{12}- and Pd_6L_{12}-based gels were assembled in a solution of DMSO-d_6 with 10% 2,2,2-trifluoroethanol-d_3 (TFE-d_3), a strong H-bond-donor solvent used previously by Fujita and coworkers as a labilizing agent in forming uniform $Pt_{12}L_{24}$ cages.[29] Although the labilizing agent had little effect on the average *G′* of Pd_6L_{12}-based gels, the addition of TFE increased the average *G′* of 100% Pt networks from 12.9 to 15.7 kDa and the experimental branch functionality from 6.3 to 7.1 (Table S2). Discrepancies between the mechanical properties of TFE-labilized Pt_6L_{12}-based networks and those of the original M_6L_{12}-based gels, however, might be due to differences in polymer–solvent interactions as well as the lower boiling point of TFE, which could affect solvent loss during the gel annealing process.

The loss moduli of M_6L_{12}-based polyMOC gels decreased with increasing Pt(II) content, displaying an order of magnitude reduction from 525.0 ± 23.1 Pa with 100% Pd(II) to

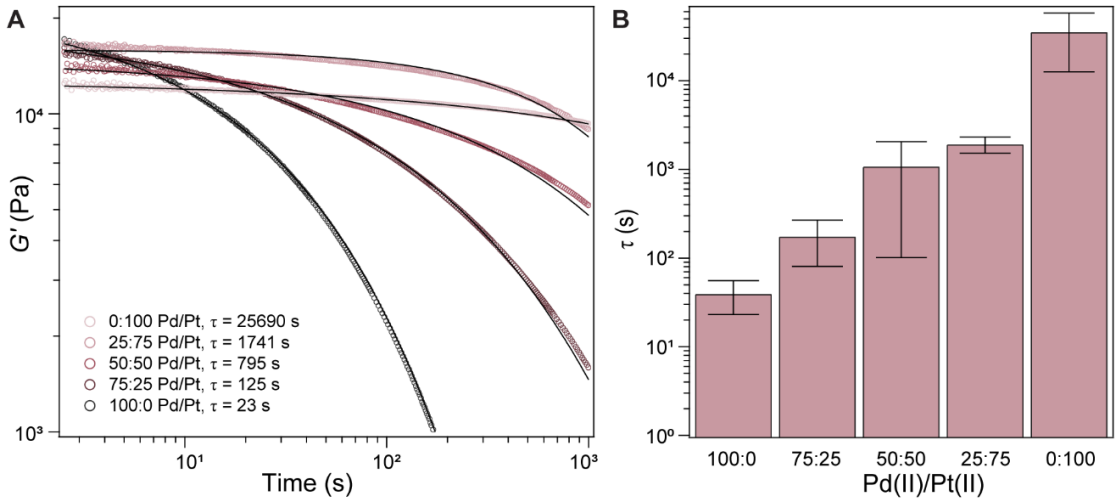

Figure 5. (A) Stress relaxation studies of M_6L_{12}-based polyMOC gels (5.2 kDa pL) formed with ratios of Pd(II)/Pt(II), with fitted lines and characteristic relaxation times (τ). (B) Average τ fitted from stress relaxation studies.

92.4 ± 3.8 Pa with 100% Pt(II) (Table 2). Because *G″* describes the ability of a material to dissipate energy over time, these data indicate that M_6L_{12}-based gels become less dynamic with increased incorporation of Pt(II), a result that corresponds with their M–N bond strengths and kinetics. These data were corroborated by stress relaxation studies performed on M_6L_{12}-based gels (Fig. 5A, Table S3), which were fit to the Kohlrausch stretched exponential function (Eq. 4) to obtain characteristic relaxation times. This equation includes an experimental fitting parameter (α) dictated by physical constraints of the material.[48,49]

$$G(t) = G_0 exp\left[-\left(\frac{t}{\tau}\right)^{\alpha}\right], \qquad 0 < \alpha < 1 \tag{4}$$

From these fits, M_6L_{12}-based gels demonstrated increasing characteristic relaxation times with increasing Pt(II) content (Fig. 5B), with three orders of magnitude difference in τ between Pd_6L_{12}-based gels (39 ± 16 s) and Pt_6L_{12}-based gels (35385 ± 16395 s).

2.3 Conclusions

Polymer networks are at the forefront of functional materials due to their dynamic behaviors: their ability to self-heal,[7] dissipate strain and deformation,[4,5] and change with environmental stimuli.[50,51] As a result, dynamic mechanical properties are an important metric in material performance. These properties are inherently coupled to network design, topology, and static mechanical properties.

In this work, an M_6L_{12} coordination cube is developed and used as a novel polymer network crosslink. Controlling characteristic relaxation time independently of elastic modulus is achieved by forming the polyMOC network with Pd(II) and Pt(II): two metals with distinct ligand coordination strengths that are able to self-assemble into homologous cubic cages. As our results demonstrate, differences in Pd(II) and Pt(II) MOC dynamics translate into very distinct polyMOC network relaxation behaviors. The ability to assemble mixed-metal cages allows tuning of relaxation behaviors by changing the incorporated metal ratio without changing network topology, which is critical in maintaining static behaviors.

These results highlight the unique advantages of the polyMOC gel platform, which relies on the cooperativity of multiple dynamic metal–ligand interactions. Previous work has demonstrated that high stoichiometry cages formed from weak metal–ligand coordination can still provide high *f* network junctions and produce robust, viscoelastic solids,[20,38] with increasingly dynamic behavior at higher temperatures.[28] Here, we show that the high stoichiometry of MOCs can serve not only to augment network elasticity but also to amplify differences in metal–ligand coordination. Embedded as network junctions, these cages maintain their well-defined architectures and provide a constant *f*, even when assembled with different metal ratios. This results in steady elastic moduli, despite a wide range of possible relaxation behaviors. This work illustrates the potential of polyMOC systems in the field of materials and gels with intentionally designed dynamic mechanical properties.

2.4 Experimental

Materials. All deuterated solvents were purchased from Cambridge Isotope Laboratories. Anhydrous 1,4-dioxane and *N,N*-dimethylformamide (DMF) were purchased from Millipore Sigma and bubbled with N_2 before use. XPhos was generously donated by Prof. Stephen Buchwald. Homo-end-functionalized bis-amine poly(ethylene glycol) (PEG) was purchased from Jenkem (M_n = 7.5 kDa) and SINOPEG (Mn = 5, 2 kDa). 4-ethylene pyridine chloride salt was purchased from Ark Pharm, Inc. Tri-tert-butylphosphonium tetrafluoroborate, $Pd(NCC_6H_5)Cl_2$, Cu(I)I, and $Pt(CH_3COCHCOCH_3)_2$ were purchased from Strem Chemicals. $Pd(MeCN)_4(OTF)_2$ was purchased from Tokyo Chemical Industry (TCI) Chemicals. All other reagents and solvents were purchased from VWR International or Fisher Scientific.

Molecular geometry optimization methods. Equilibrium geometry optimization was performed using the program SPARTAN'18 1.4.0 from Wavefunction, Inc. Density functional (DFT) method ωB97x-D was used with the 6-31G* basis set. Calculations were performed with the aid of Zachary P. Nelson and Prof. Timothy M. Swager.

Column chromatography. Flash silica column chromatography was performed using Biotage Isolera One with Accelerated Chromatographic Isolation™ flash chromatography system using KP-Sil SNAP cartridges at recommended flow rates.

Solution nuclear magnetic resonance (NMR) spectroscopy. ^{1}H and ^{13}C spectra were collected at rt (25 °C) and recorded on either a two-channel Bruker Avance-III HD Nanobay 400 MHz spectrometer, three-channel Bruker Avance Neo 500 MHz spectrometer, or four-channel Bruker Avance Neo 600 MHz spectrometer. Data were analyzed with MestReNova Version: 14.1.0-24037. Chemical shifts are expressed in parts per million (ppm), and splitting patterns are designated as s (singlet), d (doublet), t (triplet), q (quartet), m (multiplet), and b (broad). Scalar coupling constants *J* are reported in Hertz (Hz). ^{1}H and ^{13}C NMR spectra were referenced to solvent peaks as reported in literature.[52]

Magic angle spinning (MAS) solid-state NMR. ^{1}H MAS NMR spectra were recorded on a three-channel Bruker Avance Neo spectrometer using an HX probe. Annealed gel samples were loaded into a 3.2 mm zirconia rotor, which was sealed with a Vespel cap. The spectra were collected using a spinning frequency of 5 kHz at 25 °C. ^{1}H spectra were referenced to residual DMSO-d_5.

Gel permeation chromatography/multi-angle light scattering (GPC-MALS). Gel permeation chromatography (GPC) measurements were performed in DMF with 0.02 M lithium bromide (LiBr) using an Agilent 1260 Infinity system with guard column (Agilent ResiPore; 7.5 x 50 mm), and two analytical columns (Agilent ResiPore; 300 x 7.5 mm). Signals were collected using a Wyatt miniDAWN TREOS multi-angle light scattering detector and Wyatt Optilab T-rEX refractometer. All runs were performed at 1.0 mL/min flow rate at 25 °C. Samples were prepared at 3.0 mg/mL in 0.025 M LiBr with injection volume of 20.0 µL.

Preparatory gel permeation chromatography (prepGPC). PrepGPC was used to purify polymer ligand (pL) using a Japan Analytical Industry (JAI) Co. LaboACE Recycling Preparative HPLC (LC-5060) with either JAIGEL-2.5HR (20 mm D x 600 mm L) or JAIGEL-2.5H-40 (40 mm D x 600 mm L). Ethanol-stabilized chloroform was used as eluent. Samples were dissolved in eluent and filtered through 0.2 μm PTFE syringe filters before injection. Bisfunctionalized PEG product was collected on the first cycle.

Liquid chromatography-mass spectrometry (LC-MS). Reaction completion was analyzed using LC-MS, completed on a nominal mass Agilent 612B mass spectrometer attached to an Agilent 1260 Infinity LC. An Agilent InfinityLab Poroshell 120, EC-C18 column (2.1 x 100 mm, 2.7 μm) with a binary solvent system of 1% formic acid (FA) H_2O (A) and 1% FA MeCN (B) at a flow rate of 0.4 mL/min. Data were processed with Agilent OpenLab ChemStation (C.01.09). 50 μL vial inserts with precision point and plastic springs (6 x 30 mm) were used for small sample volumes.

For general analysis, the binary solvent mixture was kept at 90:10 A/B ratio for 1 min, then gradually ramped over 4 min to 0:100 A/B, where it was held for 1 min. The solvent ratio was returned to 90:10 A/B over the course of 4 min. All samples were scanned from 100–1500 m/z range using a fragmentor voltage of 70 V.

Direct analysis in real time/high resolution mass spectrometry (DART-HRMS). DART-HRMS data were collected on a high-resolution JEOL AccuTOF 4G LC-plus equipped with an ionSense DART source, operated with helium in positive mode at a gas temperature of 350 °C. Data were analyzed with msAxel Data Processing LP Version 1.0 (1.0.5.2).

Electrospray ionization-mass spectrometry (ESI-MS) and traveling-wave ion mobility-mass spectrometry (TWIM-MS). ESI-MS and TWIM-MS were recorded with a Waters Synapt G2 tandem mass spectrometer, using solutions consisting of 0.5 mg of sample in 1 mL of acetonitrile/methanol (3/1, v/v) for Pd_6L_{12}.

The TWIM-MS data were collected under the following conditions: ESI capillary voltage, 3 kV; sample cone voltage, 30 V; extraction cone voltage, 0.1 V; source temperature 100 ºC; desolvation temperature, 100 ºC; cone gas flow, 10 L/h; desolvation gas flow, 700 L/h (N_2); source gas control, 0 mL/min; trap gas control, 2 mL/min; helium cell gas control, 100 mL/min; ion mobility (IM) cell gas control, 30 mL/min; sample flow rate, 5 μL/min; IM traveling wave height, 25 V; and IM traveling wave velocity, 1000 m/s. Q was set in rf-only mode to transmit all ions produced by ESI into the triwave region for the acquisition of TWIM-MS data.

Small- and wide-angle X-ray scattering (SAXS/WAXS). SAXS/WAXS data were collected at 12-ID-B at the Advanced Photon Source, Argonne National Laboratory. Photon energy was 14 keV (λ = 0.8857 Å) with beam size 60 x 200 μm^2. Detectors used were Pilatus 2M (SAXS) and Pilatus 300K (WAXS). The sample-to-detector distances

were calibrated using silver behenate (AgBe). Exposure times of 0.5 s were used during data collection.

Rheometry. Frequency sweep and strain sweep experiments were performed on a TA Instruments Discovery Hybrid Rheometer HR-2. A parallel-plate geometry with radius of 8 mm was used and coupled with a bottom plate, with a typical gap ranging between 1.75–2 μm to maintain a starting axial force of 0.4–0.5 N. Frequency sweep experiments were performed from 0.1 to 100 rad/s at 1% strain, which was first confirmed to be in the linear viscoelastic regime using strain sweep experiments. Experiments were performed at 25 °C, with negligible solvent evaporation during the typical measurement time (< 15 min). Shear modulus (*G′*) and loss modulus (*G″*) were determined based on *G′* values at 5 rad/s. For stress relaxation experiments, loaded samples were immersed in mineral oil to reduce solvent evaporation and gel deswelling. Stress relaxation experiments were performed at 25 °C and 3% strain, also within the linear viscoelastic regime.

Calculating particle radius from ^{1}H DOSY spectra. By approximating cages as spherical particles diffusing in solution, the diffusion coefficient (*D*) can be related to particle hydrodynamic radius (*r*) through the Stokes–Einstein diffusion equation (Eq. 5), where *T* is the absolute temperature, k_B is the Boltzmann constant, and η is the solution viscosity at temperature *T*.

$$D = \frac{k_B T}{6\pi\eta r} \tag{5}$$

For our calculations, *T* = 298.15 K and η = 2.19 x 10^{-3} kg/ms (DMSO).

Calculating experimental and theoretical d-spacings and end-to-end distances. Experimental *d*-spacings were obtained through SAXS/WAXS characterization, where *q* values were determined from peak maximums and used in Eq. 2 (copied below).

$$d = \frac{2\pi}{q} \tag{2}$$

Experimental end-to-end distances R_{exp} were then calculated by subtracting the estimated cage diameter of 30 Å, the previously reported cubic dimension,[37] from the experimental *d*-spacing.

Theoretical *d*-spacings (d_{FCC}) were calculated for spherical cages distributed homogeneously on an FCC lattice as described Reference 38. In brief,

$$d_{FCC} = 2r \tag{6}$$

In Eq. 6, *r* is the largest radius that can enclose the MOC without intersection on the FCC lattice. The volume of this sphere (V_{FCC}) can be calculated from the volumetric

density of the FCC lattice (ρ_{FCC}) and the volume per cage (V_{cage}). V_{cage} can then be calculated from the gel volume (V_{gel}) and number of cages in that volume (n_{cage}).

$$V_{FCC} = \rho_{FCC} \times V_{cage} = \frac{\sqrt{2}\pi}{6}\left(\frac{V_{gel}}{n_{cage}}\right) = \frac{4}{3}\pi r^3 \quad (7)$$

With some manipulation,

$$d_{FCC} = 2^{1/6}\left(\frac{V_{gel}}{n_{cage}}\right) \quad (8)$$

With Eq. 8, d_{FCC} can now be calculated using experimental parameters. As an example, for an M_6L_{12}-based polyMOC gel formed with pL with M_n = 3.2 kDa,

V_{gel} = 300 µL of DMSO-d_6 + 20.25 mg of pL x (0.8273 µL/mg) = 3.17 x 10^{20} nm^3
N_{cage} = 0.02025 g x (3200 g/mol) x 6.02 x 10^{23} macromers/mol x 1 cage/6 macromers
= 6.4 x 10^{17} cages
d_{FCC} = 8.9 nm = 89 Å

Theoretical end-to-end distances (R_0) were calculated as described in 2.1.2 with Eq. 3, copied below.[1,38]

$$R_0 = b(N^{\alpha}) \quad (3)$$

In this equation, b and N are the Kuhn length and number of Kuhn segments, respectively. For theoretical maximum end-to-end distances, the scaling exponent α is set as 0.58; for theoretical minimum values, the scaling exponent is set to 0.50. The Kuhn length of PEG equals 0.76 nm. N is calculated using the following equation:[1]

$$N = \frac{R_{max}}{b} = \frac{nlcos(\theta/2)}{b} \quad (9)$$

The number of bonds in the chain n can be calculated from the degree of polymerization (DP) by the number of bonds per monomer (3, for PEG). For PEG, the average bond length l is 0.147 nm, and $\theta/2$ = 35.3° calculated from bond angle.[53]

As an example, for pL with M_n = 3.2 kDa,

DP = 3200 / 44.05 = 73
N = (73 x 3) x 0.147 nm x cos(35.3) / 0.76 nm = 34.6
$R_{0,max}$ = 0.76 nm x $(34.57)^{0.58}$ = 8.4 nm
$R_{0,min}$ = 0.76 x $(34.57)^{0.50}$ = 6.0 nm

Fitting stress relaxation data with stretched exponential function.[1] Stress relaxation curves were fit with the Kohlrausch stretched exponential function (Eq. 4, copied below) to obtain characteristic relaxation time τ.

$$G(t) = G_0 exp\left[-\left(\frac{t}{\tau}\right)^{\alpha}\right], \qquad 0 < \alpha < 1 \tag{4}$$

G is the experimentally measured modulus (Pa), G_0 is the plateau modulus (Pa), *t* is time (s), τ is the characteristic relaxation time (s), and α is an experimentally fitted parameter attributed to physical constraints in the material. In fitting, $0 < \alpha < 1$. Data were fit using MATLAB R2019b Curve Fitting Toolbox.

Computation of network branch functionality f from G' using phantom network theory of rubber elasticity. Network branch functionality *f* was calculated from *G'* measurements obtained at 5 rad/s with 1% strain amplitude using the following equation:

$$|G'| = \frac{\rho_{ideal} \cdot RT}{f_{ideal} \cdot M_{chain}}(f - 2) \tag{10}$$

G' = experimental storage modulus obtained at 5 rad/s and 1% strain amplitude (Pa)
ρ_{ideal} = ideal mass density of elastically active polymer chains, calculated using the mass of macromer divided by the added solvent volume (g/mL)
f_{ideal} = ideal branch functionality of the gel (12 for an M_6L_{12}-based polyMOC gel)
M_{chain} = ^{1}H NMR-derived macromer molecular weight (g/mol)
f = experimental network branch functionality
R = universal gas constant (8.31 x 10^6 $cm^3 \cdot Pa \cdot K^{-1} \cdot mol^{-1}$)
T = temperature (298.15 K)

The detailed derivation of this expression from phantom network theory can be found in Reference 38. In brief, the mass density of elastically active polymer chains ρ is related to ideal mass density ρ_{ideal}, ideal branch functionality f_{ideal}, and experimental branch functionality *f*, and the relationship is substituted into the phantom network theory.

$$|G| = \frac{\rho RT}{M_{chain}}\left(\frac{f - 2}{2}\right) \tag{11}$$

$$\rho = \frac{f}{f_{ideal}}\rho_{ideal} \tag{12}$$

As an example, the experimental branch functionality of 100% Pd M_6L_{12}-based polyMOC gel formed from 5.2 kDa macromer was calculated as shown below. Solvent evaporation during annealing was considered in calculating ρ_{ideal}.

G' (5 rad/s, 1% strain) = 9641 Pa

$$= \frac{(20.25 \times 10^{-3}\ g / 0.267\ mL) \times (8.31 \times 10^6\ cm^3 \cdot Pa \cdot K^{-1} \cdot mol^{-1}) \times (298.15\ K) \times (f - 2)}{12 \times 5200\ g \cdot mol^{-1}}$$

9641 Pa = 3015.14 (*f* – 2)
5.2 = *f*

Synthesis and characterization of compounds.

Scheme S1. Synthetic route to 9-methyl-3,6-bis(pyridine-4-ylethynyl)-9*H*-carbazole [2].

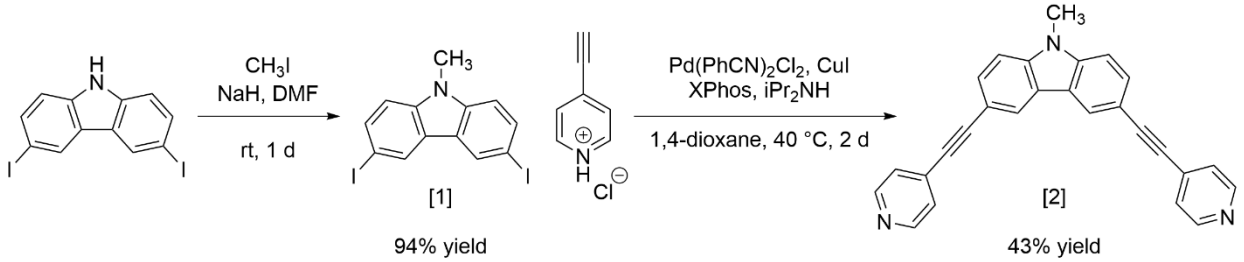

3,6-diiodo-9-methyl-9*H*-carbazole [1]. 3,6-diiodocarbazole (1.00 g, 2.39 mmol) and NaH (60 wt% in mineral oil, 143 mg, 3.58 mmol) were added to an oven-dried flask with stir bar under N_2. A gas outlet needle was added before the addition of 4 mL of dry DMF, upon which the reaction bubbled and turned yellow. It was stirred at rt for 30 min before iodomethane (165 µL, 2.63 mmol) was added dropwise to the reaction mixture. The reaction became chalky white and opaque; monitoring with TLC (10% EtOAc/hexanes) showed reaction completion within 2.5 h. The reaction mixture was diluted with DCM (~100 mL), then washed with brine (100 mL x 5) to remove DMF. The organic layer was dried over Na_2SO_4, filtered, and concentrated under reduced pressure. The resulting white solid was washed with hexanes to remove mineral oil impurities, resulting in pure product with 94% yield (971 mg, 2.24 mmol).
DART-HRMS (*m/z*) calculated for $C_{13}H_9NI_2^+$ = 432.88189 [*M*]$^+$; found 432.8834
^{1}H NMR (500 MHz, $CDCl_3$) δ 8.31 (d, *J* = 1.7 Hz, 2H), 7.73 (ddd, *J* = 8.6, 1.7, 0.7 Hz, 2H), 7.16 (d, *J* = 8.6 Hz, 2H), 3.78 (d, *J* = 0.7 Hz, 3H).
^{13}C-{^{1}H} NMR (126 MHz, $CDCl_3$) δ 140.2, 134.7, 129.4, 124.0, 110.8, 82.0, 29.4.

9-methyl-3,6-bis(pyridine-4-ylethynyl)-9*H*-carbazole [2]. [1] (750. mg, 1.69 mmol), 4-ethynylpyridine hydrochloride (851 mg, 6.09 mmol), $Pd(NCC_6H_5)Cl_2$ (130. mg, 0.339 mmol), XPhos (242 mg, 0.508 mmol), and Cu(I)I (12.9 mg, 0.0677 mmol) were added to a 50 mL oven-dried flask with stir bar under nitrogen. After sparging both solvents for 30 min, dry 1,4-dioxane (28.2 mL) was added to the reaction mixture, followed by diisopropylamine (1.83 µL, 13.1 mmol). The black reaction mixture was heated to 40 °C and allowed to stir for 48–72 h, monitoring the disappearance of intermediate monofunctionalized product using LC-MS. The reaction was cooled to rt and quenched by opening to air, then filtered through Celite with EtOAc until filtrate was colorless. The volume was reduced to ~100 mL and washed with 10% aqueous ethylene diamine (100 mL x 2) and brine (100 mL x 1) before drying the organic layer over Na_2SO_4, filtering, and concentrating under reduced pressure. The crude product was dry loaded onto silica and purified using silica column chromatography (gradient from 0→8% MeOH/DCM, with product elution at 4%). Pure product was obtained at 43% yield (279 mg, 0.728 mmol).
DART-HRMS (*m/z*) calculated for $C_{27}H_{18}N_3^+$ = 384.1496 [*M*+H]$^+$; found 384.1543
^{1}H NMR (400 MHz, DMSO-*d*$_6$) δ 8.71 – 8.60 (m, 4H), 8.57 (d, *J* = 1.4 Hz, 2H), 7.80 – 7.66 (m, 4H), 7.61 – 7.50 (m, 4H), 3.95 (s, 3H).

^{13}C-{^{1}H} NMR (126 MHz, DMSO-d_6) δ 149.9, 141.3, 130.8, 130.0, 125.2, 124.8, 121.7, 111.8, 110.3, 95.4, 85.5, 29.4.

Scheme S2. Synthetic route to pL (polymer ligand).

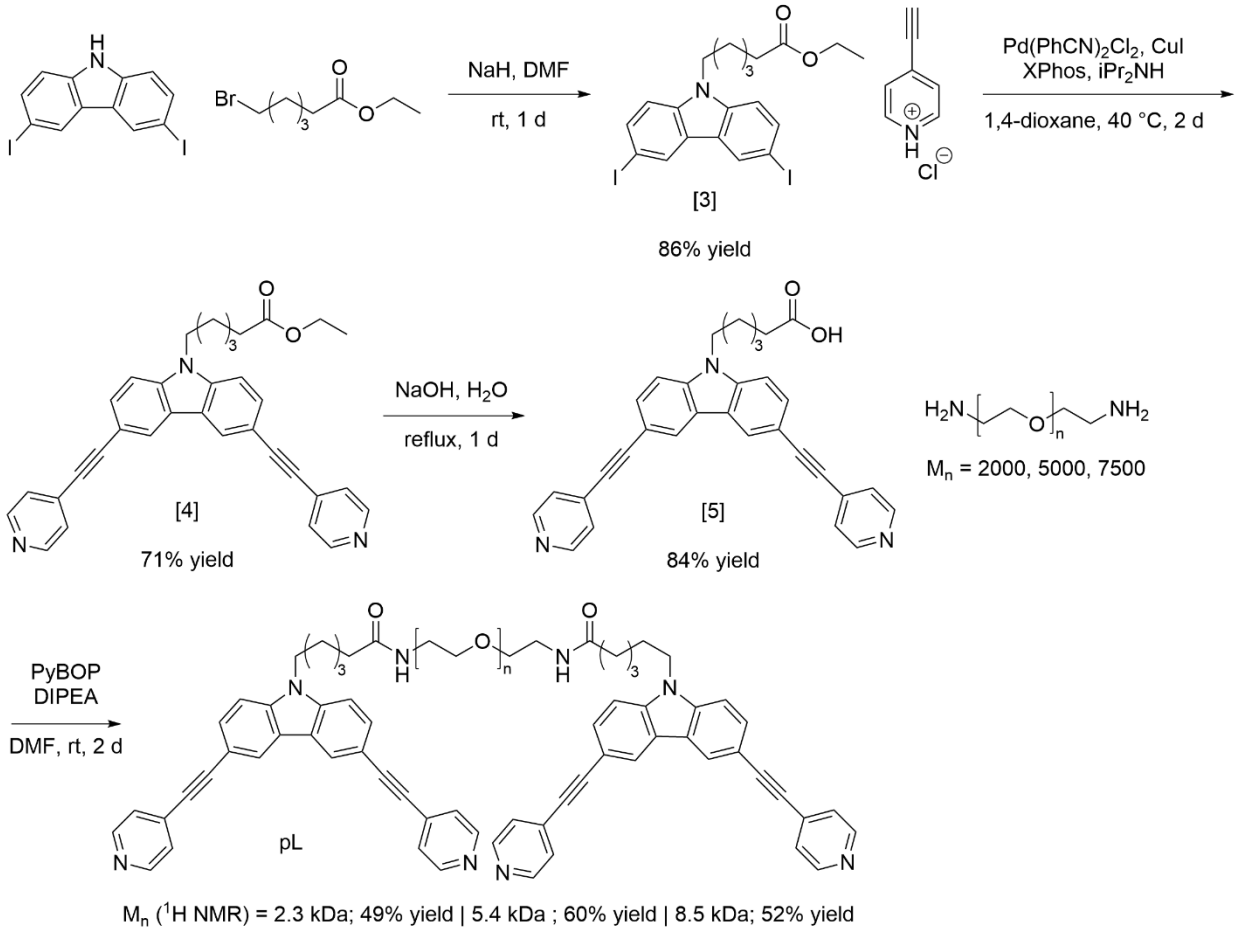

Ethyl 6-(3,6-diiodo-9*H*-carbazol-9-yl)hexanoate [3]. 3,6-diiodo-9*H*-carbazole (8.00 g, 19.1 mmol) and NaH (60 wt% in mineral oil, 1.15 g, 28.6 mmol) were added to an oven-dried 100 mL flask with stir bar under N_2. An outlet needle was added to reduce pressure caused by H_2 formation before the addition of dry DMF (15.0 mL). The reaction mixture turned yellow and was stirred for 30 min before the dropwise addition of ethyl 6-bromohexanoate (5.40 mL, 21.0 mmol). The reaction was stirred overnight at rt, turning gray with product formation. The solution was then diluted with EtOAc (100–150 mL) and washed with brine (400 mL x 5) to remove DMF, taking care to carefully quench excess NaH with the first wash. The organic layer was dried over Na_2SO_4, filtered, and concentrated to a white solid under reduced pressure. The residue was washed with hexanes to remove excess ethyl 6-bromohexanoate. The crude product was purified with silica column chromatography (100% DCM). If necessary, additional washes with hexanes were used to remove trace ethyl 6-bromohexanoate impurities. Pure product was obtained as a white solid in 86% yield (9.21 g, 16.4 mmol). DART-HRMS (*m/z*) calculated for $C_{20}H_{21}NO_2I_2^+$ = 560.96562 [*M*]$^+$; found 560.96565

^{1}H NMR (500 MHz, $CDCl_3$) δ 8.31 (d, *J* = 1.7 Hz, 2H), 7.70 (ddd, *J* = 8.6, 1.7, 0.5 Hz, 2H), 7.15 (d, *J* = 8.6 Hz, 2H), 4.22 (t, *J* = 7.1 Hz, 2H), 4.09 (q, *J* = 7.1 Hz, 2H), 2.24 (t, *J* = 7.4 Hz, 2H), 1.83 (p, *J* = 7.3 Hz, 2H), 1.64 (p, *J* = 7.5 Hz, 2H), 1.41 – 1.28 (m, 2H), 1.21 (td, *J* = 7.1, 0.5 Hz, 3H).
^{13}C-{^{1}H} NMR (126 MHz, $CDCl_3$) δ 173.5, 139.6, 134.7, 129.5, 124.1, 112.0, 81.9, 60.5, 43.1, 34.1, 34.1, 28.7, 26.8, 24.7, 14.4.

Ethyl 6-(3,6-bis(pyridine-4-ylethynyl)-9*H*-carbazol-9-yl)hexanoate) [4]. [3] (3.00 g, 5.35 mmol), 4-ethynylpyridine hydrochloride (2.69 g, 19.2 mmol), $Pd(NCC_6H_5)Cl_2$ (410. mg, 1.07 mmol), XPhos (765 mg, 1.60 mmol), and Cu(I)I (41.7 mg, 0.219 mmol) were added to a 250 mL oven-dried flask with stir bar under N_2. After sparging both solvents with N_2 for 30 min, dry 1,4-dioxane (90.0 mL) was added to the reaction mixture, followed by diisopropylamine (5.79 mL, 41.3 mmol). The black reaction mixture was heated to 40 °C and allowed to stir for 48–72 h, monitoring the disappearance of intermediate monofunctionalized product using LC-MS. The reaction was cooled to rt, then filtered through Celite and washed with EtOAc until the solvent ran colorless. The filtrate was reduced to ~100 mL and washed with 10% aqueous ethylene diamine (100 mL x 2) and brine (100 mL x 1) before drying the organic layer over Na_2SO_4, filtering, and concentrating under reduced pressure. The crude product was dry loaded onto silica gel and purified using silica column chromatography (gradient from 0→8% MeOH/DCM, with product elution at 4%). Pure product was obtained as a tan solid at 71% yield (1.94 g, 3.80 mmol).
DART-HRMS (*m/z*) calculated for $C_{34}H_{30}N_3O_2^+$ = 512.23325 [*M*+H]$^+$; found 512.23215
^{1}H NMR (500 MHz, DMSO-d_6) δ 8.72 – 8.61 (m, 4H), 8.56 (d, *J* = 1.4 Hz, 2H), 7.84 – 7.63 (m, 4H), 7.63 – 7.44 (m, 4H), 4.44 (t, *J* = 7.1 Hz, 2H), 3.98 (q, *J* = 7.1 Hz, 2H), 2.22 (t, *J* = 7.3 Hz, 2H), 1.78 (p, *J* = 7.2 Hz, 2H), 1.54 (p, *J* = 7.4 Hz, 2H), 1.31 (qd, *J* = 9.7, 9.2, 6.1 Hz, 2H), 1.10 (t, *J* = 7.1 Hz, 3H).
^{13}C-{^{1}H} NMR (126 MHz, DMSO-d_6) δ 172.7, 149.9, 140.7, 130.8, 130.0, 125.2, 124.9, 121.8, 111.8, 110.4, 95.4, 85.5, 59.6, 42.5, 33.3, 28.2, 25.8, 24.2, 14.0.

6-(3,6-bis(pyridin-4ylethynyl)-9*H*-carbazol-9-yl)hexanoic acid [5]. [4] (1.87 g, 3.66 mmol) was transferred to a flask using THF (10.0 mL), to which 5 M NaOH aqueous solution (4.00 mL) and a stir bar was added. The biphasic orange solution was refluxed overnight, during which the reaction mixture turned a dark brown color. After cooling to rt, 1 M HCl was added until pH 6 was reached, resulting in precipitation of the product as a light brown solid. This solid was filtered and washed with water and dried to obtain the brown product in 84% yield (1.49 g, 3.08 mmol).
DART-HRMS (*m/z*) calculated for $C_{32}H_{26}N_3O_2^+$ = 484.20195 [*M*+H]$^+$; found 484.20221
^{1}H NMR (500 MHz, DMSO-d_6) δ 8.75 – 8.61 (m, 4H), 8.61 – 8.52 (m, 2H), 7.87 – 7.66 (m, 4H), 7.62 – 7.51 (m, 4H), 4.45 (t, *J* = 7.1 Hz, 2H), 2.16 (t, *J* = 7.3 Hz, 2H), 1.78 (p, *J* = 7.3 Hz, 2H), 1.53 (p, *J* = 7.4 Hz, 2H), 1.33 (tt, *J* = 10.0, 6.3 Hz, 2H).
^{13}C-{^{1}H} NMR (126 MHz, DMSO-d_6) δ 174.4, 150.0, 140.7, 130.8, 130.0, 125.2, 124.9, 121.8, 111.8, 110.4, 95.4, 85.5, 42.6, 33.6, 28.3, 26.0, 24.2.

Polymer ligand (pL). 1 equiv. of bifunctional PEG amine (average M_n = 2000, 5000, 7500), 3.5 equiv. of [5], and 3.5 equiv. of PyBOP coupling reagent was added to an

oven-dried flask with stir bar under N_2, to which dry DMF was added to obtain a reaction concentration of 125 mg/mL. 8 eq of dry N,N-diisopropylethylamine was added to the brown reaction mixture, which was briefly heated to solubilize all reagents. Although this coupling reaction completes with 3 h of stirring, it was typically allowed to stir for 2 days at rt to ensure maximum end functionalization. The crude product was precipitated in cold Et_2O to obtain a brown solid, which was then purified using prepGPC ($CHCl_3$) to separate bisfunctionalized polymer ligand. A $NaHCO_3$ wash of the product in $CHCl_3$ was necessary to deprotonate the final beige product, which was precipitated again in cold Et_2O to obtain 50–70% yield.

pL (2.3 kDa).
^{1}H NMR (400 MHz, $CDCl_3$) δ 8.62 (s, 4H), 8.31 (d, *J* = 1.5 Hz, 2H), 7.68 (dd, *J* = 8.5, 1.6 Hz, 2H), 7.49 – 7.34 (m, 6H), 6.08 (s, 1H), 4.33 (t, *J* = 7.2 Hz, 2H), 3.86 – 3.35 (m, 104H), 2.16 (t, *J* = 7.4 Hz, 2H), 1.92 (p, *J* = 7.4 Hz, 2H), 1.79 – 1.65 (m, 4H), 1.43 (p, *J* = 8.0 Hz, 2H).

pL (5.2 kDa).
^{1}H NMR (600 MHz, $CDCl_3$) δ 8.67 – 8.56 (m, 4H), 8.31 (d, *J* = 1.5 Hz, 2H), 7.68 (dd, *J* = 8.4, 1.6 Hz, 2H), 7.48 – 7.33 (m, 6H), 6.14 (t, *J* = 5.6 Hz, 1H), 4.33 (t, *J* = 7.3 Hz, 2H), 3.81 – 3.36 (m, 238H), 2.16 (t, *J* = 7.4 Hz, 2H), 1.92 (p, *J* = 7.5 Hz, 2H), 1.77 – 1.66 (m, 12H), 1.50 – 1.36 (m, 2H).

pL (8.8 kDa).
^{1}H NMR (600 MHz, $CDCl_3$) δ 8.73 – 8.51 (m, 8H), 8.33 (d, *J* = 1.5 Hz, 4H), 7.52 – 7.37 (m, 12H), 6.09 (t, *J* = 5.6 Hz, 2H), 4.35 (t, *J* = 7.3 Hz, 4H), 3.66 (s, 797H), 2.18 (t, *J* = 7.4 Hz, 5H), 1.94 (t, *J* = 7.6 Hz, 5H), 1.51 – 1.37 (m, 5H).

Pt(MeCN)$_4$(OTf)$_2$. $Pt(MeCN)_4(OTf)_2$ was synthesized following reported procedures in Reference 54.

Scheme S3. Self-assembly of [2] to form M_6L_{12} solution cage assemblies with mixed metal ratios of Pd(II)/Pt(II).

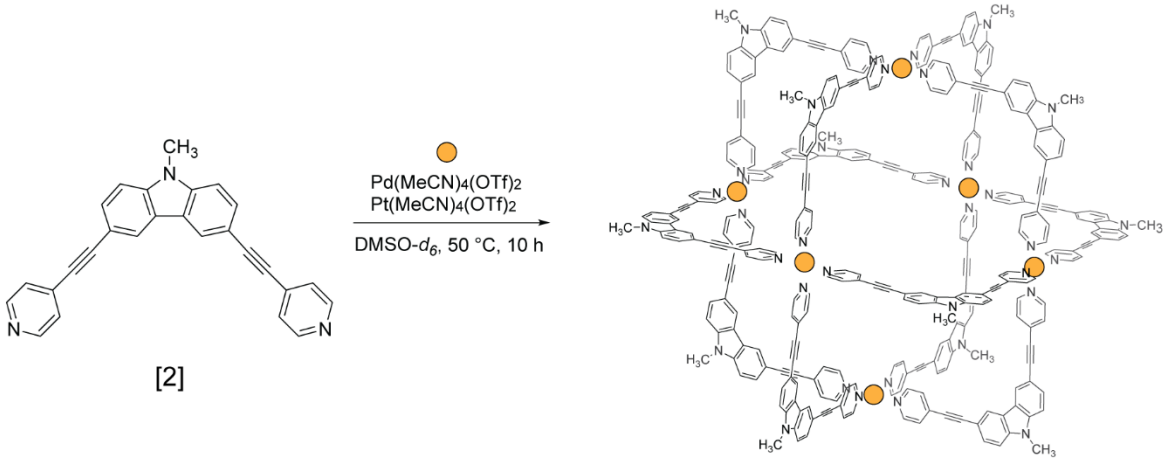

[2]

M_6L_{12} cube

M_6L_{12} coordination cube solution assembly. Cages were self-assembled through the mixture of DMSO-d_6 stock solutions of [2] (10.0 mg, 0.0261 mmol) and metal salts (0.131 mmol): $Pd(MeCN)_4(OTf)_2$ and/or $Pt(MeCN)_4(OTf)_2$. The ratio of metal/ligand was maintained at 1.1:2, and cage assemblies were formed with Pd(II)/Pt(II) ratios of 100:0, 75:25, 50:50, 25:75, and 0:100. For multi-metal gels, Pd(II) and Pt(II) metal stock solutions were mixed before their addition to [2]. The mixed [2] and metal salt stock solutions were then annealed at 50 °C for 10 h.
ESI-MS (*m/z*) calculated for $[Pd_6L_{12}-6OTf^-]^{6+}$ = 1022.31; found 1022.31. Calculated for $[Pd_6L_{12}-7OTf^-]^{7+}$ = 854.99); found 854.98. Calculated for $[Pd_6L_{12}-8OTf^-]^{8+}$ = 729.49; found 729.49. Calculated for $[Pd_6L_{12}-9OTf^-]^{9+}$ = 631.77; found 631.78.

Scheme S4. Self-assembly of pL with Pd(II) and Pt(II) metal salts to form M_6L_{12}-based polyMOC gels.

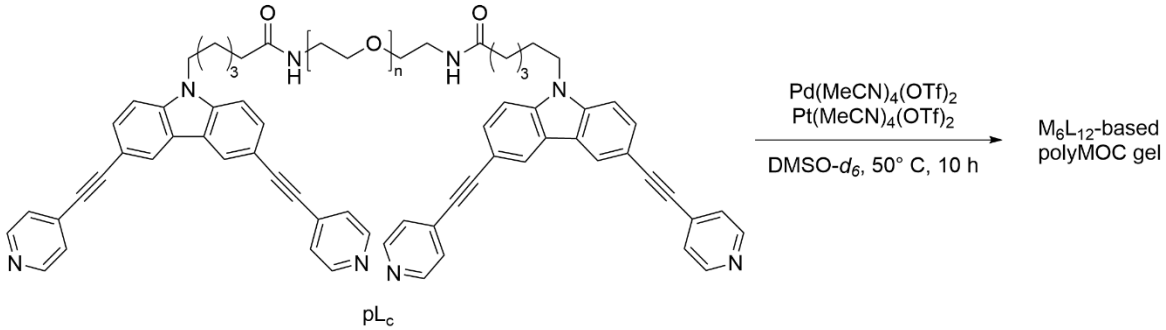

M_6L_{12}-based polyMOC gel synthesis. Gels were self-assembled under inert atmosphere through the mixture of DMSO-d_6 stock solutions of pL and Pd(II)/Pt(II) metal salts, combined at a ratio of 1:1.2. Gels were formed with Pd(II)/Pt(II) ratios of 100:0, 75:25, 50:50, 25:75, and 0:100. Measured masses of pL, $Pd(MeCN)_4(OTf)_2$, and $Pt(MeCN)_4(OTf)_2$ were brought into a N_2 glove box. Stock solutions of pL and metal salt were made with DMSO-d_6 ([pL] = 135 μg/μL; [metal] = polymer M_n-dependent). Examples of stock solution concentrations are given below. For multi-metal gels, Pd(II) and Pt(II) metal stock solutions were mixed before their addition to solutions of polymer ligand. To form the gels, 90 μL of pL stock solution was aliquoted in each 8 mm diameter Teflon mold, which was placed on a hot plate at 70 °C. This was quickly followed by the addition of 90 μL of metal stock solution, dispersed evenly over the solution surface. The open-faced molds were heated 7 min, which was necessary for Pt(II) gel solidification and resulted in a small amount of solvent evaporation (~20 μL for each sample mold). Heterogeneities in the resulting gels were evened out through crosshatching (drawing two perpendicular series of parallel lines) using a small gauge needle. Gels were allowed to cool and further solidify before the molds were bound closed using Teflon squares and binder clips and placed in a Schlenk chamber, which was sealed tightly with electrical tape and clamp. The Schlenk chamber was then removed from glovebox and transferred to an isothermal oven maintained at 50 °C, where the gels were annealed under an inert atmosphere for 48 h. Once removed, the chamber was allowed to cool to rt before gels were removed for rheology studies.

5.2 kDa 50:50 Pd(II)/Pt(II) pL gel synthesis example. To make samples in triplicate, 36.5 mg (7.01 μmol) of pL (5.2 kDa) was diluted with 270. μL DMSO-d_6. Since 8.42 μmol of metal is needed to obtain a 1:1.2 ratio of polymer ligand:metal, this amounts to 4.21 μmol of each metal for a 50:50 Pd(II)/Pt(II) gel. As a result, 2.39 mg of $Pd(MeCN)_4(OTf)_2$ and 2.76 mg of $Pd(MeCN)_4(OTf)_2$ were diluted with 135 μL DMSO-d_6 each. Metal stock solutions were combined following dilution. 90.0 μL of pL stock solution was aliquoted in each Teflon mold heated at 70 °C, followed by 90.0 μL of combined metal stock solution to each mold. Gels were heated for 7 min, then homogenized and cooled before molds were bound shut. Sealed in a Schlenk chamber, gels were annealed under N_2 in an isothermal vacuum at 50 °C for 48 h. The chamber was not opened until cooled to rt.

	Mass (mg)	**Volume dilution (μL)**	**Concentration**	
			Molar (mM)	**Mass (μg/μL)**
pL (5.2 kDa)	36.5	270.	26.0	135
$Pd(MeCN)_4(OTf)_2$	2.39	135	31.2	17.7
$Pt(MeCN)_4(OTf)_2$	2.76	135	31.2	20.5

8.8 kDa 100:0 Pd(II)/Pt(II) pL gel synthesis example. To make samples in triplicate, 36.45 mg (4.14 μmol) of pL (8.8 kDa) was diluted with 270. μL DMSO-d_6. 4.97 μmol of metal is needed to obtain a 1:1.2 ratio of polymer ligand:metal, so 2.83 mg of $Pd(MeCN)_4(OTf)_2$ was diluted with 270. μL DMSO-d_6. 90.0 μL of pL stock solution was aliquoted in each Teflon mold heated at 70 °C, followed by 90.0 μL of Pd(II) metal stock solution. Gels were heated for 7 min, then homogenized and cooled before molds were bound shut. Sealed in a Schlenk chamber, gels were annealed in an isothermal vacuum at 50 °C for 48 h. The chamber was not opened until cooled to rt.

	Mass (mg)	**Volume dilution (μL)**	**Concentration**	
			Molar (mM)	**Mass (μg/μL)**
pL (8.8 kDa)	36.5	270.	15.3	135
$Pd(MeCN)_4(OTf)_2$	2.83	270.	18.4	10.5
$Pt(MeCN)_4(OTf)_2$	0	0	0	0

2.5 Supplementary

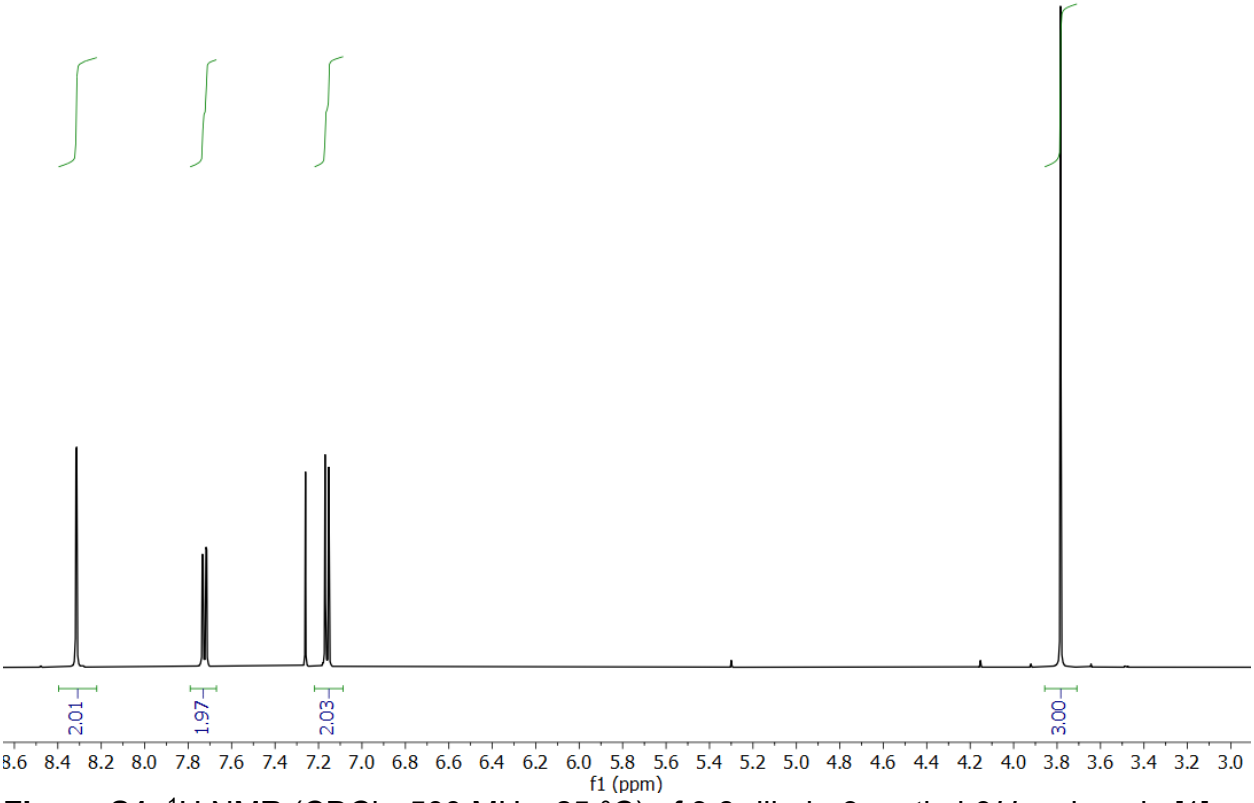

Figure S1. ^{1}H NMR ($CDCl_3$, 500 MHz, 25 °C) of 3,6-diiodo-9-methyl-9*H*-carbazole [1].

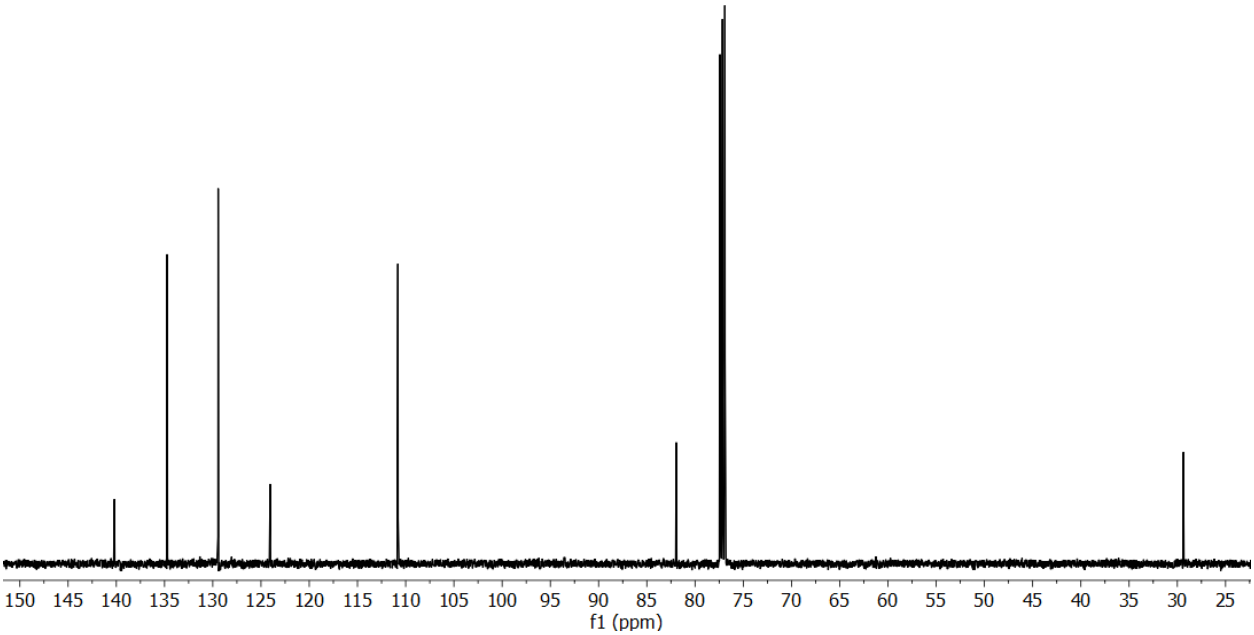

Figure S2. ^{13}C-{^{1}H} NMR ($CDCl_3$, 126 MHz, 25 °C) spectrum of 3,6-diiodo-9-methyl-9*H*-carbazole [1].

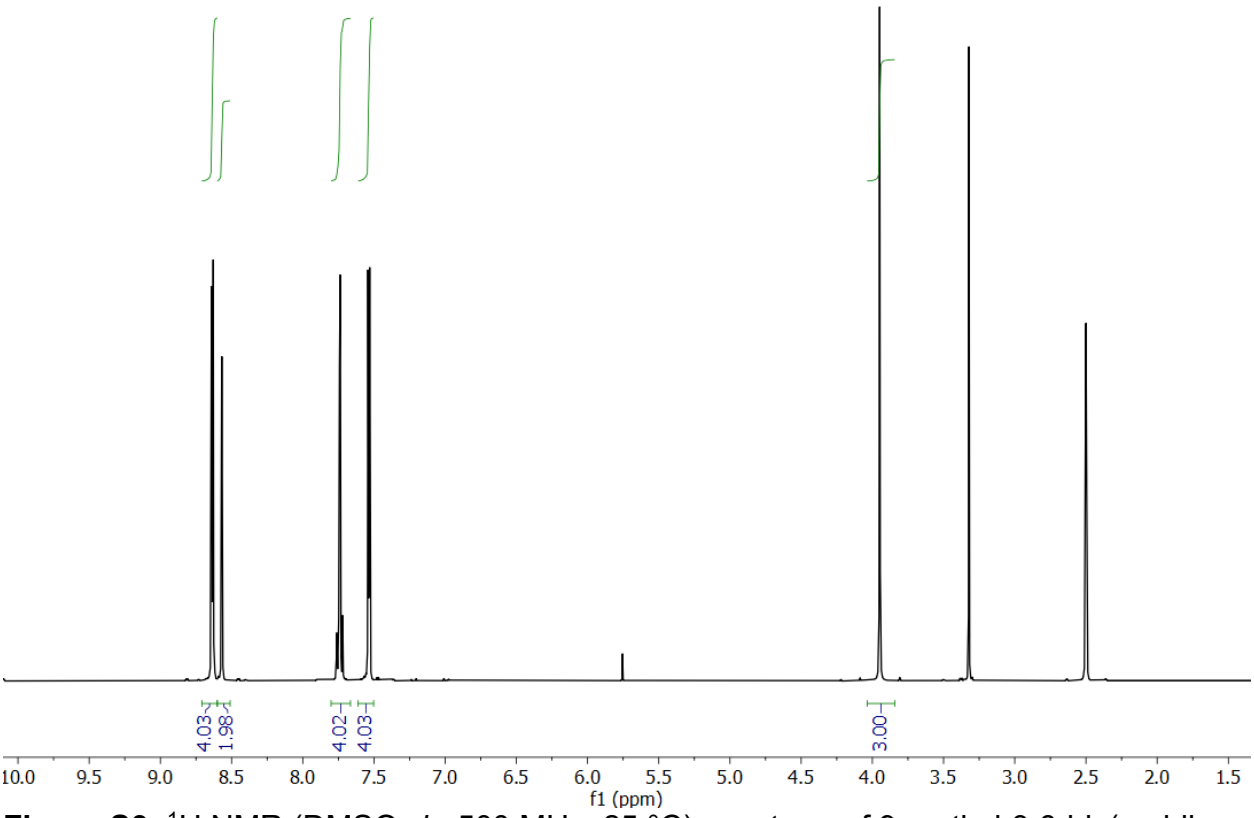

Figure S3. ^{1}H NMR (DMSO-*d*$_6$, 500 MHz, 25 °C) spectrum of 9-methyl-3,6-bis(pyridine-4-ylethynyl)-9*H*-carbazole [2].

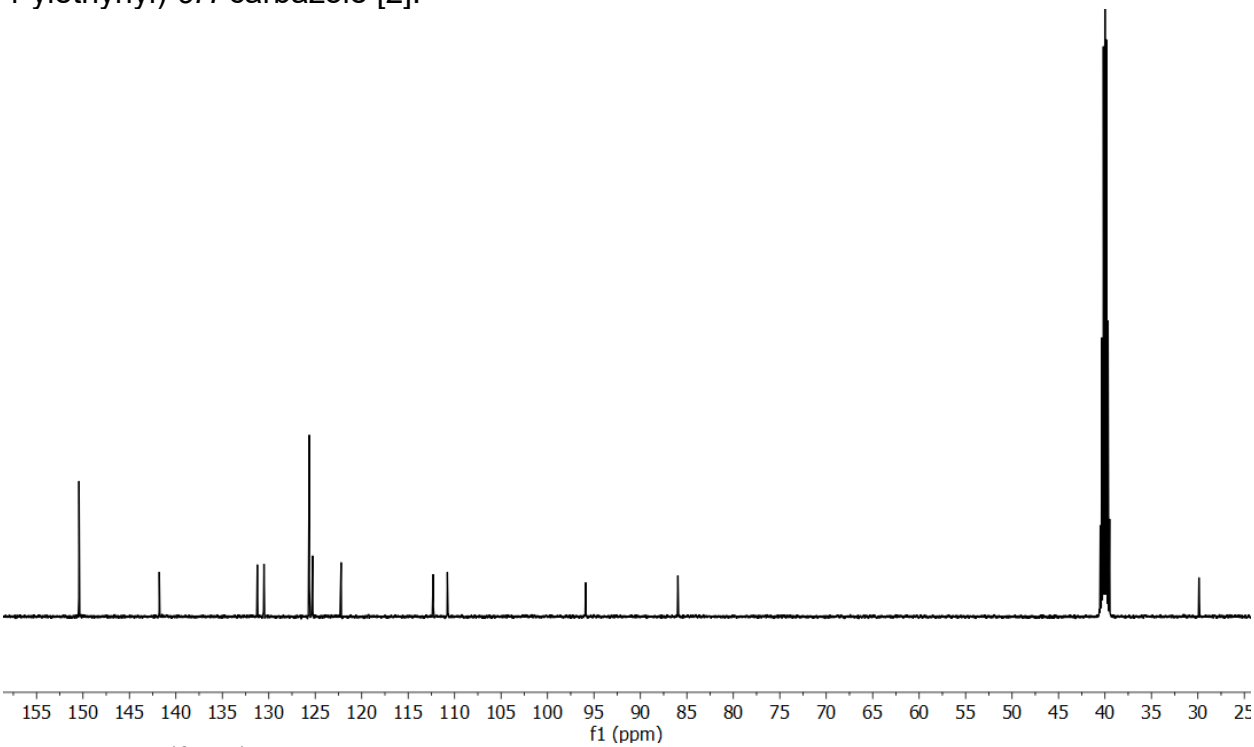

Figure S4. ^{13}C-{^{1}H} NMR (DMSO-*d*$_6$, 126 MHz, 25 °C) spectrum of 9-methyl-3,6-bis(pyridine-4-ylethynyl)-9*H*-carbazole [2].

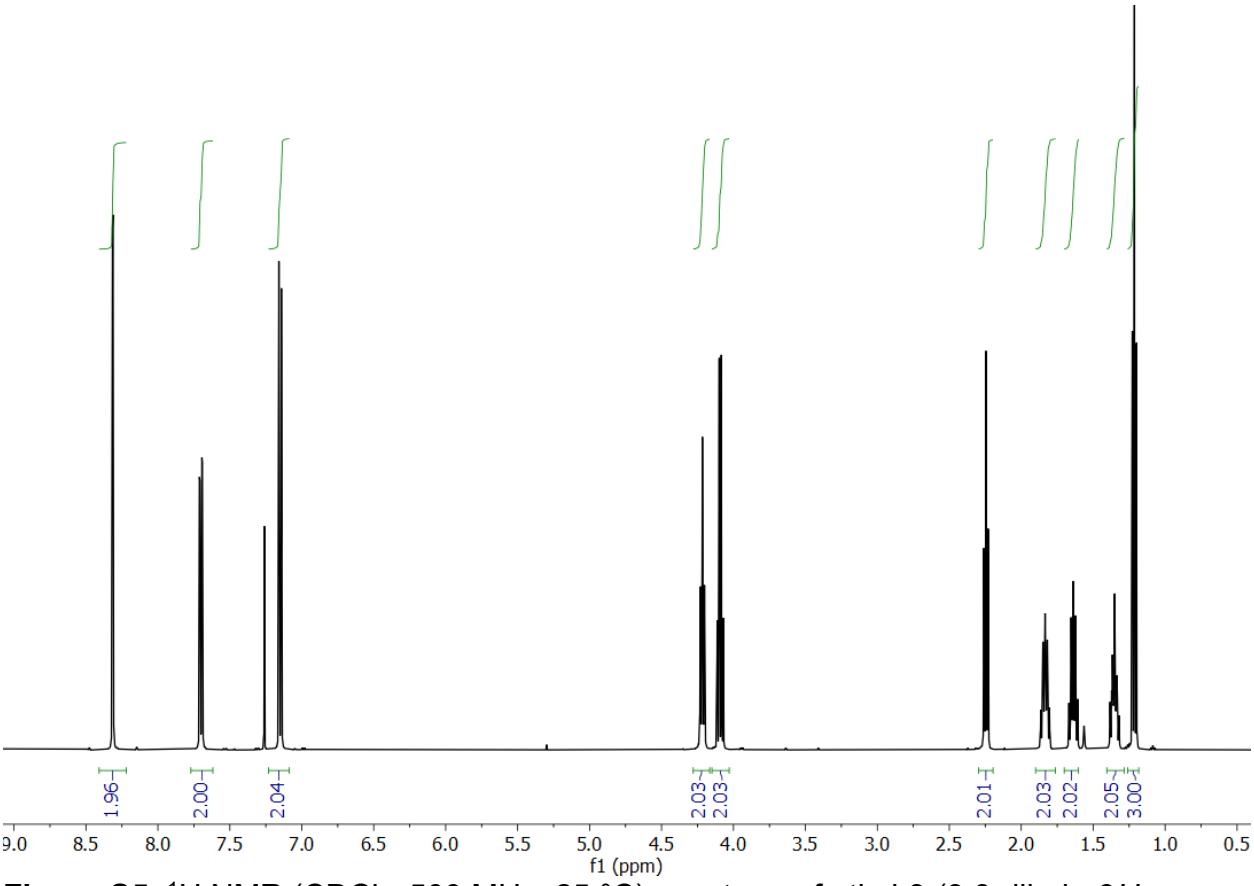

Figure S5. ^{1}H NMR ($CDCl_3$, 500 MHz, 25 °C) spectrum of ethyl 6-(3,6-diiodo-9*H*-carbazol-9-yl)hexanoate [3].

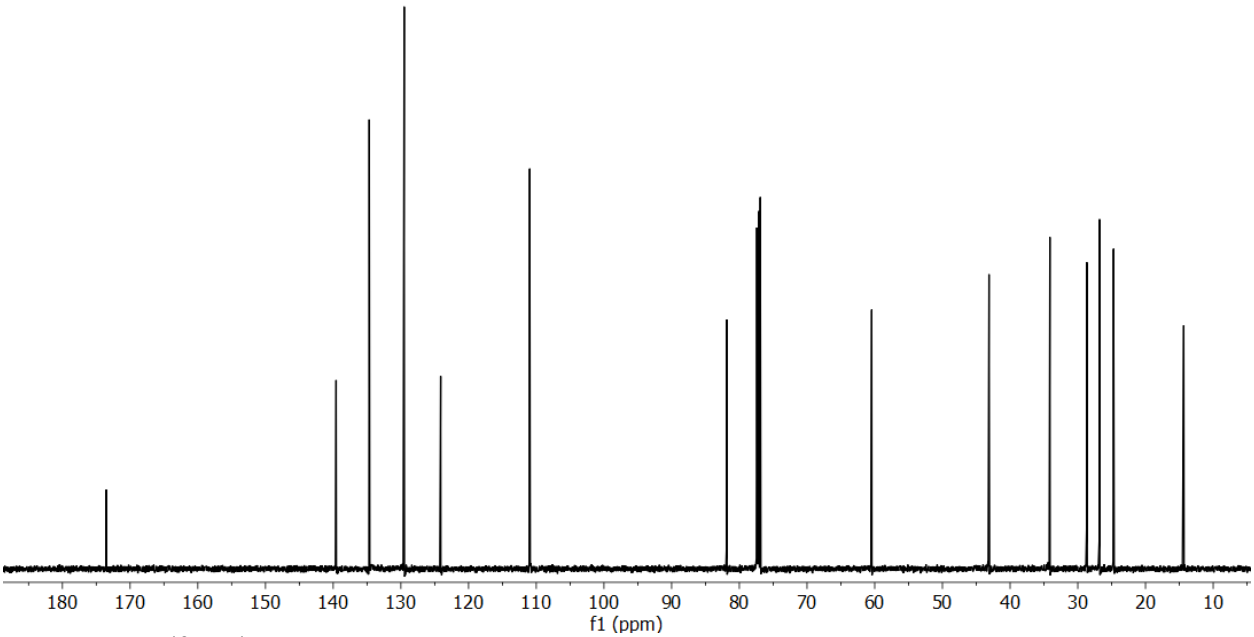

Figure S6. ^{13}C-{^{1}H} NMR ($CDCl_3$, 126 MHz, 25 °C) spectrum of ethyl 6-(3,6-diiodo-9*H*-carbazol-9-yl)hexanoate [3].

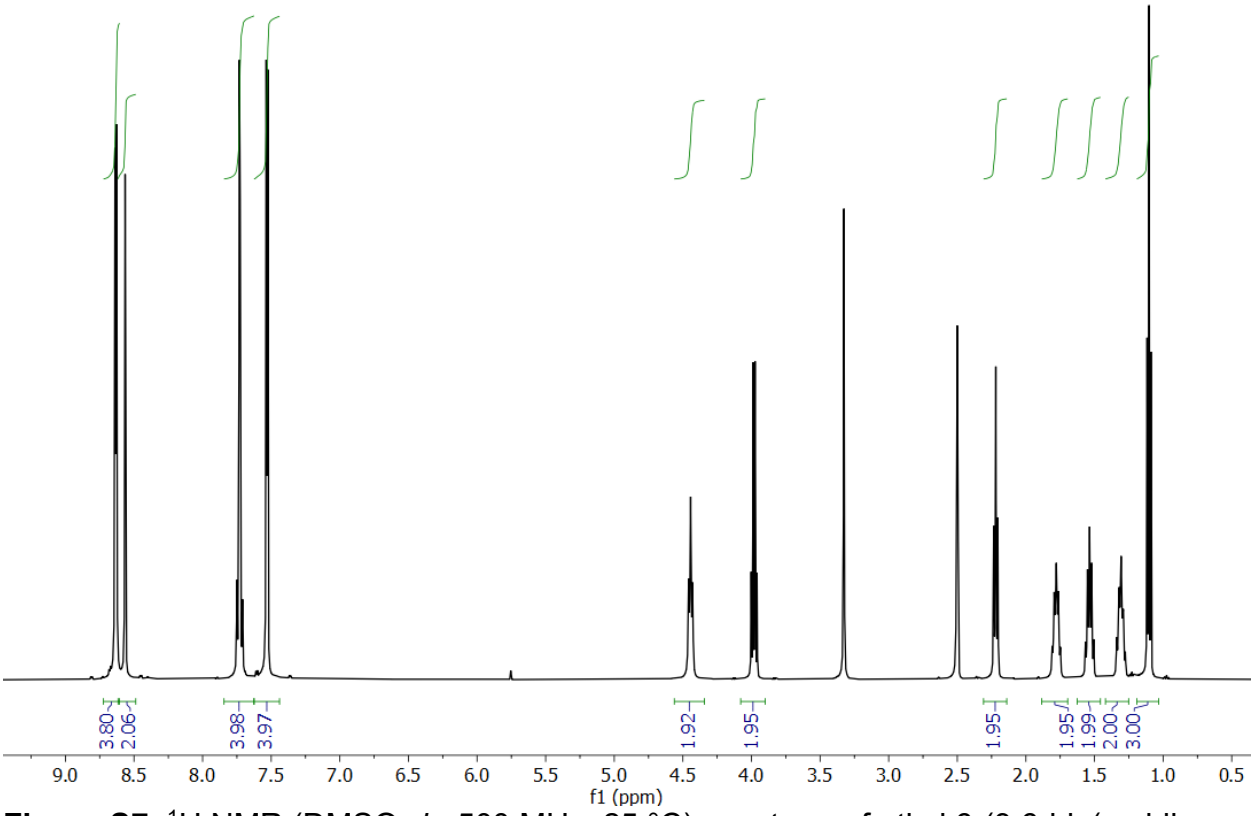

Figure S7. ^{1}H NMR (DMSO-*d*$_6$, 500 MHz, 25 °C) spectrum of ethyl 6-(3,6-bis(pyridine-4-ylethynyl)-9*H*-carbazol-9-yl)hexanoate) [4].

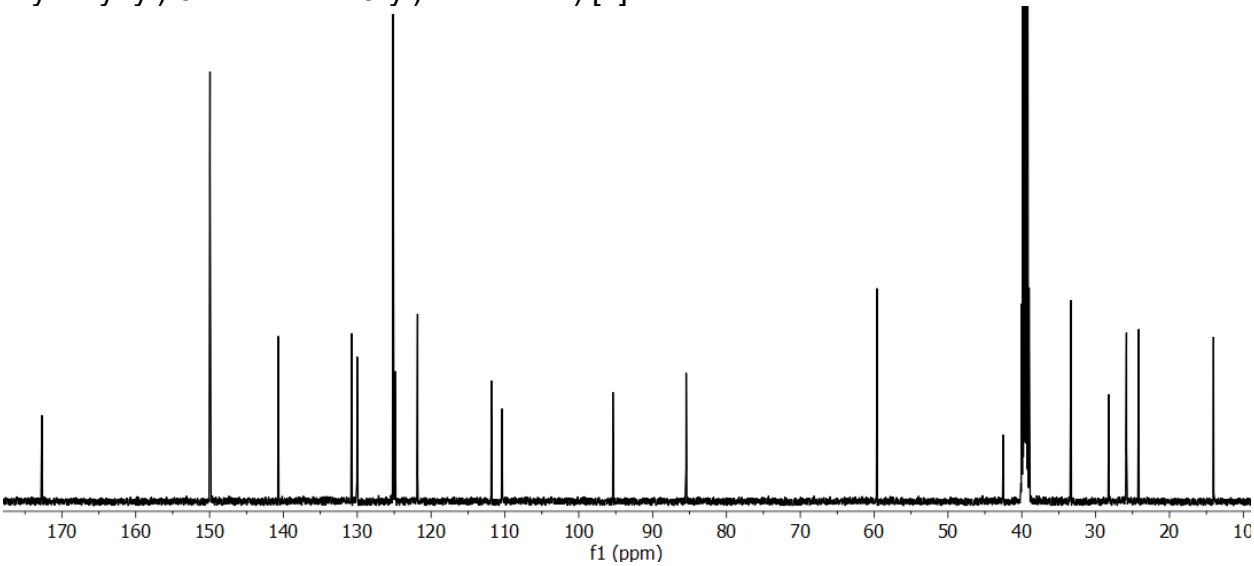

Figure S8. ^{13}C-{^{1}H} NMR (DMSO-*d*$_6$, 126 MHz, 25 °C) spectrum of ethyl 6-(3,6-bis(pyridine-4-ylethynyl)-9*H*-carbazol-9-yl)hexanoate) [4].

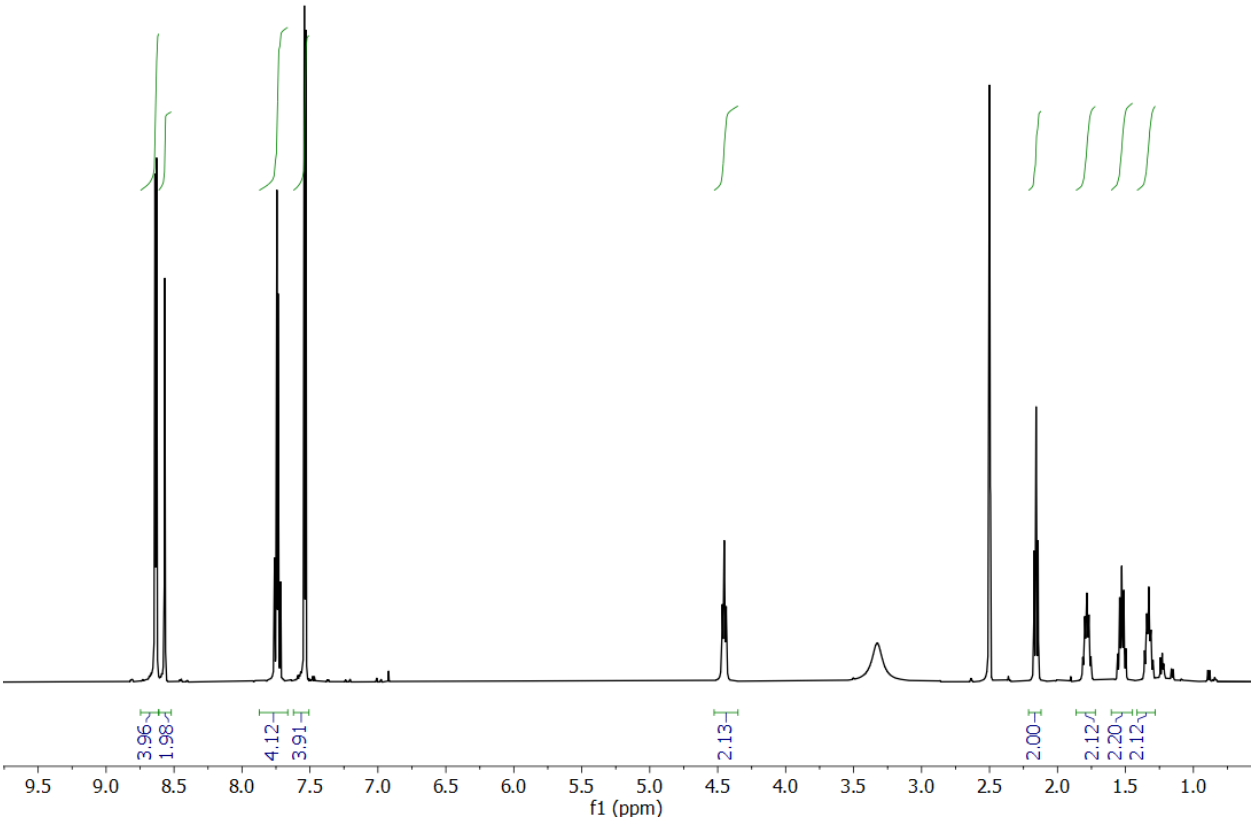

Figure S9. ^{1}H NMR (DMSO-d_6, 500 MHz, 25 °C) of 6-(3,6-bis(pyridin-4ylethynyl)-9*H*-carbazol-9-yl)hexanoic acid [5].

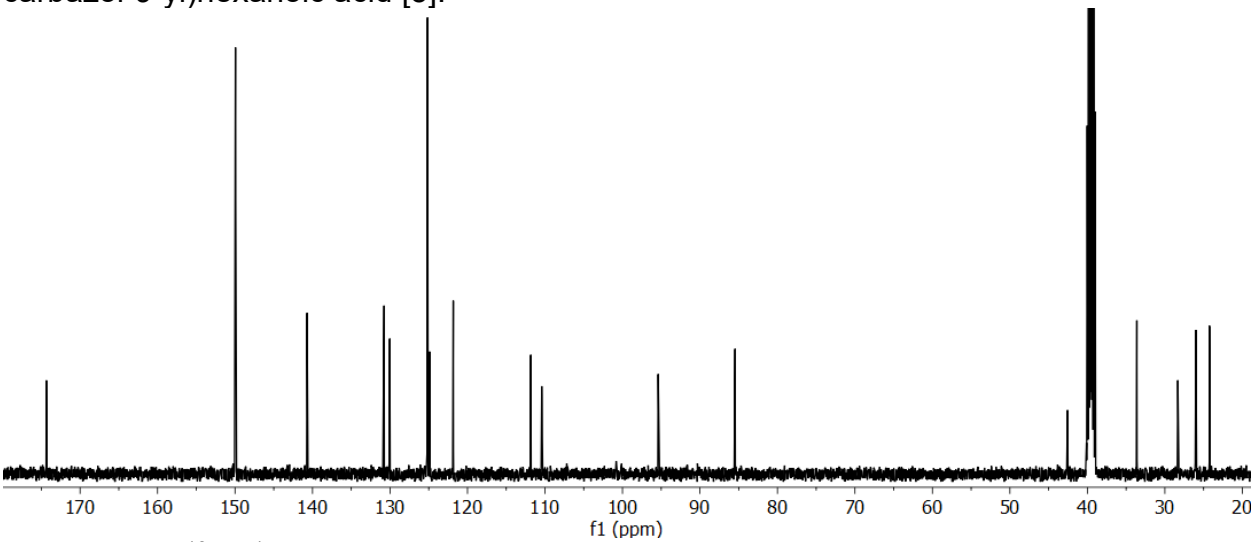

Figure S10. ^{13}C-{^{1}H} NMR (DMSO-d_6, 126 MHz, 25 °C) spectrum of 6-(3,6-bis(pyridin-4ylethynyl)-9*H*-carbazol-9-yl)hexanoic acid [5].

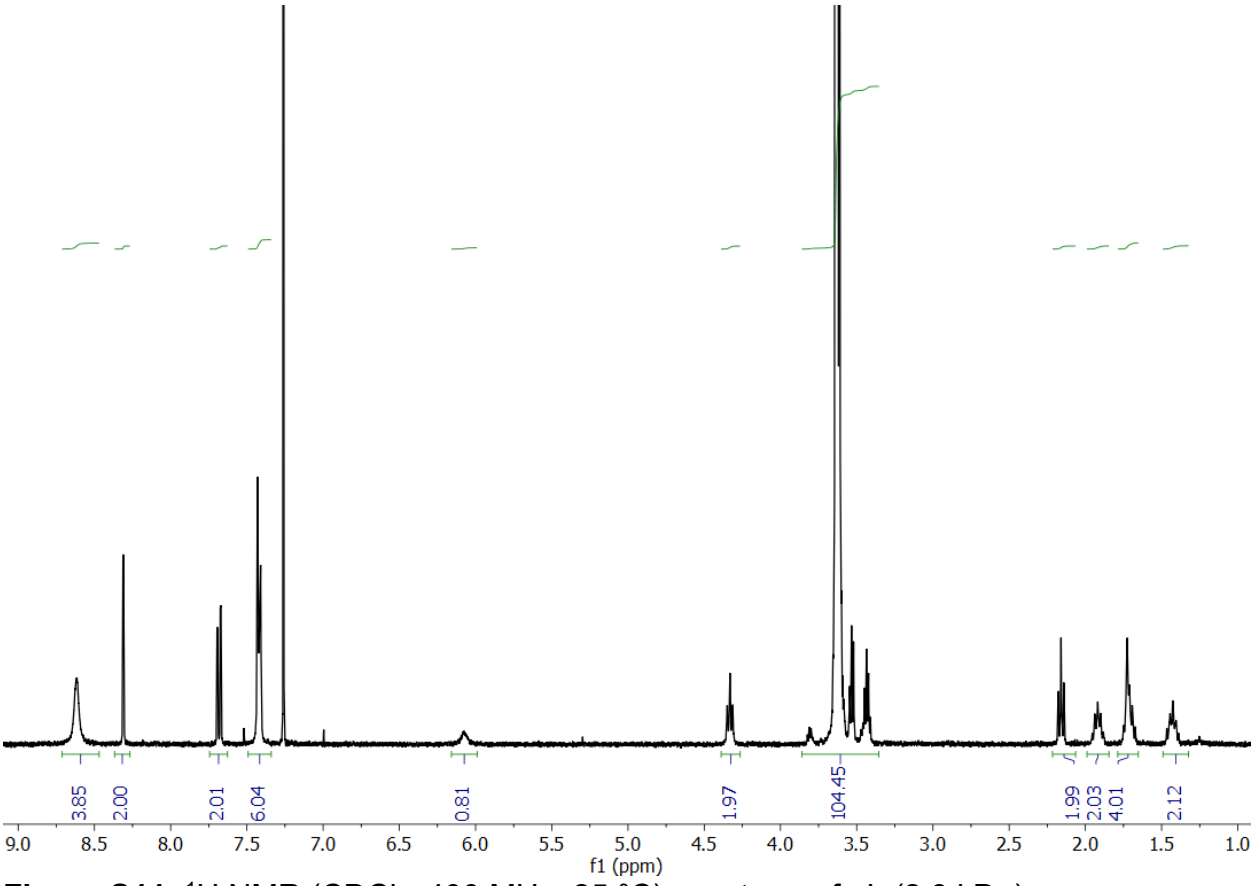

Figure S11. ^{1}H NMR ($CDCl_3$, 400 MHz, 25 °C) spectrum of pL (2.3 kDa).

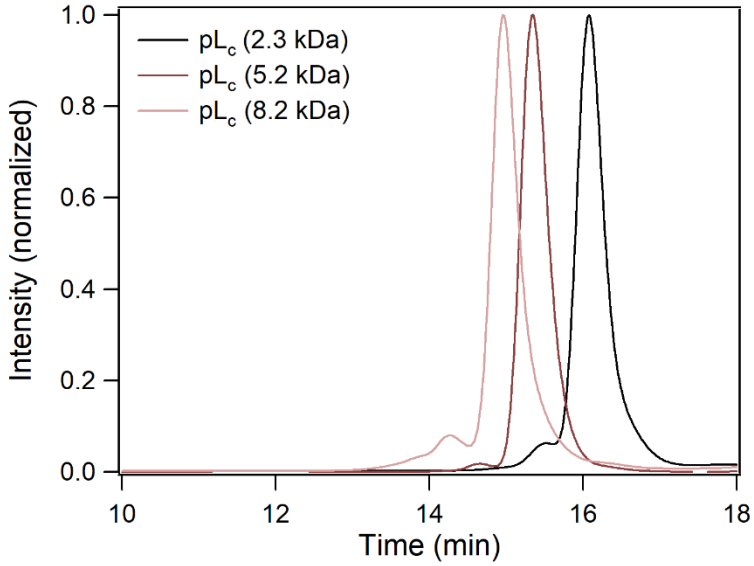

Figure S12. GPC (0.025 M LiBr in DMF, 25 °C) refractive index (RI) traces of pL (2.3, 5.2, 8.2 kDa). The high molecular weight shoulder was reduced but not entirely removed through prepGPC ($CHCl_3$).

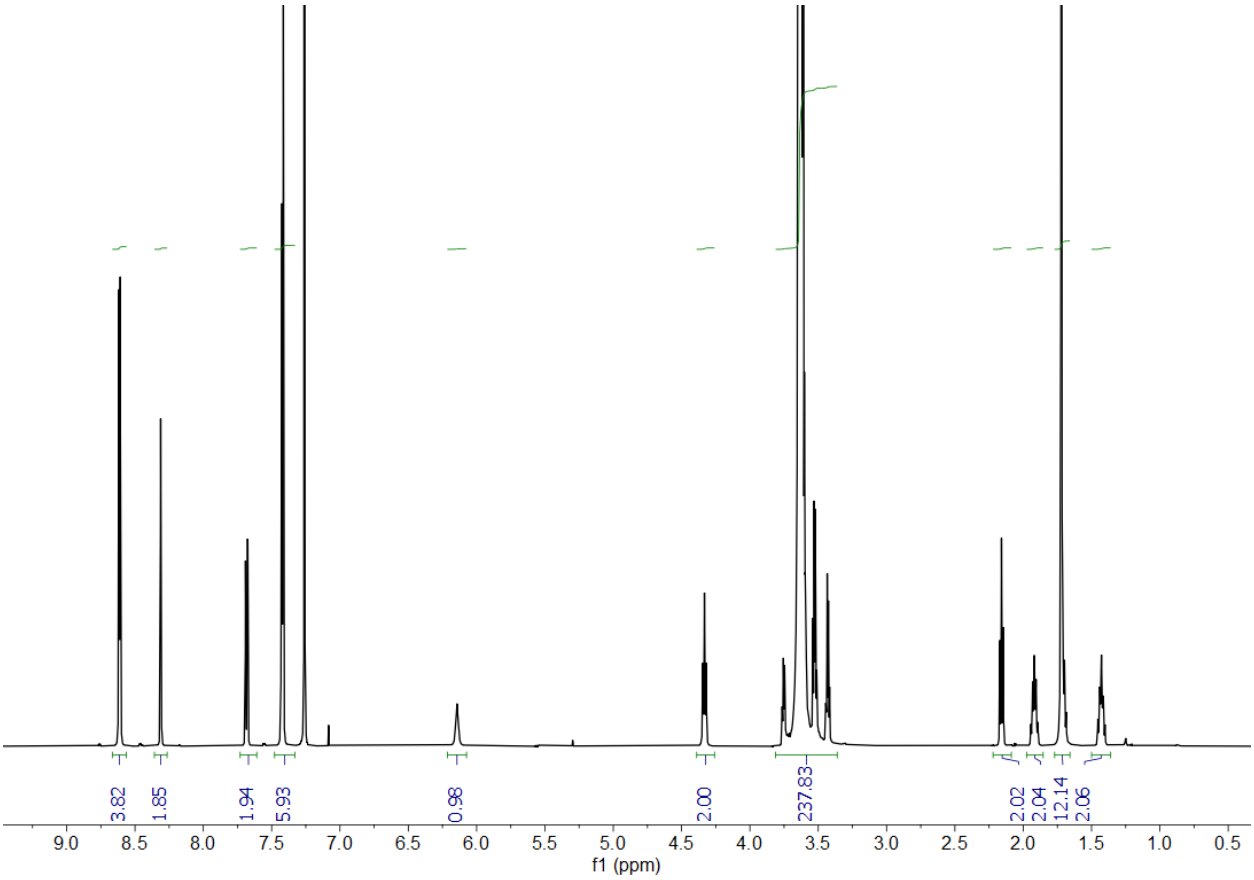

Figure S13. ^{1}H NMR ($CDCl_3$, 600 MHz, 25 °C) spectrum of pL (5.2 kDa).

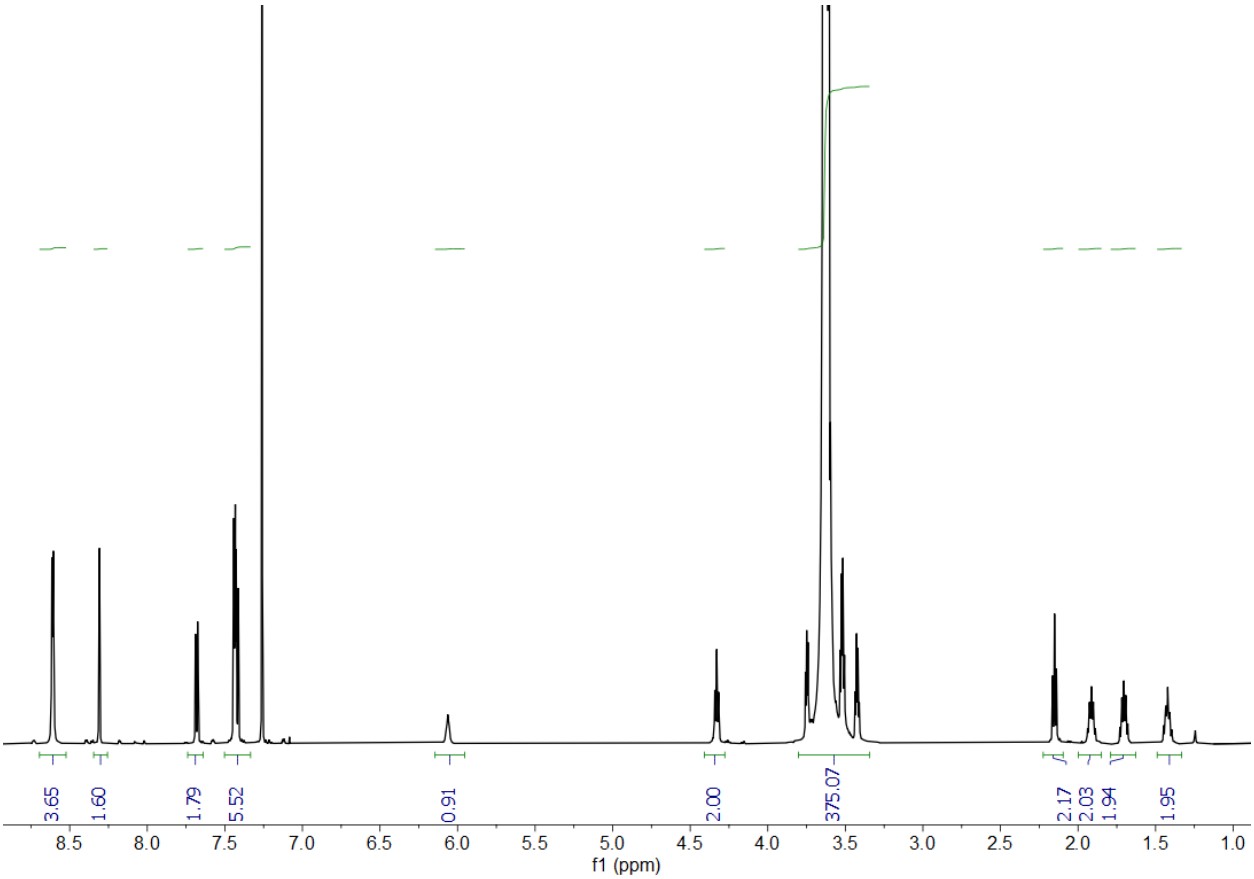

Figure S14. ^{1}H NMR ($CDCl_3$, 600 MHz, 25 °C) spectrum of pL (8.2 kDa).

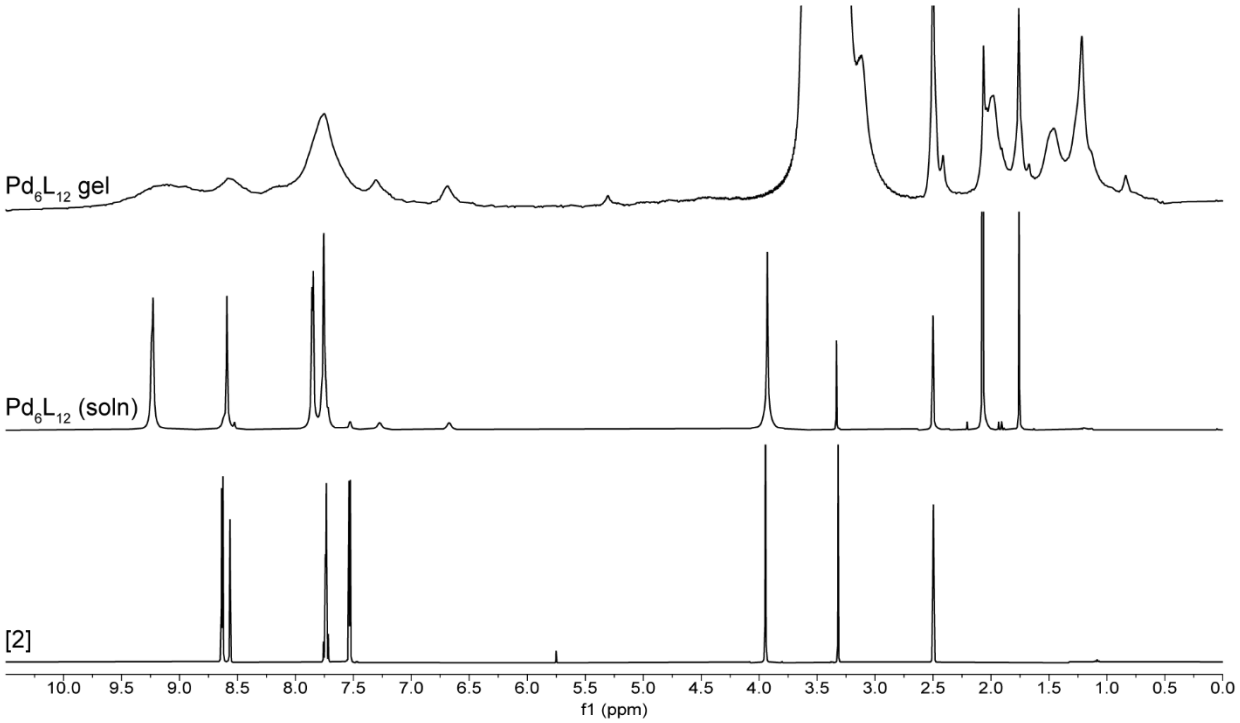

Figure S15. ^{1}H NMR (DMSO-d_6, 500 MHz, 25 °C) spectra of ligand [2] (bottom), Pd_6L_{12} cage assembly of [2] with $Pd(MeCN)_4(OTf)_2$ (middle), and ^{1}H solid-state NMR (500 MHz, 25 °C, 5 kHz spin rate) Pd_6L_{12}-based gel (top).

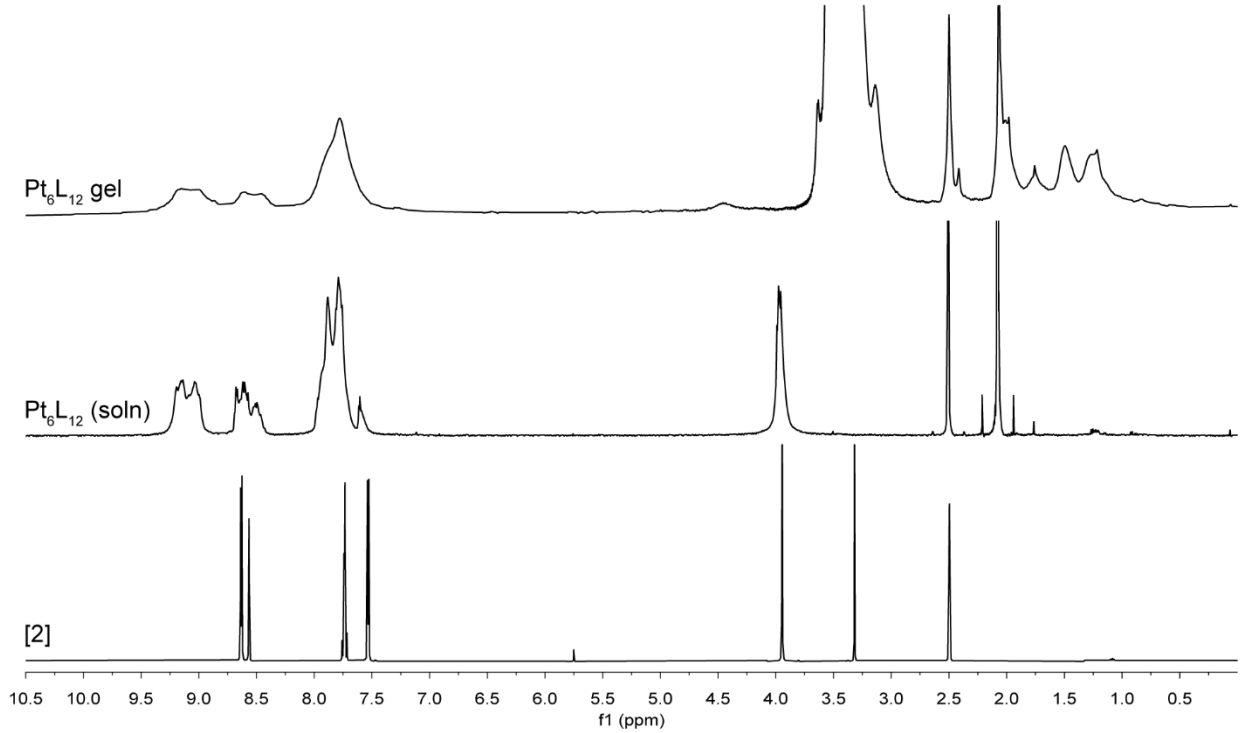

Figure S16. ^{1}H NMR (DMSO-d_6, 500 MHz, 25 °C) spectra of ligand [2] (bottom), Pt_6L_{12} cage assembly of [2] with $Pt(MeCN)_4(OTf)_2$ (middle), and ^{1}H solid-state NMR (500 MHz, 25 °C, 5 kHz spin rate) Pt_6L_{12}-based gel (top).

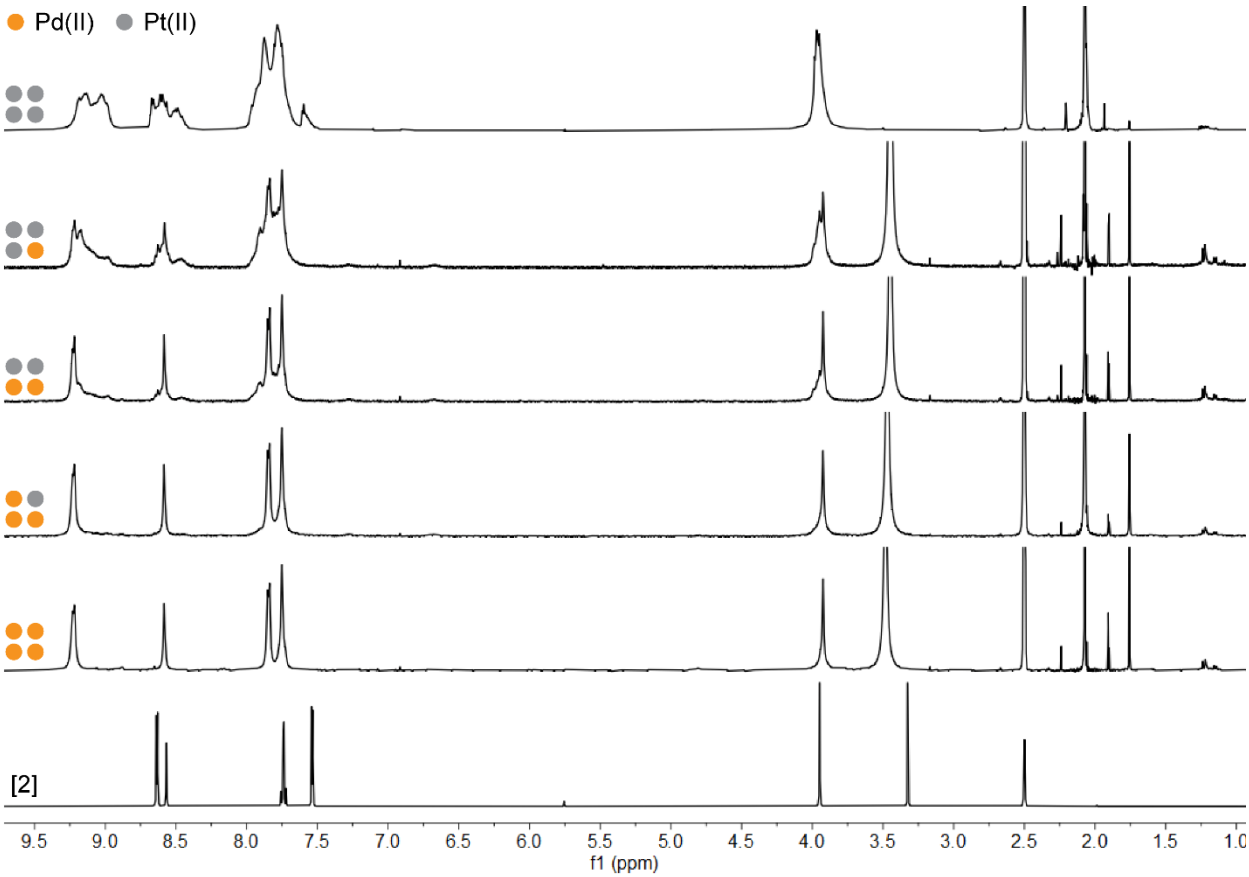

Figure S17. ^{1}H NMR (DMSO-d_6, 400 MHz, 25 °C) spectra of M_6L_{12} cage assembly of [2] with ratios of Pd(II)/Pt(II) of 100:0, 75:25, 50:50, 25:75, and 0:100 (bottom to top).

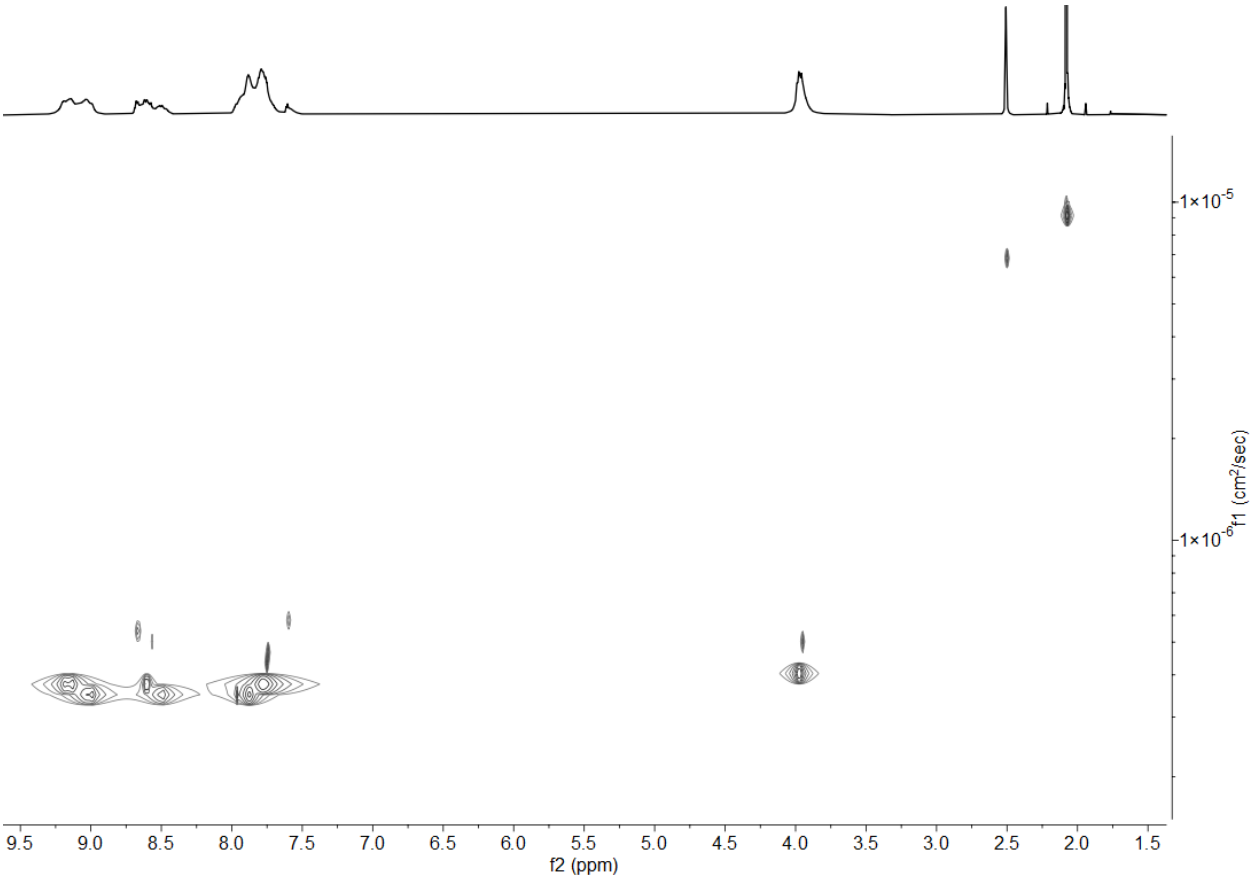

Figure S18. ^{1}H DOSY NMR (DMSO-d_6, 500 MHz, 25 °C) spectrum of Pd_6L_{12} cage assembly of ligand [2]. The aromatic peaks align at D = 6.78 x 10^{-7} cm^2/s.

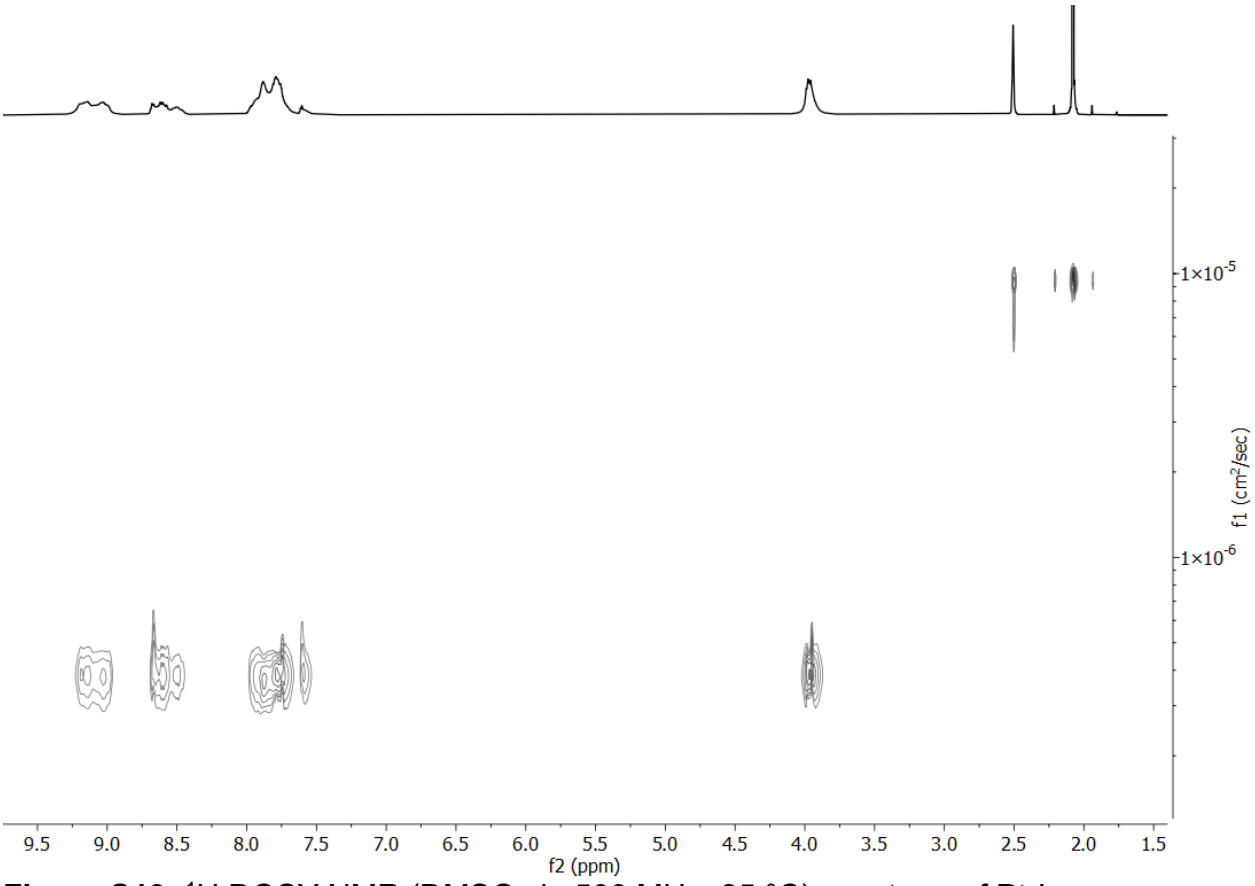

Figure S19. ^{1}H DOSY NMR (DMSO-d_6, 500 MHz, 25 °C) spectrum of Pt_6L_{12} cage assembly of ligand [2]. The aromatic peaks align at D = 3.92 x 10^{-7} cm^2/s.

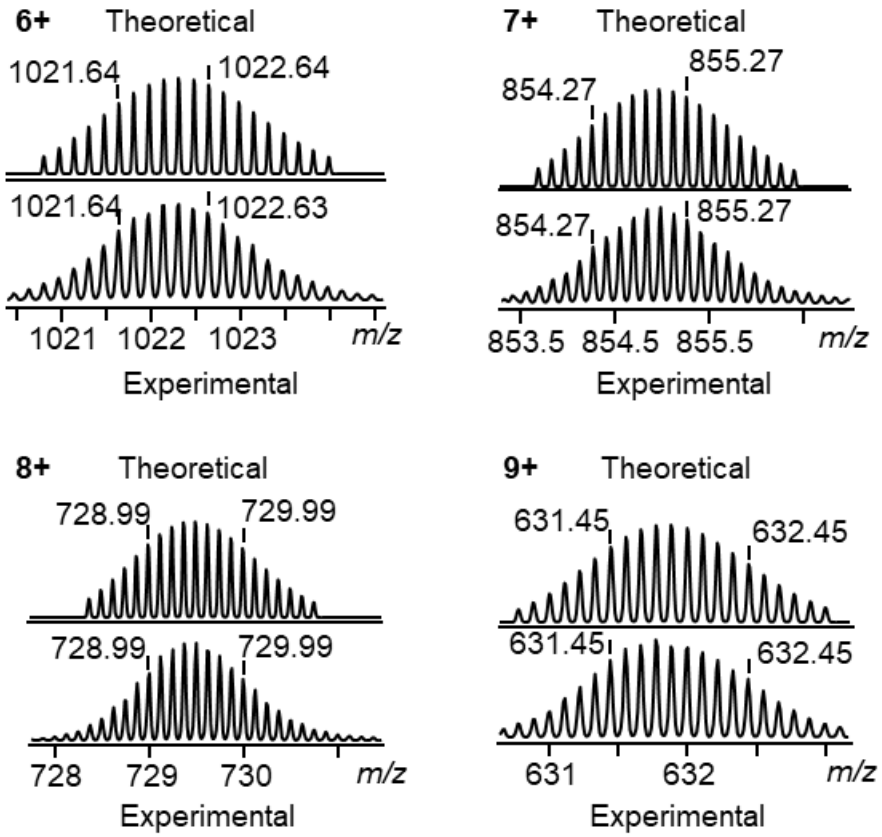

Figure S20. 100:0 Pd(II)/Pt(II) isotope patterns. Experimental (bottom) and calculated (top) isotope patterns for different charge states observed from Pd_6L_{12} (OTf^- as counterion). Experiments were performed by Dr. Heng Wang and Prof. Xiaopeng Li at University of South Florida.

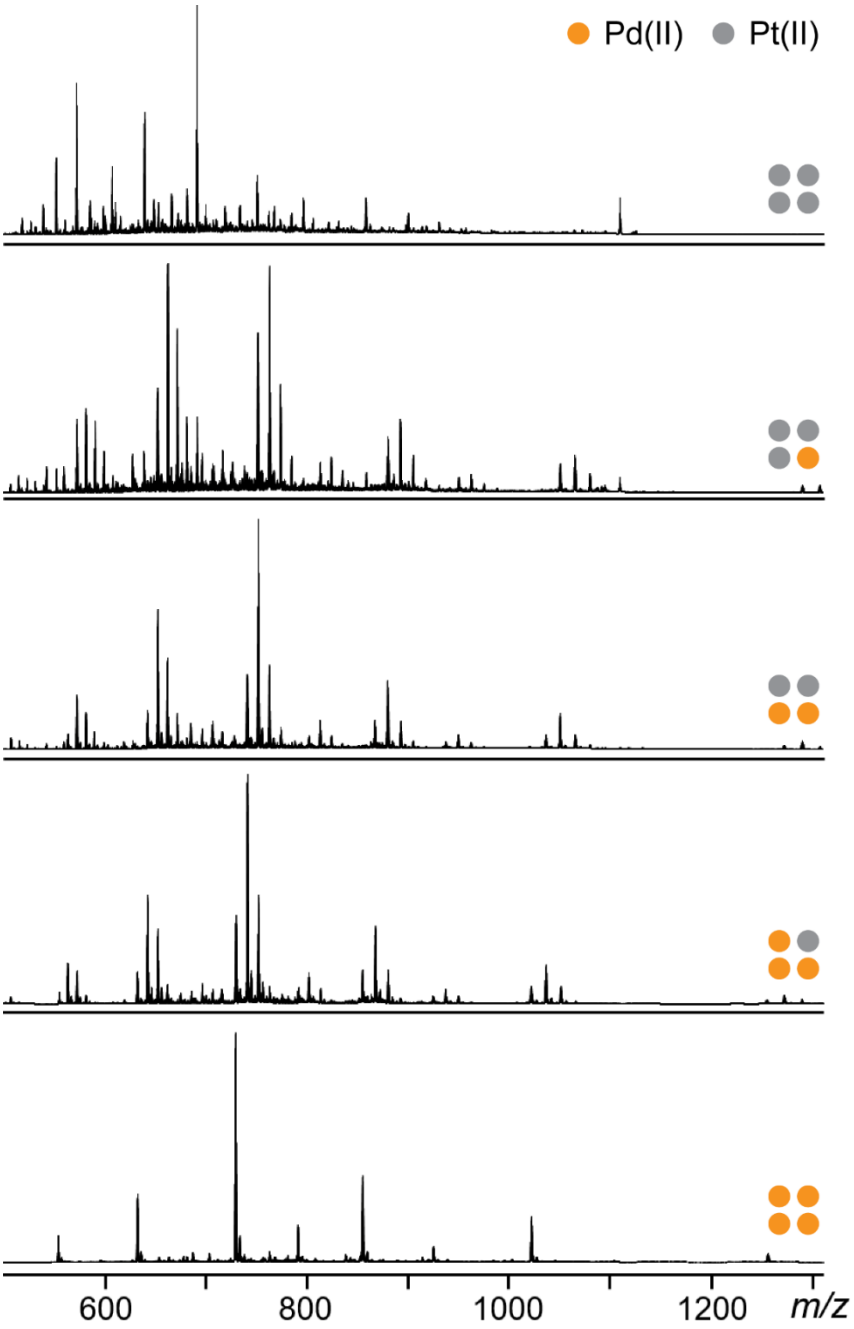

Figure S21. ESI-MS (full range) of the assemblies with ratios of Pd(II)/Pt(II) of 100:0, 75:25, 50:50, 25:75, and 0:100 (bottom to top). Experiments were performed by Dr. Heng Wang and Prof. Xiaopeng Li at University of South Florida.

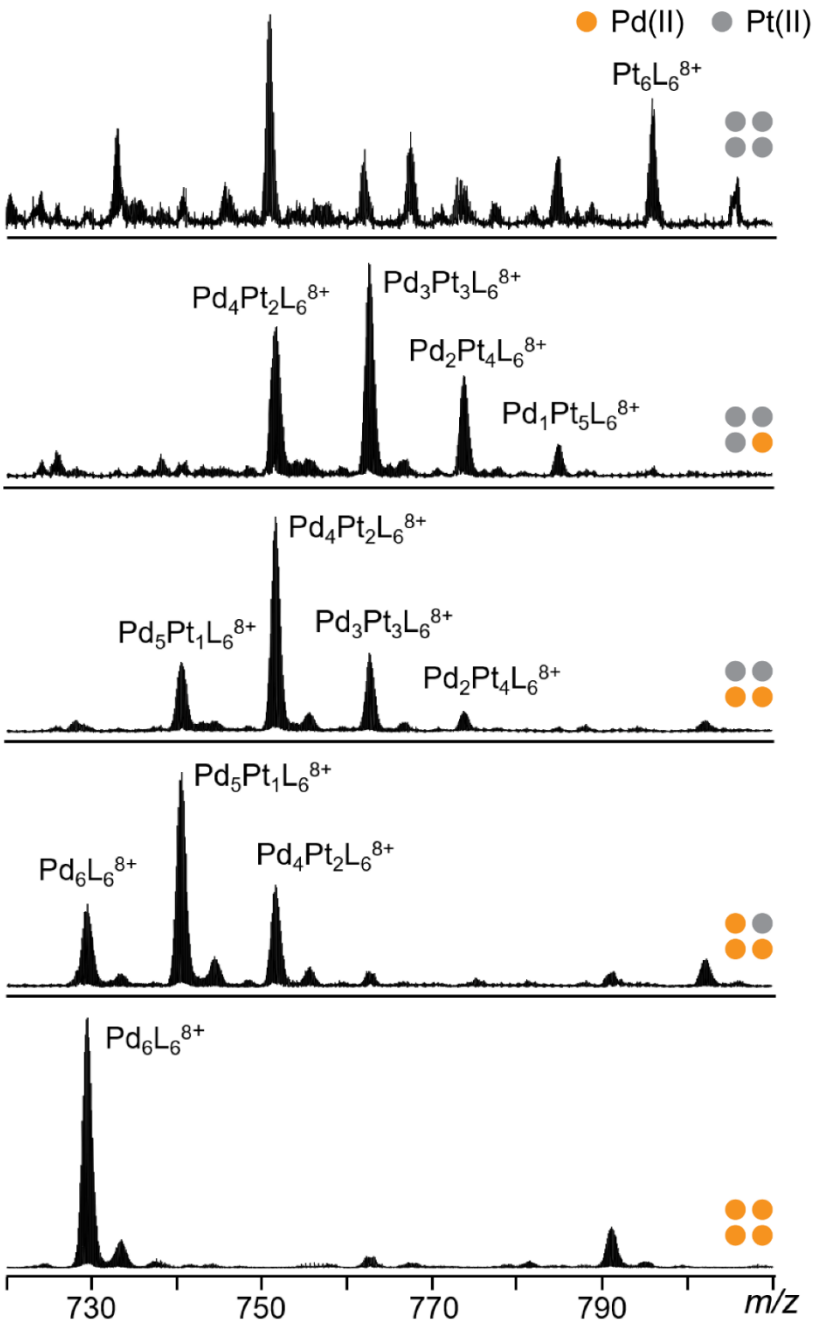

Figure S22. ESI-MS (partial) of the assemblies with ratios of Pd(II)/Pt(II) of 100:0, 75:25, 50:50, 25:75, and 0:100 (bottom to top). Experiments were performed by Dr. Heng Wang and Prof. Xiaopeng Li at University of South Florida.

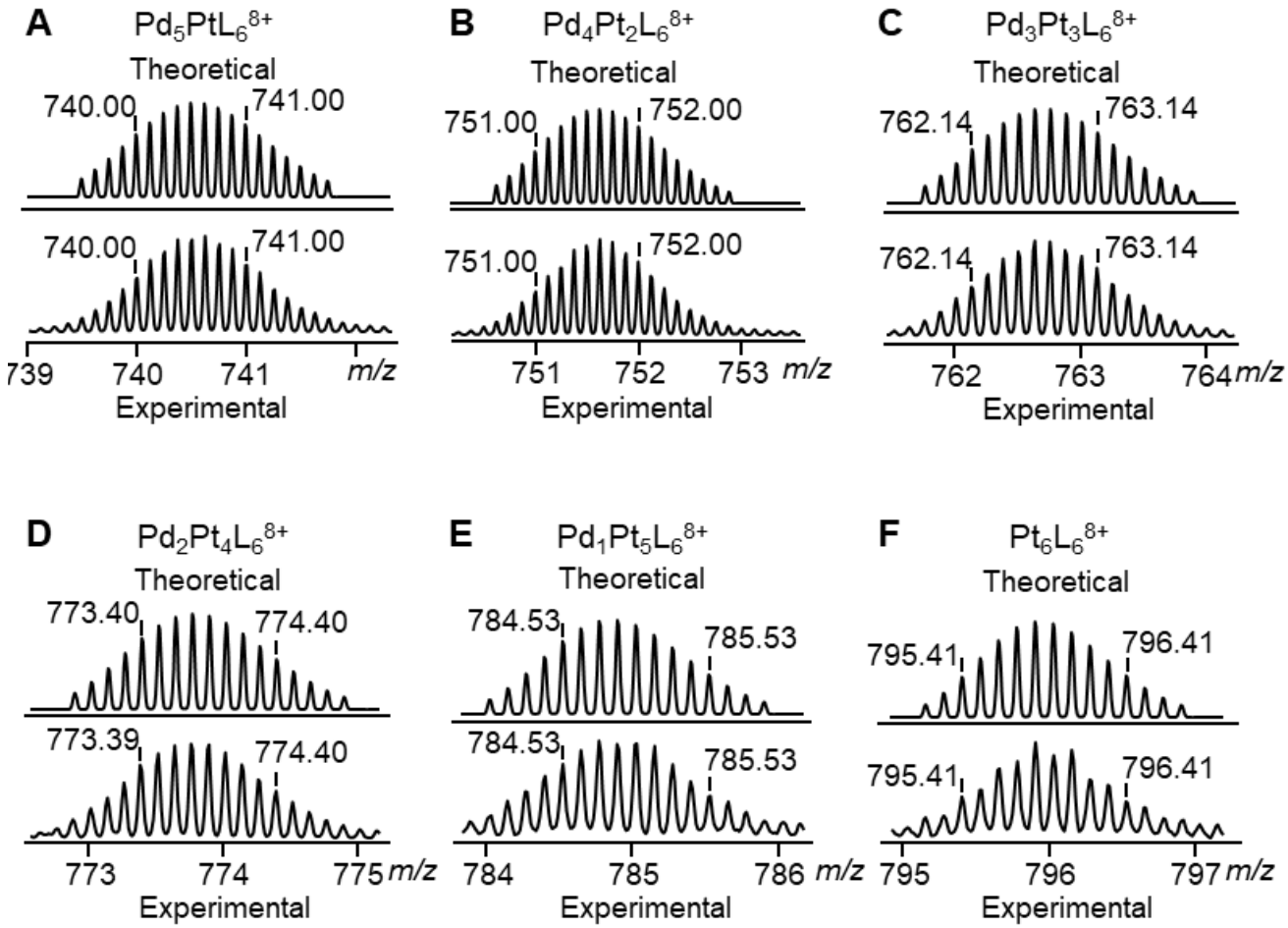

Figure S23. Experimental (bottom) and calculated (top) isotope patterns for (A) $Pd_5PtL_6^{8+}$; (B) $Pd_4Pt_2L_6^{8+}$; (C) $Pd_3Pt_3L_6^{8+}$; (D) $Pd_2Pt_4L_6^{8+}$; (E) $Pd_1Pt_5L_6^{8+}$; (F) $Pt_6L_6^{8+}$. Experiments were performed by Dr. Heng Wang and Prof. Xiaopeng Li at University of South Florida.

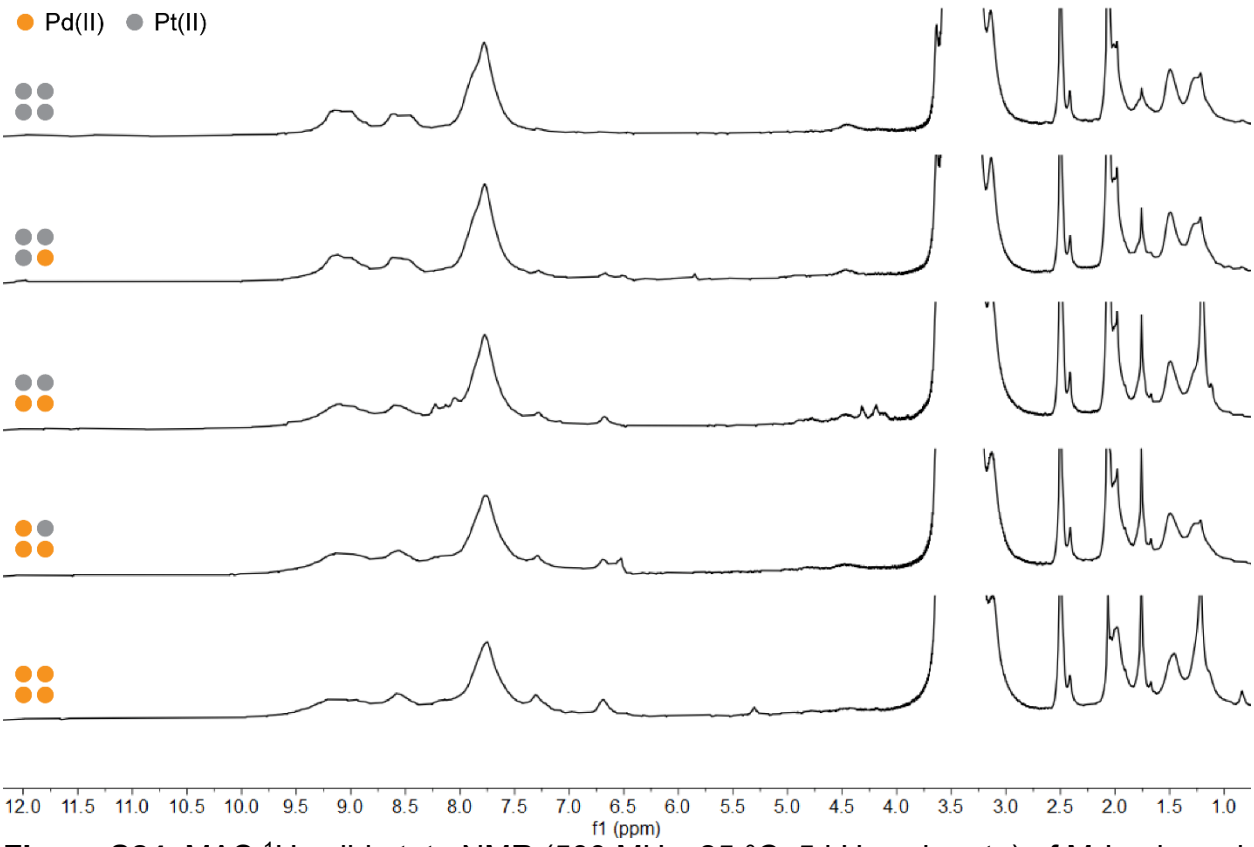

Figure S24. MAS ^{1}H solid-state NMR (500 MHz, 25 °C, 5 kHz spin rate) of M_6L_{12}-based polyMOC gels formed with Pd(II)/Pt(II) ratios of 100:0, 75:25, 50:50, 25:75, and 0:100 (bottom to top).

Table S1. Individual and averaged storage (*G′*) and loss moduli (*G″*), calculated branch functionality *f* of M_6L_{12}-based gel samples (5.2 kDa pL)

Pd(II)/Pt(II)	Sample	*G′* (Pa)*	*G″* (Pa)*	*f*
100:0	Averaged	14443.8 ± 267.7	525.0 ± 23.1	6.8
	A	14048.6	512.9	
	B	14564.9	501.3	
	C	14492.0	530.9	
	D	14766.4	518.1	
	E	14346.9	561.7	
75:25	Averaged	14772.8 ± 457.2	404.2 ± 47.1	6.9
	A	15074.0	360.1	
	B	14246.7	453.9	
	C	14997.8	398.5	
50:50	Averaged	14631.7 ± 1104.7	248.5 ± 23.5	6.9
	A	15399.9	225.1	
	B	14809.2	238.7	
	C	12934.4	230.3	
	D	13774.0	280.7	
	E	15969.7	241.0	
	F	14903.1	275.0	
25:75	Averaged	14773.2 ± 258.8	174.8 ± 16.6	6.9
	A	15023.5	174.3	
	B	14789.4	158.5	
	C	14506.7	191.6	
0:100	Averaged	12.851.8 ± 392.8	92.4 ± 3.8	6.3
	A	12843.3	96.1	
	B	13248.8	88.4	
	C	12463.3	92.8	

* Measured at 5 rad/s

Table S2. Storage moduli *G′* (*Pa*), loss moduli *G″* (*Pa*), and calculated branch functionality *f* of 100% Pd and 100% Pt M_6L_{12}-based gels (5.2 kDa pL) with 0 and 10% TFE

Pd(II)/Pt(II)	% TFE	Sample	*G′* (*Pa*)*	*G″* (*Pa*)*	*f*
100:0	0	Averaged	14368.5 ± 279.4	515.0 ± 14.9	6.8
		A	14048.6	512.9	
		B	14564.9	501.3	
		C	14492.0	530.9	
100:0	10	Averaged	14544.0 ± 734.6	411.6 ± 9.7	6.7
		A	13946.5	407.4	
		B	15364.2	422.6	
		C	14321.3	404.7	
0:100	0	Averaged	12851.8 ± 392.8	92.4 ± 3.8	6.3
		A	12843.3	96.1	
		B	13248.8	88.4	
		C	12463.3	92.8	
0:100	10	Averaged	15697.3 ± 458.0	88.2 ± 4.3	7.1
		A	16225.7	85.8286	
		B	15453.9	85.5306	
		C	15412.4	93.1787	

*Measured at 5 rad/s

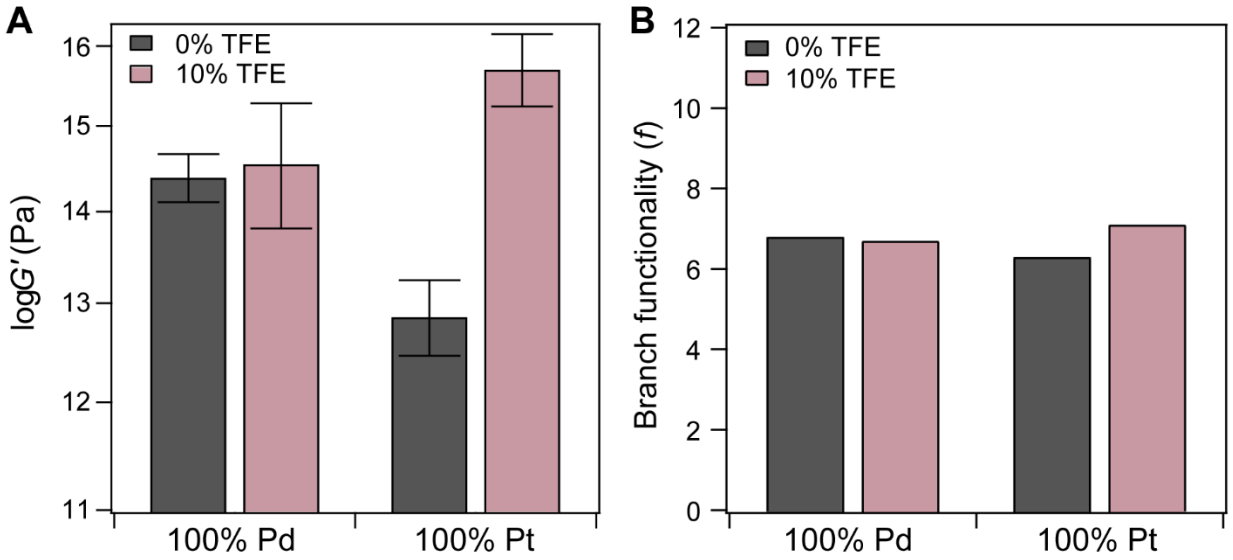

Figure S25. (A) Storage moduli *G′* (Pa) of 100% Pd and 100% Pt M_6L_{12}-based gels with TFE/DMSO of 0:100 and 10:90, recorded at 5 rad/s. (B) Experimental branch functionality *f* calculated from storage moduli.

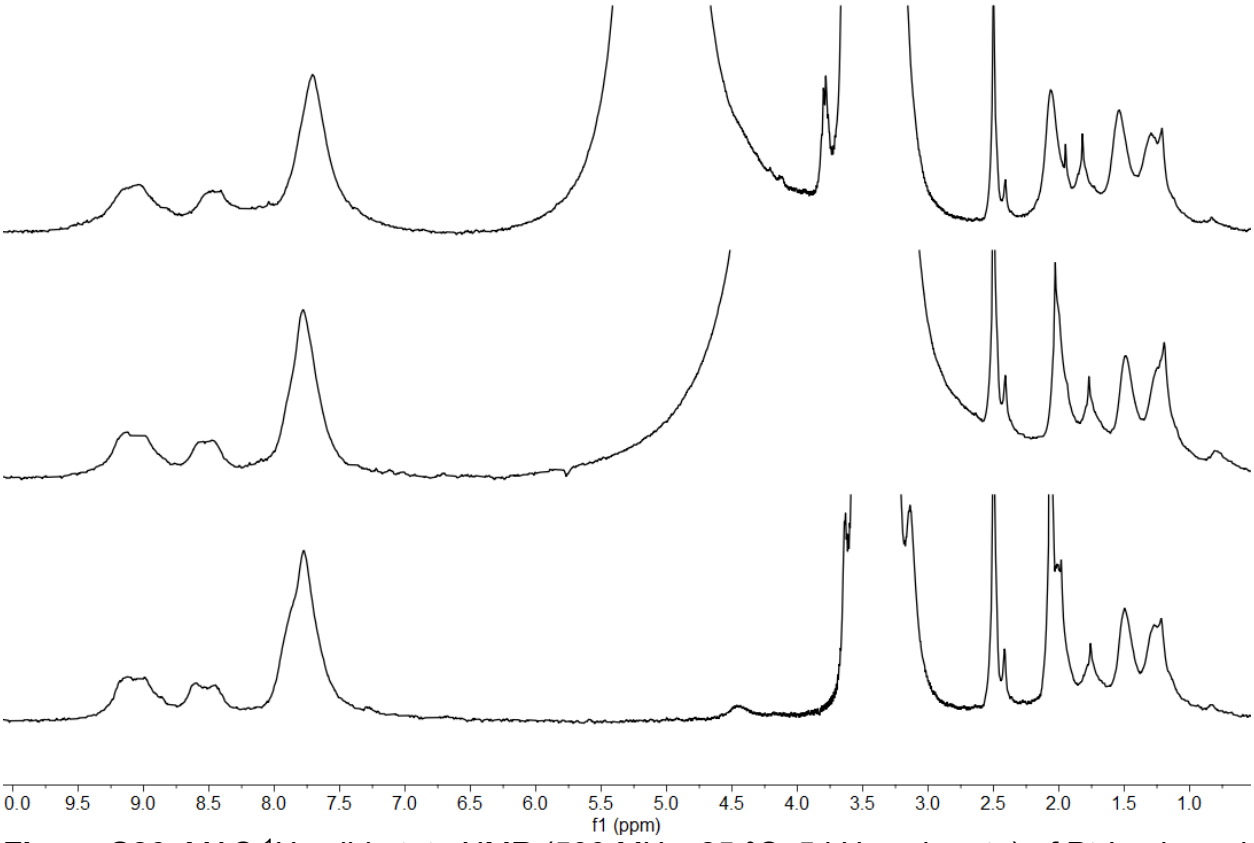

Figure S26. MAS ^{1}H solid-state NMR (500 MHz, 25 °C, 5 kHz spin rate) of Pt_6L_{12}-based polyMOC gel self-assembled with 0%, 10%, and 60% TFE-d_3 in DMSO-d_6 (bottom to top). No significant changes were seen in pyridyl coordination peaks 9.25–7.4 ppm. The broad TFE-d_3 peak moves from ~4.0 ppm to ~5.0 ppm due to interactions with DMSO-d_6.

Table S3. Plateau moduli (G_0), characteristic relaxation time (τ), and α of M_6L_{12}-based polyMOC gels (5.2 kDa pL), calculated by fitting stress relaxation studies with the Kohlrausch stretched exponential function.

Pd(II)/Pt(II)	*Sample*	G_0 (Pa)	τ (s)	α
100:0	Averaged	21380 ± 2301	39 ± 16	0.54 ± 0.04
	A	23300	50	0.55
	B	20030	31	0.50
	C	22430	22	0.56
	D	23310	22	0.46
	E	17550	61	0.55
	F	20700	50	0.55
75:25	Averaged	16487 ± 4910	175 ± 94	0.52 ± 0.25
	A	19900.0	116	0.31
	B	10860.0	283	0.81
	C	18700.0	125	0.45
50:50	Averaged	15810 ± 1619	1259 ± 968	0.39 ± 0.09
	A	18440	2660	0.27
	B	14410	738	0.46
	C	16460	1829	0.32
	D	15950	272	0.38
	E	14660	797	0.49
25:75	Averaged	13748 ± 1656	1916 ± 397	0.65 ± 0.23
	A	12110	1935	0.79
	B	15890	1741	0.83
	C	12850	2565	0.65
	D	14140	1501	0.33
0:100	Averaged	12673 ± 1112	35385 ± 16395	0.30 ± 0.10
	A	12420	55060	0.20
	B	14140	53000	0.25
	C	11450	7791	0.40
	D	12680	25690	0.36

2.6 References

1. Rubinstein, M.; Colby, R. H. *Polymer physics*; Oxford University Press: Oxford, 2003.
2. Leibler, L.; Rubinstein, M.; Colby, R. H. Dynamics of reversible networks. *Macromolecules* **1991**, *24* (16), 4701–4707.
3. Tang, S.; Wang, M.; Olsen, B. D. Anomalous self-diffusion and sticky rouse dynamics in associative protein hydrogels. *J. Am. Chem. Soc.* **2015**, *137* (11), 3946–3957.
4. Sun, J.-Y.; Zhao, X.; Illeperuma, W. R. K.; Chaudhuri, O.; Oh, K. H.; Mooney, D. J.; Vlassak, J. J.; Suo, Z. Highly stretchable and tough hydrogels. *Nature* **2012**, *489* (7414), 133–136.
5. Karino, T.; Shibayama, M.; Ito, K. Slide-ring gel: topological gel with freely movable cross-links. *Phys. B Condens. Matter* **2006**, *385-386* (1), 692–696.
6. Liu, C.; Kadono, H.; Mayumi, K.; Kato, K.; Yokoyama, H.; Ito, K. Unusual fracture behavior of slide-ring gels with movable cross-links. *ACS Macro Lett.* **2017**, *6* (12), 1409–1413.
7. Herbst, F.; Döhler, D.; Michael, P.; Binder, W. H. Self-healing polymers via supramolecular forces. *Macromol. Rapid Commun.* **2013**, *34* (3), 203–220.
8. Yount, W. C.; Loveless, D. M.; Craig, S. L. Strong means slow: dynamic contributions to the bulk mechanical properties of supramolecular networks. *Angew. Chem. Int. Ed.* **2005**, *44* (18), 2746–2748.
9. Rosales, A. M.; Anseth, K. S. The design of reversible hydrogels to capture extracellular matrix dynamics. *Nat. Rev. Mater.* **2016**, *1* (15012), 1–15.
10. Wang, H.; Heilshorn, S. C. Adaptable hydrogel networks with reversible linkages for tissue engineering. *Adv. Mater.* **2015**, *27* (25), 3717–3736.
11. Zhang, Z.; Chen, Q.; Colby, R. H. Dynamics of associative polymers. *Soft Matter* **2018**, *14* (16), 2961–2977.
12. Chaudhuri, O.; Gu, L.; Darnell, M.; Klumpers, D.; Bencherif, S. A.; Weaver, J. C.; Huebsch, N.; Mooney, D. J. Substrate stress relaxation regulates cell spreading. *Nat. Commun.* **2015**, *6* (1), 1–7.
13. Chaudhuri, O.; Gu, L.; Klumpers, D.; Darnell, M.; Bencherif, S. A.; Weaver, J. C.; Huebsch, N.; Lee, H.-P.; Lippens, E.; Duda, G. N.; Mooney, D. J. Hydrogels with tunable stress relaxation regulate stem cell fate and activity. **2016**, *15* (3), 326–334.
14. Grindy, S. C.; Learsch, R.; Mozhdehi, D.; Cheng, J.; Barrett, D. G.; Guan, Z.; Messersmith, P. B.; Holten-Andersen, N. Control of hierarchical polymer mechanics with bioinspired metal-coordination dynamics. *Nat. Mater.* **2015**, *14* (12), 1210–1216.
15. Holten-Andersen, N.; Jaishankar, A.; Harrington, M. J.; Fullenkamp, D. E.; Dimarco, G.; He, L.; Mckinley, G. H.; Messersmith, P. B.; Yee, K.; Lee, C. Metal-coordination: using one of nature's tricks to control soft material mechanics. *J. Mater. Chem. B* **2014**, *2* (17), 2467–2472.
16. Chaudhuri, O.; Gu, L.; Darnell, M.; Klumpers, D.; Bencherif, S. A.; Weaver, J. C.; Huebsch, N.; Mooney, D. J. Substrate stress relaxation regulates cell spreading. *Nat. Commun.* **2015**, *6*, 6364.
17. Brown, T. E.; Carberry, B. J.; Worrell, B. T.; Dudaryeva, O. Y.; McBride, M. K.; Bowman, C. N.; Anseth, K. S. Photopolymerized dynamic hydrogels with tunable viscoelastic properties through thioester exchange. *Biomaterials* **2018**, *178*, 496–503.
18. Dooling, L. J.; Tirrell, D. A. Engineering the dynamic properties of protein networks through sequence variation. *ACS Cent. Sci.* **2016**, *2* (11), 812–819.
19. Leininger, S.; Olenyuk, B.; Stang, P. J. Self-assembly of discrete cyclic nanostructures mediated by transition metals. *Chem. Rev.* **2000**, *100* (3), 853–907.
20. Zhukhovitskiy, A. V.; Zhong, M.; Keeler, E. G.; Michaelis, V. K.; Sun, J. E. P.; Hore, M. J. A.; Pochan, D. J.; Griffin, R. G.; Willard, A. P.; Johnson, J. A. Highly branched and loop-rich gels via formation of metal–organic cages linked by polymers. *Nat. Chem.* **2016**, *8* (1), 33–41.
21. Yiu-Yan Tam, A.; Wing-Wah Yam, V. Recent advances in metallogels. *Chem. Soc. Rev* **2013**, *42*, 1540–1567.
22. Sato, S.; Ishido, Y.; Fujita, M. Remarkable stabilization of $M_{12}L_{24}$ spherical frameworks through the cooperation of 48 Pd(II)–pyridine interactions. *J. Am. Chem. Soc.* **2009**, *131* (17), 6064–6065.
23. Yoneya, M.; Tsuzuki, S.; Yamaguchi, T.; Sato, S.; Fujita, M. Coordination-directed self-assembly of $M_{12}L_{24}$ nanocage: effects of kinetic trapping on the assembly process. *ACS Nano* **2014**, *8* (2), 1290–1296.

24. Weilandt, T.; Löw, N. L.; Schnakenburg, G.; Daniels, J.; Nieger, M.; Schalley, C. A.; Lützen, A. Exploring the palladium– and platinum–bis(pyridine) complex motif by NMR spectroscopy, X-ray crystallography, (tandem) mass spectrometry, and isothermal titration calorimetry: do substituent effects follow chemical intuition? *Chem. Eur. J.* **2012**, *18* (52), 16665–16676.
25. Weilandt, T.; Troff, R. W.; Saxell, H.; Rissanen, K.; Schalley, C. A. Metallo-supramolecular self-assembly: The case of triangle-square equilibria. *Inorg. Chem.* **2008**, *47* (17), 7588–7598.
26. Schalley, C. A.; Müller, T.; Linnartz, P.; Witt, M.; Schäfer, M.; Lützen, A. Mass spectrometric characterization and gas-phase chemistry of self-assembling supramolecular squares and triangles. *Chem. Eur. J.* **2002**, *8* (15), 3538–3551.
27. Fujita, M.; Yazaki, J.; Ogura, K. Spectroscopic observation of self-assembly of a macrocyclic tetranuclear complex composed of Pt^{2+} and 4,4′-bipyridine. *Chem. Lett.* **1991**, *20* (6), 1031–1032.
28. Wang, Y.; Gu, Y.; Keeler, E. G.; Park, J. V.; Griffin, R. G.; Johnson, J. A. Star polyMOCs with diverse structures, dynamics, and functions by three-component assembly. *Angew. Chem. Int. Ed.* **2017**, *56* (1), 188–192.
29. Fujita, D.; Takahashi, A.; Sato, S.; Fujita, M. Self-assembly of Pt(II) spherical complexes via temporary labilization of the metal–ligand association in 2,2,2-trifluoroethanol. *J. Am. Chem. Soc.* **2011**, *133* (34), 13317–13319.
30. Fujita, M.; Tominaga, M.; Hori, A.; Therrien, B. Coordination assemblies from a Pd(II)-cornered square complex. *Acc. Chem. Res.* **2005**, *38* (4), 369–378.
31. Pyykko, P.; Desclaux, J. P. Relativity and the periodic system of elements. *Acc. Chem. Res.* **1979**, *12* (8), 276–281.
32. Mckelvey, D. R. Relativistic effects on chemical properties. *J. Chem. Educ.* **1983**, *60* (2), 112; UTC, 2020; Vol. 13.
33. Yatsimirskii, K. B.; Pisarzhevskii, L. V. Relativistic effects in chemistry. *Theor. Exp. Chem.* **1995**, *31* (3), 153–168.
34. Bond, G. C. Relativistic phenomena in the chemistry of the platinum group metals. *Platin. Met. Rev.* **2000**, *44* (4), 146–155.
35. Fujita, M.; Ibukuro, F.; Ogura, K.; Yamaguchi, K. A molecular lock. *J. Am. Chem. Soc.* **1995**, *117* (14), 4175–4176.
36. Yamashita, K. I.; Kawano, M.; Fujita, M. Photoswitchable molecular lock. One-way catenation of a Pt(II)-linked coordination ring via the photolabilization of a Pt(II)-pyridine bond. *J. Am. Chem. Soc.* **2007**, *129* (7), 1850–1851.
37. Suzuki, K.; Tominaga, M.; Kawano, M.; Fujita, M. Self-assembly of an M_6L_{12} coordination cube. *Chem. Commun.* **2009**, *13*, 1638–1640.
38. Zhukhovitskiy, A. V.; Zhao, J.; Zhong, M.; Keeler, E. G.; Alt, E. A.; Teichen, P.; Griffin, R. G.; Hore, M. J. A.; Willard, A. P.; Johnson, J. A. Polymer structure dependent hierarchy in polyMOC gels. *Macromolecules* **2016**, *49* (18), 6896–6902.
39. Wang, Y.; Zhong, M.; Park, J. V.; Zhukhovitskiy, A. V.; Shi, W.; Johnson, J. A. Block co-polyMOCs by stepwise self-assembly. *J. Am. Chem. Soc.* **2016**, *138* (33), 10708–10715.
40. Shanmugaraju, S.; Vajpayee, V.; Lee, S.; Chi, K. W.; Stang, P. J.; Mukherjee, P. S. Coordination-driven self-assembly of 2D-metallamacrocycles using a new carbazole-based dipyridyl donor: synthesis, characterization, and C60 binding study. *Inorg. Chem.* **2012**, *51* (8), 4817–4823.
41. Giles, K.; Pringle, S. D.; Worthington, K. R.; Little, D.; Wildgoose, J. L.; Bateman, R. H. Applications of a travelling wave-based radio-frequency-only stacked ring ion guide. *Rapid Commun. Mass Spectrom.* **2004**, *18* (20), 2401–2414.
42. Pringle, S. D.; Giles, K.; Wildgoose, J. L.; Williams, J. P.; Slade, S. E.; Thalassinos, K.; Bateman, R. H.; Bowers, M. T.; Scrivens, J. H. An investigation of the mobility separation of some peptide and protein ions using a new hybrid quadrupole/travelling wave IMS/oa-ToF instrument. *Int. J. Mass Spectrom.* **2007**, *261* (1), 1–12.
43. Sato, S.; Iida, J.; Suzuki, K.; Kawano, M.; Ozeki, T.; Fujita, M. Fluorous nanodroplets structurally confined in an organopalladium sphere. *Science* **2006**, *313* (5791), 1273–1276.
44. Shibayama, M. Small-angle neutron scattering on polymer gels: phase behavior, inhomogeneities and deformation mechanisms. *Polym. J.* **2010**, *43* (1), 18–34.
45. Zhukhovitskiy, A. V.; Zhao, J.; Zhong, M.; Keeler, E. G.; Alt, E. A.; Teichen, P.; Griffin, R. G.; Hore, M. J. A.; Willard, A. P.; Johnson, J. A. Polymer structure dependent hierarchy in polyMOC gels. *Macromolecules* **2016**, *49* (18), 6896–6902.

46. De Gennes, P. G. *Scaling concepts in polymer physics*; Cornell University Press: Ithaca NY, 1979.
47. Devanand, K.; Selser, J. C. Asymptotic behavior and long-range interactions in aqueous solutions of poly(ethylene oxide). *Macromolecules* **1991**, *24* (22), 5943–5947.
48. Cathé, N.; Collet, A.; Viguier, M.; Berret, J.-F. O. Synthesis and linear viscoelasticity of fluorinated hydrophobically modified ethoxylated urethanes. *Macromolecules* **1998**, *31* (4), 1305–1311.
49. Palmer, R. G.; Stein, D. L.; Abrahams, E.; Anderson, P. W. Models of hierarchically constrained dynamics for glassy relaxation. *Phys. Rev. Lett.* **1984**, *53* (10), 958–961.
50. Yan, X.; Wang, F.; Zheng, B.; Huang, F. Stimuli-responsive supramolecular polymeric materials. *Chem. Soc. Rev.* **2012**, *41* (18), 6042–6065.
51. Goujon, A.; Lang, T.; Mariani, G.; Moulin, E.; Fuks, G.; Raya, J.; Buhler, E.; Giuseppone, N. bistable [*c*2] daisy chain rotaxanes as reversible muscle-like actuators in mechanically active gels. *J. Am. Chem. Soc.* **2017**, *139* (42), 14825–14828.
52. Gottlieb, H. E.; Kotlyar, V.; Nudelman, A. NMR chemical shifts of common laboratory solvents as trace impurities. *J. Org. Chem.* **1997**, *62* (21), 7512-7515.
53. Mark, J. E.; Flory, P. J. The configuration of the polyoxyethylene chain. *J. Am. Chem. Soc.* **1965**, *87* (7), 1415–1423.
54. Wendt, O. F.; Kaiser, N.-F. K.; Elding, L. I. Acetonitrile and propionitrile exchange at palladium(II) and platinum(II). *J. Chem. Soc., Dalton Trans.* **1997**, *24*, 4733–4738.

Chapter 3. Application of polyMOC gels towards water purification

3.1 Introduction

Access to safe drinking water remains a contemporary global issue, not only in developing countries but also in industrialized nations. In low- and middle-income countries with limited resources, developing cost-effective water treatment methods remains a priority to remove pathogens, particulate matter, natural chemicals, and man-made chemicals.[1] In industrialized nations, effective removal of man-made chemicals and other pollutants is a primary concern in water treatment. Just in the past ten years, United States citizens have faced several cases of contaminated water supplies, including the 2014 Flint Water Crisis caused by lead leaching from aging pipes[2] as well as the identification of novel fluorinated chemicals in North Carolina in 2015.[3] From industrial waste[4] to agricultural pesticides[5] and firefighting foam,[6] large amounts of man-made chemicals are directly released into the environment with real risks of contaminating surface waters.

Current methods of surface and waste water treatment include multiple purification steps, each targeting specific pollutant groups.[1,4] Surface water is purified through coarse and fine screening, sedimentation, several filtration methods, and disinfection. These conventional water treatments are less effective in removing emerging contaminants in water purification and treatment, such as perfluoroalkyl substances (PFAS) from public water sources[7,8] or pharmaceuticals and personal care products (PPCPs) from sewage.[9] New, adaptable materials are needed to address these emerging challenges in water purification.

Due to its modularity, the polyMOC gel platform is a strong candidate for addressing this need. Robust polyMOC gels can be reproducibly self-assembled from polymer ligand, metal salt, and free ligand (Fig. 1).[10] The ability to incorporate free ligands provides a facile method of functionalizing the polymer network without significantly changing its chemistry or material properties. This characteristic is unique to high *f* polyMOC gels, which possess high stoichiometry MOC junctions that allow the limited incorporation of free ligand without affecting the elastic modulus of the material. This capability is particularly advantageous in adapting the functional material to new targets.

Furthermore, MOCs are able to encapsulate different molecules, a unique ability enhanced by the covalent attachment of functional groups to cage ligands.[11–15] The formation of $M_{12}L_{24}$ cage-confined phases using *endo*-functionality has been studied extensively by Fujita and coworkers. Localized hydrophobic environments were established in $Pd_{12}L_{24}$ MOCs by installing internal alkyl chains, where hydrophobicity was tuned with alkyl chain length;[13] perfluoroalkyl functionalization produced a fluorous phase within cages that promoted encapsulation of perfluoroalkanes from a polar organic solution.[12] When internally decorated with oligo(ethylene oxide), these $Pd_{12}L_{24}$ cages behaved as poly(ethylene glycol) (PEG) “pseudo-nanoparticles,” which demonstrated absorption of La(III) ions through binding to ether oxygen atoms.[14] Similarly, “coronene nanodroplets” within $Pd_{12}L_{24}$ cages provided a psuedosolvent

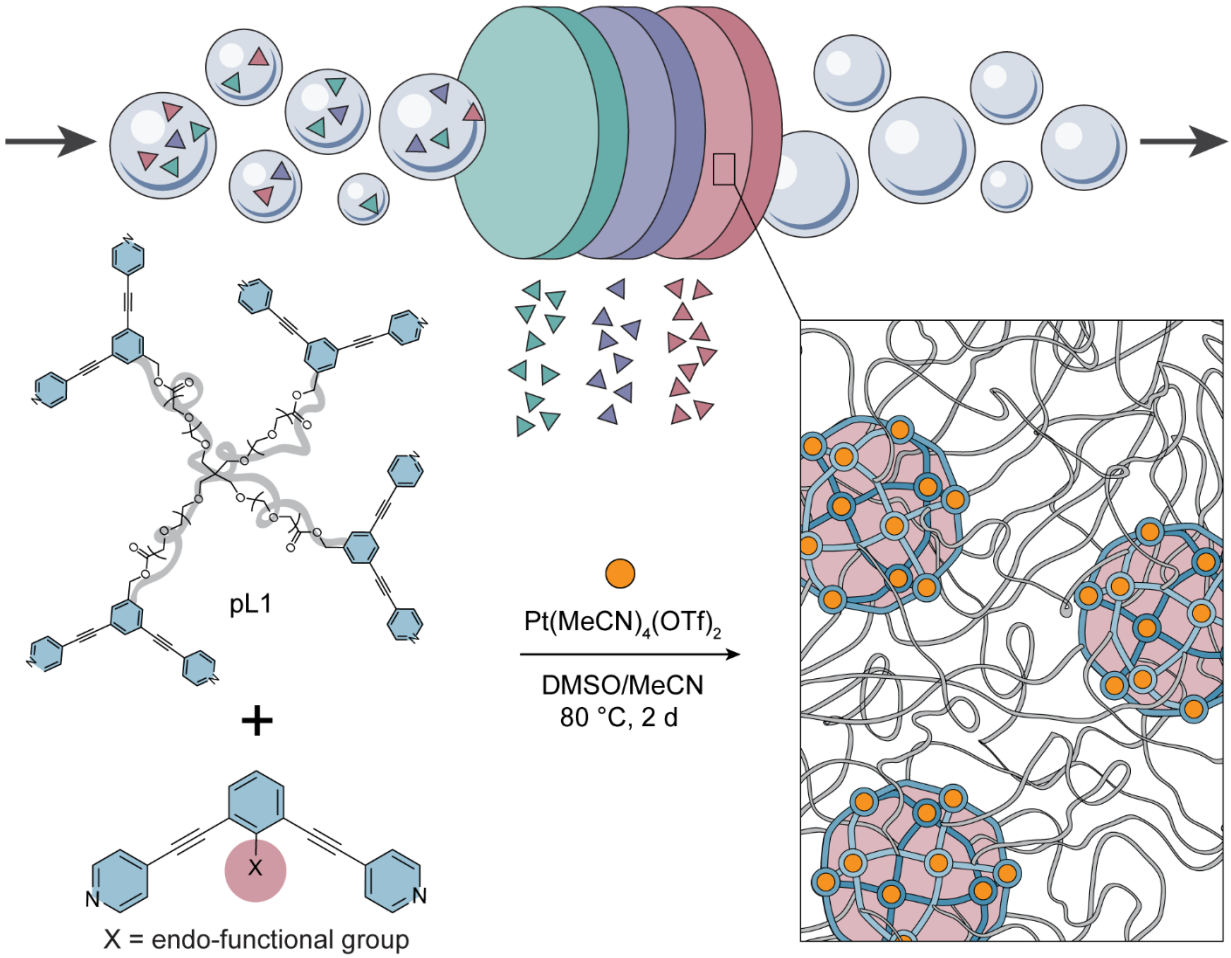

Figure 1. Modular polyMOC gel platform applied to water purification. The three-component assembly of polyMOC gels allows for facile functionalization of the material through chemical modification of free ligands without altering the polymer scaffold. Using this platform, the internal cage environment can be adapted to absorb emerging water contaminants while maintaining the polymer network topology and material processing steps. PolyMOC gels with tailored absorption might be used sequentially to remove several compound families from aqueous solutions.

phase with enhanced fullerene solubility that was attributed to the confinement of 24 pendant coronene molecules within each cage.[15] Given these examples, MOC *endo*-functionalities can likely be tuned to absorb many different pollutants with high specificity, addressing the growing need to remove novel complex compounds from water. While functionalized MOCs provide a microenvironment for the encapsulation of molecular contaminants, the polymer network in polyMOC gels provides a heterogeneous scaffold that allows the reuse of these materials. Gels could be column packed in series to sequentially remove multiple impurities and recycled following solvent washes (Fig. 1).

In this work, an $M_{12}L_{24}$-based polyMOC network was optimized for water purification and reuse. A library of ligands was designed and synthesized to target three different chemical families: aromatic, perfluorinated, and alkylated groups. PolyMOC gel purification performance was tested for aromatic compounds and perfluoroalkyl

substances (PFAS). These evaluations demonstrated some successes in the absorption of selected model compounds; however, absorption in all cases was accompanied with nonspecific binding of unfunctionalized control gels. Potential absorption mechanisms contributing to this nonspecific binding are discussed. Future work to better determine interaction mechanisms is necessary for improved design and function of polyMOC gels towards water treatment applications.

3.2 Results and discussion

3.2.1 System design and optimization

Three design elements in $M_{12}L_{24}$-based polyMOC gels were adapted to optimize material performance and recyclability in water purification applications.

(1) To maximize the volume of encapsulation, the $M_{12}L_{24}$ cage diameter was extended from 3.5 to 4.6 nm through the insertion of an acetylene spacer between phenyl and pyridyl groups (Fig. 1). This extended $M_{12}L_{24}$ cage, developed by Fujita and

Scheme 1. Library of $M_{12}L_{24}$-forming bispyridine ligands with different functional groups.

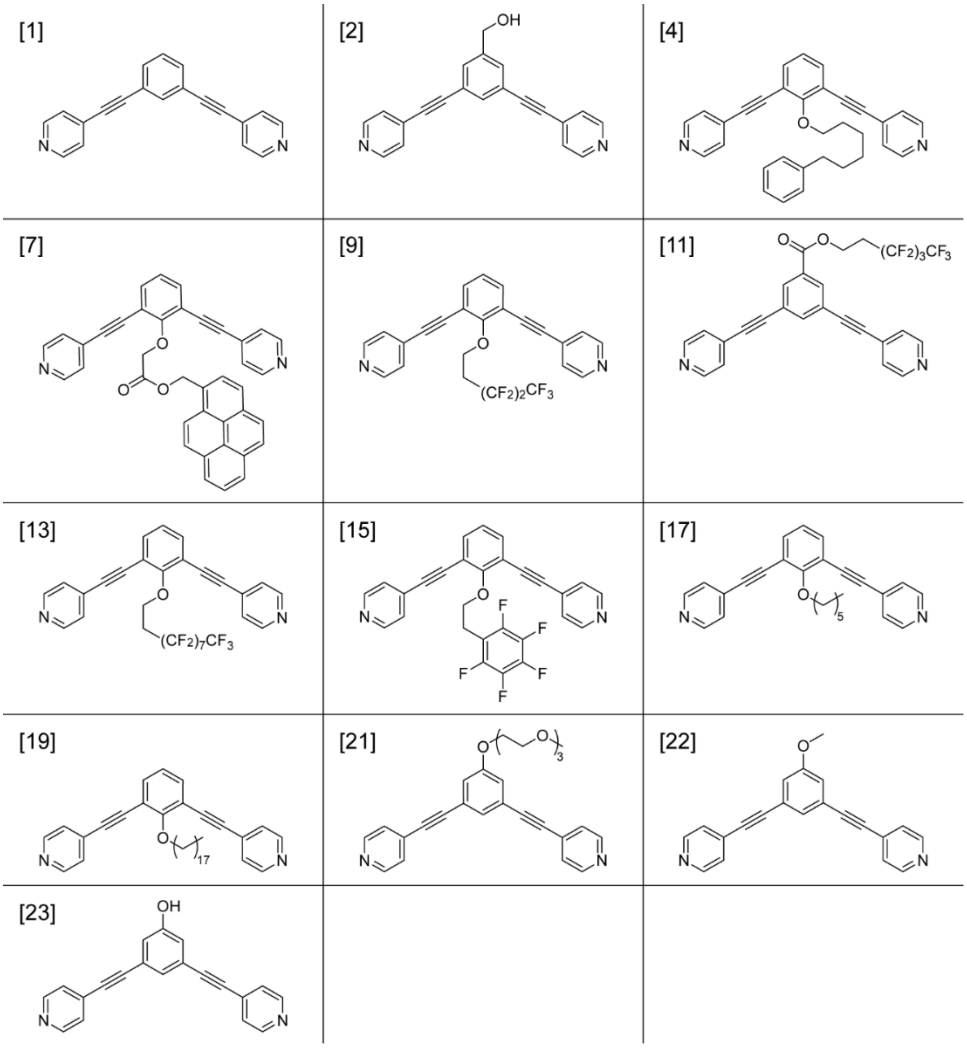

coworkers,[12–14,16] doubles the cage encapsulation volume of previously reported polyMOC gels.[10,17–19]

(2) A tetra-arm polymer structure (Fig. 1) was chosen to allow higher ratios of free ligand incorporation, which might enhance the MOC microenvironment and promote absorption. Linear polyMOCs are limited to ~12.5% free ligand incorporation without affecting mechanical properties of the network.[17] On the other hand, star polyMOC gels can attain 83% free ligand incorporation when self-assembled using a 1:5 molar ratio of polymer ligand to free ligand, which produces optimal shear elastic moduli and relaxation times in these networks.[18] PEG was selected as the water-soluble polymer.

(3) Finally, polyMOC gel durability was improved through self-assembly with Pt(II) rather than the Pd(II) salts used in previous studies on $M_{12}L_{24}$-based polyMOC systems. As discussed in Chapter 2, cages formed from kinetically inert Pt(II)–pyridine interactions produce less dynamic polyMOC networks compared to Pd(II) analogues; this difference was visually demonstrated in preliminary application studies on $Pt_{12}L_{24}$- and $Pd_{12}L_{24}$-based polyMOC gels, which showed dramatically different durability after five cycles of use (Fig. S72).

3.2.2 Building a ligand library

A ligand library was designed to target aromatics, PFAS, and alkyl pollutants through the *endo*- or *exo*-functionalization of similar chemical moieties (Scheme 1). Absorption specificity was introduced through the covalent attachment of chemical groups similar in nature to targeted pollutants. For ligands [4] and [7], π-π stacking interactions between attached functionalities and aromatic compounds should promote absorption and encapsulation within the MOC. For fluorinated ([9], [11], [13], [15]) and alkyl substituents ([17], [19]), this strategy should produce a separate phase within each MOC to allow for encapsulation through phase separation. Successful synthesis was typically accomplished through two steps: functionalization of a dibrominated phenol, followed by Sonogashira cross-coupling to attach ethynyl pyridyl groups (Scheme 2).

Scheme 2. General Mitsunobu and Sonogashira reaction route to *endo*-functionalized, $M_{12}L_{24}$-forming bispyridine ligand.

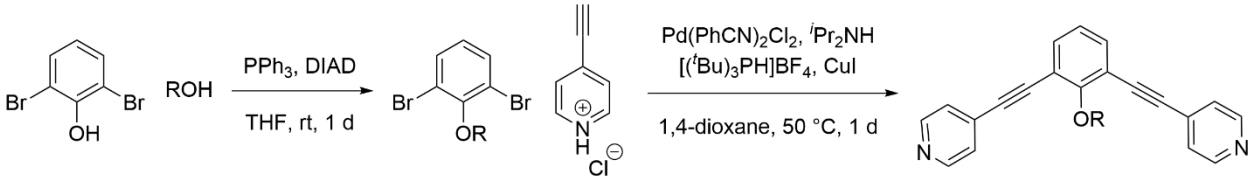

3.2.3 Absorption of aromatic compounds

PolyMOC absorption of aromatic pollutants was tested with three model compounds: bisphenol A (BPA), metolachlor, and coumarin. BPA, a known endocrine disrupter, was an obvious choice due to its toxic reproductive and developmental effects in animals and humans.[20,21] This chemical serves as a building block for polycarbonate plastics and epoxy resins used in food and beverage storage containers and container coatings,

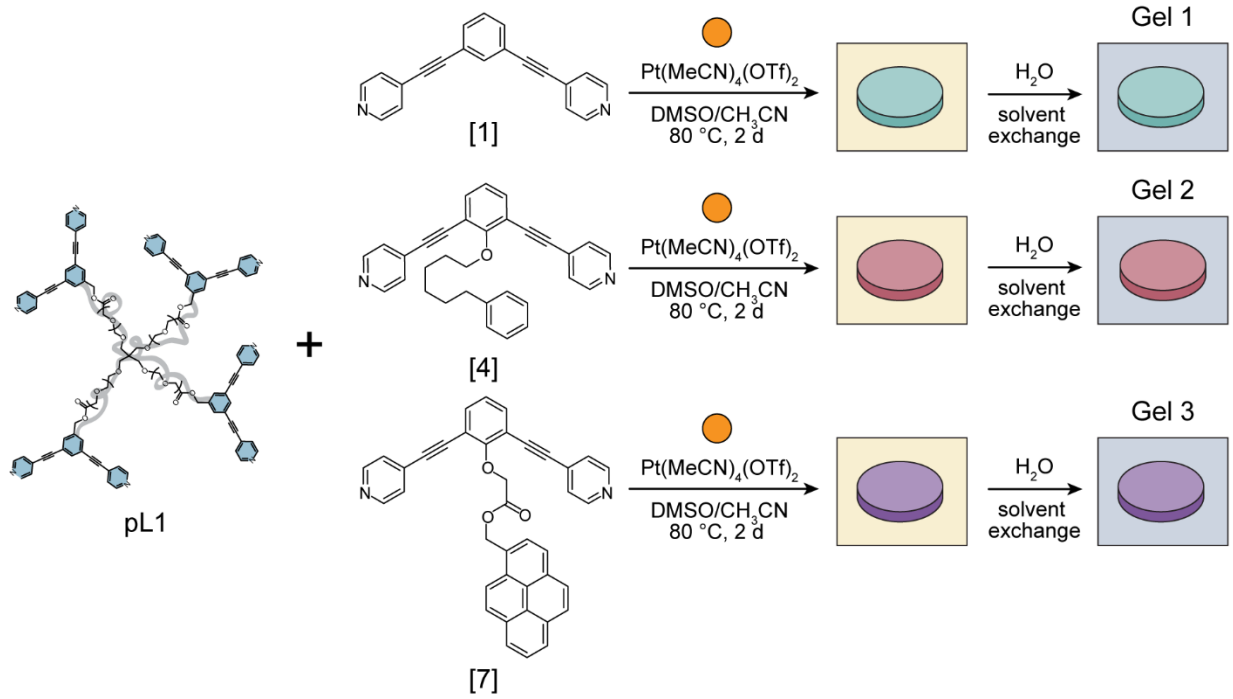

Figure 2. Assembly of ligands [1], [4], and [7] with pL1 and Pt(II) metal salt to form Gels 1–3, studied in the absorption of aromatic compounds.

leaching BPA into consumed substances. Furthermore, over one million pounds of BPA are released into the environment each year, with wastewaters from industrial disposal and paper recycling plants measuring BPA concentrations toxic to aquatic life.[22] Metolachlor is a persistent contaminant in soil due to its use as a herbicide, causing contamination of groundwater and surface water.[23,24] The EPA has classified this chemical as a potential human carcinogen. Coumarin, which has demonstrated no health risks to humans,[25] was selected for its ultraviolet (UV) absorption properties as well as its water solubility. This chemical occurs naturally in plants and spices and is frequently used as a flavorant due to its pleasant odor; however, coumarin is banned as a food additive by many countries due to hepatotoxic effects demonstrated in rats.[26]

For polyMOC gel assembly, one equivalent of star polymer ligand (pL1) was combined with five equivalents of free ligand and 1.4 equivalents of $Pt(MeCN)_4(OTf)_2$ in DMSO and MeCN. As a control, Gel 1 was formed with [1], free ligand possessing no *endo*- or *exo*-functionalities (Fig. 2). Gels 2 and 3 were formed from [4] and [7] with phenyl and pyrene *endo*-functional groups, respectively. Gels were annealed at 80 °C to allow full assembly of Pt(II)-based cages, after which they were washed with refluxing DCM using a Soxhlet extractor. Solvent exchange was performed by transferring gels to soak in acetone twice, followed by two soaks in deionized (DI) water (see Experimental). For absorption studies, gels were placed in 10 mL of 0.1 mM solutions of BPA, metolachlor, and coumarin for 24 h, as initial studies demonstrated incomplete absorption at shorter experimental times (Fig. S73). Changes in ultraviolet-visible (UV-Vis) spectra were used to characterize absorption.

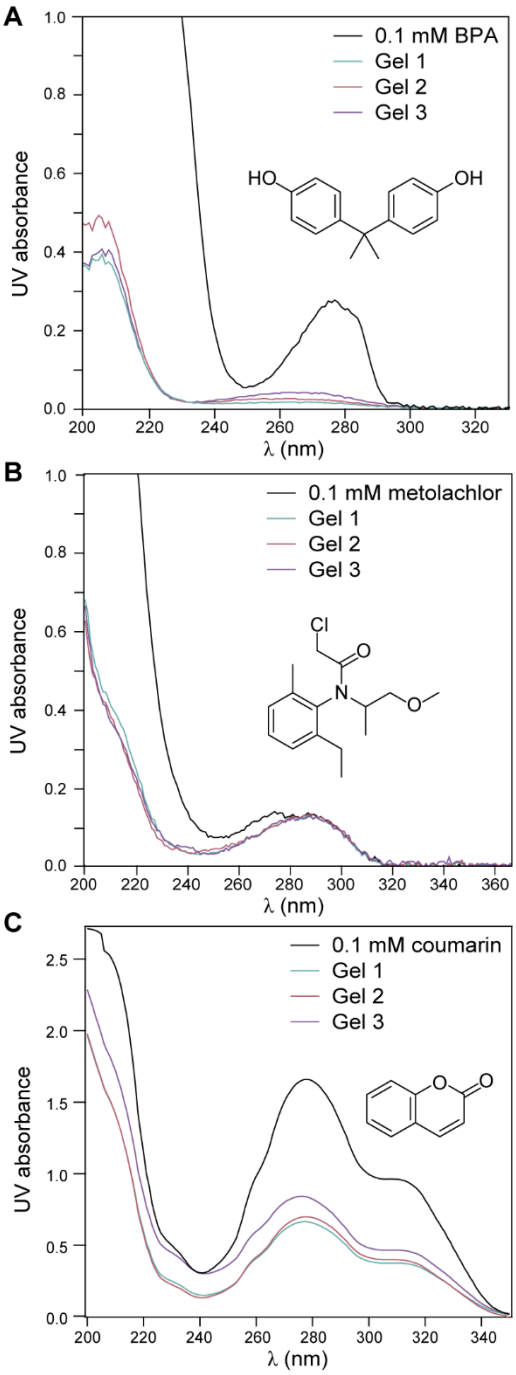

Figure 3. UV-Vis spectra of 0.1 mM (A) BPA, (B) metolachlor, and (C) coumarin solutions before and after 24 h absorption studies using Gels 1–3.

The absorption performance of polyMOC gels varied across model compounds (Fig. 3). BPA and coumarin purification was observed for all three gels, including control Gel 1. Nearly complete absorption of BPA was observed across all gels, while coumarin absorption ranged from 50–60%. While all three gels demonstrated absorption of BPA and coumarin, little change was seen in the concentration of metolachlor.

The nonspecific absorption of BPA and coumarin by control Gel 1 was attributed to two possible explanations. (1) MOC-forming ligands are also aromatic. The encapsulation of absorbates anticipated through π-π interactions between targeted and functionalized aromatic compounds might also occur through targeted compounds and the cages themselves. (2) Even unfunctionalized, the hydrophobic interior of aromatic cages might produce a separate microphase encouraging encapsulation of nonpolar contaminants. Gels became extremely brittle after exchange from organic to aqueous solvents. However, experimental absorption performance did not match trends in solubility (coumarin >> metolachlor > BPA), which disagrees with the hypothesis that greater compound insolubility might encourage encapsulation. As a result, no trend in performance could be determined based off these data.

The absorption of coumarin was repeated for quantitative comparisons of purification performance between gels, which was calculated through the Beer–Lambert Law. The best performance was seen in control Gel 1, which absorbed 60% of coumarin in solution. Gel 2 absorbed 57%, and Gel 3 absorbed 49% coumarin (Table S1). From these results, purification performance appears to decrease with increasing *endo*-functionality; however, additional replicate studies with coumarin and other absorbates are necessary to make any conclusions.

3.2.5 Absorption of per- and polyfluoroalkyl substances (PFAS)

PFAS are a family of highly fluorinated aliphatic compounds with widespread industrial applications, particularly in nonstick and water repellant coatings.[27] The largest environmental emissions of PFAS result from their use in firefighting foams and as industrial polymerization aids.[28] These chemicals tend to accumulate in the environment and in biological systems due to the slow degradation of their strong carbon–fluorine bonds. Human exposure to PFAS has been linked to immunotoxicity, high cholesterol, and other adverse health effects; this exposure occurs through common consumer products using PFAS, seafood, and contaminated drinking water.[29] Due to the detrimental health effects of low concentrations of PFAS exposure,[30] the lifetime health advisory level of PFOA and PFAS assigned by the US Environmental Protection Agency is 0.07 μg/L in drinking water.[31] While steps have been taken to reduce the industrial manufacture and use of PFAS, PFAS contamination continues to be a problem in large public water supplies.[7] Granulated activated carbon (GAC) is currently the best solution to remove PFAS at water treatment plants, with limitations: the efficacy of GAC decreases with decreasing PFAS chain length, and GAC must be replaced or regenerated frequently to ensure highest levels of PFAS removal.[1] While novel materials have demonstrated successes in PFAS purification, these materials are especially designed for the absorption of organofluorines and not broadly applicable to the purification of other compounds.[32,33]

PFAS purification was tested with Gels 1, 4, and 5, which were self-assembled using [1], [9], and [11]. PFOA was selected as an easily accessible model compound for absorption studies; this chemical was commonly used as an industrial surfactant in fluoropolymerization before it was phased out due to health concerns, but it remains a problematic pollutant in water treatment and purification.[34] Gels were placed in 10 mL of 160 μg/L PFOA solution, and aliquots were removed each hour and analyzed with liquid chromatography-mass spectrometry (LC-MS) in single ion monitoring (SIM) mode (see Experimental). Concentrations of PFOA were determined through a calibration curve. For comparison purposes, calculated concentrations were normalized by aliquots taken at t = 0 h, and reported values are given as the percentage of PFOA absorbed from solution.

Nearly complete PFOA absorption was observed for all three gels within three hours of the six hour study (Fig. 5A, C). Gel 1 demonstrated successful water purification of PFOA despite lack of functionalization, and no difference in absorption was seen between the *endo*- and *exo*-functionalized cages of Gels 4 and 5. We hypothesized that this nonspecific binding might be the result of ionic interactions between PFOA and MOC junctions, which are self-assembled from metal cations and possess a net positive charge. As the reported pKa of PFOA is 3.8, the majority of molecules in aqueous solution are deprotonated and therefore negatively charged at neutral pH.[35] Furthermore, a growing number of materials successfully developed for PFAS removal have relied on a combination of fluorous interactions and ionic exchange.[32,33,36–39] For example, Dichtel and coworkers developed and refined β-cyclodextrin polymer networks with fluorinated and aminated aryl crosslinks to adsorb PFAS from water,[32,39] while an

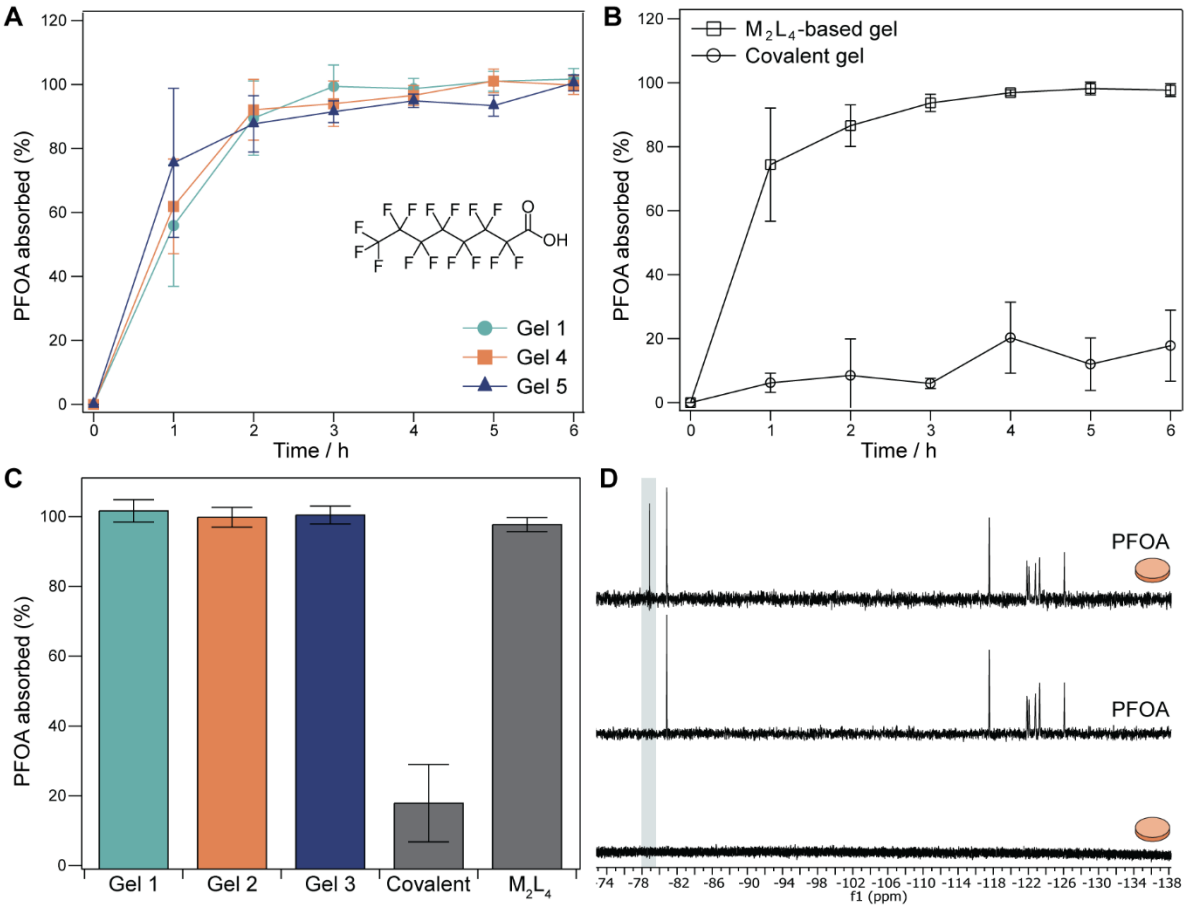

Figure 5. PFOA absorption studies with (A) Gels 1, 4, 5 and (B) M_2L_4-based polyMOC gels and covalently crosslinked gels, studied as controls. Gels were placed in PFOA solution with a starting concentration of 160 µg/L. Aliquot concentrations taken each hour were normalized to initial concentrations measured at t = 0. (C) Comparison of total % PFOA absorption at 6 h across all gels. (D) ^{19}F NMR (471 MHz, D_2O, 25 °C) spectra of Gel 2 (bottom), PFOA (middle), and Gel 2 + PFOA (top). The appearance of OTf^- fluorine peak at −78.9 ppm is highlighted.

ionic fluorogel designed by Leibfarth and coworkers demonstrated adsorption of PFAS through synergistic mechanisms of fluorous interaction and ion exchange.[33]

To investigate the mechanism of absorption, PFOA purification studies were performed on two control gels with similar network topologies. An M_2L_4-based star polyMOC network provided a control gel with cationic but smaller cage junctions (Scheme S18, synthesized by David J. Lundberg at MIT), while a covalently linked A_2 + B_4 PEG network was used to isolate any PEG contributions toward PFOA absorption (Scheme S19, synthesized by Dr. Nathan J. Oldenhuis at MIT). As seen in Fig. 5B, M_2L_4-based gels demonstrated near complete PFOA absorption within three hours, while covalent PEG networks absorbed limited amounts of PFOA. These data indicate that PFOA absorption is largely dependent on the presence of MOCs but independent of cage volume, which was originally thought to be a vital component of compound encapsulation.

More substantial evidence supporting electrostatic absorption was provided by ^{19}F solution-state NMR spectra of Gel 2 in D_2O, taken before and after the addition of PFOA (Fig. 5D). While no fluorine species were observed for the solid gel placed in D_2O, the addition of PFOA induced the appearance of an unexpected peak at −78.9 ppm. Based off its chemical shift, this peak was assigned to the triflate counteranion (OTf^-), which was introduced to the system as part of the $Pt(MeCN)_4(OTf)_2$ complex used for gel assembly. The appearance of triflate in the ^{19}F NMR spectrum indicates that the counteranion is initially tightly associated with the gel and only dissociates into solution upon anion exchange with PFOA.

These mechanistic studies strongly suggest that electrostatic interactions between PFOA and cage junctions play a large role in the absorption of PFOA by polyMOC materials. Quantitative ^1H and ^{19}F NMR studies to determine relative contributions of electrostatic and fluorous mechanisms of PFOA absorption were conducted by measuring changes in peak integration of PFOA and triflate after absorption (see Experimental, Fig. S74). Unfortunately, these experiments were ultimately inconclusive, most likely due to gel saturation artifacts caused by the concentration of absorbate necessary to meet detection limits.

3.3 Conclusions and future work

PolyMOC gels are a modular material system that can be easily adapted towards different applications. High stoichiometry cages used as crosslinks allow the three-component self-assembly of these gels from polymer ligand, metal salt, and free ligand. The ability to chemically modify free ligands facilitates the functionalization of polyMOC gels without altering overall network topology, which is dictated by the cage architecture as well as the polymer ligand.

In this work, we study the application of polyMOC gels towards water purification. Because discrete phases and microenvironments can be formed within MOCs through *endo*-functionalization,[12,14,15,40] we imagined a heterogeneous polyMOC gel comprising water soluble polymer and functionalized cage junctions might provide a synthetically accessible method to purify multiple families of small molecule pollutants. To this end, the polyMOC system design was optimized for this application: extended cages were chosen to enlarge encapsulation volume, Pd(II)-based cages were replaced with Pt(II) counterparts to allow gel recycling, and a star polymer ligand was adapted to accommodate a greater fraction of functionalized free ligand. A ligand library was built to target aromatic and alkyl compounds as well as PFAS. Absorption specificity was programmed through the attachment of functional groups that would form appropriate microphase environments within cages.

The purification performance of polyMOC gels was evaluated for aromatic compounds and PFAS. In both studies, nonspecific absorption of model compounds was observed. Different mechanisms were attributed to the unexpected absorption demonstrated by control gels: aromatic pollutants might be interacting with MOC ligand aromaticity, while absorption of PFOA is most likely the result of electrostatic interactions. While

purification was ultimately successful for BPA and PFOA, these results suggest mechanisms of absorption that were not anticipated at the outset of this study.

Based on these results, future work on the application of polyMOC gels towards water purification would benefit from additional studies to verify mechanisms of absorption. For example, testing the purification performance for a greater diversity of aromatic absorbates could clarify the relative contributions of hydrophobic and π-π interactions towards absorption. PFAS purification should be evaluated for other organofluorine compounds that cannot interact electrostatically with cationic cage junctions, and differences in absorption between gels at lower and environmentally relevant concentrations of PFOA need to be evaluated. Lower limits of PFOA detection are needed not only to answer these mechanistic questions, but also to test the purification of extremely low concentrations of PFOA (~1 μg/L), which remains the primary challenge in PFAS purification. Using these studies, absorption performance and specificity might be improved by revisiting ligand functionalization and design.

Absorbate capacity, recycling performance, and purification capacity of these materials should be assessed and optimized as well. With several iterations of engineering design, polyMOCs are a potential solution in addressing contemporary problems in water purification, and general system improvements can also inform the application of polyMOC materials towards alternative functions, such as catalysis[41] and separation processes.

3.4 Experimental

Materials. 4-ethynylpyridine hydrochloride was purchased from Ark Pharm. $Pd(NCC_6H_5)_2Cl_2$, $[(t\text{-}Bu)_3PH]BF_4$, Cu(I)I, and $Pt(acac)_2$ were purchased from Strem Chemicals. $Pd(MeCN)_4(OTf)_2$ was purchased from Tokyo Chemical Industry (TCI) Chemicals. 2 kDa PEG was purchased from SinoPEG, and 10 kDa tetra-arm PEG was purchased from Creative PEGWorks. Dry 1,4-dioxane, diisopropylamine, *N,N*-dimethylformamide (DMF), and other anhydrous solvents were purchased from Millipore Sigma and sparged with nitrogen before use in air-sensitive experiments. All deuterated solvents were purchased from Cambridge Isotope Laboratories. All other reagents and solvents were purchased from VWR International or Fisher Scientific.

Column chromatography. Flash column chromatography was performed using Biotage Isolera One with Accelerated Chromatographic Isolation flash chromatography system using KP-Sil SNAP and Sfär cartridges at recommended flow rates.

Solution nuclear magnetic resonance (NMR) spectroscopy. ^{1}H, ^{13}C, and ^{19}F spectra were recorded on either a two-channel Bruker Avance-III HD Nanobay 400 MHz spectrometer, three-channel Bruker Avance Neo 500 MHz spectrometer, or four-channel Bruker Avance Neo 600 MHz spectrometer. Data were analyzed with MestReNova Version: 14.1.0-24037.

Magic angle spinning (MAS) solid-state NMR. ^{1}H MAS NMR spectra were recorded on a three-channel Bruker Avance Neo spectrometer using an HX probe. Annealed gel samples were loaded into a 3.2 mm zirconia rotor, which was sealed with a Vespel cap. The spectra were collected using a spinning frequency of 5 kHz at 25 °C. ^{1}H spectra were referenced to residual DMSO-d_5.

Gel permeation chromatography/multi-angle light scattering (GPC-MALS). Gel permeation chromatography (GPC) measurements were performed in DMF with 0.025 M lithium bromide (LiBr) using an Agilent 1260 Infinity system with guard column (Agilent ResiPore; 7.5 x 50 mm), and two analytical columns (Agilent ResiPore; 300 x 7.5 mm). Signals were collected using a Wyatt miniDAWN TREOS multi-angle light scattering detector and Wyatt Optilab T-rEX refractometer. All runs were performed at 1.0 mL/min flow rate at 25 °C. Samples were prepared at 3.0 mg/mL in 0.025 M LiBr with injection volume of 20.0 µL.

Direct analysis in real time/high resolution mass spectrometry (DART-HRMS). DART-HRMS data were collected on a high-resolution JEOL AccuTOF 4G LC-plus equipped with an ionSense DART source, operated with helium in positive mode at a gas temperature of 350 °C. Data were analyzed with msAxel Data Processing LP Version 1.0 (1.0.5.2).

Liquid chromatography-mass spectrometry (LC-MS). Reaction completion and water purification studies were analyzed using LC-MS, completed on a nominal mass Agilent 612B mass spectrometer attached to an Agilent 1260 Infinity LC. An Agilent InfinityLab

Poroshell 120, EC-C18 column (2.1 x 100 mm, 2.7 µm) with a binary solvent system of 1% formic acid (FA) H_2O (A) and 1% FA MeCN (B) at a flow rate of 0.4 mL/min. Data were processed with Agilent OpenLab ChemStation (C.01.09). 50 µL vial inserts with precision point and plastic springs (6 x 30 mm) were used for small sample volumes.

For general analysis, the binary solvent mixture was kept at 90:10 A/B ratio for 1 min, then gradually ramped over 4 min to 0:100 A/B, where it was held for 1 min. The solvent ratio was returned to 90:10 A/B over the course of 4 min. All samples were scanned from 100–1500 m/z range using a fragmentor voltage of 70 V.

Single ion monitoring (SIM) was used for the study of perfluorooctanoic acid (PFOA) absorption. For this method, the binary solvent mixture was kept at 95:5 A/B for 1 min, after which it was ramped to 0:100 A/B over 6 min. This ratio was held for an additional 2 min before it was ramped back to 95:5 A/B over 1 min for a total method time of 10 min. The mass spectrometer detector was set in negative SIM mode to detect potential PFOA ions and fragments with masses: 412.90, 369.00, 347.00. The integrated area of SIM mass chromatograms was used to quantify PFOA in solution. Negative ion 369.00 was the most reliable in calibration curves and used throughout all studies.

Ultraviolet-visible (UV-Vis) spectroscopy. UV-Vis absorbance spectra of solutions were collected on a Molecular Devices SpectraMax M3. Data were collected and processed with SoftMax Pro 7.0 (Build number:226962).

Small- and wide-angle X-ray scattering (SAXS/WAXS). SAXS/WAXS data were collected at 12-ID-B at the Advanced Photon Source, Argonne National Laboratory. Photon energy was 14 keV (λ = 0.8857 Å) with beam size 60 x 200 μm^2. Detectors used were Pilatus 2M (SAXS) and Pilatus 300K (WAXS). The sample-to-detector distances were calibrated using silver behenate (AgBe). Exposure times of 0.5 s were used during data collection.

Synthesis and characterization of compounds.

General Mitsunobu etherification reaction. 2,6-dibromophenol (1 equiv.) and triphenylphosphine (1 equiv.) were added under nitrogen to a vial with stir bar, followed by THF (0.4 M) and diisopropyl azodicarboxylate (1 equiv.). The reaction mixture was stirred at rt for 30 min, after which the alcohol (1 equiv.) was added. Reaction progress was monitored using thin layer chromatography (TLC). The reaction mixture was stirred for 12 h under N_2, then concentrated under reduced pressure. The resulting viscous oil was dry loaded onto silica gel and purified through column chromatography (gradient from 0→50% EtOAc/hexanes). Any variations in purification and reaction conditions are listed under individual compounds.

General Sonogashira coupling reaction. Dibrominated precursor (1 equiv.), 4-ethynylpyridine hydrochloride (2.5 equiv.), $Pd(NCC_6H_5)_2Cl_2$, (0.06 equiv.), $[(t\text{-}Bu)_3PH]BF_4$ (0.16 equiv.), and Cu(I)I (0.08 equiv.) were added to an oven-dried flask with stir bar under N_2. After sparging both solvents with N_2 for 30 min, dry 1,4-dioxane

(0.2 M) was added to the reaction mixture, followed by diisopropylamine (7.6 equiv.). The reaction mixture was heated to 50 °C and allowed to stir for 24 h, monitoring the disappearance of monofunctionalized intermediate product using LC-MS. The reaction was cooled to rt, then filtered through Celite with EtOAc until the solvent ran colorless. If needed, the volume was reduced to ~100 mL and washed with 10% aqueous ethylene diamine (100 mL x 2) and brine (100 mL x 1) before drying the organic layer over Na_2SO_4, filtering, and concentrating under reduced pressure. The crude product was dry loaded onto silica gel and purified using silica column chromatography (gradient from 0→8% MeOH/DCM, with product elution at 4%). Any variations in purification and reaction conditions are listed under individual compounds.

Scheme S2. Synthesis of 1,3-bis(pyridin-4-ylethynyl)benzene [1].

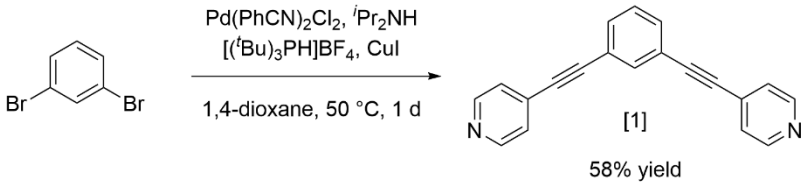

1,3-bis(pyridin-4-ylethynyl)benzene [1]. See Sonogashira coupling reaction procedure outlined above. Reagents: 1,3-dibromobenzene (1.00 g, 4.24 mmol), 4-ethynylpyridine hydrochloride (1.48 g, 10.6 mmol), $Pd(NCC_6H_5)_2Cl_2$ (97.3 mg, 0.254 mmol), [(t-Bu)$_3$PH]BF_4 (197 mg, 0.678 mmol), Cu(I)I (64.6 mg, 0.339 mmol), dry 1,4-dioxane (23.6 mL), diisopropylamine (4.52 mL, 32.0 mmol). Pure brown product was obtained at 58% yield (689 mg, 2.46 mmol).
DART-HRMS (*m/z*) calculated for $C_{20}H_{12}N_2^+$ = 280.09950 [*M*]$^+$; found 280.09974
^{1}H NMR (600 MHz, $CDCl_3$) δ 8.72 – 8.54 (m, 4H), 7.76 (dt, *J* = 1.7, 1.1 Hz, 1H), 7.57 (dd, *J* = 7.8, 1.7 Hz, 2H), 7.46 – 7.34 (m, 5H).
^{1}H NMR (600 MHz, DMSO-*d*$_6$) δ 8.74 – 8.54 (m, 4H), 7.86 (d, *J* = 1.8 Hz, 1H), 7.71 (dd, *J* = 7.8, 1.7 Hz, 2H), 7.62 – 7.48 (m, 5H).
^{13}C-{^{1}H} NMR (151 MHz, $CDCl_3$) δ 149.6, 135.3, 135.2, 132.6, 131.6, 129.0, 125.8, 122.8, 93.2, 87.5.

Scheme S3. Synthesis of (3,5-bis(pyridin-4-ylethynyl)phenyl)methanol [2].

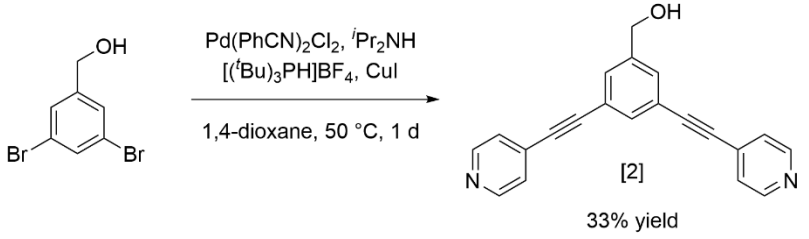

(3,5-bis(pyridin-4-ylethynyl)phenyl)methanol [2]. See Sonogashira coupling reaction procedure outlined above. Reagents: 3,5-dibromobenzyl alcohol (2.00 g, 7.52 mmol), 4-ethynylpyridine hydrochloride (2.62 g, 18.8 mmol), $Pd(NCC_6H_5)_2Cl_2$ (173 mg, 0.450 mmol), [(t-Bu)$_3$PH]BF_4 (349 mg, 1.20 mmol), Cu(I)I (115 mg, 0.602 mmol), dry 1,4-dioxane (41.8 mL), diisopropylamine (8.01 mL, 57.2 mmol). Pure brown product was obtained at 33% yield (770. mg, 2.48 mmol).

DART-HRMS (*m/z*) calculated for $C_{21}H_{15}N_2O^+$ = 311.11789 [*M*+H]$^+$; found 311.11885
^{1}H NMR (600 MHz, $CDCl_3$) δ 8.71 – 8.48 (m, 4H), 7.66 (t, J = 1.6 Hz, 1H), 7.58 (dd, J = 1.6, 0.8 Hz, 2H), 7.45 – 7.31 (m, 4H), 4.85 – 4.64 (m, 2H), 2.78 (s, 1H).
^{13}C NMR{^{1}H} (151 MHz, $CDCl_3$) δ 149.8, 142.3, 134.1, 131.3, 130.8, 125.7, 123.0, 92.9, 87.5, 64.1.

Scheme S4. Synthesis of 4,4'-((2-((6-phenylhexyl)oxy)-1,3-phenylene)bis(ethyne-2,1-diyl))dipyridine [4].

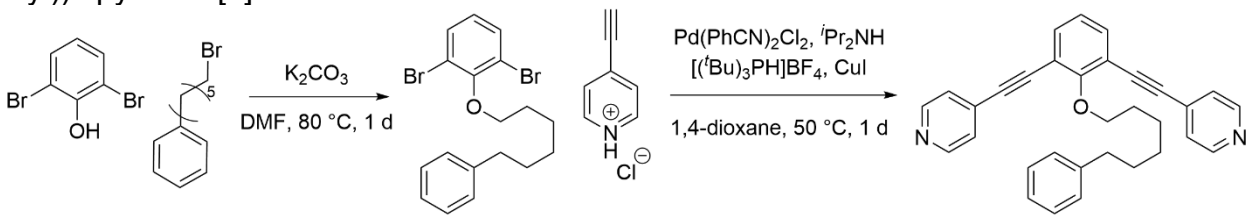

[3] 54% yield

[4] 50% yield

1,3-dibromo-2-((6-phenylhexyl)oxy)benzene [3]. 2,6-dibromophenol (0.500 g, 1.98 mmol), 1-bromo-6-phenylhexane (431 mg, 1.79 mmol), K_2CO_3 (302 mg, 2.18 mmol), and DMF (10.0 mL) were added to an oven-dried flask with stir bar. The reaction mixture was heated at 80 °C for 2 d. After cooling, the reaction was worked up by addition of ~50 mL DCM, then brine wash (5 x 100 mL) to remove DMF. The organic layer was dried with Na_2SO_4 before filtering and concentrating. The crude product was dry loaded onto silica gel and purified using silica column chromatography (gradient from 0→10% EtOAc/hexanes, with product elution at 3%). Pure product was obtained as a clear, lightly yellowed oil at 54% yield (438 mg, 1.07 mmol).
DART-HRMS (*m/z*) calculated for $C_{18}H_{24}Br_2NO^+$ = 428.02192 [*M*+NH_4]$^+$;
found 428.02253
^{1}H NMR (600 MHz, $CDCl_3$) δ 7.50 (dd, *J* = 8.1, 1.7 Hz, 2H), 7.30 (td, *J* = 8.0, 2.8 Hz, 2H), 7.24 – 7.16 (m, 3H), 6.85 (td, *J* = 8.0, 1.1 Hz, 1H), 4.02 (td, *J* = 6.6, 2.4 Hz, 2H), 2.66 (td, *J* = 7.8, 2.6 Hz, 2H), 1.94 – 1.84 (m, 2H), 1.70 (qd, *J* = 7.2, 6.4, 3.5 Hz, 2H), 1.66 – 1.56 (m, 2H), 1.46 (ddt, *J* = 15.6, 9.3, 5.1 Hz, 2H).
^{13}C-{^{1}H} NMR (151 MHz, $CDCl_3$) δ 153.7, 142.9, 132.8, 128.5, 128.4, 126.2, 125.7, 118.7, 73.5, 36.1, 31.5, 30.1, 29.2, 25.9.

4,4'-((2-((6-phenylhexyl)oxy)-1,3-phenylene)bis(ethyne-2,1-diyl))dipyridine [4]. See Sonogashira coupling reaction procedure outlined above. Reagents: [3] (1.40 g, 3.40 mmol), 4-ethynylpyridine hydrochloride (1.19 g, 8.49 mmol), $Pd(NCC_6H_5)_2Cl_2$ (78.0 mg, 0.203 mmol), $[(t\text{-}Bu)_3PH]BF_4$ (17.8 mg, 0.543 mmol), Cu(I)I (51.8 mg, 0.271 mmol), dry 1,4-dioxane (19.0 mL), diisopropylamine (3.62 mL, 25.8 mmol). Pure product obtained was dark brown solid, 50% yield (775 mg, 1.70 mmol).
DART-HRMS (*m/z*) calculated for $C_{32}H_{29}N_2O^+$ = 457.22744 [*M*+H]$^+$; found 457.22828
^{1}H NMR (600 MHz, $CDCl_3$) δ 8.68 – 8.48 (m, 4H), 7.54 (d, *J* = 7.7 Hz, 2H), 7.44 – 7.34 (m, 4H), 7.26 (t, *J* = 7.6 Hz, 2H), 7.22 – 7.15 (m, 1H), 7.11 (t, *J* = 7.6 Hz, 3H), 4.32 (t, *J* = 6.3 Hz, 2H), 2.56 (t, *J* = 7.7 Hz, 2H), 1.95 – 1.79 (m, 2H), 1.69 – 1.53 (m, 4H), 1.47 – 1.31 (m, 2H).

^{13}C-{^{1}H} NMR (151 MHz, $CDCl_3$) δ 162.0, 149.8, 142.6, 134.9, 131.6, 128.4, 128.4, 125.8, 125.6, 123.7, 117.0, 91.2, 90.2, 75.1, 36.0, 31.5, 30.6, 29.3, 26.3.

Scheme S5. Synthetic route to pyren-1-ylmethyl 2-(2,6-bis(pyridin-4-ylethynyl)phenoxy)acetate [7].

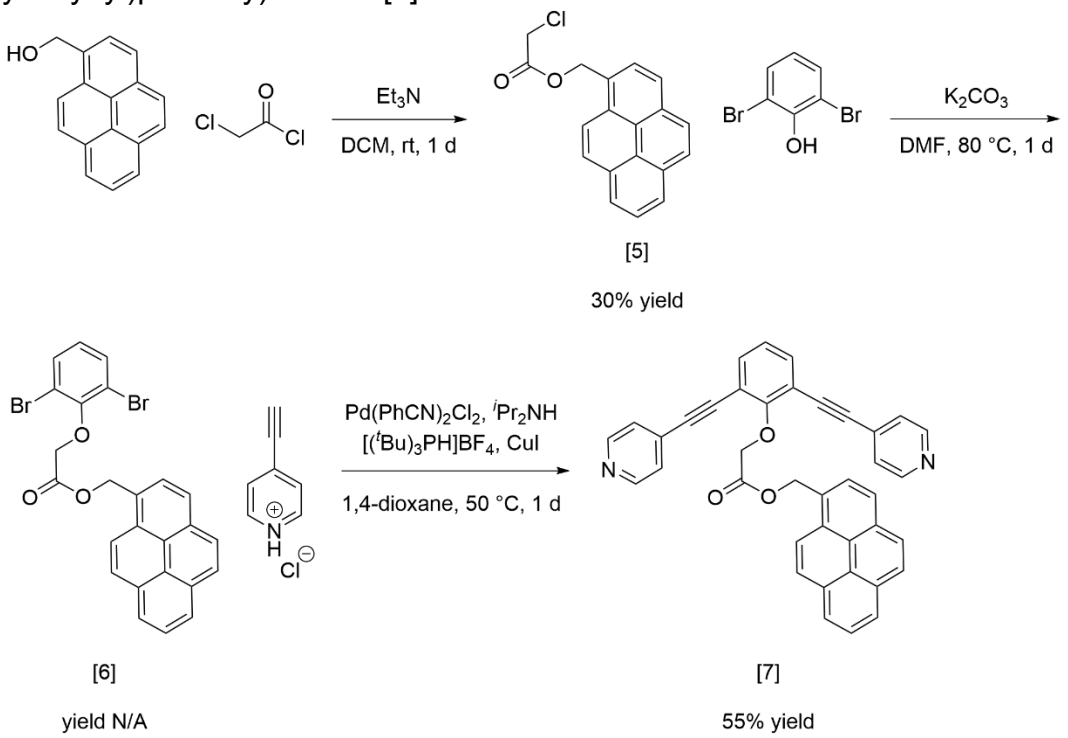

Pyren-1-ylmethyl 2-chloroacetate [5]. 1-pyrenemethanol (166 mg, 0.715 mmol), chloroacetyl chloride (171 µL, 2.14 mmol), and triethylamine (299 µL, 2.14 mmol) were added to an oven-dried flask with DCM (2.00 mL) and stir bar. The reaction mixture was stirred at rt for 1 d until complete, as monitored by TLC and LC-MS. The reaction mixture was washed with brine (3 x 10 mL) before it was dry loaded on silica gel. The crude product was purified using silica column chromatography (gradient from 0→10% EtOAc/hexanes, with product elution at 7%). The light tan solid product was obtained with mild impurities at 30% yield (66.1 mg, 0.215 mmol).
DART-HRMS (*m/z*) calculated for $C_{19}H_{13}O_2Cl^+$ = 308.05986 [*M*]$^+$; found 308.06021
^{1}H NMR (600 MHz, $CDCl_3$) δ 8.28 – 8.19 (m, 3H), 8.19 – 8.12 (m, 2H), 8.11 – 8.01 (m, 4H), 5.93 (s, 2H), 4.12 (s, 2H).
^{13}C-{^{1}H} NMR (151 MHz, $CDCl_3$) δ 167.5, 132.2, 131.3, 130.8, 129.8, 128.6, 128.2, 128.1, 127.8, 127.4, 126.3, 125.8, 125.7, 124.9 (d, *J* = 36.0 Hz), 124.7, 124.7 (d, *J* = 2.6 Hz), 122.8, 66.5, 41.1.

Pyren-1-ylmethyl 2-(2,6-dibromophenoxy)acetate [6]. 2,6-dibromophenol (26.0 mg, 0.103 mmol), [5] (28.7 mg, 0.0929 mmol), and K_2CO_3 (15.7 mg, 0.114 mmol) were added to an oven-dried flask with stir bar and DMF (2.00 mL). The reaction mixture was heated to 100 °C and stirred overnight. Reaction completion was monitored with TLC. When complete, the reaction mixture was cooled to rt and worked up by diluting with DCM (~35 mL) and washing with brine (5 x 50 mL) to remove DMF. The organic layer

was dried with Na_2SO_4 before filtering and concentrating under reduced atmosphere. Crude product was dry loaded onto silica gel and purified using silica column chromatography (gradient from 0→10% EtOAc/hexanes, with product elution at 2%).*
^{1}H NMR (500 MHz, $CDCl_3$) δ 8.33 (d, *J* = 9.2 Hz, 1H), 8.26 – 8.15 (m, 4H), 8.15 – 7.99 (m, 4H), 7.47 (dd, *J* = 8.4, 3.1 Hz, 2H), 6.92 – 6.77 (m, 1H), 6.03 (d, *J* = 3.2 Hz, 2H), 4.68 (d, *J* = 3.0 Hz, 2H).
*Product yield, DART-HRMS, and ^{13}C NMR characterization data were not successfully obtained due to the Spring 2020 COVID-19 shutdown of MIT research facilities.

Pyren-1-ylmethyl 2-(2,6-bis(pyridin-4-ylethynyl)phenoxy)acetate [7]. See Sonogashira coupling reaction procedure outlined above. [6] (386 mg, 0.736 mmol), 4-ethynylpyridine hydrochloride (257 mg, 1.84 mmol), $Pd(NCC_6H_5)_2Cl_2$ (17.0 mg, 0.0441 mmol), $[(t\text{-}Bu)_3PH]BF_4$ (34.2 mg, 0.118 mmol), Cu(I)I (11.2 mg, 0.0589 mmol), dry 1,4-dioxane (4.00 mL), diisopropylamine (784 µL, 5.60 mmol). Off-white product was obtained at 55% yield (230. mg, 0.405 mmol).
DART-HRMS (*m/z*) calculated for $C_{39}H_{25}N_2O_3^+$ = 569.18597 [*M*+H]$^+$; found 569.18897
^{1}H NMR (600 MHz, $CDCl_3$) δ 8.45 (s, 4H), 8.27 – 8.16 (m, 3H), 8.11 (d, *J* = 8.9 Hz, 1H), 8.09 – 8.01 (m, 4H), 7.98 (d, *J* = 7.7 Hz, 1H), 7.49 (d, *J* = 7.7 Hz, 2H), 7.25 (s, 5H), 7.10 (t, *J* = 7.7 Hz, 1H), 5.94 (s, 2H), 5.05 (s, 2H).
^{13}C-{^{1}H} NMR (151 MHz, $CDCl_3$) δ 168.5, 160.1, 149.4, 135.0, 132.1, 131.3, 131.3, 130.7, 129.8, 128.5, 128.3, 128.2, 128.0, 127.4, 126.4, 125.9, 125.7, 125.6, 124.9, 124.7, 124.6, 124.2, 122.8, 116.1, 92.0, 89.4, 70.1, 65.6.

Scheme S6. Synthetic route to 4,4'-((2-((3,3,4,4,5,5,6,6,6-nonafluorohexyl)oxy)-1,3-phenylene)bis(ethyne-2,1-diyl))dipyridine [9].

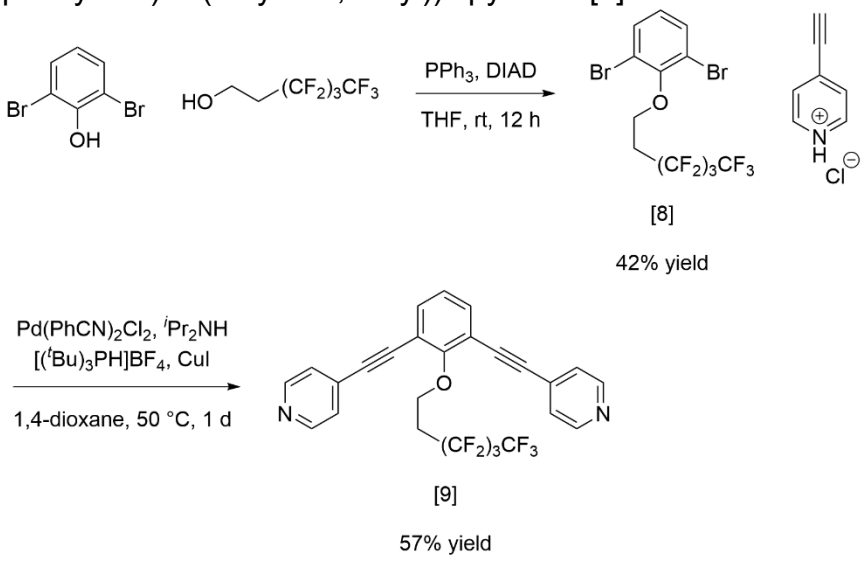

1,3-dibromo-2-((3,3,4,4,5,5,6,6,6-nonafluorohexyl)oxy)benzene [8]. See Mitsunobu etherification reaction procedure outlined above. Reagents: 2,6-dibromophenol (0.750 g, 2.98 mmol), triphenylphosphine (781 mg, 2.98 mmol), THF (7.00 mL), diisopropyl azodicarboxylate (585 µL, 2.98 mmol), *1H,1H,2H,2H*-perfluorohexan-1-ol (495 µL, 2.98 mmol). The product was a clear viscous oil obtained at 42% yield (245 mg, 1.25 mmol).

DART-HRMS (*m/z*) calculated for $C_{12}H_7Br_2F_9O^+$ = 495.87145 [*M*]$^+$; found 495.87351
^{1}H NMR (600 MHz, $CDCl_3$) δ 7.52 (d, J = 8.1 Hz, 2H), 6.90 (t, J = 8.0 Hz, 1H), 4.31 (t, J = 7.1 Hz, 2H), 2.88 – 2.56 (m, 2H).
^{13}C-{^{1}H,^{19}F} NMR (151 MHz, $CDCl_3$) δ 153.0, 133.0, 127.0, 118.5, 117.6, 117.5, 110.48, 108.9, 65.1, 31.9.
^{19}F NMR (282 MHz, $CDCl_3$) δ -81.4 (tt, *J* = 9.7, 3.3 Hz, 3H), -113.0 – -114.6 (m, 2H), -124.3 – -125.5 (m, 2H), -126.4 (qt, *J* = 10.3, 6.0 Hz, 2H).

4,4'-((2-((3,3,4,4,5,5,6,6,6-nonafluorohexyl)oxy)-1,3-phenylene)bis(ethyne-2,1-diyl))dipyridine [9]. See general Sonogashira coupling reaction procedure outlined above. Reagents: [8] (0.500 g, 1.00 mmol), 4-ethynylpyridine hydrochloride (0.350 g, 2.51 mmol), $Pd(NCC_6H_5)_2Cl_2$ (23.0 mg, 0.0601 mmol), $[(t\text{-}Bu)_3PH]BF_4$ (46.6 mg, 0.161 mmol), Cu(I)I (15.3 mg, 0.0803 mmol), dry 1,4-dioxane (5.58 mL), diisopropylamine (1.07 mL, 7.63 mmol). Product was obtained as a beige solid at 57% yield (310. mg, 0.572 mmol).
DART-HRMS (*m/z*) calculated for $C_{26}H_{16}Br_2F_9O^+$ = 543.11134 [*M*+H]$^+$; found 543.11165
^{1}H NMR (400 MHz, $CDCl_3$) δ 8.77 – 8.50 (m, 4H), 7.57 (d, *J* = 7.7 Hz, 2H), 7.46 – 7.30 (m, 4H), 7.18 (t, *J* = 7.7 Hz, 1H), 4.61 (t, *J* = 6.7 Hz, 2H), 2.75 (tt, *J* = 18.9, 6.9 Hz, 2H).
^{13}C-{^{1}H,^{19}F} NMR (151 MHz, $CDCl_3$) δ 160.7, 149.8, 135.0, 131.3, 125.6, 124.7, 117.0, 91.7, 89.3, 66.3, 66.2, 66.2, 32.3, 32.2, 32.0.
^{19}F NMR (376 MHz, $CDCl_3$) δ -80.4 – -82.0 (m, 3H), -112.9 – -113.8 (m, 2H), -124.0 – -124.8 (m, 2H), -126.0 (dt, *J* = 13.9, 11.0 Hz, 2H).

Scheme S7. Synthetic route to 3,3,4,4,5,5,6,6,6-nonafluorohexyl 3,5-bis(pyridin-4-ylethynyl)benzoate [11].

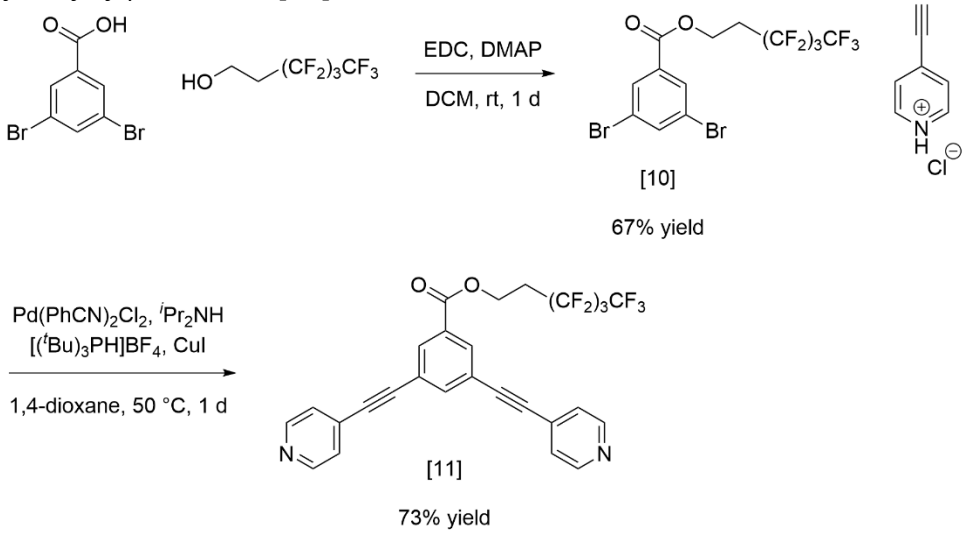

3,3,4,4,5,5,6,6,6-nonafluorohexyl 3,5-dibromobenzoate [10]. 3,5-dibromobenzoic acid (0.500 g, 1.79 mmol), N-(3-dimethylaminopropyl)-N′-ethylcarbodiimide hydrochloride (EDC, 685 mg, 3.57 mmol), 4-dimethylaminopyridine (DMAP, 437 mg, 3.57 mmol), DCM (6.00 mL), and *1H,1H,2H,2H*-perfluorohexan-1-ol (297 µL, 1.79 mmol) were added to a 20 mL microwave vial with stir bar. The heterogeneous reaction was stirred at rt for 1 d. The reaction was worked up by washing with brine (20 mL x 3) and drying

the organic layer with Na_2SO_4 before concentrating under reduced pressure. The crude product was purified with silica column chromatography (gradient from 1→15% EtOAc/hexanes, with product elution at 4%). The product was obtained as a clear oil at 67% yield (627 mg, 1.20 mmmol).
DART-HRMS (*m/z*) calculated for $C_{13}H_8Br_2F_9O_2^+$ = 524.87418 [*M*+H]$^+$; found 524.87607
^{1}H NMR (600 MHz, $CDCl_3$) δ 8.09 (d, *J* = 1.8 Hz, 2H), 7.26 (s, 1H), 4.64 (t, *J* = 6.5 Hz, 2H), 2.72 – 2.51 (m, 2H).
^{13}C-{^{1}H,^{19}F} NMR (151 MHz, $CDCl_3$) δ 163.8, 138.9, 132.8, 131.6, 123.3, 117.5, 110.4, 108.8, 57.7, 30.6.
^{19}F NMR (565 MHz, $CDCl_3$) δ -81.0 (t, *J* = 9.4 Hz, 3H), -113.7 (td, J = 18.0, 9.1 Hz, 2H), -124.4 (td, *J* = 9.7, 5.0 Hz, 2H), -125.9 (qq, *J* = 10.6, 6.3, 5.8 Hz, 2H).

3,3,4,4,5,5,6,6,6-nonafluorohexyl 3,5-bis(pyridin-4-ylethynyl)benzoate [11]. See general Sonogashira coupling reaction procedure outlined above. Reagents: [10] (0.500 g, 0.951 mmol), 4-ethynylpyridine hydrochloride (332 mg, 2.38 mmol), $Pd(NCC_6H_5)_2Cl_2$ (21.8 mg, 0.0569 mmol), $[(t\text{-}Bu)_3PH]BF_4$ (44.1 mg, 0.152 mmol), Cu(I)I (14.5 mg, 0.0760 mmol), dry 1,4-dioxane (5.28 mL), diisopropylamine (1.01 mL, 7.22 mmol). Crude product was dry loaded on silica gel and purified with silica column chromatography (gradient from 10→70% EtOAc/hexanes, with product elution at 40%). White solid product was obtained at 73% yield (396 mg, 0.694 mmol).
DART-HRMS (*m/z*) calculated for $C_{27}H_{16}F_9N_2O_2^+$ = 571.10626 [*M*+H]$^+$; found 571.10863
^{1}H NMR (600 MHz, $CDCl_3$) δ 8.73 – 8.56 (m, 4H), 8.20 (d, *J* = 1.6 Hz, 2H), 7.93 (t, *J* = 1.6 Hz, 1H), 7.49 – 7.33 (m, 4H), 4.69 (t, *J* = 6.4 Hz, 2H), 2.65 (tt, *J* = 18.2, 6.5 Hz, 2H).
^{13}C-{^{1}H,^{19}F} NMR (151 MHz, $CDCl_3$) δ 164.6, 149.8, 139.2, 133.4, 131.0, 130.7, 125.8, 123.6, 117.5, 117.5, 110.4, 108.8, 91.7, 88.5, 57.6, 30.7.
^{19}F NMR (565 MHz, $CDCl_3$) δ -81.0 (t, *J* = 9.7 Hz, 3H), -113.7 (p, *J* = 15.7 Hz, 2H), -124.4 (dq, *J* = 14.5, 8.4, 6.8 Hz, 2H), -125.9 (td, *J* = 12.7, 4.2 Hz, 2H).

Scheme S8. Synthetic route to 4,4'-((2-((3,3,4,4,5,5,6,6,7,7,8,8,9,9,10,10,10-heptadecafluorodecyl)oxy)-1,3-phenylene)bis(ethyne-2,1-diyl))dipyridine [13].

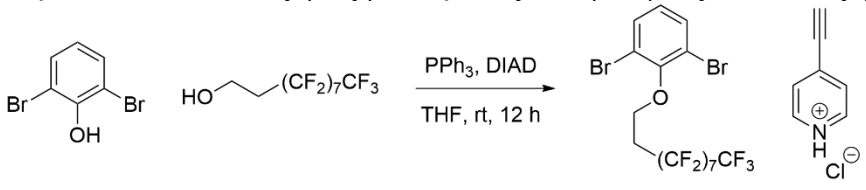

[12]

61% yield

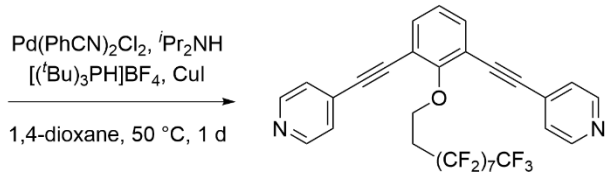

[13]

62% yield

1,3-dibromo-2-((3,3,4,4,5,5,6,6,7,7,8,8,9,9,10,10,10-heptadecafluorodecyl)oxy)benzene [12]. See Mitsunobu etherification reaction procedure outlined above. Reagents: 2,6-dibromophenol (0.750 g, 2.97 mmol), triphenylphosphine (781 mg, 2.97 mmol), THF (7.00 mL), diisopropyl azodicarboxylate (585 µL, 2.97 mmol), *1H,1H,2H,2H*-perfluorodecan-1-ol (1.38 g, 2.97 mmol). The product was a clear viscous oil obtained at 61% yield (1.26 g, 1.81 mmol).
DART-HRMS (*m/z*) calculated for $C_{16}H_8Br_2F_{17}O_2^+$ = 698.86507 [*M*+H]$^+$; found 698.86830
^{1}H NMR (600 MHz, $CDCl_3$) δ 7.52 (d, *J* = 8.1 Hz, 2H), 6.90 (t, *J* = 8.0 Hz, 1H), 4.31 (t, *J* = 7.1 Hz, 2H), 2.77 (tt, *J* = 18.3, 7.2 Hz, 2H).
^{13}C-{^{1}H,^{19}F} NMR (151 MHz, $CDCl_3$) δ 153.0, 133.0, 127.0, 118.5, 117.7, 117.3, 111.3, 111.04, 110.95, 110.9, 110.4, 108.6, 65.2, 32.0.
^{19}F NMR (565 MHz, $CDCl_3$) δ -80.8 (t, *J* = 10.2 Hz, 3H), -113.1 (p, *J* = 17.0 Hz, 2H), -121.5 – -121.7 (m, 2H), -121.8 – -122.0 (m, 2H), -122.7 (dt, *J* = 25.1, 11.8 Hz, 2H), -123.5 (t, *J* = 14.9 Hz, 2H), -126.0 – -126.2 (m, 2H).

4,4'-((2-((3,3,4,4,5,5,6,6,7,7,8,8,9,9,10,10,10-heptadecafluorodecyl)oxy)-1,3-phenylene)bis(ethyne-2,1-diyl))dipyridine [13]. See general Sonogashira coupling reaction procedure outlined above. [12] (1.00 g, 1.43 mmol), 4-ethynylpyridine hydrochloride (.500 g, 3.58 mmol), $Pd(NCC_6H_5)_2Cl_2$ (32.9 mg, 0.0857 mmol), $[(t\text{-}Bu)_3PH]BF_4$ (66.5 mg, 0.229 mmol), Cu(I)I (21.8 mg, 0.115 mmol), dry 1,4-dioxane (7.96 mL), diisopropylamine (1.53 mL, 10.9 mmol). White solid product obtained at 62% yield (658 mg, 0.887 mmol).
DART-HRMS (*m/z*) calculated for $C_{30}H_{16}F_{17}N_2O^+$ = 743.09857 [*M*+H]$^+$; found 743.10002
^{1}H NMR (400 MHz, $CDCl_3$) δ 8.72 – 8.53 (m, 4H), 7.58 (d, *J* = 7.7 Hz, 2H), 7.44 – 7.31 (m, 4H), 7.18 (t, *J* = 7.7 Hz, 1H), 4.61 (t, *J* = 6.7 Hz, 2H), 2.75 (tt, *J* = 18.5, 6.8 Hz, 2H).
^{13}C-{^{1}H,^{19}F} NMR (151 MHz, $CDCl_3$) δ 160.7, 149.8, 135.0, 131.3, 125.6, 124.7, 117.8, 117.3, 117.0, 111.3, 111.0, 110.8 (d, *J* = 9.6 Hz), 110.3, 108.5, 106.3, 91.7, 89.3, 66.3, 32.3.
^{19}F NMR (376 MHz, $CDCl_3$) δ -80.7 (t, *J* = 10.0 Hz, 3H), -113.1 (qdd, *J* = 18.9, 13.6, 5.4 Hz, 2H), -121.6 (dt, *J* = 25.2, 8.9 Hz, 2H), -121.9 (dq, *J* = 19.7, 10.7 Hz, 4H), -122.7 (dp, *J* = 27.7, 9.5, 8.1 Hz, 2H), -123.4 (d, *J* = 15.4 Hz, 2H), -126.1 (qd, *J* = 16.3, 14.6, 7.0 Hz, 2H).

Scheme S9. Synthetic route to 4,4'-((2-(2-(perfluorophenyl)ethoxy)-1,3-phenylene)bis(ethyne-2,1-diyl))dipyridine [15].

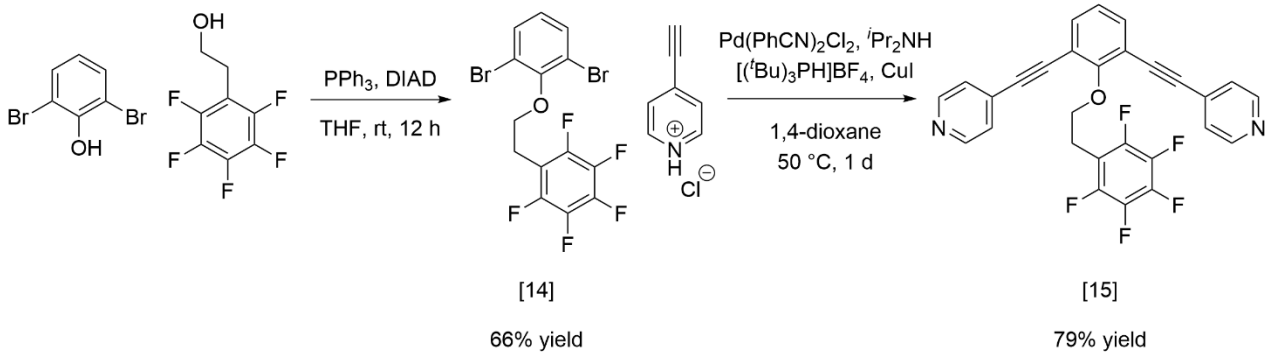

[14] 66% yield

[15] 79% yield

1-(2-(2,6-dibromophenoxy)ethyl)-2,3,4,5,6-pentafluorobenzene [14]. See general Mitsunobu etherification reaction procedure outlined above. Reagents: 2,6-dibromophenol (0.750 g, 2.98 mmol), triphenylphosphine (781 mg, 2.98 mmol), THF (7.44 mL), diisopropyl azodicarboxylate (585 µL, 2.98 mmol), 2-(perfluorophenyl)ethan-1-ol (414 µL, 2.98 mmol). The product was obtained as a white powder at 66% yield (877 mg, 1.97 mmol).
DART-HRMS (*m/z*) calculated for $C_{14}H_7Br_2F_5O^+$ = 445.87639 [*M*]$^+$; found 445.87842
^{1}H NMR (600 MHz, $CDCl_3$) δ 7.48 (d, J = 8.0 Hz, 2H), 6.86 (t, J = 8.0 Hz, 1H), 4.18 (t, J = 6.6 Hz, 2H), 3.29 (tt, J = 6.6, 1.6 Hz, 2H).
^{13}C-{^{1}H} NMR (151 MHz, $CDCl_3$) δ 152.8, 145.8 (d, *J* = 234.1 Hz), 140.2 (d, *J* = 249.7 Hz), 137.6 (d, *J* = 249.6 Hz), 132.9 (dd, *J* = 247.5, 2.6 Hz), 126.8, 118.5, 111.6, 70.4, 23.4.
^{19}F NMR (282 MHz, $CDCl_3$) δ -143.3 (d, *J* = 14.6 Hz, 2H), -157.1 (t, *J* = 20.7 Hz, 2H), -162.8 – -164.7 (m, 2H).

4,4'-((2-(2-(perfluorophenyl)ethoxy)-1,3-phenylene)bis(ethyne-2,1-diyl))dipyridine [15]. See general Sonogashira coupling reaction procedure outlined above. Reagents: [14] (639 mg, 1.43 mmol), 4-ethynylpyridine hydrochloride (0.500 g, 3.58 mmol), $Pd(NCC_6H_5)_2Cl_2$ (32.9 mg, 0.0857 mmol), $[(t\text{-}Bu)_3PH]BF_4$ (66.5 mg, 0.229 mmol), Cu(I)I (21.8 mg, 0.115 mmol), dry 1,4-dioxane (7.96 mL), diisopropylamine (1.53 mL, 10.4 mmol). Manilla-colored solid product obtained at 79% yield (555 mg, 1.13 mmol).
DART-HRMS (*m/z*) calculated for $C_{28}H_{16}F_5N_2O^+$ = 491.11773 [*M*+H]$^+$; found 491.11830
^{1}H NMR (600 MHz, $CDCl_3$) δ 8.73 – 8.57 (m, 4H), 7.53 (d, *J* = 7.7 Hz, 2H), 7.37 – 7.31 (m, 4H), 7.14 (t, *J* = 7.7 Hz, 1H), 4.48 (t, *J* = 6.8 Hz, 2H), 3.30 (tt, *J* = 6.9, 1.6 Hz, 2H).
^{13}C-{^{1}H} NMR (151 MHz, $CDCl_3$) δ 160.6, 150.1, 150.0, 145.6 (d, *J* = 240.5 Hz), 140.1 (d, *J* = 250.8 Hz), 137.5 (d, *J* = 251.4 Hz), 134.8, 132.0, 126.2, 125.4, 124.4, 117.1, 91.4, 89.1, 71.6, 23.9.
^{19}F NMR (282 MHz, $CDCl_3$) δ -143.5 (dd, *J* = 22.4, 8.4 Hz, 2H), -156.4 (t, *J* = 20.9 Hz, 2H), -162.6 (td, *J* = 22.1, 8.4 Hz, 2H).

Scheme S10. Synthetic route to 4,4'-((2-(hexyloxy)-1,3-phenylene)bis(ethyne-2,1-diyl))dipyridine [17].

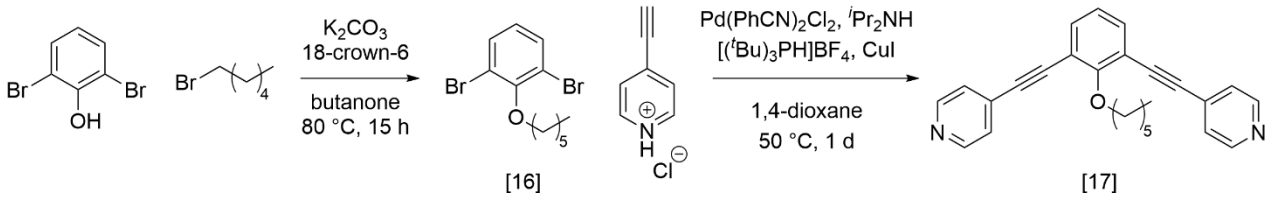

1,3-dibromo-2-(hexyloxy)benzene [16]. 2,6-dibromophenol (1.00 g, 3.97 mmol), K_2CO_3 (1.65 g, 11.9 mmol), butanone (4.00 mL), 1-bromohexane (1.67 mL, 11.9 mmol), and 18-crown-6 (65.0 mg, 0.250 mmol) were added to a 40 mL scintillation vial with stir bar and 3 Å molecular sieves (~40 granules, oven-activated). The vial was sealed and heated at 80 °C for 15 h. After cooling to rt, the reaction mixture was filtered over a cotton plug, then through a 0.45 µm PTFE syringe filter. The filtrate was concentrated

and purified through column chromatography on silica gel (100% hexanes). The product was a clear oil, obtained at 81% yield (1.07 g, 3.22 mmol).
DART-HRMS (*m/z*) calculated for $C_{12}H_{16}Br_2O^+$ = 333.95624 $[M]^+$; found 333.95720
^{1}H NMR (600 MHz, $CDCl_3$) δ 7.49 (d, *J* = 8.0 Hz, 2H), 6.84 (t, *J* = 8.0 Hz, 1H), 4.00 (t, *J* = 6.6 Hz, 2H), 1.95 – 1.78 (m, 2H), 1.54 (tt, *J* = 9.8, 6.1 Hz, 2H), 1.43 – 1.30 (m, 4H), 0.97 – 0.85 (m, 3H).
^{13}C-{^{1}H} NMR (151 MHz, $CDCl_3$) δ 153.7, 132.8, 126.2, 118.7, 73.7, 31.8, 30.2, 25.7, 22.8, 14.2.

4,4'-((2-(hexyloxy)-1,3-phenylene)bis(ethyne-2,1-diyl))dipyridine [17]. See general Sonogashira coupling reaction procedure outlined above. Reagents: [16] (632 mg, 1.88 mmol), 4-ethynylpyridine hydrochloride (656 mg, 4.70 mmol), $Pd(NCC_6H_5)_2Cl_2$ (43.2 mg, 0.113 mmol), $[(t\text{-}Bu)_3PH]BF_4$ (87.3 mg, 0.301 mmol), Cu(I)I (28.6 mg, 0.150 mmol), dry 1,4-dioxane (10.4 mL), diisopropylamine (2.00 mL, 14.3 mmol). Product was a clear yellow oil obtained at 61% yield (436 mg, 1.15 mmol).
DART-HRMS of $C_{26}H_{24}N_2O^+$ = 380.18831 $[M]^+$; found 380.18877
^{1}H NMR (600 MHz, $CDCl_3$) δ 8.70 – 8.53 (m, 4H), 7.52 (d, *J* = 7.7 Hz, 2H), 7.42 – 7.30 (m, 4H), 7.09 (t, *J* = 7.7 Hz, 1H), 4.31 (t, *J* = 6.4 Hz, 2H), 1.93 – 1.78 (m, 2H), 1.56 (p, *J* = 7.5 Hz, 2H), 1.39 – 1.18 (m, 4H), 0.83 (t, *J* = 7.2 Hz, 3H).
^{13}C-{^{1}H} NMR (151 MHz, $CDCl_3$) δ 162.0, 150.0, 134.8, 131.4, 125.5, 123.7, 117.0, 91.2, 90.0, 75.1, 31.8, 30.6, 26.1, 22.7, 14.1.

Scheme S11. Synthetic route to 4,4'-((2-(octadecyloxy)-1,3-phenylene)bis(ethyne-2,1-diyl))dipyridine [19].

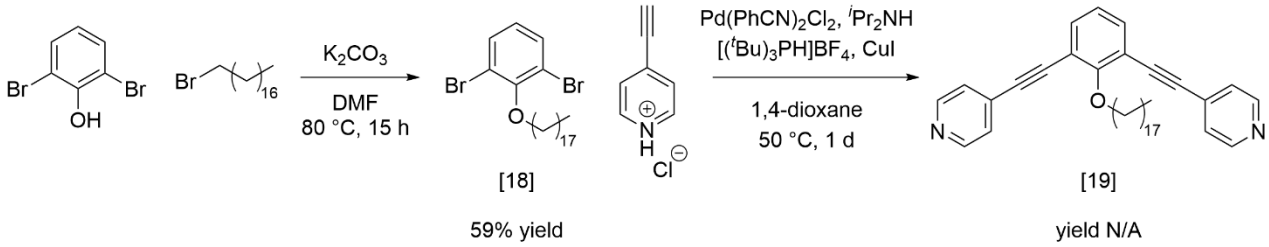

1,3-dibromo-2-(octadecyloxy)benzene [18]. 2,6-dibromophenol (1.00 g, 3.97 mmol), 1-bromooctadecane (1.72 g, 5.16 mmol), and K_2CO_3 (604 mg, 4.37 mmol) were added to oven-dried flask with stir bar and DMF (20.0 mL). The reaction was stirred at 80 °C for 1 d and monitored with TLC (10% EtOAc/hex). Once complete, the reaction was cooled to rt before the reaction mixture was diluted with DCM (100 mL) and washed with brine (5 x 100 mL) to remove DMF. The organic layer was dried with Na_2SO_4 before filtering and concentrating. The resulting solid was dry loaded onto silica gel before purification through silica column chromatography (100% hexanes). Pure product was obtained as a white, chunky solid at 59% yield (1.18 g, 2.34 mmol).
DART-HRMS (*m/z*) calculated for $C_{24}H_{40}OBr_2^+$ = 502.14404 $[M]^+$; found 502.14651
^{1}H NMR (600 MHz, $CDCl_3$) δ 7.49 (dd, *J* = 8.1, 1.4 Hz, 2H), 6.84 (td, *J* = 8.0, 1.4 Hz, 1H), 4.00 (t, *J* = 6.6 Hz, 2H), 1.87 (p, *J* = 6.9 Hz, 2H), 1.53 (dd, *J* = 10.9, 4.9 Hz, 2H), 1.42 – 1.20 (m, 28H), 0.92 – 0.84 (m, 3H).
^{13}C-{^{1}H} NMR (151 MHz, $CDCl_3$) δ 153.7, 132.8, 126.2, 118.7, 73.7, 32.1, 30.2, 29.9, 29.84, 29.82, 29.78, 29.75, 29.6, 29.5, 26.0, 22.9, 14.3.

4,4'-((2-(octadecyloxy)-1,3-phenylene)bis(ethyne-2,1-diyl))dipyridine [19]. See general Sonogashira coupling reaction procedure outlined above. Reagents: [18] (1.50 g, 2.97 mmol), 4-ethynylpyridine hydrochloride (1.04 g, 7.43 mmol), $Pd(NCC_6H_5)_2Cl_2$ (68.3 mg, 0.178 mmol), $[(t\text{-}Bu)_3PH]BF_4$ (138 mg, 0.476 mmol), Cu(I)I (45.3 mg, 0.238 mmol), dry 1,4-dioxane (16.5 mL), diisopropylamine (3.17 mL, 22.6 mmol). Product was a gray solid.*
DART-HRMS (*m/z*) calculated for $C_{38}H_{49}N_2O^+$ = 549.38394 [*M*+H]$^+$; found 549.38166
^{1}H NMR (600 MHz, $CDCl_3$) δ 8.65 – 8.54 (m, 4H), 7.53 (d, *J* = 7.7 Hz, 2H), 7.41 – 7.32 (m, 4H), 7.09 (t, *J* = 7.7 Hz, 1H), 4.31 (t, *J* = 6.4 Hz, 2H), 1.92 – 1.80 (m, 2H), 1.63 – 1.50 (m, 2H), 1.36 – 1.17 (m, 28H), 0.87 (t, *J* = 7.0 Hz, 3H).
^{13}C-{^{1}H} NMR (151 MHz, $CDCl_3$) δ 162.0, 150.0, 134.8, 131.4, 125.5, 123.6, 117.0, 91.2, 90.0, 75.1, 32.0, 30.7, 29.82, 29.78, 29.75, 29.69, 29.5, 26.5, 22.8, 14.2.
*Product yield was not successfully obtained due to the Spring 2020 COVID-19 shutdown of MIT research facilities.

Scheme S12. Synthetic route to 4,4'-((5-(2-(2-(2-methoxyethoxy)ethoxy)ethoxy)-1,3-phenylene)bis(ethyne-2,1-diyl))dipyridine [21].

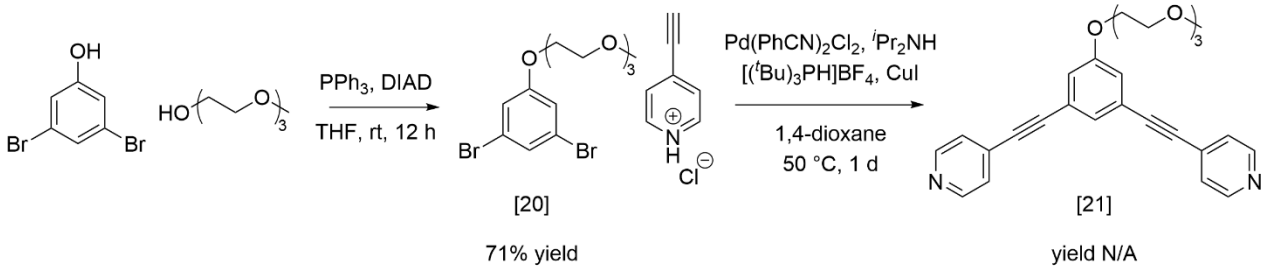

1,3-dibromo-5-(2-(2-(2-methoxyethoxy)ethoxy)ethoxy)benzene [20]. See general Mitsunobu etherification reaction procedure outlined above. Reagents: 2,6-dibromophenol (0.750 g, 2.98 mmol), triphenylphosphine (781 mg, 2.98 mmol), THF (5.95 mL), diisopropyl azodicarboxylate (585 µL, 2.98 mmol), triethylene glycol monomethyl ether (465 µL, 2.98 mmol). The product was obtained as a pale yellow solid at 71% (837 mg, 2.12 mmol), with a large 2-propanol impurity that could not be removed and had no effect in the sequential reaction step.
DART-HRMS (*m/z*) calculated for $C_{13}H_{19}O_4Br_2^+$ = 396.96474 [*M*+H]$^+$; found 396.96461
^{1}H NMR (400 MHz, $CDCl_3$) δ 7.24 (t, *J* = 1.6 Hz, 1H), 7.02 (d, *J* = 1.6 Hz, 2H), 4.12 – 4.06 (m, 2H), 3.85 – 3.80 (m, 2H), 3.74 – 3.69 (m, 2H), 3.69 – 3.63 (m, 4H), 3.57 – 3.52 (m, 2H), 3.38 (s, 3H).
^{13}C-{^{1}H} NMR (151 MHz, $CDCl_3$) δ 160.1, 126.7, 123.2, 117.3, 72.0, 71.0, 70.8, 70.7, 69.5, 68.2, 59.2.

4,4'-((5-(2-(2-(2-methoxyethoxy)ethoxy)ethoxy)-1,3-phenylene)bis(ethyne-2,1-diyl))dipyridine [21]. See general Sonogashira coupling reaction procedure outlined above. Reagents: [20] (0.500 g, 1.26 mmol), 4-ethynylpyridine hydrochloride (438 mg, 3.14 mmol), $Pd(NCC_6H_5)_2Cl_2$ (28.8 mg, 0.0752 mmol), $[(t\text{-}Bu)_3PH]BF_4$ (58.3 mg, 0.201 mmol), Cu(I)I (19.1 mg, 0.100 mmol), dry 1,4-dioxane (6.98 mL), diisopropylamine (1.34 mL, 9.55 mmol). Product was collected as a waxy solid.*

DART-HRMS (*m/z*) calculated for $C_{27}H_{27}N_2O_4^+$ = 443.19653 [*M*+H]$^+$; found 443.19728
^{1}H NMR (600 MHz, $CDCl_3$) δ 8.67 – 8.56 (m, 4H), 7.40 – 7.36 (m, 4H), 7.35 (t, *J* = 1.4 Hz, 1H), 7.12 (d, *J* = 1.4 Hz, 2H), 4.20 – 4.15 (m, 2H), 3.90 – 3.86 (m, 2H), 3.77 – 3.72 (m, 2H), 3.70 – 3.67 (m, 2H), 3.67 – 3.64 (m, 2H), 3.57 – 3.52 (m, 2H), 3.38 (s, 3H).
^{13}C-{^{1}H} NMR (151 MHz, $CDCl_3$) δ 158.8, 149.9, 131.24, 128.1, 125.7, 123.7, 119.1, 92.9, 87.3, 72.1, 71.1, 70.8, 70.7, 69.7, 68.1, 59.19, 59.18.
*Product yield was not obtained due to the Spring 2020 COVID-19 shutdown of MIT research facilities.

Scheme S13. Synthetic route to 4,4'-((5-methoxy-1,3-phenylene)bis(ethyne-2,1-diyl))dipyridine [22].

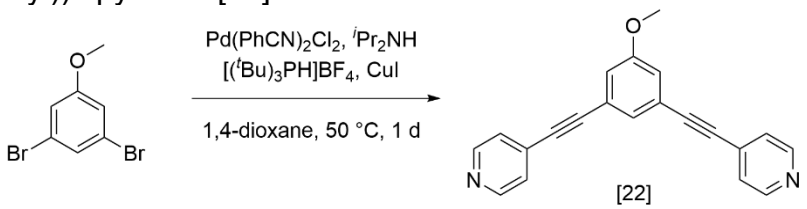

[22]

yield N/A

4,4'-((5-methoxy-1,3-phenylene)bis(ethyne-2,1-diyl))dipyridine [22]. See general Sonogashira coupling reaction procedure outlined above. Reagents: 3,5-dibromoanisole (0.500 g, 1.88 mmol), 4-ethynylpyridine hydrochloride (656 mg, 4.70 mmol), $Pd(NCC_6H_5)_2Cl_2$ (43.2 mg, 0.113 mmol), $[(t\text{-}Bu)_3PH]BF_4$ (87.3 mg, 0.301 mmol), Cu(I)I (28.6 mg, 0.150 mmol), dry 1,4-dioxane (10.4 mL), diisopropylamine (2.00 mL, 14.3 mmol). Manilla solid product with mild impurities was collected after purification.*
DART-HRMS (*m/z*) calculated for $C_{21}H_{14}N_2O^+$ = 310.11006 [*M*]$^+$; found 310.11118
^{1}H NMR (600 MHz, $CDCl_3$) δ 8.65 – 8.58 (m, 4H), 7.40 – 7.37 (m, 4H), 7.36 (d, *J* = 1.4 Hz, 1H), 7.10 (d, *J* = 1.4 Hz, 2H), 3.86 (s, 3H).
^{13}C-{^{1}H} NMR (151 MHz, $CDCl_3$) δ 159.6, 149.9, 131.2, 127.9, 125.7, 123.7, 118.4, 92.9, 87.3, 55.7.
*Pure product and product yield were not obtained due to the Spring 2020 COVID-19 shutdown of MIT research facilities.

Scheme S14. Synthesis of 3,5-bis(pyridin-4-ylethynyl)phenol [23].

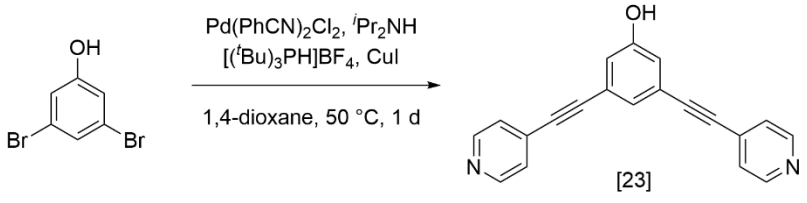

[23]

49% yield

3,5-bis(pyridin-4-ylethynyl)phenol [23]. See general Sonogashira coupling reaction procedure outlined above. Reagents: 3,5-dibromophenol (0.750 g, 2.98 mmol), 4-ethynylpyridine hydrochloride (1.039 g, 7.44 mmol), $Pd(NCC_6H_5)_2Cl_2$ (68.3 mg, 0.178 mmol), $[(t\text{-}Bu)_3PH]BF_4$ (138 mg, 0.476 mmol), Cu(I)I (45.4 mg, 0.238 mmol), dry 1,4-

dioxane (16.5 mL), diisopropylamine (3.17 mL, 22.6 mmol). A light brown solid was obtained at 49% yield (432 mg, 1.46 mmol).
HRMS (*m/z*) calculated for $C_{20}H_{13}N_2O^+$ = 297.10224 [*M*+H]$^+$; found = 297.10361
^{1}H NMR (600 MHz, DMSO-d_6) δ 8.75 – 8.54 (m, 1H), 7.60 – 7.46 (m, 1H).
^{13}C{^{1}H} NMR (151 MHz, DMSO-d_6) δ 157.8, 150.0, 129.8, 125.7, 125.4, 122.9, 119.5, 92.3, 87.0.

Scheme S15. Synthesis of polymer ligand 1 (pL1).

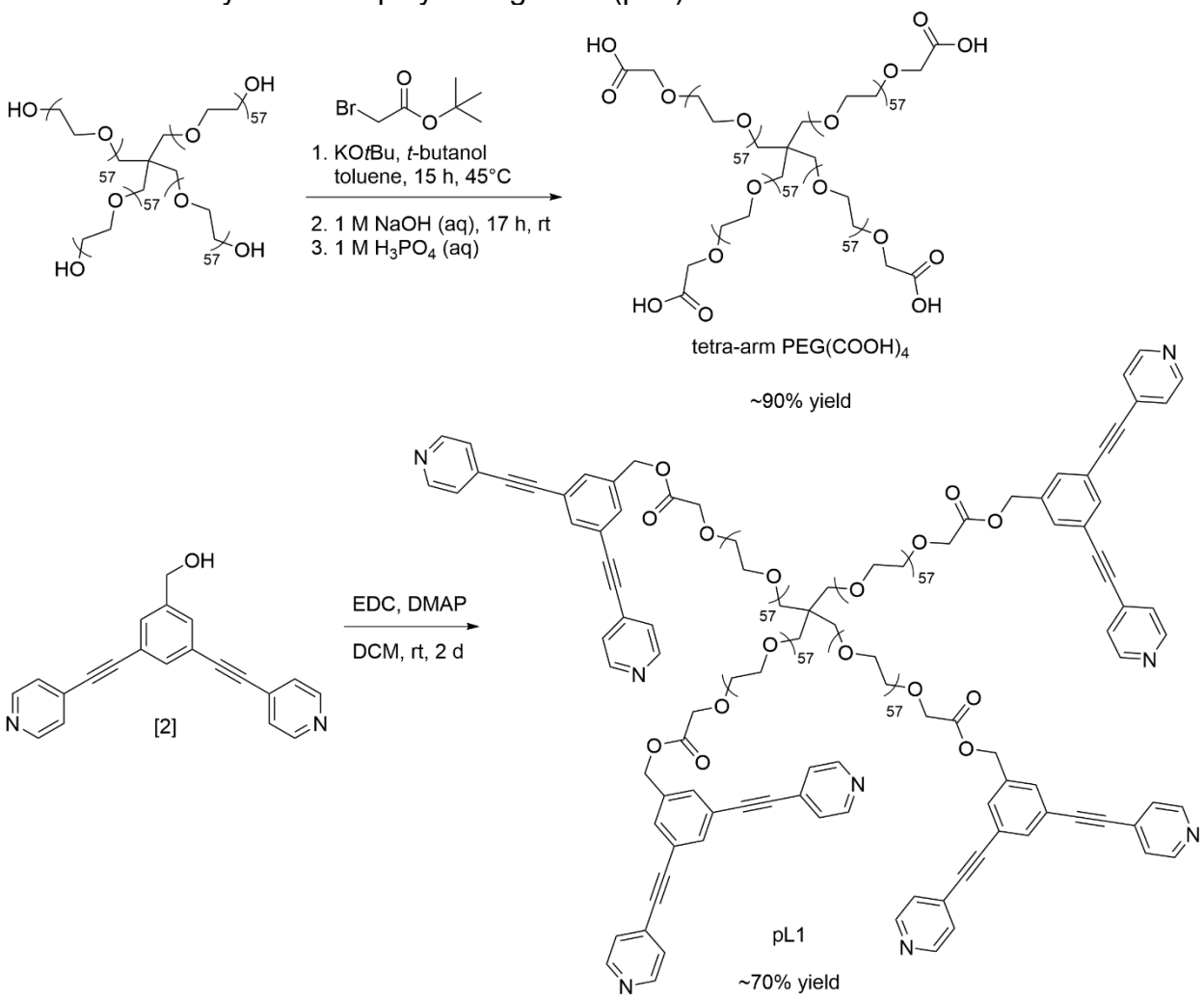

Tetra-arm PEG(COOH)$_4$ (10 kDa). The carboxylic acid end-functionalization of tetra-arm PEG was based off procedures detailed in US Patent 8,067,505 B2.[42] After azeotroping a solution of 10 kDa tetra-arm PEG(OH)$_4$ (2.00 g, 0.200 mmol) in toluene at reduced pressure, potassium tert-butoxide (229 mg, 2.00 mmol), tert-butanol (2.28 mL, 24.0 mmol), and dried toluene (28.4 mL) were added with stir bar. The reaction mixture was stirred for 3.5 h at 45 °C before the addition of tert-butyl bromoacetate (396 mL, 2.68 mmol). The reaction mixture was stirred at 45 °C for an additional 12 h under inert atmosphere before the toluene was removed under reduced pressure. The white solid was redissolved in 50 mL DI H_2O, and the pH was adjusted and maintained at 12 with 1

M NaOH for 17 h with stirring. The pH was then adjusted to 1.5 with 1 M phosphoric acid, after which the product was extracted with DCM (3 x 50 mL), dried with Na_2SO_4, filtered, and reduced to <10 mL in volume. The product was precipitated in cold diethyl ether, filtered, and dried, resulting in a white powder in ~90% yield (1.80 g, 0.180 mmol).

Polymer ligand 1 (pL1). Tetra-arm PEG(COOH)$_4$ (2.00 g, 0.200 mmol), [2] (404 mg, 1.30 mmol), *N*-(3-Dimethylaminopropyl)-*N*′-ethylcarbodiimide hydrochloride (EDC, 709 mg, 3.69 mmol), 4-(dimethylamino)pyridine (DMAP, 90.5 mg, 0.741 mmol), and DCM (50.0 mL) were added to an oven-dried flask with stir bar. The reaction mixture was allowed to stir for 2 d at rt before it was dialyzed in DCM with regenerated cellulose (RC) dialysis tubing (MWCO = 1 kDa) over 2 d, with at least 4 solvent changes. Dialyzed polymer was precipitated in cold Et_2O to produce a tan, powdery solid with ~70% yield (1.86 g, 1.86 mmol).
^{1}H NMR (500 MHz, $CDCl_3$) δ 8.65 (s, 14H), 7.71 (s, 3H), 7.57 (s, 7H), 7.40 (s, 14H), 5.20 (s, 8H), 4.25 (s, 8H), 3.64 (s, 1078H), 3.41 (s, 11H).
M_n (^{1}H NMR) = 9.3 kDa
GPC (0.025 M LiBr in DMF, 25 °C) M_W = 9.5 kDa, $Đ$ = 1.5

Scheme S16. Synthetic route to polymer ligand 2 (pL2).

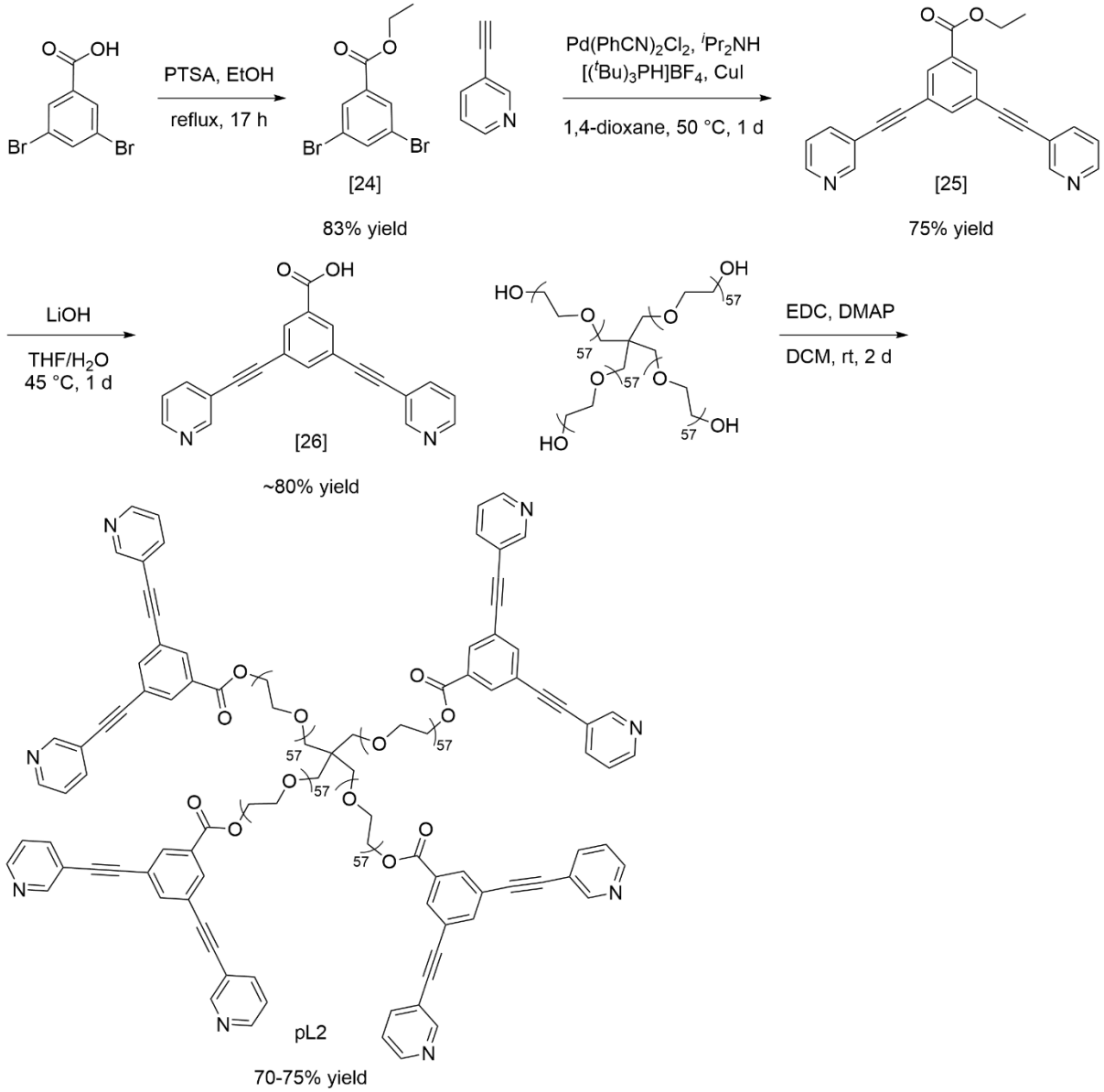

Ethyl 3,5-dibromobenzoate [24]. 3,5-dibromobenzoic acid (3.00 g, 10.7 mmol), *p*-toluenesulfonic acid monohydrate (3.00 g, 16.1 mmol), and ethanol (100. mL) were added to a 100 mL round bottom flask with stir bar. The reaction mixture was stirred under reflux for 17 h. The reaction was cooled to rt and dried under reduced pressure. The resulting light yellow solid was dissolved in 125 mL of EtOAc and washed with saturated $NaHCO_3$ (2 x 100 mL) and brine (1 x 100 mL). The organic layer was dried over $NaSO_4$, filtered, and concentrated on a rotary evaporator. Product was obtained at 83% yield (2.72 g, 8.88 mmol).
DART-HRMS (*m/z*) calculated for $C_9H_9O_2Br_2^+$ = 306.89638 $[M+H]^+$; found 306.89792
^{1}H NMR (600 MHz, $CDCl_3$) δ 8.10 (d, *J* = 1.8 Hz, 2H), 7.84 (t, *J* = 1.8 Hz, 1H), 4.39 (q, *J* = 7.1 Hz, 2H), 1.40 (t, *J* = 7.1 Hz, 3H).

^{13}C-{^{1}H} NMR (151 MHz, $CDCl_3$) δ 164.17, 164.15, 138.3, 133.83, 133.82, 131.5, 123.1, 62.0, 14.4.
Synthesized by David J. Lundberg at MIT.

Ethyl 3,5-bis(pyridin-3-ylethynyl)benzoate [25]. See general Sonogashira coupling procedure above. Reagents: [24] (2.00 g, 6.54 mmol), 3-ethynylpyridine (1.74 g, 16.9 mmol), $Pd(NCC_6H_5)_2Cl_2$ (186 mg, 0.485 mmol), $[(t\text{-}Bu)_3PH]BF_4$ (226 mg, 0.779 mmol), Cu(I)I (43.8 mg, 0.230 mmol), dry dioxane (75.0 mL), diisopropylamine (9.43 mL, 67.3 mmol). Product was obtained at 75% yield (1.73 g, 4.91 mmol).
DART-HRMS (*m/z*) calculated for $C_{23}H_{17}N_2O_2^+$ = 353.12845 [*M*+H]$^+$; found 353.13003
^{1}H NMR (600 MHz, $CDCl_3$) δ 8.79 (d, *J* = 2.1 Hz, 2H), 8.59 (dd, *J* = 4.9, 1.7 Hz, 2H), 8.19 (d, *J* = 1.6 Hz, 2H), 7.89 (t, *J* = 1.6 Hz, 1H), 7.85 (dt, *J* = 7.9, 1.9 Hz, 2H), 7.35 – 7.30 (m, 2H), 4.43 (q, *J* = 7.1 Hz, 2H), 1.44 (t, *J* = 7.1 Hz, 3H).
^{13}C-{^{1}H} NMR (151 MHz, $CDCl_3$) δ 165.2, 152.3, 149.0, 138.9, 138.4, 132.9, 131.6, 123.7, 123.4, 120.1, 90.9, 87.6, 61.8, 14.5.
Synthesized by David J. Lundberg at MIT.

3,5-bis(pyridin-3-ylethynyl)benzoic acid [26]. [25] (1.00 g, 2.84 mmol), lithium hydroxide (0.340 g, 14.2 mmol), and THF (~25 mL), DI H_2O (~5 mL) were added to a 40 mL vial with stir bar. The reaction was stirred at 45 °C overnight or until TLC indicated the complete absence of starting material. The reaction mixture was concentrated under reduced pressure, then diluted with DI H_2O (~40 mL). The mixture was cooled in an ice bath and stirred. Product was precipitated by adjusting the pH to 4 using 1 M HCl, then collected by vacuum filtration. The precipitate was dried under vacuum to afford the product with small impurities in ~80% yield (736 mg, 2.27 mmol).
DART-HRMS (*m/z*) calculated for $C_{21}H_{13}N_2O_2^+$ = 325.09715 [*M*+H]$^+$; found 325.09736
^{1}H NMR (600 MHz, DMSO-d_6) δ 8.82 (d, *J* = 2.1 Hz, 2H), 8.64 – 8.61 (m, 2H), 8.12 (s, 2H), 8.04 (dd, *J* = 7.8, 2.2 Hz, 3H), 7.50 (dd, *J* = 7.9, 4.9 Hz, 2H).*
^{13}C-{^{1}H} NMR (151 MHz, DMSO-d_6) δ 165.7, 151.9, 149.5, 138.8, 137.6, 132.3, 123.7, 123.0, 118.8, 90.2, 87.8, 54.9, 40.1, 30.7.*
Synthesized by David J. Lundberg at MIT.
*Higher quality NMR spectra could not be obtained due to Spring 2020 COVID-19 shutdown of MIT research facilities.

Polymer ligand 2 (pL2). [26] (0.200 g, 0.615 mmol), $PEG(OH)_4$ (10 kDa, 1.03 g, 0.103 mmol), EDC (196 mg, 1.03 mmol), and DMAP (76.0 mg, 0.615 mmol were added to an oven-dried 40 mL vial with stir bar under N_2. Anhydrous DCM (10.0 mL) was added via syringe, after which the reaction mixture was left to stir at rt for 24 h. The reaction mixture was diluted to approximately 125 mL with DCM and washed with saturated $NaHCO_3$ solution (2 x 100 mL) and once with brine (100 mL). The organic phase was dried over Na_2SO_4, filtered, and concentrated on a rotary evaporator. The product was precipitated from a minimal amount of DCM in cold Et_2O and collected by vacuum filtration. The polymer was then purified with prepGPC ($CHCl_3$). Product was obtained at 70–75% yield.

^{1}H NMR (600 MHz, $CDCl_3$) δ 9.18 – 8.38 (m, 12H), 8.20 (d, J = 1.6 Hz, 7H), 7.92 – 7.82 (m, 10H), 7.41 (s, 7H), 4.54 – 4.48 (m, 7H), 3.88 – 3.82 (m, 7H), 3.76 – 3.46 (m, 835H), 3.40 (s, 8H).
M_n (^{1}H NMR) = 9.2 kDa
GPC (0.025 M LiBr in DMF, 25 °C) M_W = 9.1 kDa, $Đ$ = 1.0
Synthesized by David J. Lundberg at MIT.

3-(3-(prop-2-yn-1-yloxy)-2,2-bis((prop-2-yn-1-yloxy)methyl)propoxy)prop-1-yne [27].
This compound was synthesized according to literature procedure (Reference 43).
DART-HRMS (*m/z*) calculated for $C_{17}H_{24}NO_4^+$ = 306.16998 [M+NH_4]$^+$; found 306.17129
^{1}H NMR (600 MHz, $CDCl_3$) δ 4.12 (d, J = 2.4 Hz, 8H), 3.53 (s, 8H), 2.40 (d, J = 4.8 Hz, 3H).
^{13}C-{^{1}H} NMR (151 MHz, $CDCl_3$) δ 80.2, 74.2, 69.2, 58.9, 44.9.
Synthesized by Dr. Nathan J. Oldenhuis at MIT.

Linear PEG bis(azide) (2 kDa). This compound was synthesized according to literature procedure (Reference 44).
^{1}H NMR (600 MHz, $CDCl_3$) δ 3.62 (d, J = 14.1 Hz, 196H), 3.35 (t, J = 5.1 Hz, 4H).
M_n (^{1}H NMR) = 2.2 kDa
GPC-MALS (0.025 M LiBr in DMF, 25 °C) M_n = 2.0 kDa, M_W = 2.2 kDa, $Đ$ = 1.1.
Synthesized by Dr. Nathan J. Oldenhuis at MIT.

$Pt(MeCN)_4(OTf)_2$. This compound was synthesized according to literature procedure (Reference 45).

Scheme S17. Self-assembly of pL1 with platinum metal salt and free ligand to form $M_{12}L_{24}$-based polyMOC gels for water purification.

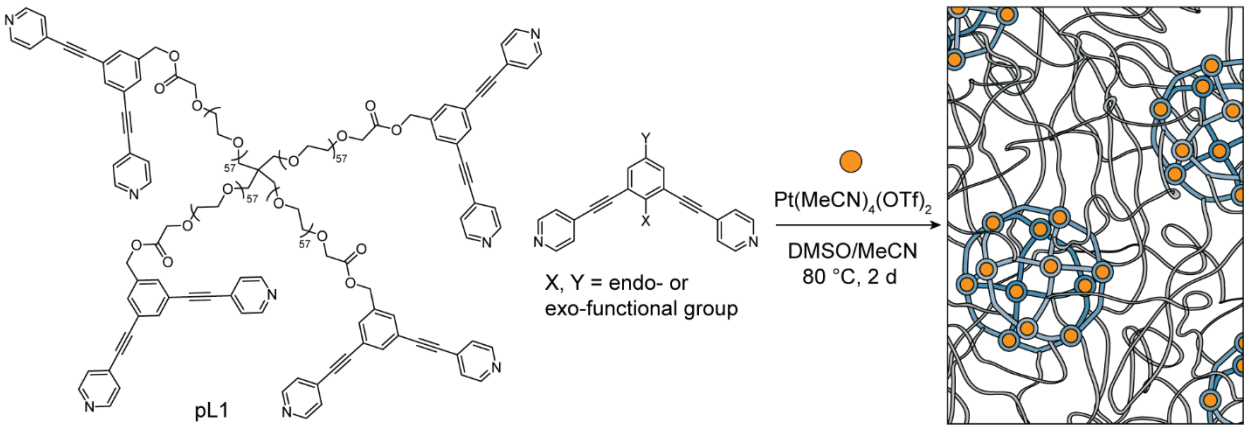

$M_{12}L_{24}$-based gel synthesis and solvent exchange. $Pt_{12}L_{24}$-based polyMOC gels were formed from pL1 (1 equiv.), $Pt(MeCN)_4(OTf)_2$ (0.7 equiv.), and free ligand (20 equiv.), which amounts to a polymer ligand/free ligand ratio of 1:5. pL1 was dissolved in DMSO to make a stock solution with a concentration of 60.0 mg/mL, and Pt(II) salt was dissolved in MeCN at a concentration of 331 mg/mL. To form one gel, pL1 stock solution (250. µL, 1.50 µmol) was added to free ligand (30.0 mmol) in a 4 mL scintillation vial, which was mixed through light heating and vortexing. Pt(II) stock

solution (50.0 µL, 25.2 µmol) was added to the pL1 and free ligand mixture. The vial was capped with N_2 and sealed tightly before annealing for 2 d at 80 °C. After cooling to rt, the gel was broken out of the vial.

Gels were washed using DCM reflux in a Soxhlet extractor for at least 6 h, after which they were transferred into 10 mL of acetone and soaked for 2–3 h at rt on an orbital shaker. The acetone was replaced and the gel was soaked again for 2–3 h. This process was repeated in DI H_2O twice before gels were used in absorption studies.

Scheme S18. Formation of M_2L_4-based polyMOC networks through the self-assembly of pL2 with $Pt(MeCN)_4(OTf)_2$.

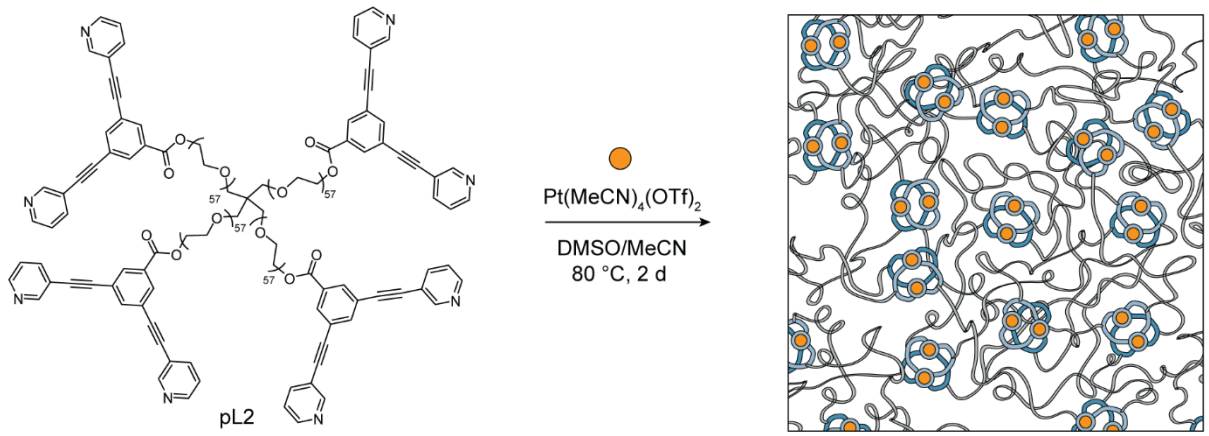

<u>M_2L_4-based gel (control) synthesis and solvent exchange.</u> Pt_2L_4-based polyMOC gels were formed from pL2 (1 equiv.) and $Pt(MeCN)_4(OTf)_2$ (2.1 equiv.) pL2 was dissolved in DMSO to make a stock solution with a concentration of 60.0 mg/mL, and Pt(II) salt was dissolved in MeCN at a concentration of 42.5 mg/mL. To form one gel, pL2 stock solution (250. µL, 1.50 µmol) was mixed with Pt(II) stock solution (50.0 µL, 3.23 µmol) in a 4 mL vial. The vial was capped with N_2 and sealed tightly before annealing for 2 d at 80 °C. After cooling to rt, the gel was broken out of the vial.

Gels were soaked in 10 mL of DCM for 2–3 h at rt on an orbital shaker, after which the DCM was replaced and the process was repeated. The gel was then transferred to acetone (x 2), followed by DI H_2O (x 2) before gels were used in absorption studies.

Scheme S19. A_4 + B_2 azide-alkyne click reaction to form a covalently crosslinked polymer network.

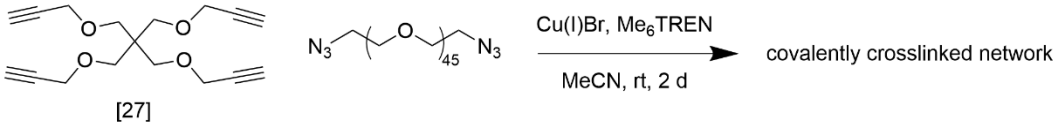

<u>Covalent click gel (control) synthesis and solvent exchange.</u> Covalently linked polymer networks were formed from [27] (1 equiv.), linear PEG bis(azide) (2 kDa, 2 equiv.), Cu(I)Br (4 equiv.), and Me_6TREN (4.4 equiv.) in MeCN to achieve 10 wt% gels. Preweighed amounts of [27], linear PEG bis(azide), and Cu(I)Br were brought into a N_2

glovebox with degassed Me_6TREN. Stock solutions in MeCN were made for [27] (29.4 mg/mL) and PEG bis(azide) (135 mg/mL). Cu(I)Br/Me_6TREN stock solution was made at a 1:1.1 ratio, with a final Cu(I)Br concentration of 58.5 mg/mL. To form a gel, [27] stock solution (36.8 µL, 3.75 µmol) was mixed with PEG stock solution (111 µL, 7.50 µmol) and Cu(I)Br/Me_6TREN stock solution (36.8 µL, 15.0 µmol Cu(I)Br). The mixture was lightly vortexed, sealed, and left to gel at rt for 2 d. Gels were removed from the glovebox and broken out of the vial.

Gels were soaked in 10 mL of DCM for 2–3 h at rt on an orbital shaker, after which the DCM was replaced and the process was repeated. The gel was then transferred to acetone (x 2), followed by DI H_2O (x 2) before gels were used in absorption studies.

Water purification of aromatic compounds. Gels were prepared as described above. After solvent exchange, samples were immersed in 10 mL of 0.1 mM solutions of selected absorbate (bisphenol A, metolachlor, coumarin) and soaked for 24 h at rt without stirring. Solutions were then removed for UV-Vis characterization. Calibration curves with known concentrations of absorbate were used for quantitative analysis of absorption.

Water purification of perfluoroalkyl substances (PFAS). Gels were prepared as described above. Following solvent exchange, samples were immersed in 10 mL of 160 µg/L perfluorooctanoic acid (PFOA) solution with stir bar at rt. 50 µL aliquots were collected every hour over the course of 8 h and analyzed using LC-MS in SIM. Mass chromatogram area integrations of negative ion 369 (PFOA with detached carboxylic group) were used to quantify the amount of PFOA remaining in solution over time. Area integrations were correlated to PFOA concentration through calibration curves.

Quantitative NMR studies to determine mechanism of PFOA absorption. Gels 1, 4, and 5 were placed in NMR tubes with ~0.4 mg/mL solutions of PFOA, octanoic acid, and perfluorooctanol (PFOH) in D_2O (Fig. S1). Octanoic acid and perfluorooctanol served as controls and were chosen to isolate fluorous and electrostatic interactions contributing to PFOA absorption. Trifluoroethanol (TFE) was added to absorbate solutions (~0.4 mg/mL) to provide an internal standard that could be used across ^1H and ^{19}F NMR spectroscopy. ^1H and ^{19}F NMR spectra were taken of adsorbate solutions before the addition of pre-massed gels, after which gels were soaked for 24 h before the sample was characterized again.

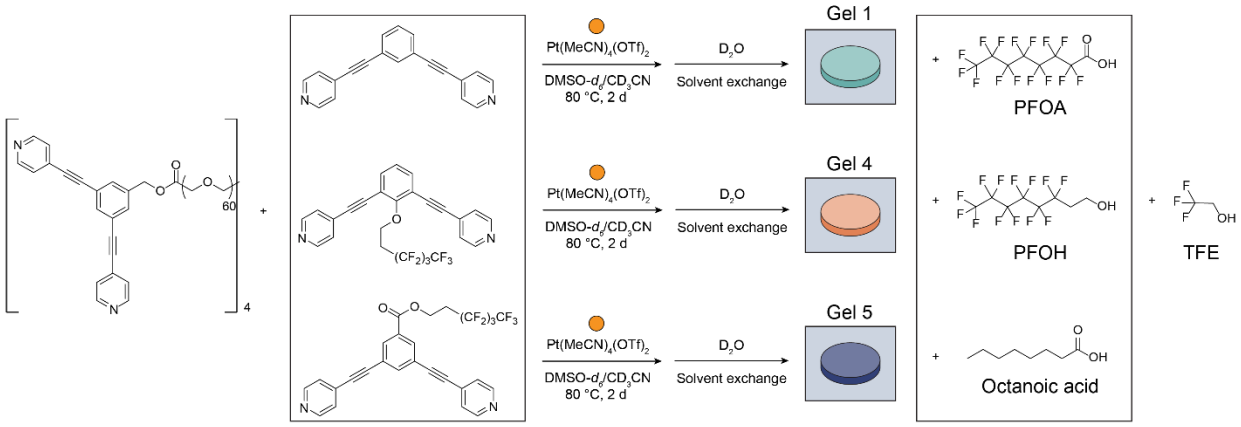

Figure S1. Gel 1, 4, and 5 assembly and processing for quantitative NMR experiments with absorbates PFOA, PFOH, and octanoic acid. TFE is added as an internal standard.

NMR spectra were processed as normal (phasing and baseline correction) before the integration of each spectrum was normalized to TFE. The area of integration was then recorded for the absorbate as well as the triflate anion peaks, before and after the addition of the gel. Total absorption was quantified by the change in absorbate peak area, and relative electrostatic contributions to absorption were calculated by dividing the triflate peak area by total absorption.

3.5 Supplementary

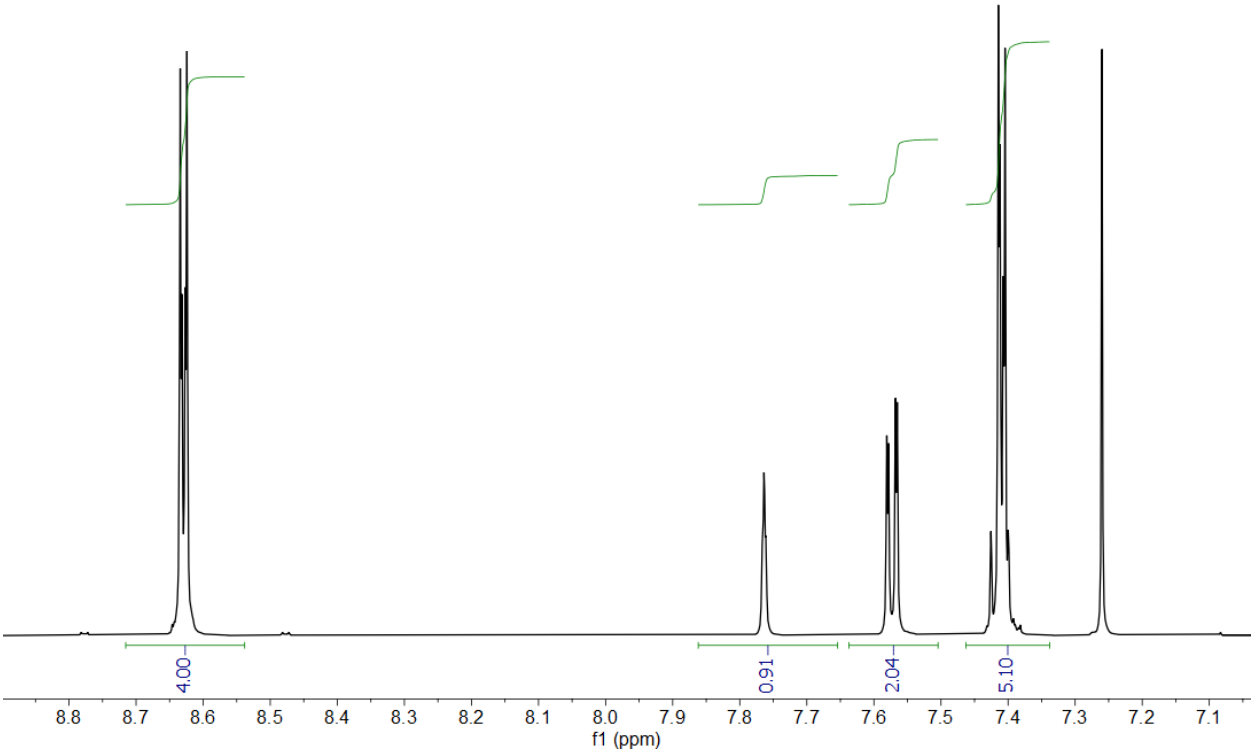

Figure S2. ^{1}H NMR ($CDCl_3$, 600 MHz, 25 °C) spectrum of 1,3-bis(pyridin-4-ylethynyl)benzene [1].

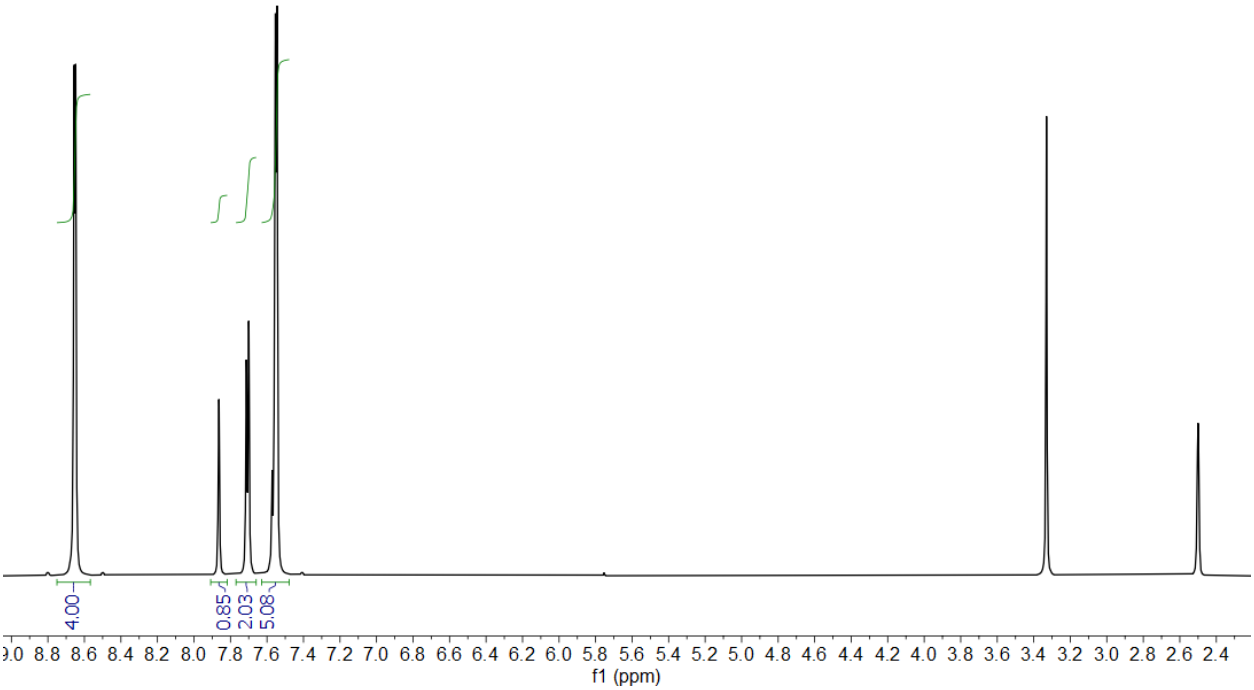

Figure S3. ^{1}H NMR (DMSO-d_6, 600 MHz, 25 °C) spectrum of 1,3-bis(pyridin-4-ylethynyl)benzene [1].

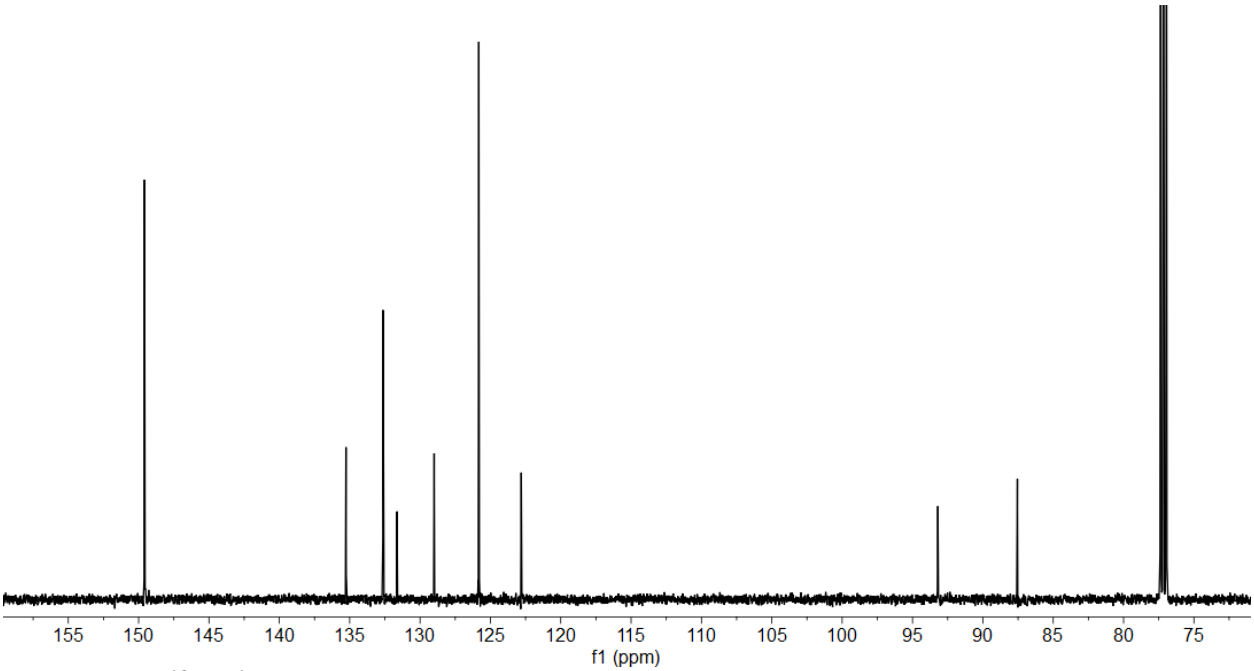

Figure S4. ^{13}C-{^{1}H} NMR ($CDCl_3$, 151 MHz, 25 °C) spectrum of 1,3-bis(pyridin-4-ylethynyl)benzene [1].

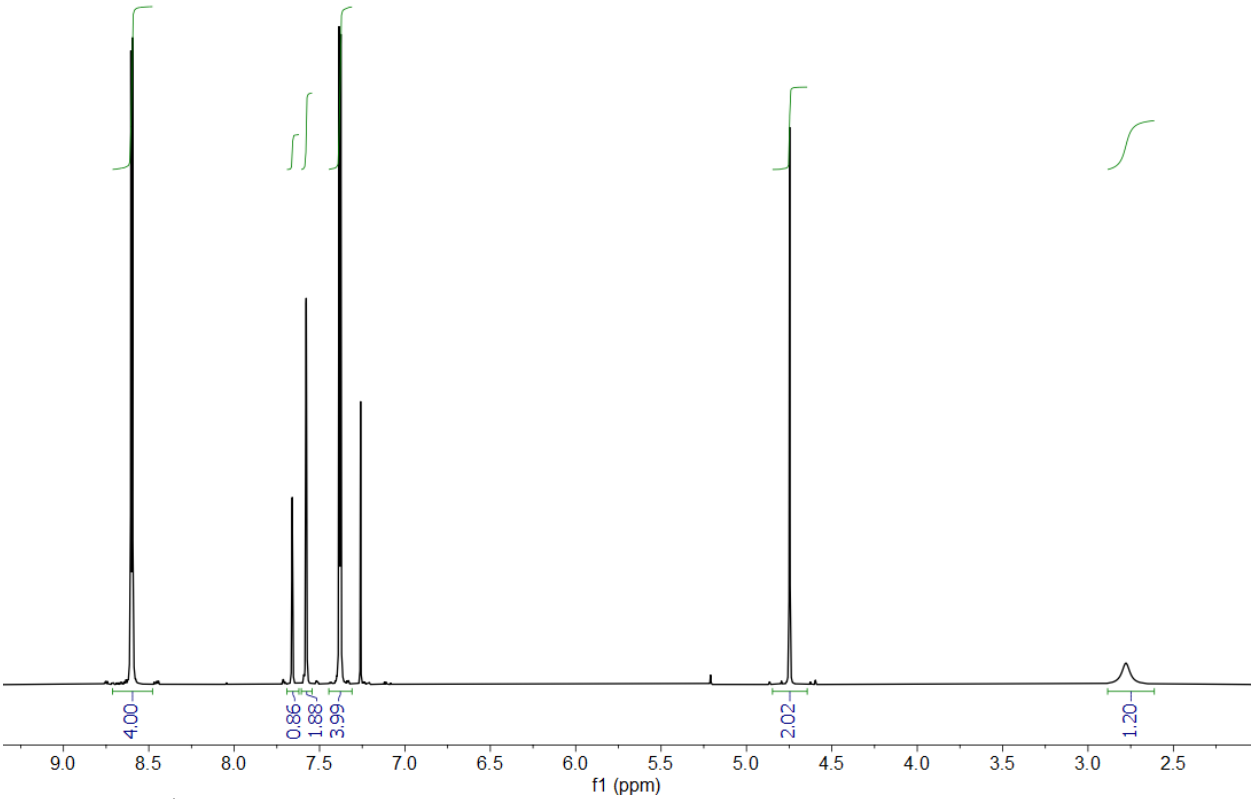

Figure S5. ^{1}H NMR ($CDCl_3$, 600 MHz, 25 °C) spectrum of (3,5-bis(pyridin-4-ylethynyl)phenyl)methanol [2].

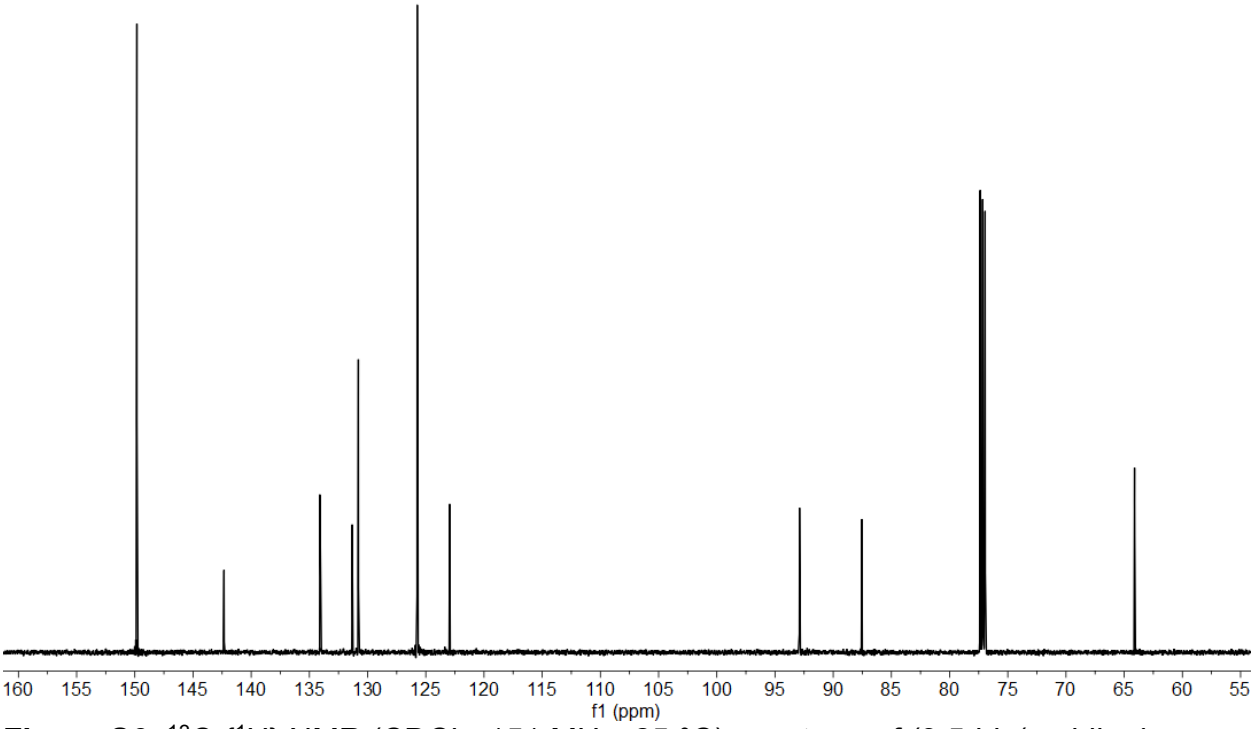

Figure S6. ^{13}C-{^{1}H} NMR ($CDCl_3$, 151 MHz, 25 °C) spectrum of (3,5-bis(pyridin-4-ylethynyl)phenyl)methanol [2].

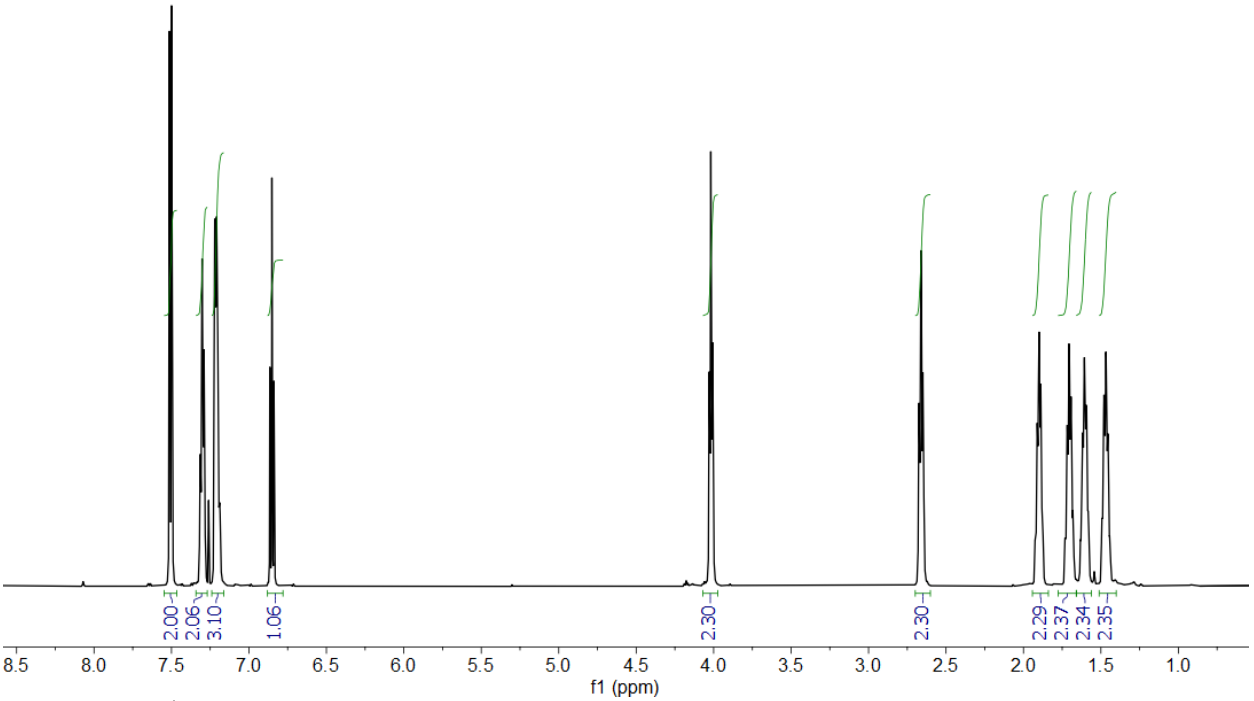

Figure S7. ^{1}H NMR ($CDCl_3$, 600 MHz, 25 °C) spectrum of 1,3-dibromo-2-((6-phenylhexyl)oxy)benzene [3].

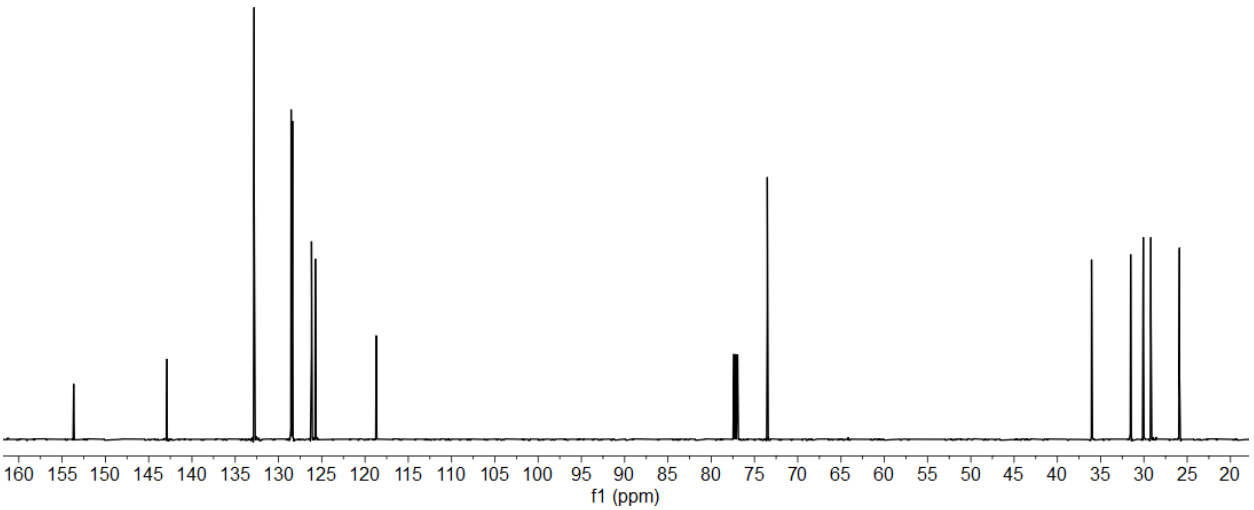

Figure S8. ^{13}C-{^{1}H} NMR ($CDCl_3$, 151 MHz, 25 °C) spectrum of 1,3-dibromo-2-((6-phenylhexyl)oxy)benzene [3].

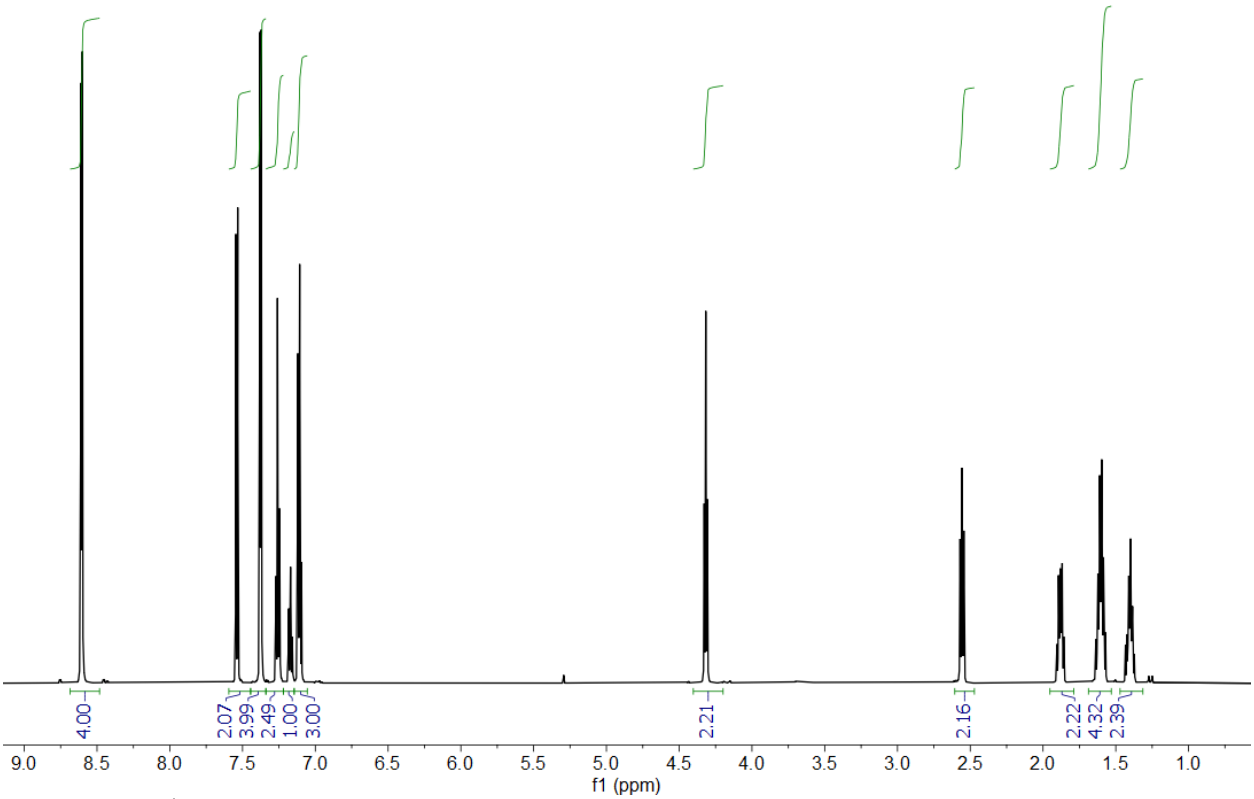

Figure S9. ^{1}H NMR ($CDCl_3$, 600 MHz, 25 °C) spectrum of 4,4'-((2-((6-phenylhexyl)oxy)-1,3-phenylene)bis(ethyne-2,1-diyl))dipyridine [4].

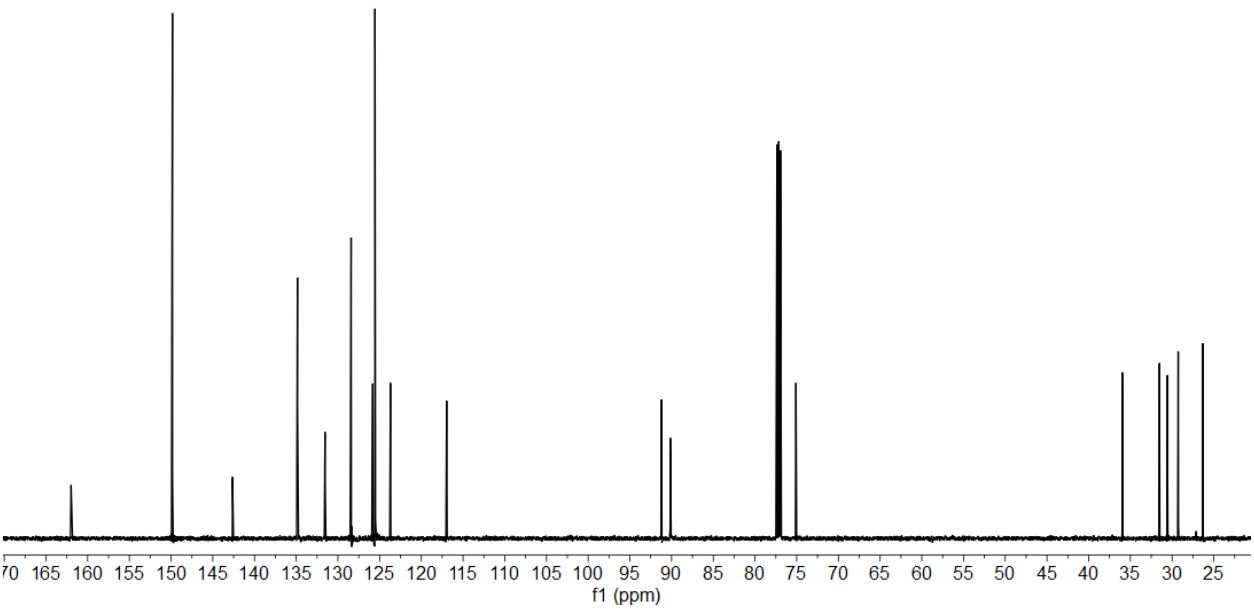

Figure S10. ^{13}C-{^{1}H} NMR ($CDCl_3$, 151 MHz, 25 °C) spectrum of 4,4'-((2-((6-phenylhexyl)oxy)-1,3-phenylene)bis(ethyne-2,1-diyl))dipyridine [4].

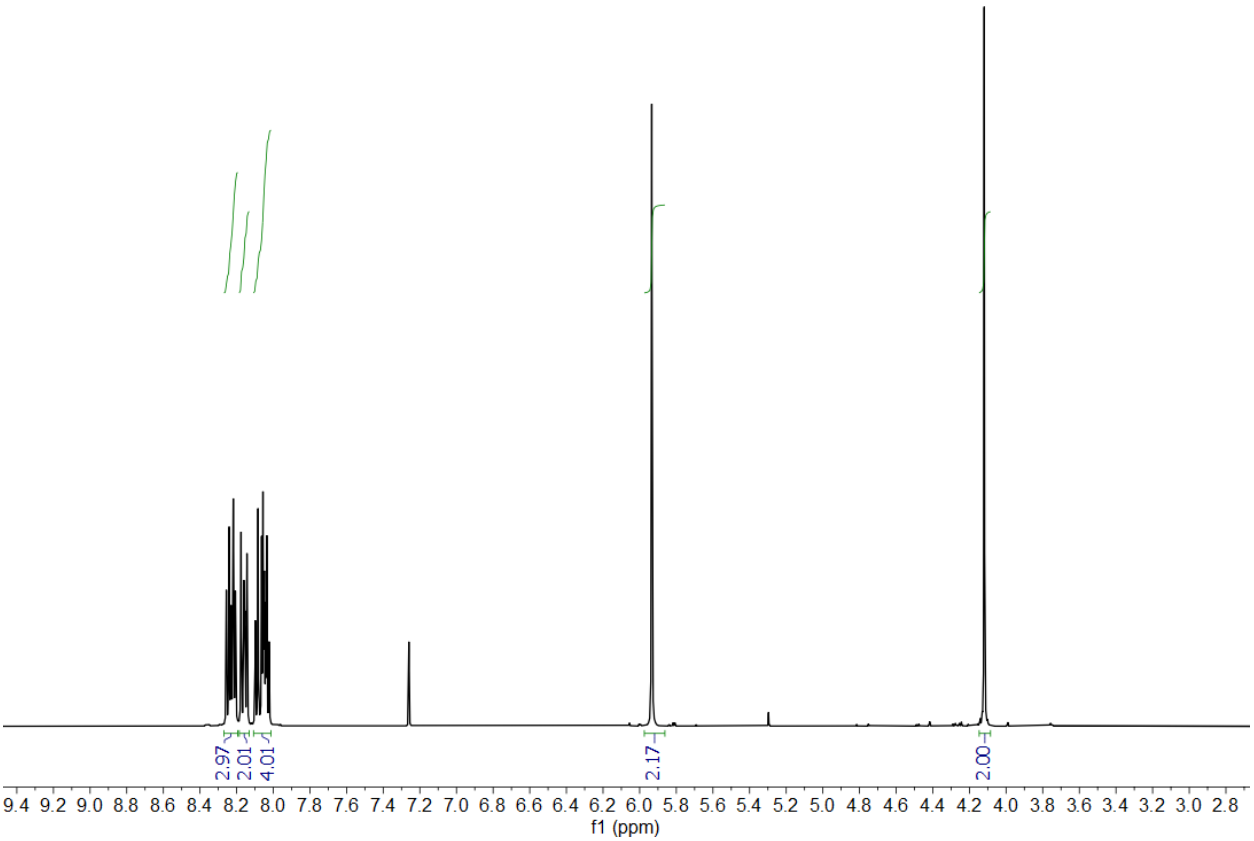

Figure S11. ^{1}H NMR ($CDCl_3$, 600 MHz, 25 °C) of pyren-1-ylmethyl 2-chloroacetate [5].

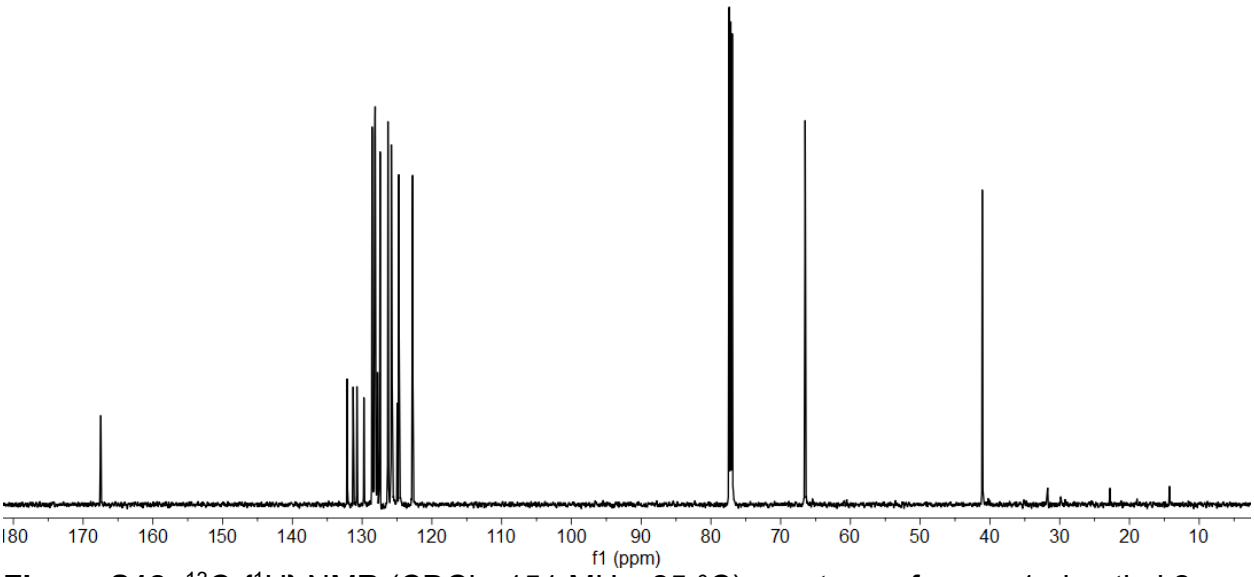

Figure S12. ^{13}C-{^{1}H} NMR ($CDCl_3$, 151 MHz, 25 °C) spectrum of pyren-1-ylmethyl 2-chloroacetate [5]. The rightmost peaks (35 – 15 ppm) are unassigned and assumed to be impurities.

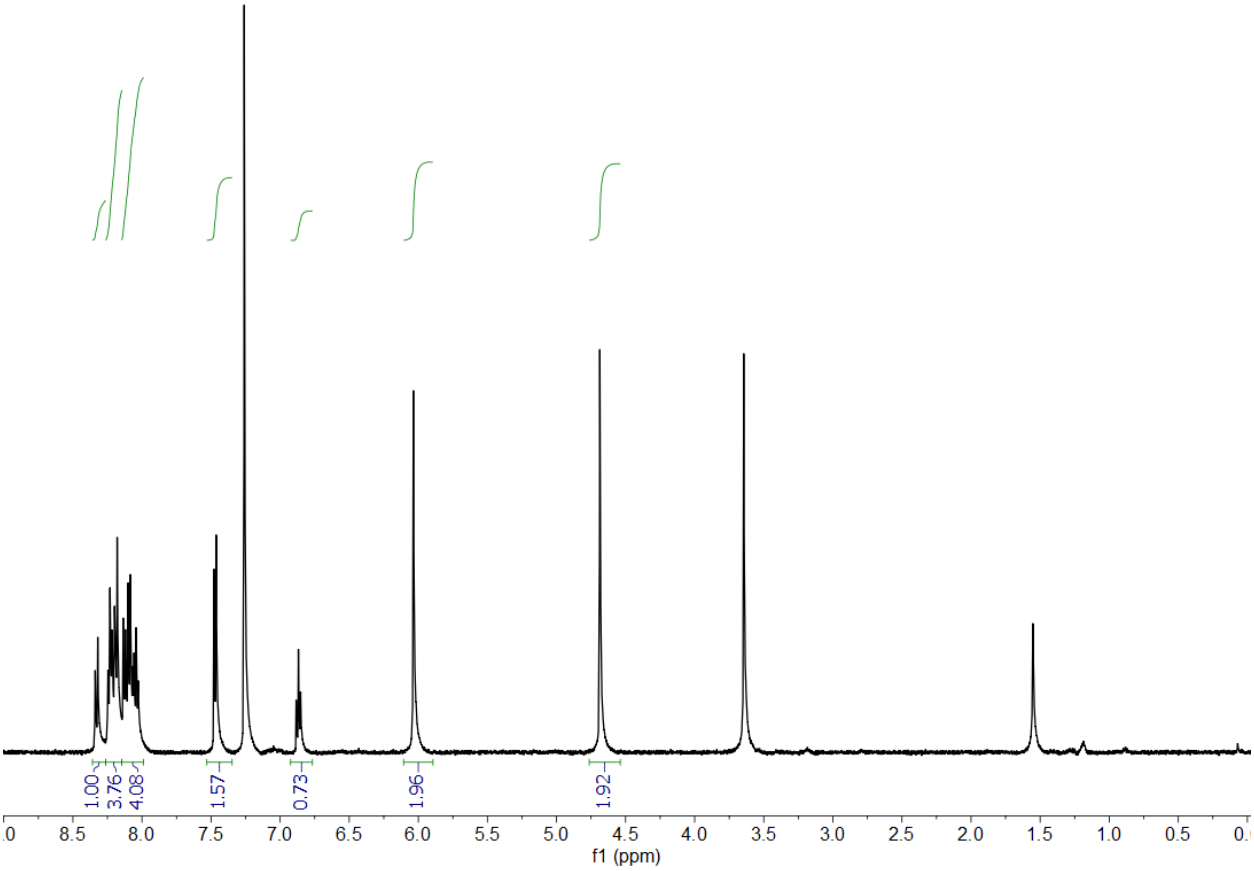

Figure S13. ^{1}H NMR ($CDCl_3$, 500 MHz, 25 °C) spectrum of pyren-1-ylmethyl 2-(2,6-dibromophenoxy)acetate [6]. Impurities at 3.63 and 1.54 ppm were not removed due to time restrictions caused by the Spring 2020 COVID-19 shutdown of MIT research facilities. These impurities did not affect subsequent reaction steps.

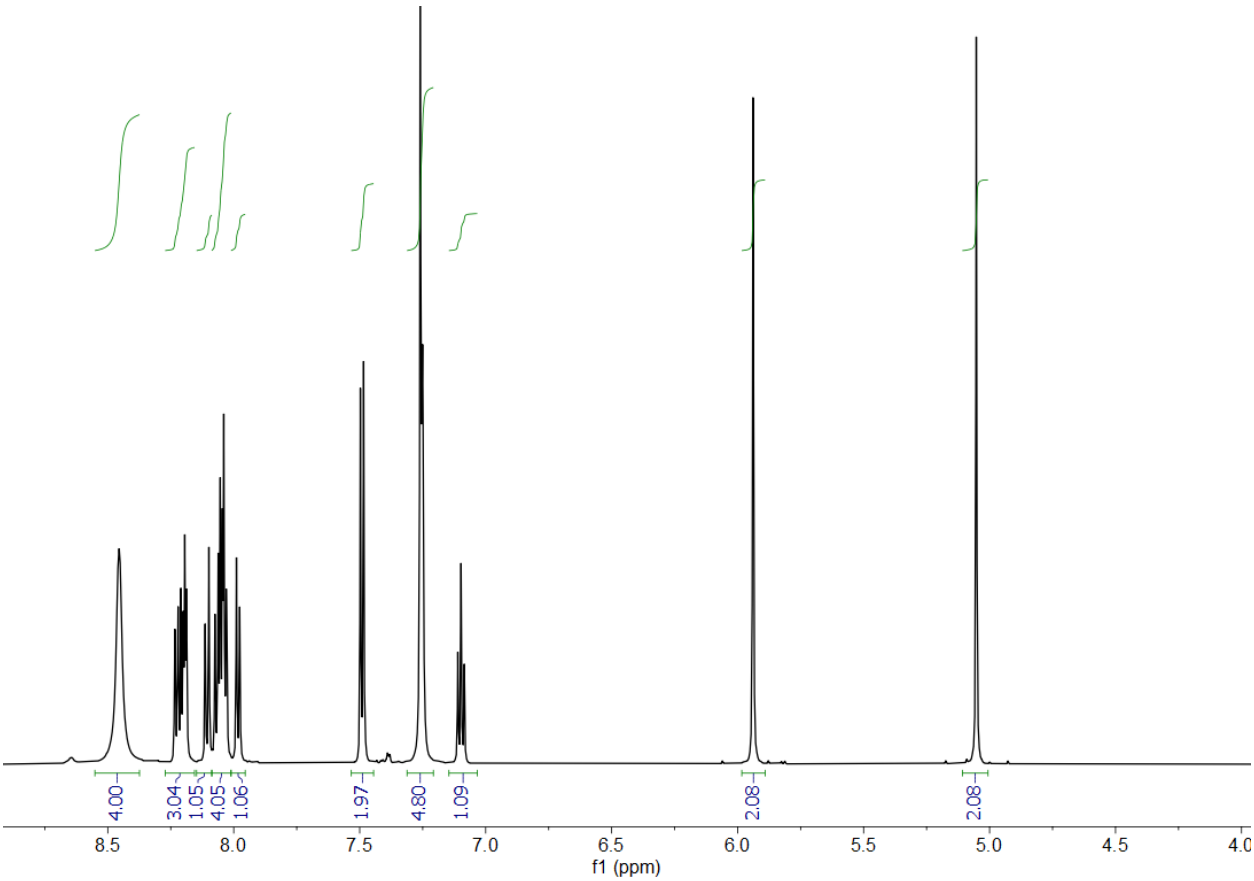

Figure S14. ^{1}H NMR ($CDCl_3$, 600 MHz, 25 °C) spectrum of pyren-1-ylmethyl 2-(2,6-bis(pyridin-4-ylethynyl)phenoxy)acetate [7].

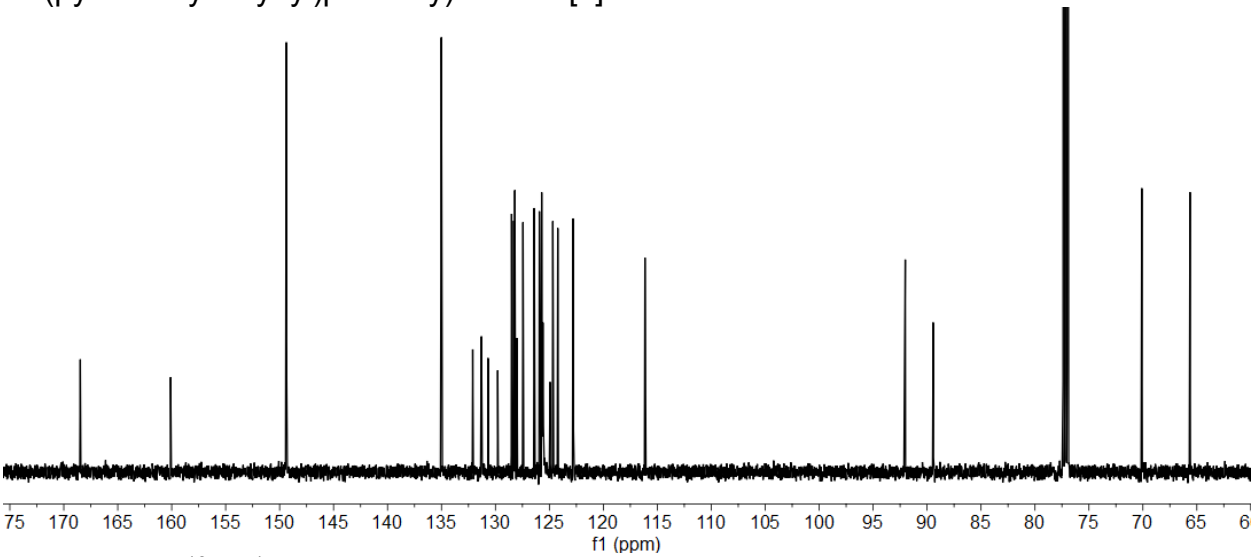

Figure S15. ^{13}C-{^{1}H} NMR ($CDCl_3$, 151 MHz, 25 °C) spectrum of pyren-1-ylmethyl 2-(2,6-bis(pyridin-4-ylethynyl)phenoxy)acetate [7].

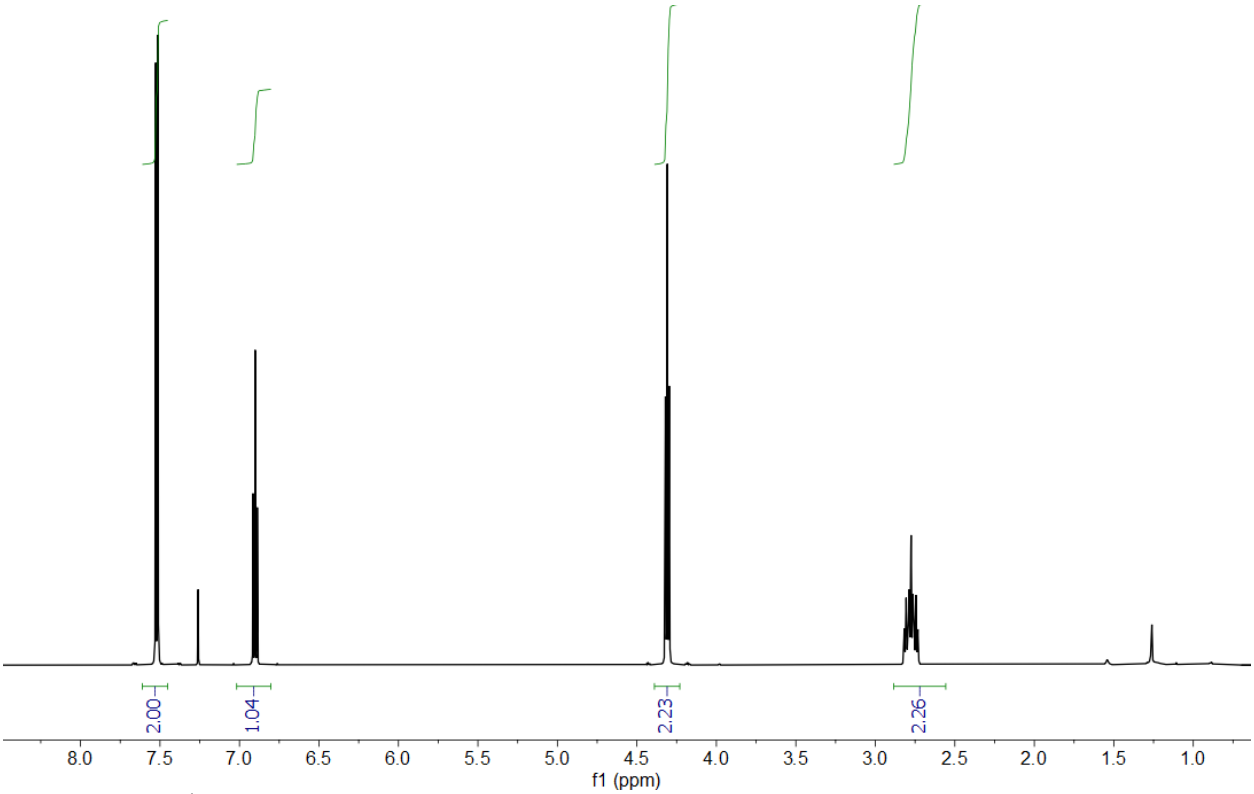

Figure S16. ^{1}H NMR ($CDCl_3$, 600 MHz, 25 °C) spectrum of 1,3-dibromo-2-((3,3,4,4,5,5,6,6,6-nonafluorohexyl)oxy)benzene [8].

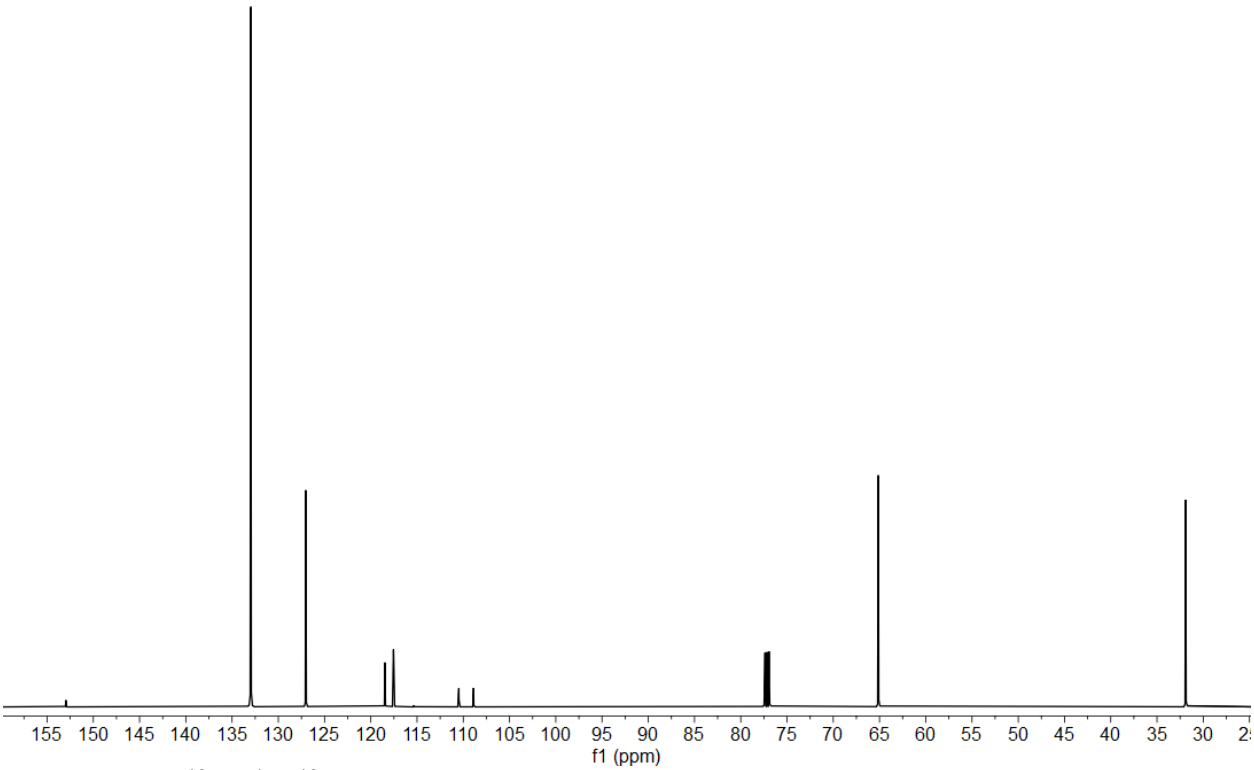

Figure S17. ^{13}C-{^{1}H,^{19}F} NMR ($CDCl_3$, 151 MHz, 25 °C) spectrum of 1,3-dibromo-2-((3,3,4,4,5,5,6,6,6-nonafluorohexyl)oxy)benzene [8].

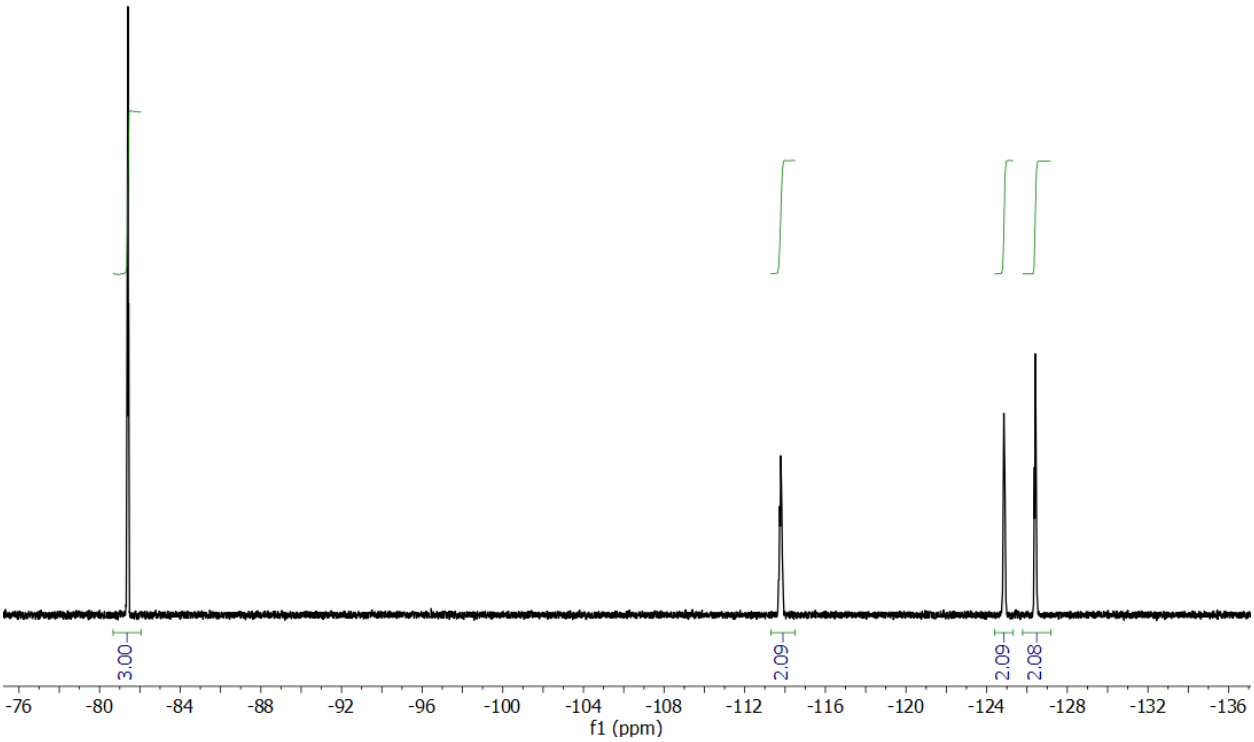

Figure S18. ^{19}F NMR (282 MHz, $CDCl_3$, 25 °C) spectrum of 1,3-dibromo-2-((3,3,4,4,5,5,6,6,6-nonafluorohexyl)oxy)benzene [8].

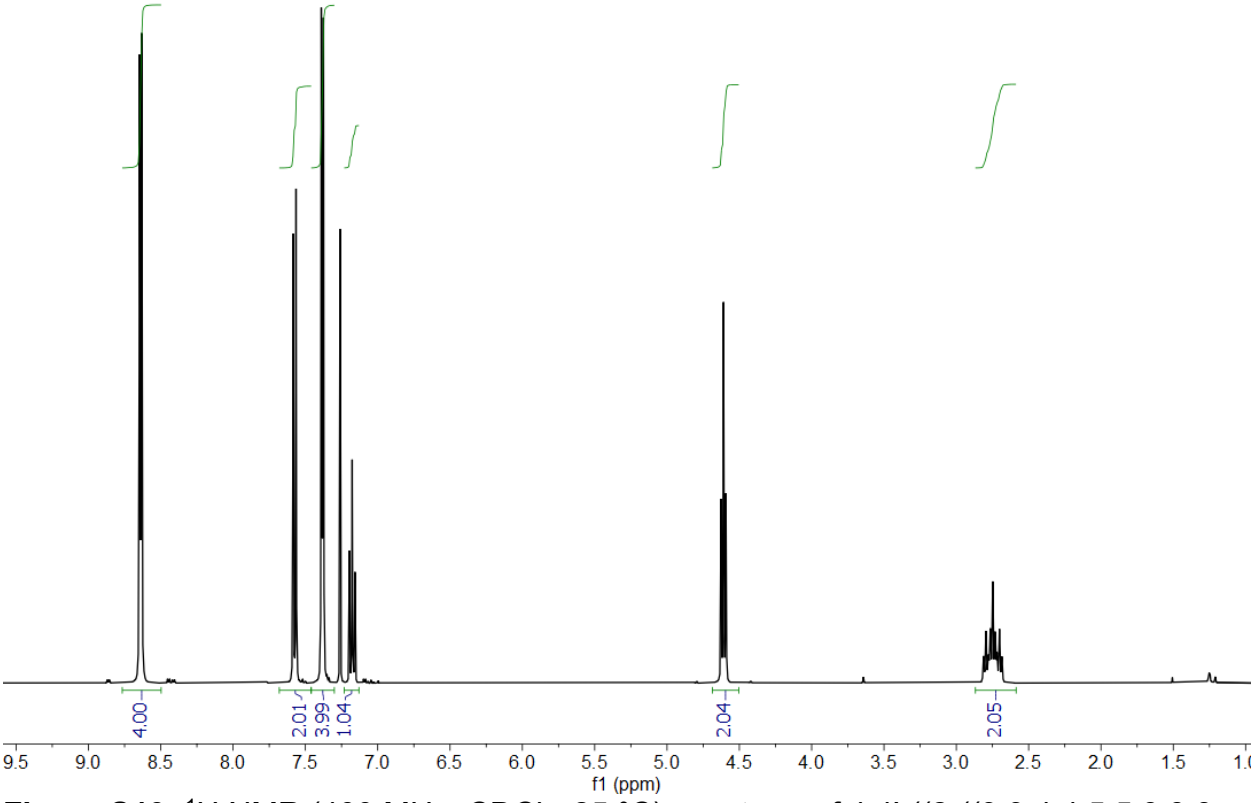

Figure S19. ^{1}H NMR (400 MHz, $CDCl_3$, 25 °C) spectrum of 4,4'-((2-((3,3,4,4,5,5,6,6,6-nonafluorohexyl)oxy)-1,3-phenylene)bis(ethyne-2,1-diyl))dipyridine [9].

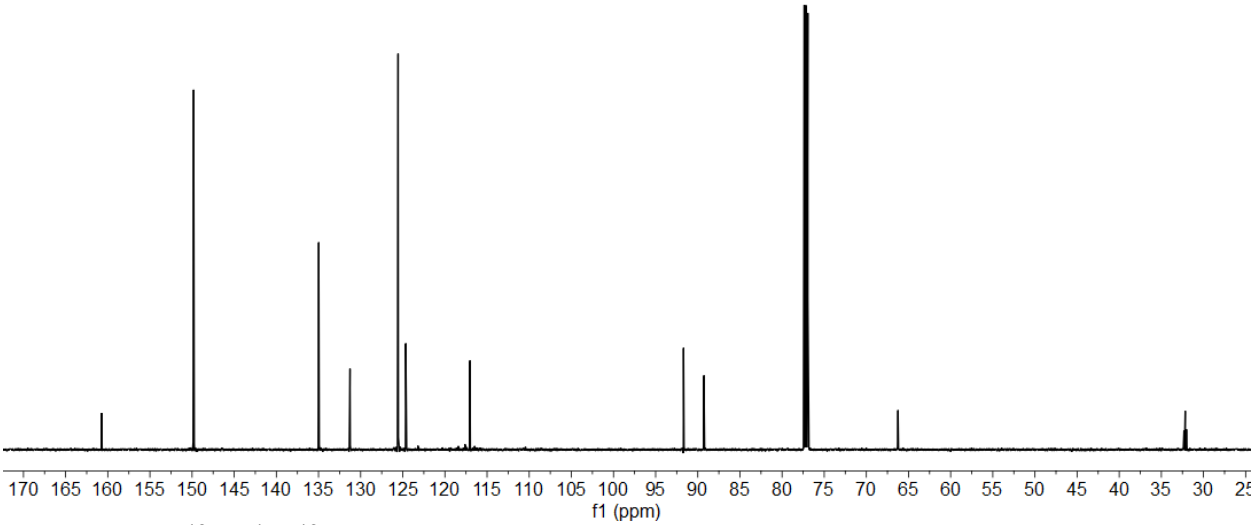

Figure S20. ^{13}C-{^{1}H,^{19}F} NMR ($CDCl_3$, 151 MHz, 25 °C) of 4,4'-((2-((3,3,4,4,5,5,6,6,6-nonafluorohexyl)oxy)-1,3-phenylene)bis(ethyne-2,1-diyl))dipyridine [9].

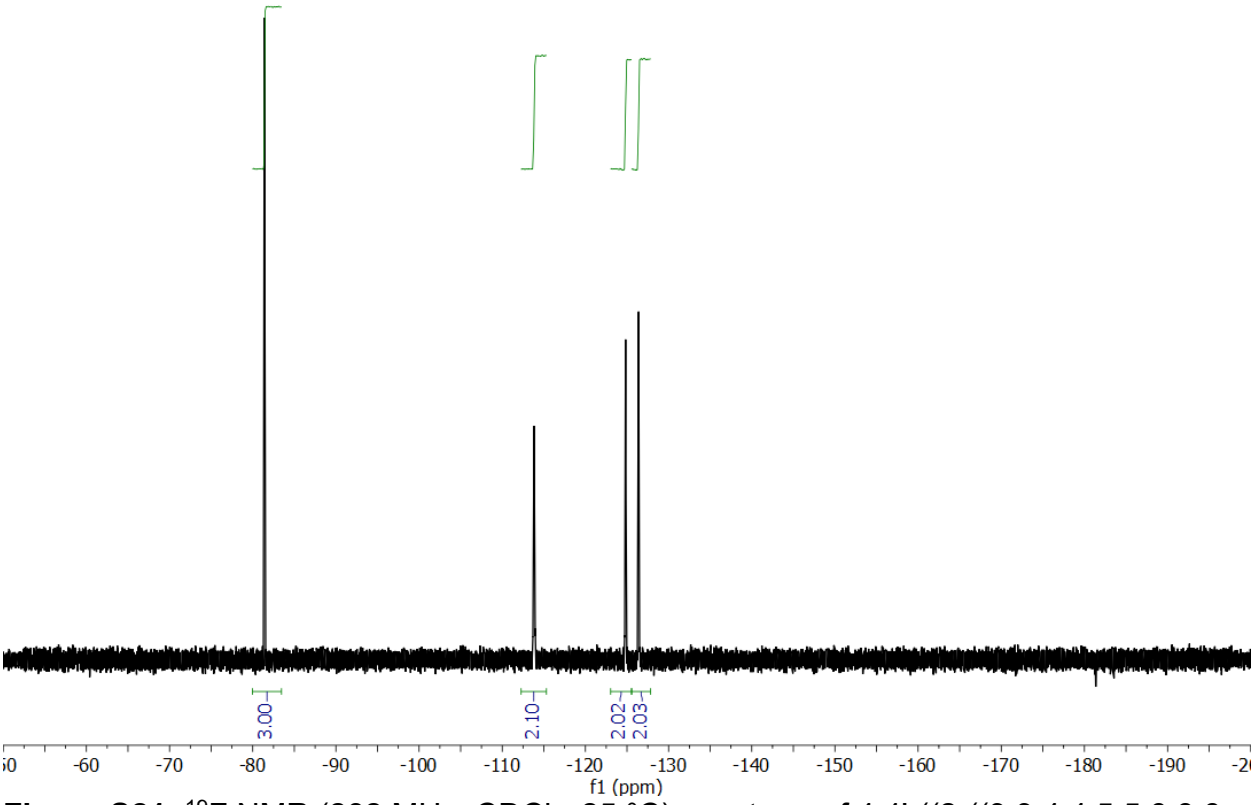

Figure S21. ^{19}F NMR (282 MHz, $CDCl_3$, 25 °C) spectrum of 4,4'-((2-((3,3,4,4,5,5,6,6,6-nonafluorohexyl)oxy)-1,3-phenylene)bis(ethyne-2,1-diyl))dipyridine [9].

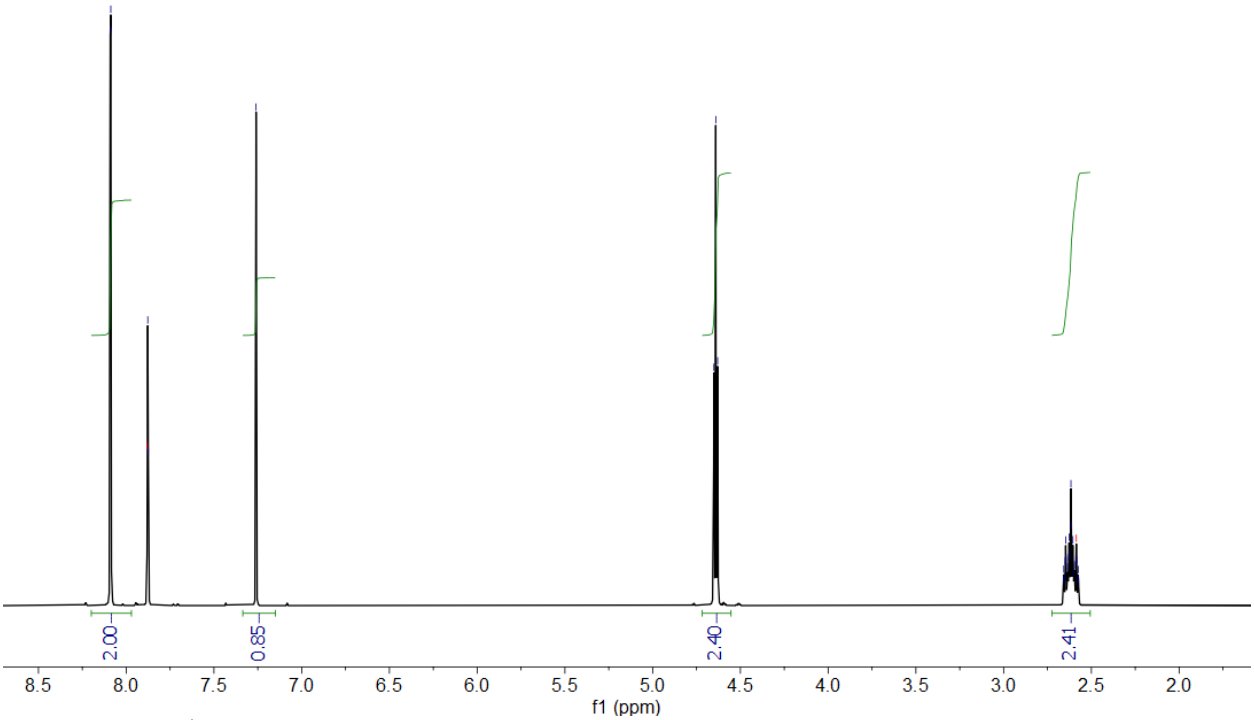

Figure S22. ^{1}H NMR (600 MHz, $CDCl_3$, 25 °C) spectrum of 3,3,4,4,5,5,6,6,6-nonafluorohexyl 3,5-dibromobenzoate [10].

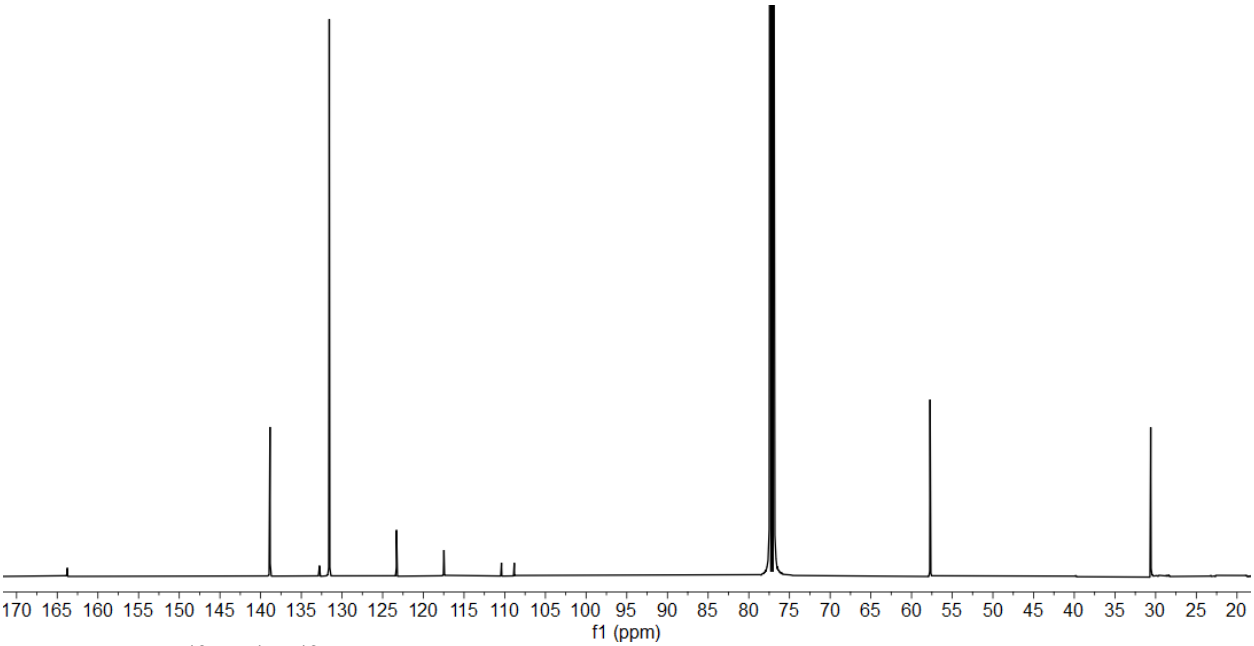

Figure S23. ^{13}C-{^{1}H,^{19}F} NMR (151 MHz, $CDCl_3$, 25 °C) spectrum of 3,3,4,4,5,5,6,6,6-nonafluorohexyl 3,5-dibromobenzoate [10].

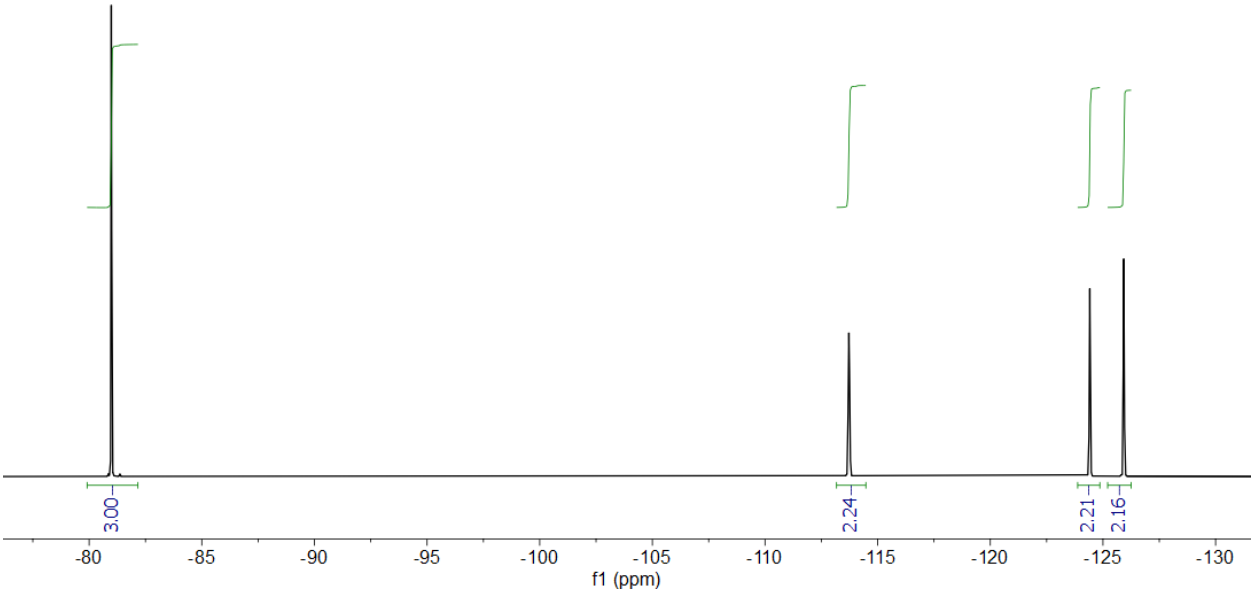

Figure S24. ^{19}F NMR (565 MHz, $CDCl_3$, 25 °C) spectrum of 3,3,4,4,5,5,6,6,6-nonafluorohexyl 3,5-dibromobenzoate [10].

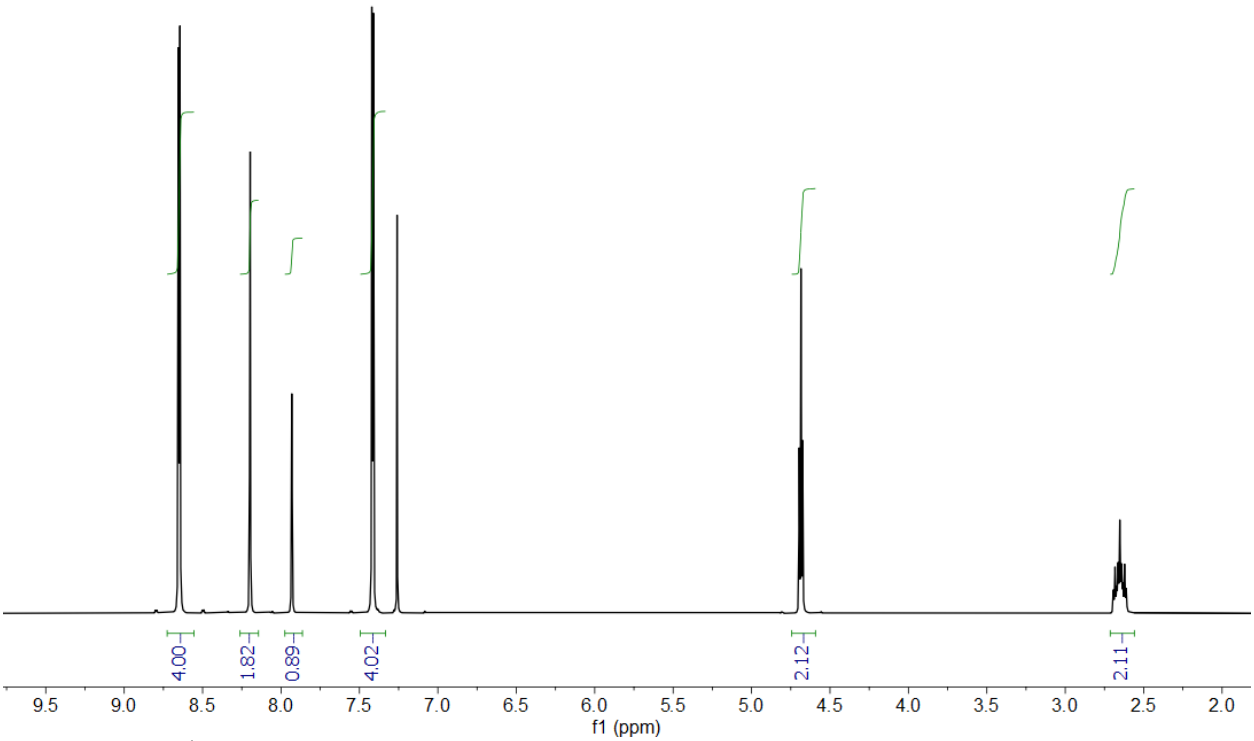

Figure S25. ^{1}H NMR (600 MHz, $CDCl_3$, 25 °C) spectrum of 3,3,4,4,5,5,6,6,6-nonafluorohexyl 3,5-bis(pyridin-4-ylethynyl)benzoate [11].

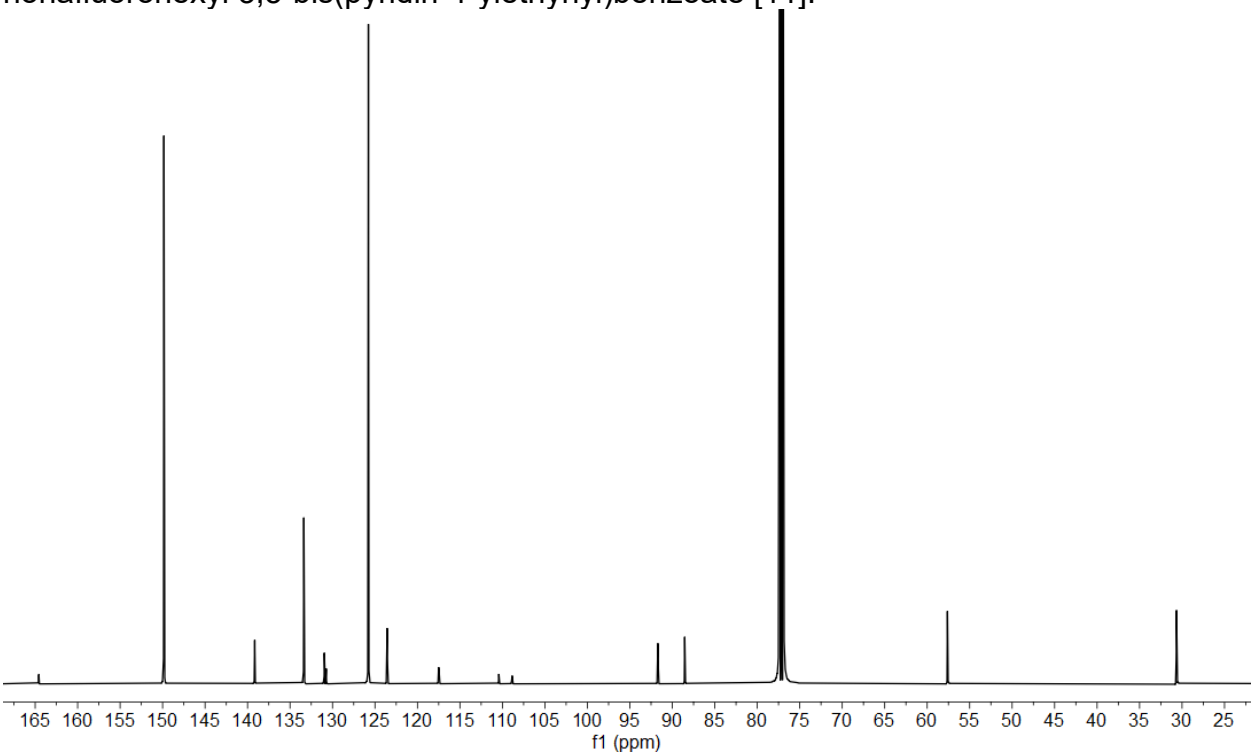

Figure S26. ^{13}C-{^{1}H,^{19}F} NMR (151 MHz, $CDCl_3$, 25 °C) spectrum of 3,3,4,4,5,5,6,6,6-nonafluorohexyl 3,5-bis(pyridin-4-ylethynyl)benzoate [11].

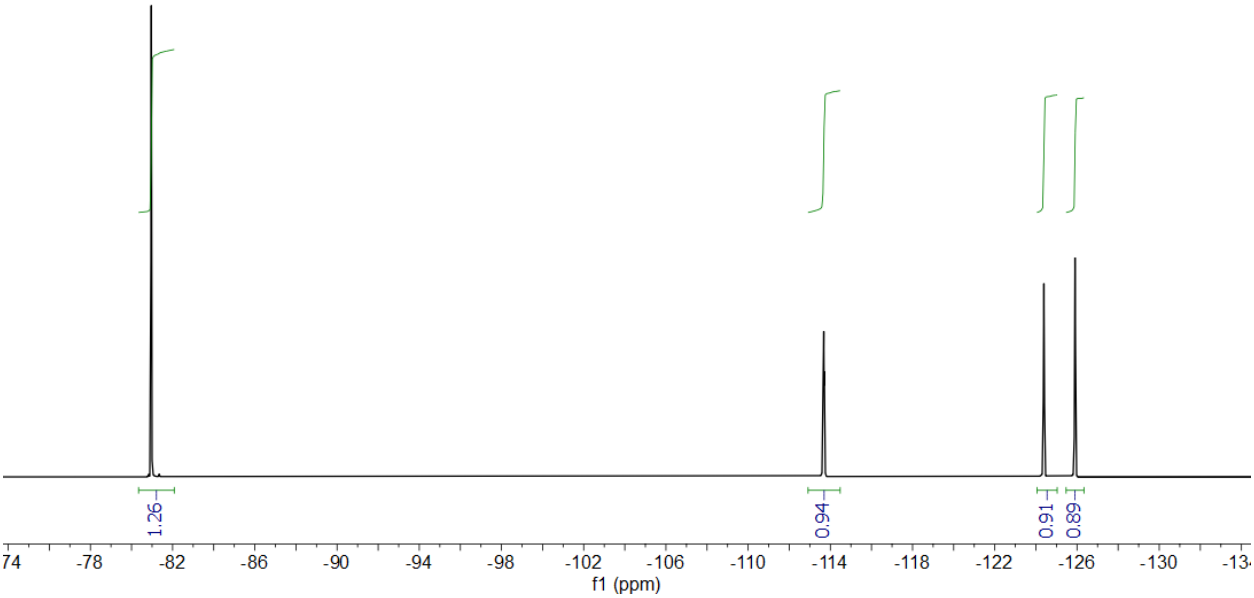

Figure S27. ^{19}F NMR (565 MHz, $CDCl_3$, 25 °C) spectrum of 3,3,4,4,5,5,6,6,6-nonafluorohexyl 3,5-bis(pyridin-4-ylethynyl)benzoate [11].

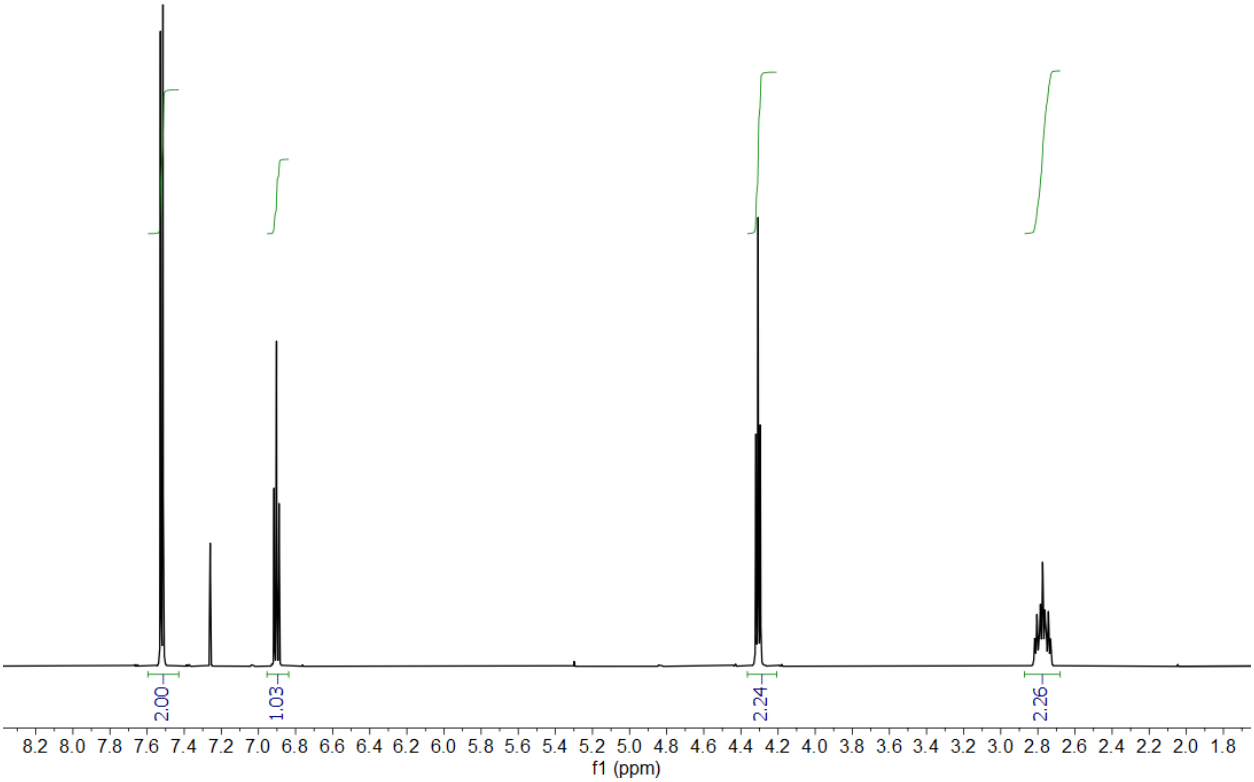

Figure S28. ^{1}H NMR (600 MHz, $CDCl_3$, 25 °C) spectrum of 1,3-dibromo-2-((3,3,4,4,5,5,6,6,7,7,8,8,9,9,10,10,10-heptadecafluorodecyl)oxy)benzene [12].

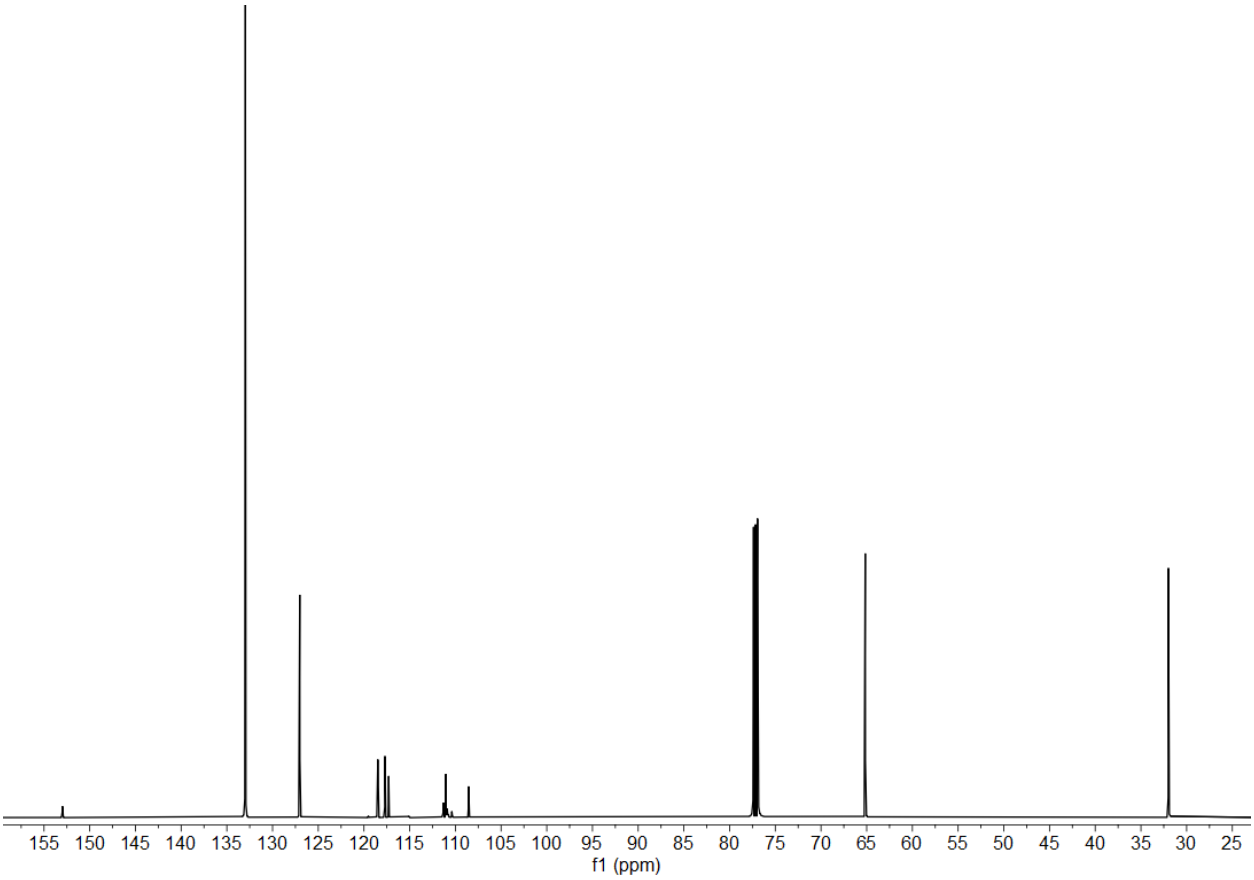

Figure S29. ^{13}C-{^{1}H,^{19}F} NMR (151 MHz, $CDCl_3$, 25 °C) spectrum of 1,3-dibromo-2-((3,3,4,4,5,5,6,6,7,7,8,8,9,9,10,10,10-heptadecafluorodecyl)oxy)benzene [12].

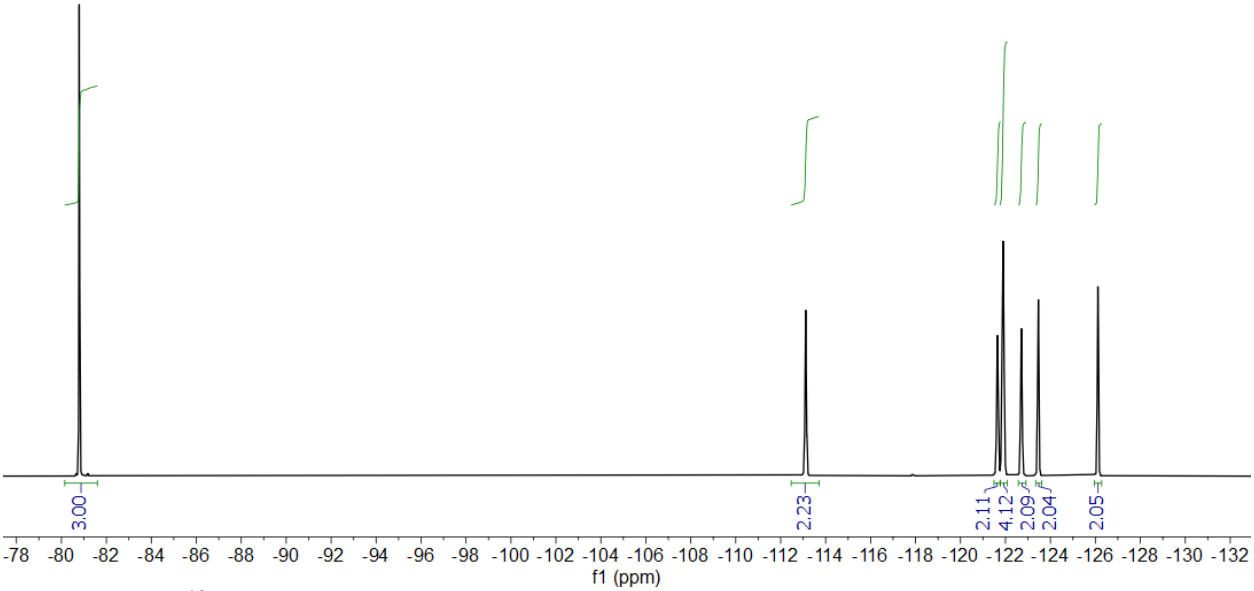

Figure S30. ^{19}F NMR (565 MHz, $CDCl_3$, 25 °C) spectrum of 1,3-dibromo-2-((3,3,4,4,5,5,6,6,7,7,8,8,9,9,10,10,10-heptadecafluorodecyl)oxy)benzene [12].

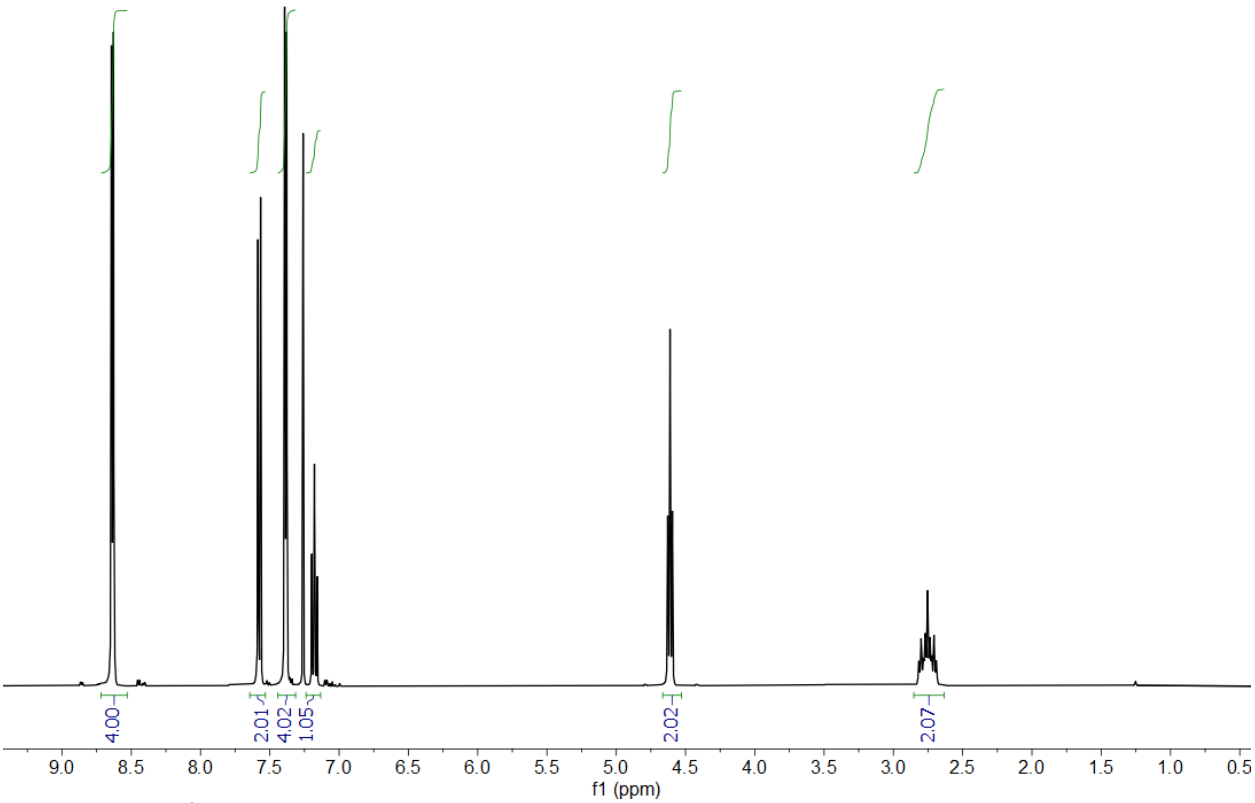

Figure S31. ^{1}H NMR (400 MHz, $CDCl_3$, 25 °C) spectrum of 4,4'-((2-((3,3,4,4,5,5,6,6,7,7,8,8,9,9,10,10,10-heptadecafluorodecyl)oxy)-1,3-phenylene)bis(ethyne-2,1-diyl))dipyridine [13].

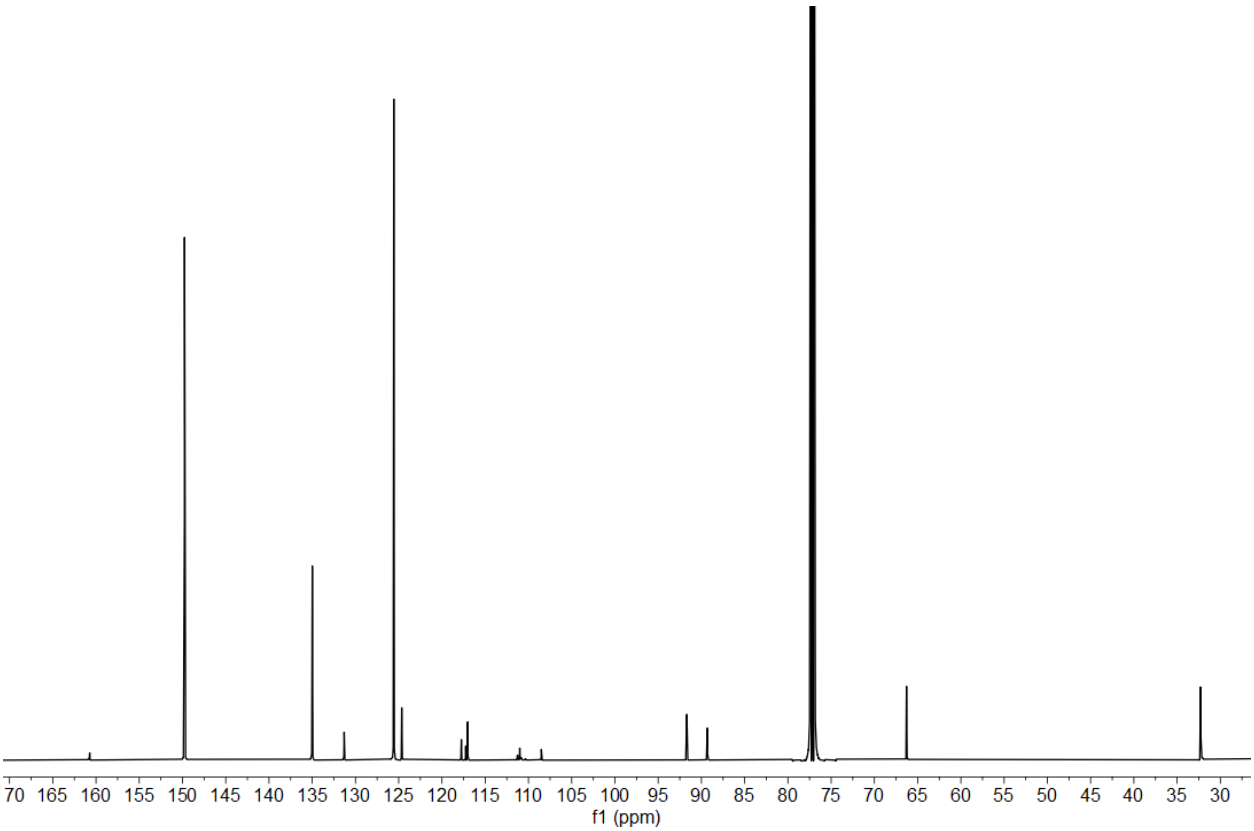

Figure S32. ^{13}C-{^{1}H,^{19}F} NMR (151 MHz, $CDCl_3$, 25 °C) spectrum of 4,4'-((2-((3,3,4,4,5,5,6,6,7,7,8,8,9,9,10,10,10-heptadecafluorodecyl)oxy)-1,3-phenylene)bis(ethyne-2,1-diyl))dipyridine [13].

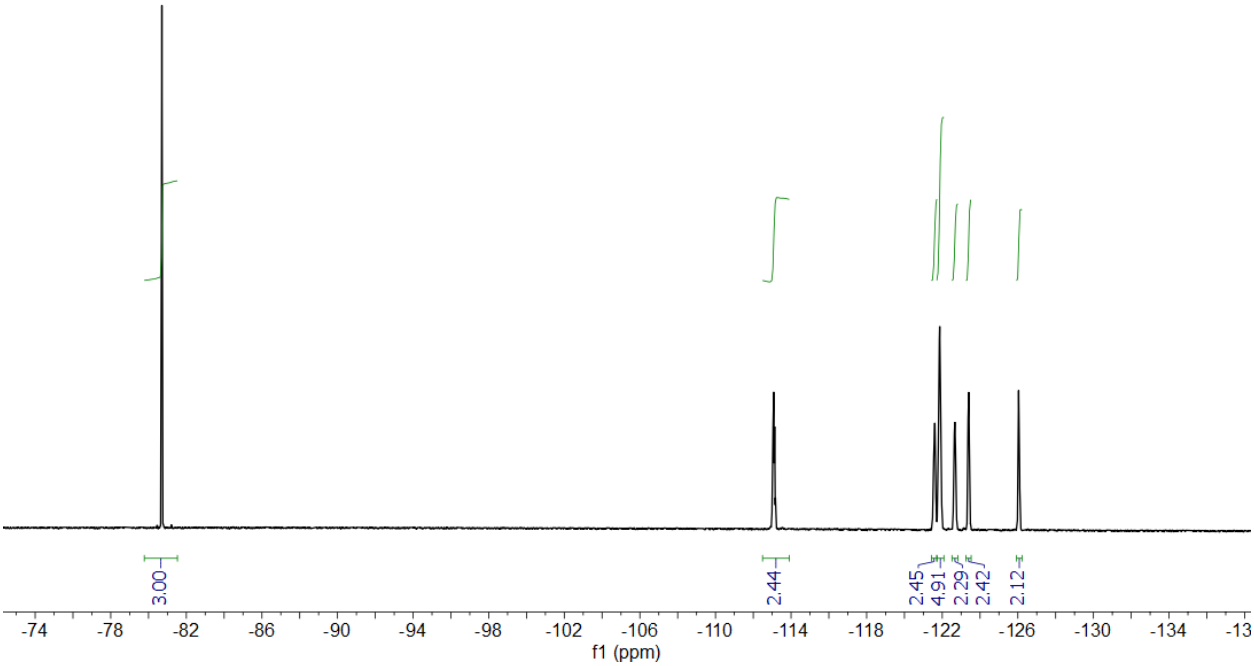

Figure S33. ^{19}F NMR (376 MHz, $CDCl_3$, 25 °C) spectrum of 4,4'-((2-((3,3,4,4,5,5,6,6,7,7,8,8,9,9,10,10,10-heptadecafluorodecyl)oxy)-1,3-phenylene)bis(ethyne-2,1-diyl))dipyridine [13].

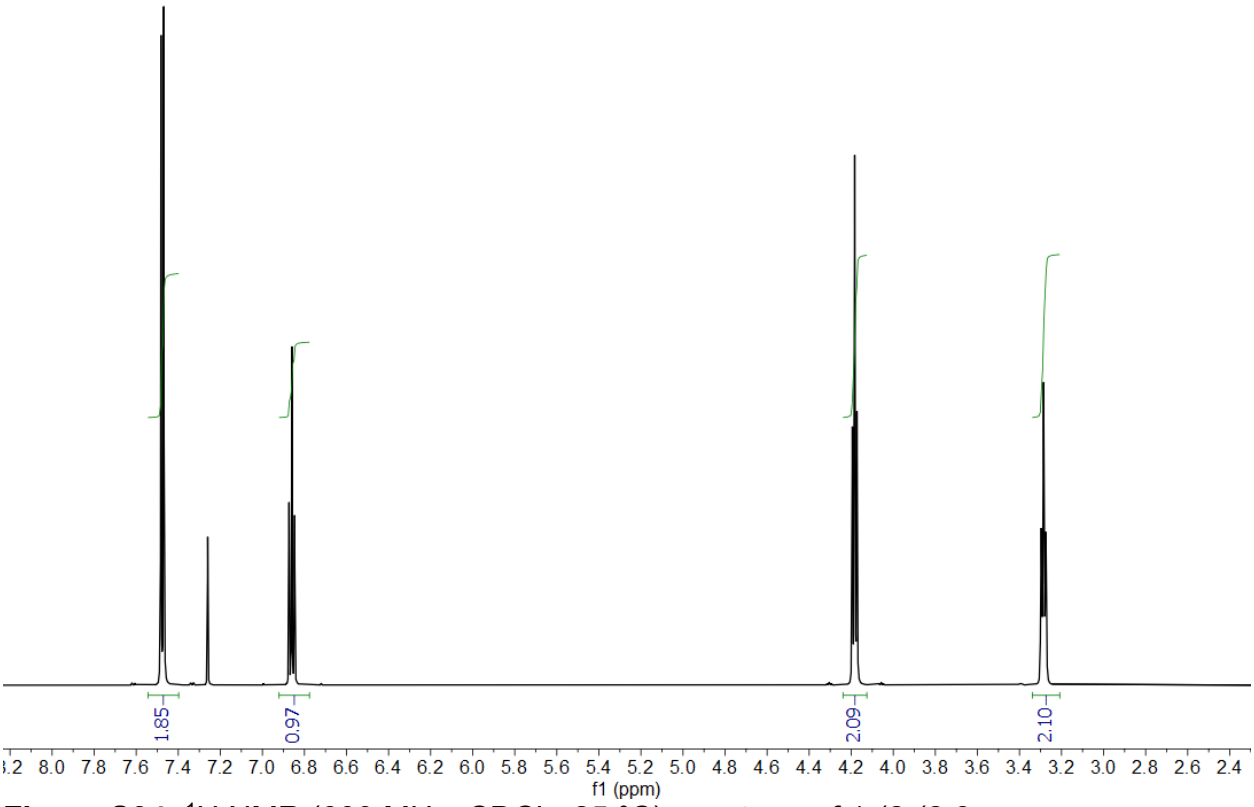

Figure S34. ^{1}H NMR (600 MHz, $CDCl_3$, 25 °C) spectrum of 1-(2-(2,6-dibromophenoxy)ethyl)-2,3,4,5,6-pentafluorobenzene [14].

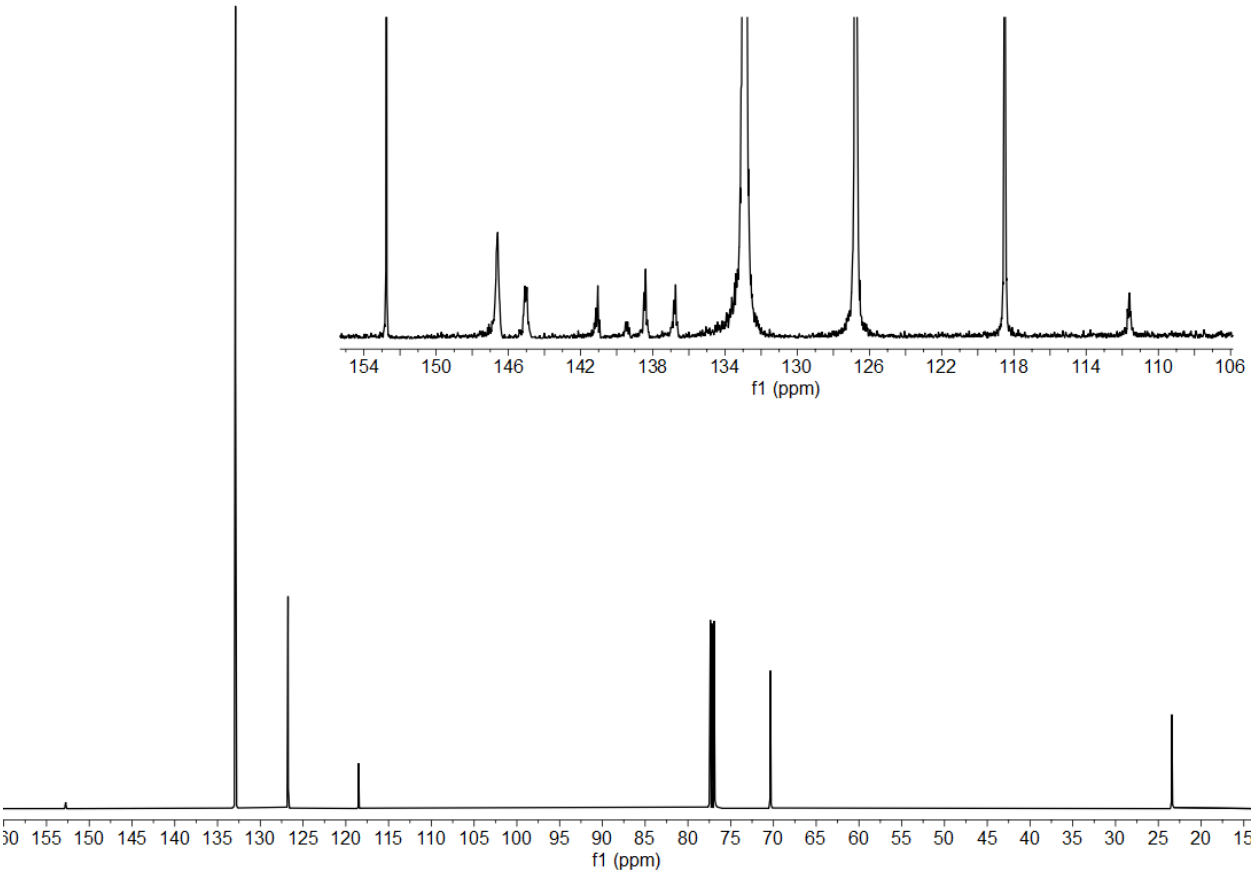

Figure S35. ^{13}C-{^{1}H} NMR (151 MHz, $CDCl_3$, 25 °C) spectrum of 1-(2-(2,6-dibromophenoxy)ethyl)-2,3,4,5,6-pentafluorobenzene [14]. Inset spectrum shows fluorine-split doublets.

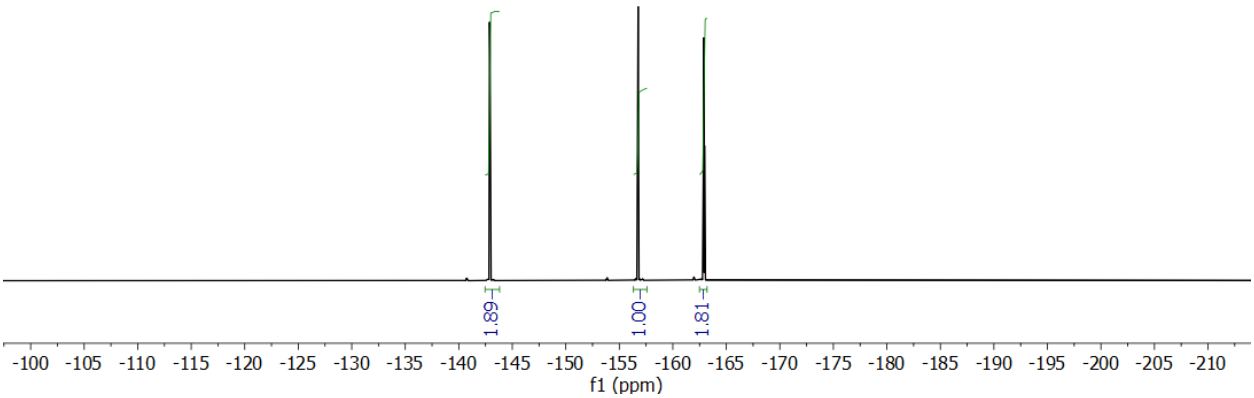

Figure S36. ^{19}F NMR (282 MHz, $CDCl_3$, 25 °C) spectrum of 1-(2-(2,6-dibromophenoxy)ethyl)-2,3,4,5,6-pentafluorobenzene [14].

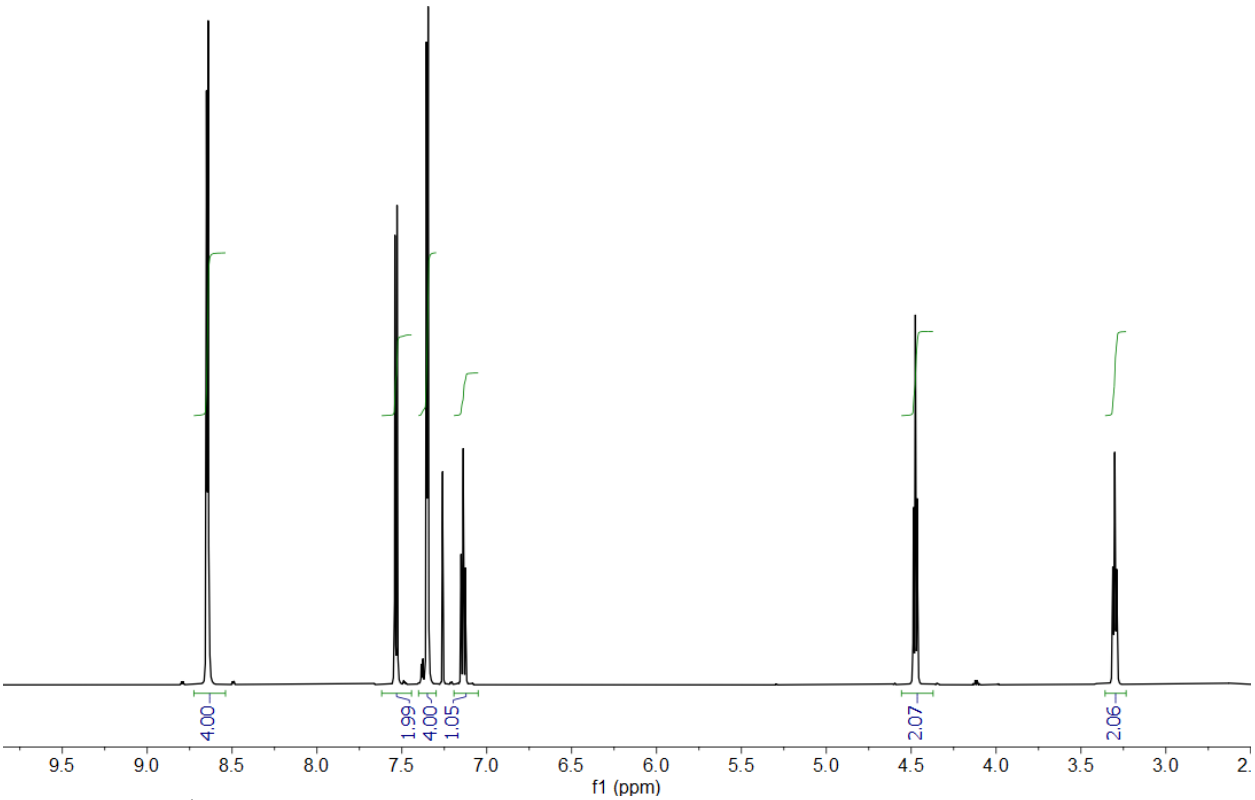

Figure S37. ^{1}H NMR (600 MHz, $CDCl_3$, 25 °C) spectrum of 4,4'-((2-(2-(perfluorophenyl)ethoxy)-1,3-phenylene)bis(ethyne-2,1-diyl))dipyridine [15].

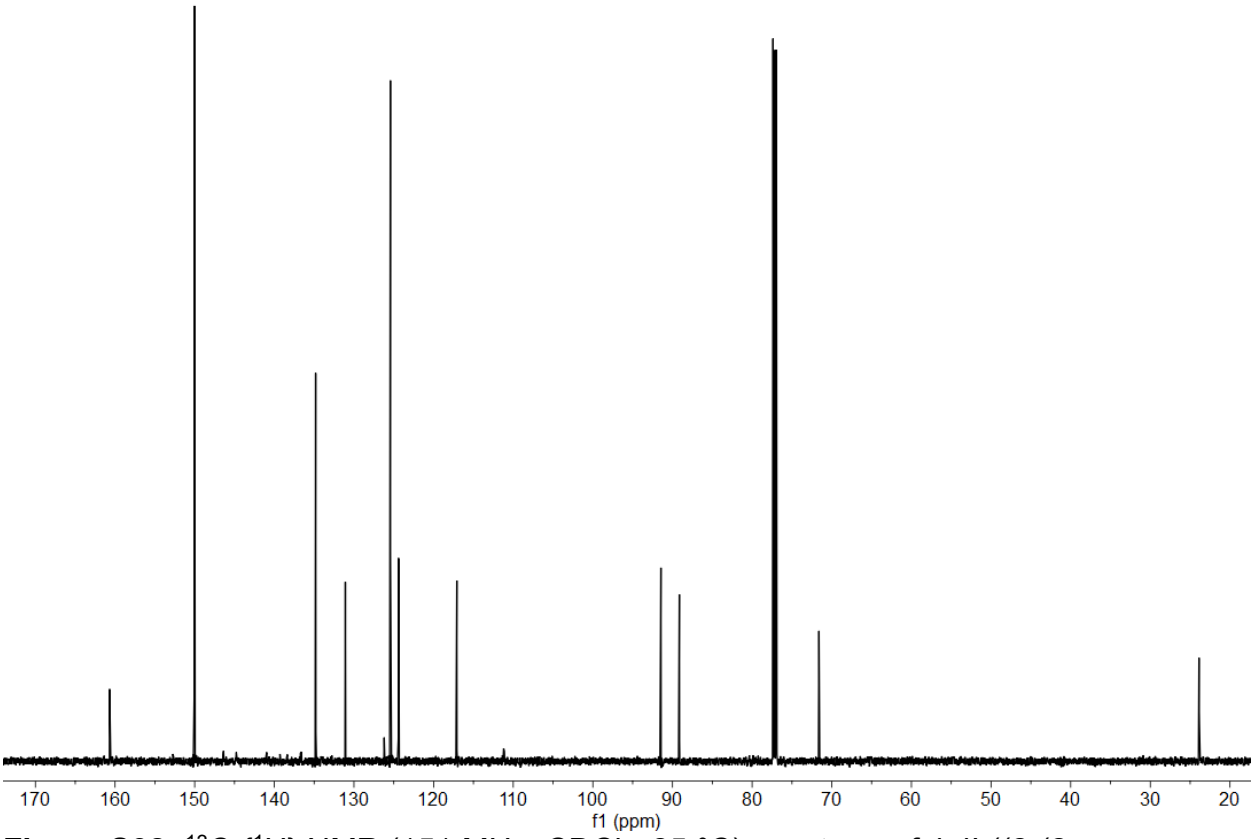

Figure S38. ^{13}C-{^{1}H} NMR (151 MHz, $CDCl_3$, 25 °C) spectrum of 4,4'-((2-(2-(perfluorophenyl)ethoxy)-1,3-phenylene)bis(ethyne-2,1-diyl))dipyridine [15].

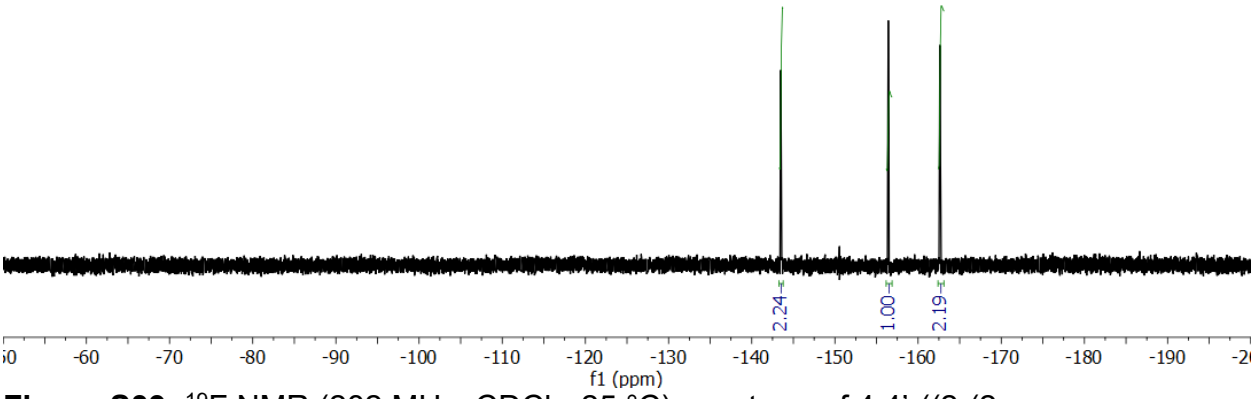

Figure S39. ^{19}F NMR (282 MHz, $CDCl_3$, 25 °C) spectrum of 4,4'-((2-(2-(perfluorophenyl)ethoxy)-1,3-phenylene)bis(ethyne-2,1-diyl))dipyridine [15].

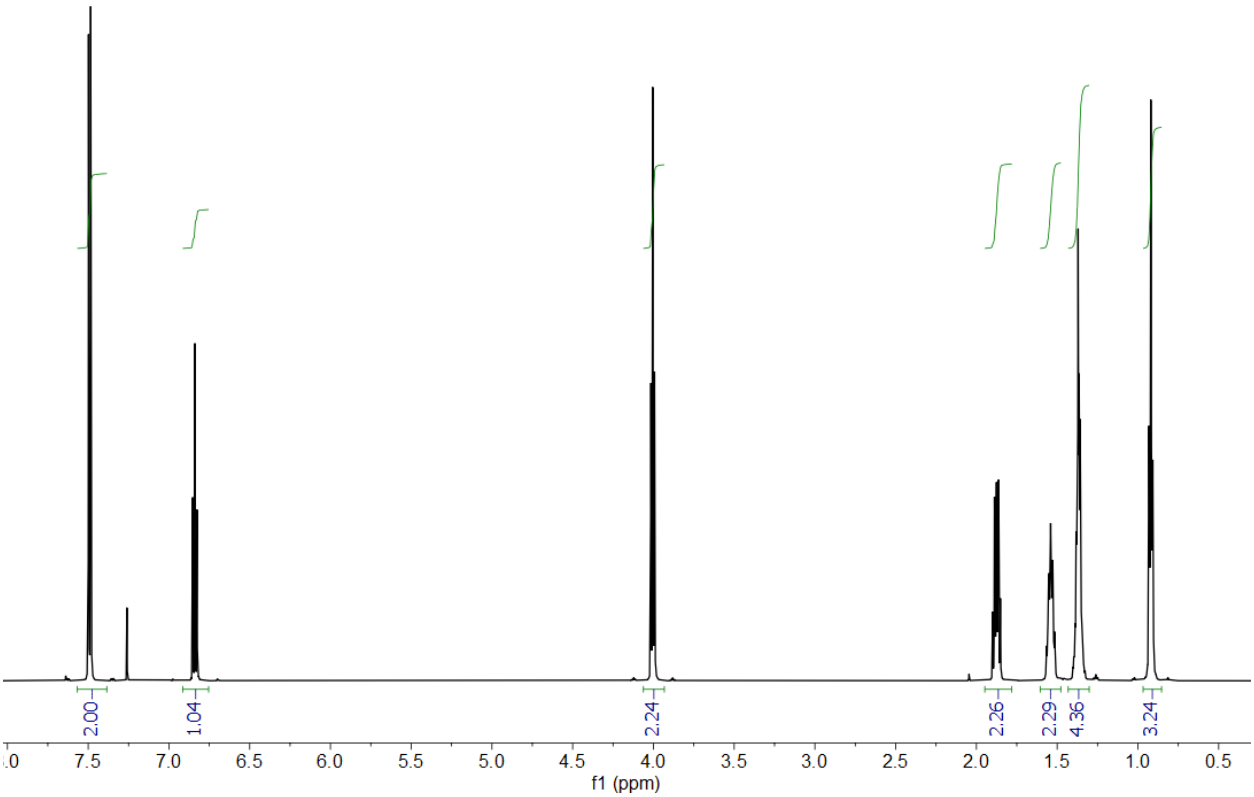

Figure S40. ^{1}H NMR (600 MHz, $CDCl_3$, 25 °C) spectrum of 1,3-dibromo-2-(hexyloxy)benzene [16].

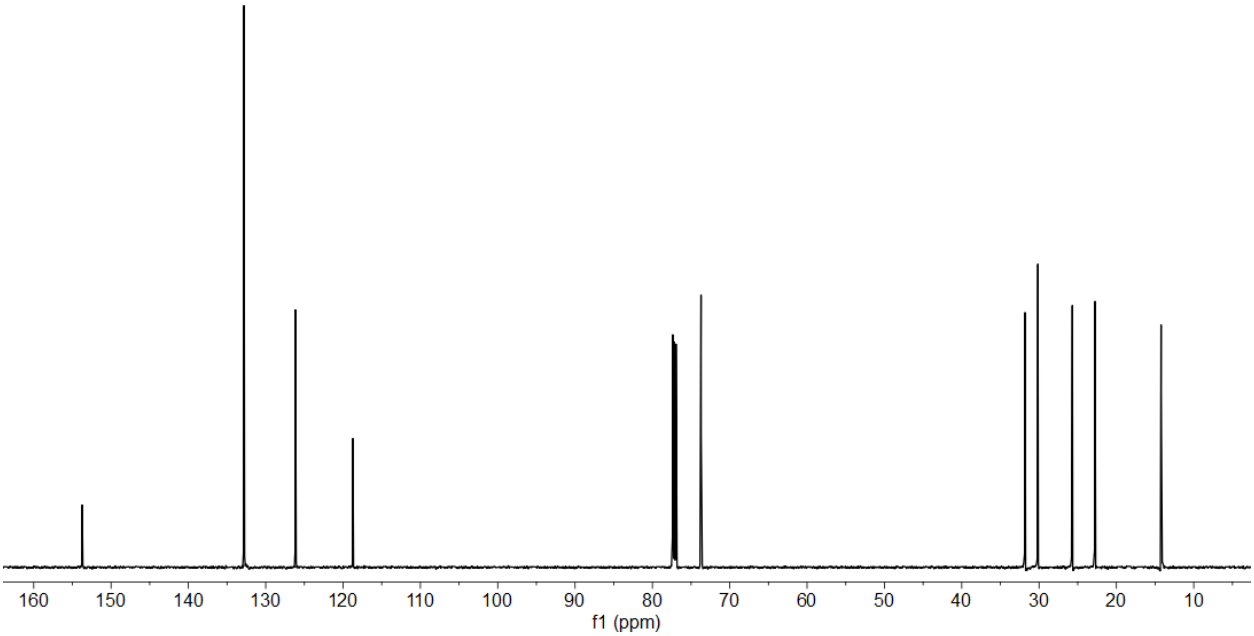

Figure S41. ^{13}C-{^{1}H} NMR (151 MHz, $CDCl_3$, 25 °C) spectrum of 1,3-dibromo-2-(hexyloxy)benzene [16].

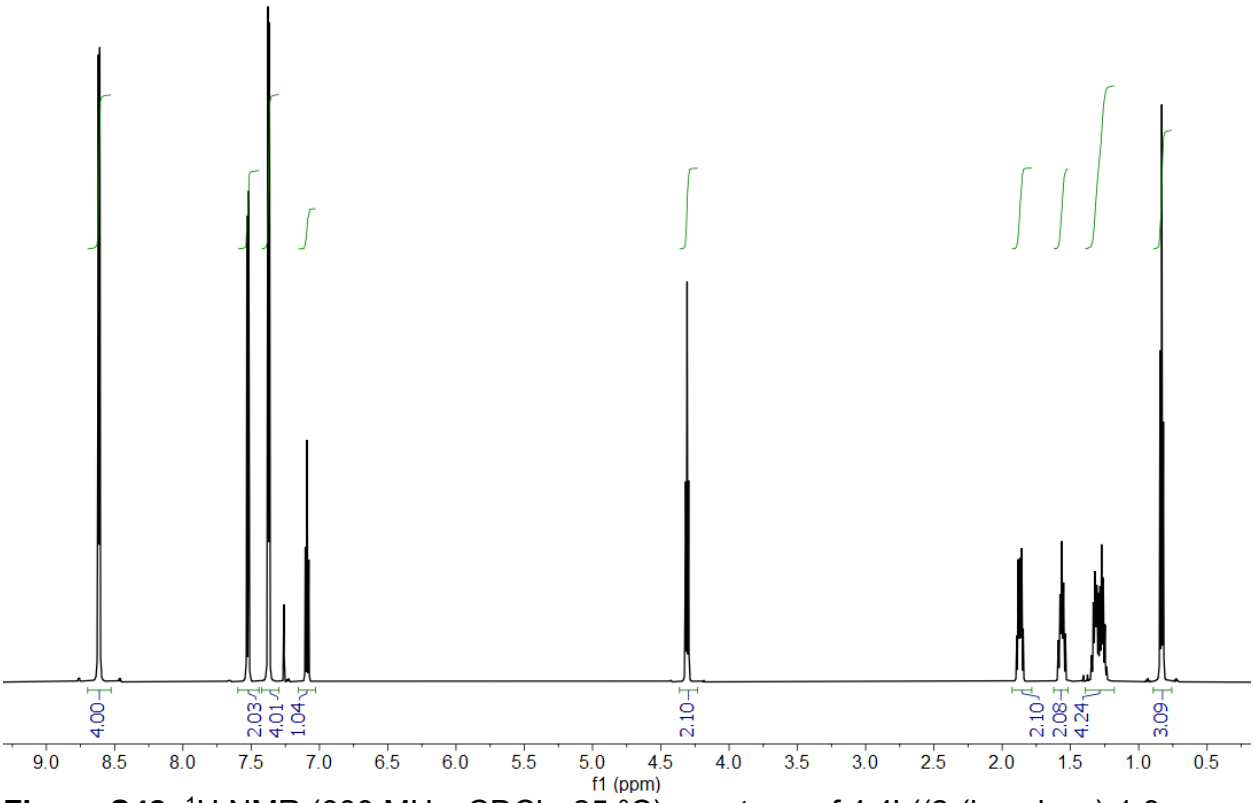

Figure S42. ^{1}H NMR (600 MHz, $CDCl_3$, 25 °C) spectrum of 4,4'-((2-(hexyloxy)-1,3-phenylene)bis(ethyne-2,1-diyl))dipyridine [17].

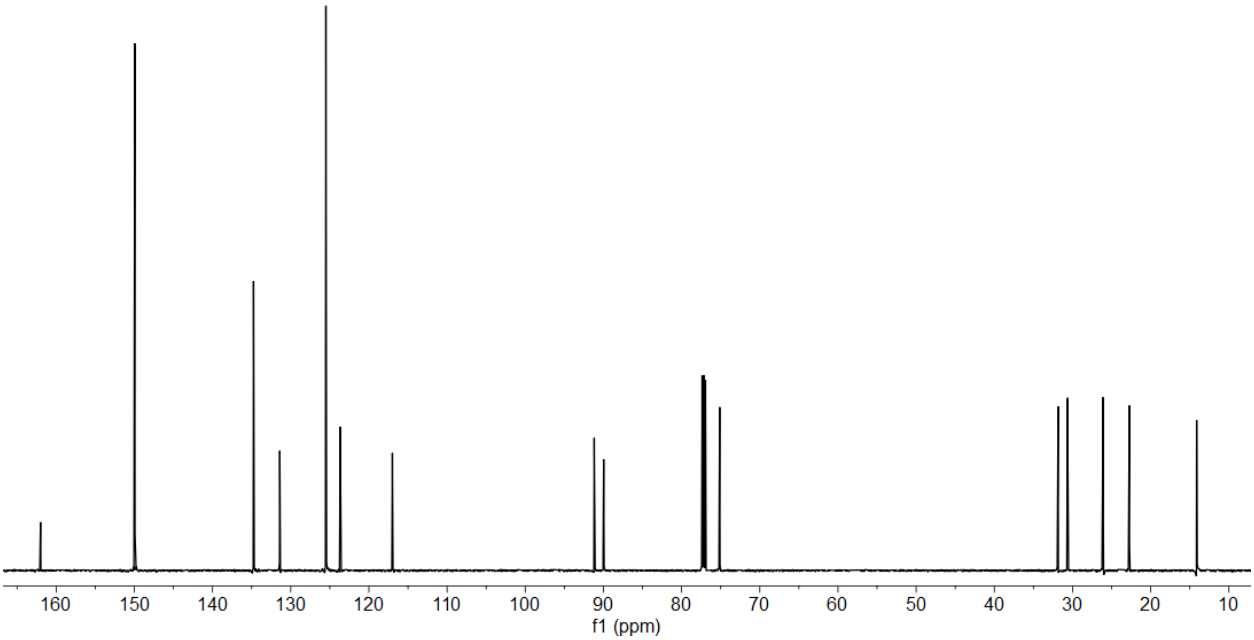

Figure S43. ^{13}C-{^{1}H} NMR (151 MHz, $CDCl_3$, 25 °C) spectrum of 4,4'-((2-(hexyloxy)-1,3-phenylene)bis(ethyne-2,1-diyl))dipyridine [17].

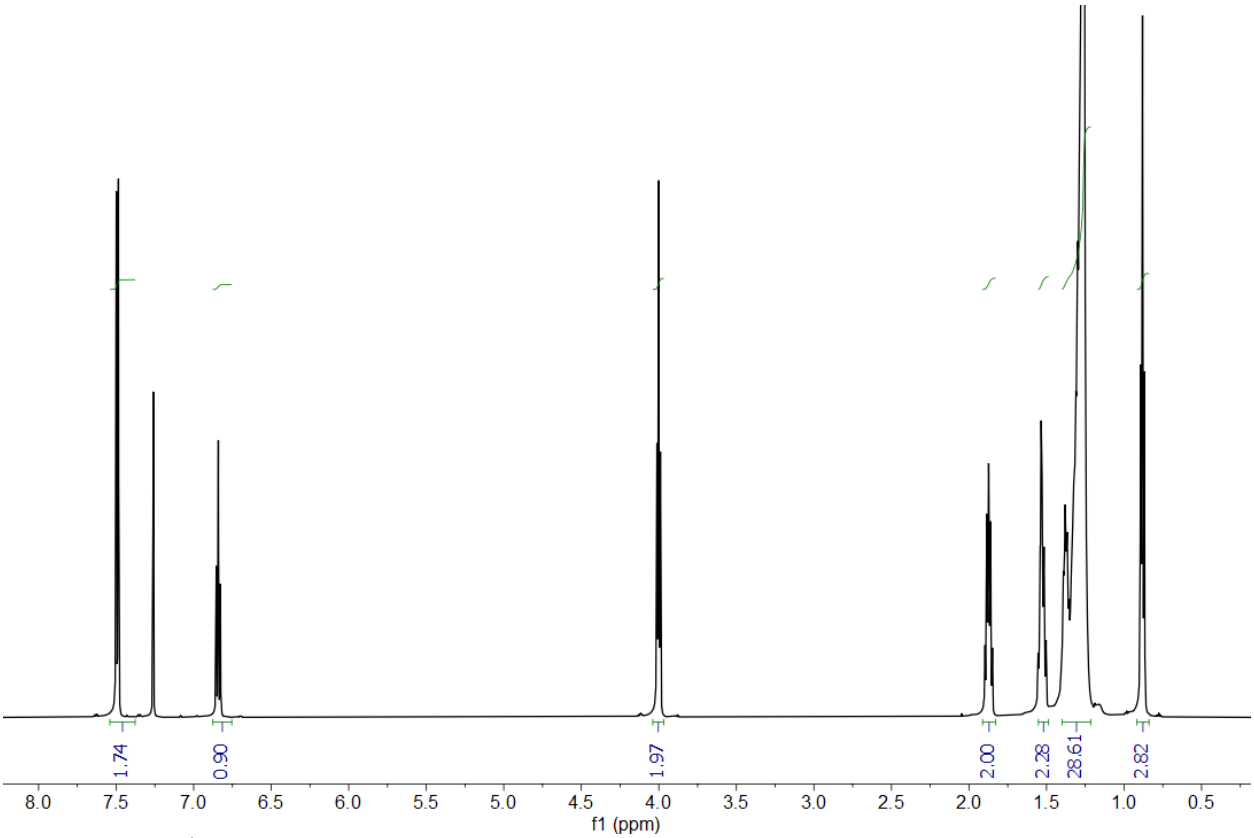

Figure S44. ^{1}H NMR (600 MHz, $CDCl_3$, 25 °C) spectrum of 1,3-dibromo-2-(octadecyloxy)benzene [18].

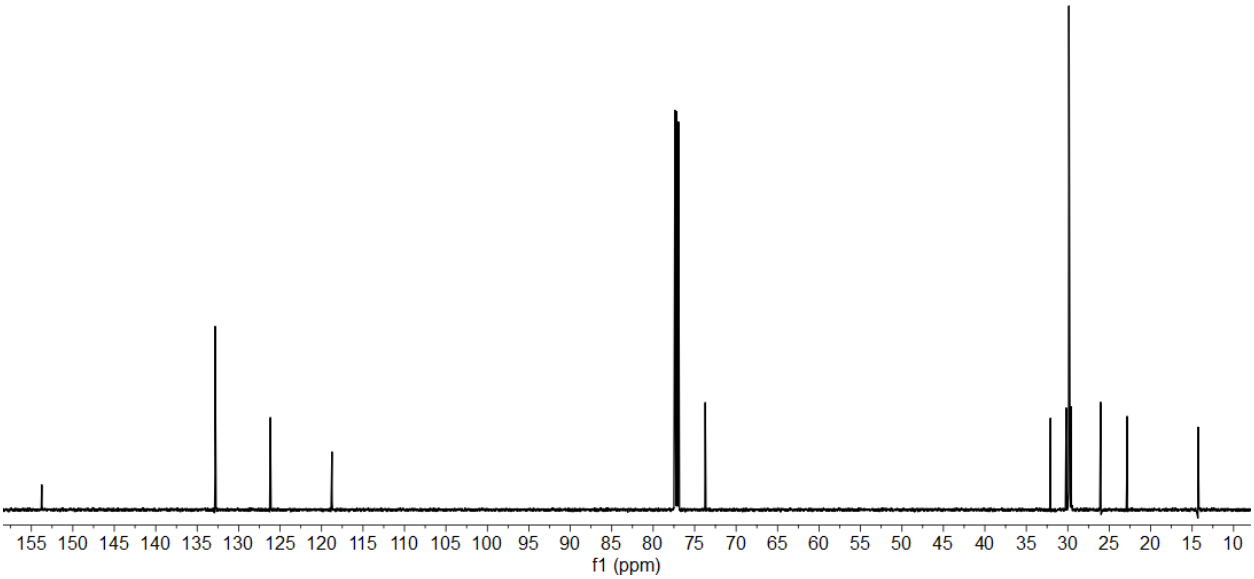

Figure S45. ^{13}C-{^{1}H} NMR (151 MHz, $CDCl_3$, 25 °C) spectrum of 1,3-dibromo-2-(octadecyloxy)benzene [18].

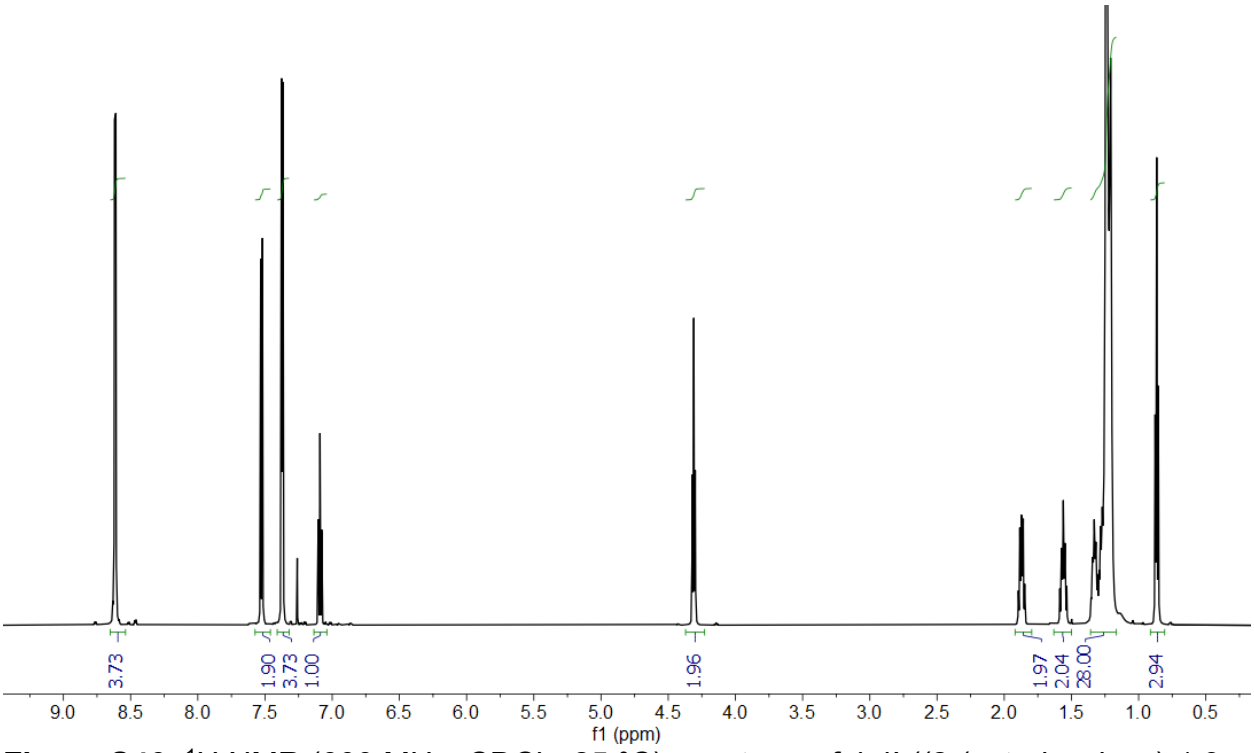

Figure S46. ^{1}H NMR (600 MHz, $CDCl_3$, 25 °C) spectrum of 4,4'-((2-(octadecyloxy)-1,3-phenylene)bis(ethyne-2,1-diyl))dipyridine [19].

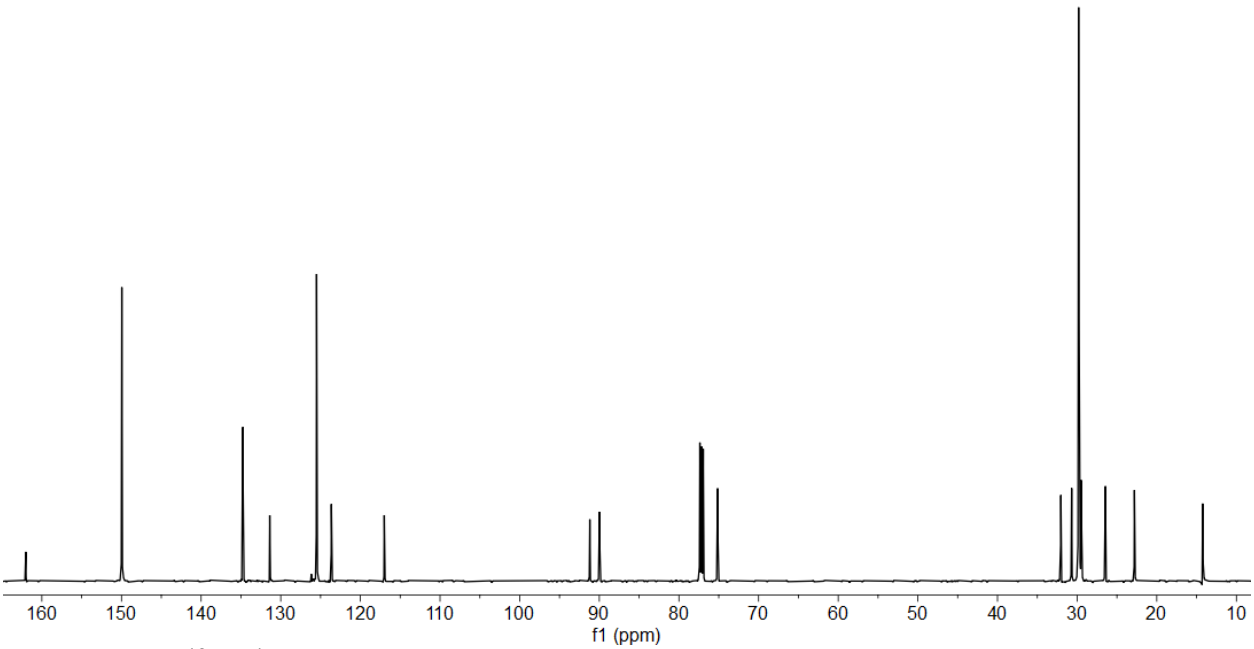

Figure S47. ^{13}C-{^{1}H} NMR (151 MHz, $CDCl_3$, 25 °C) spectrum of 4,4'-((2-(octadecyloxy)-1,3-phenylene)bis(ethyne-2,1-diyl))dipyridine [19].

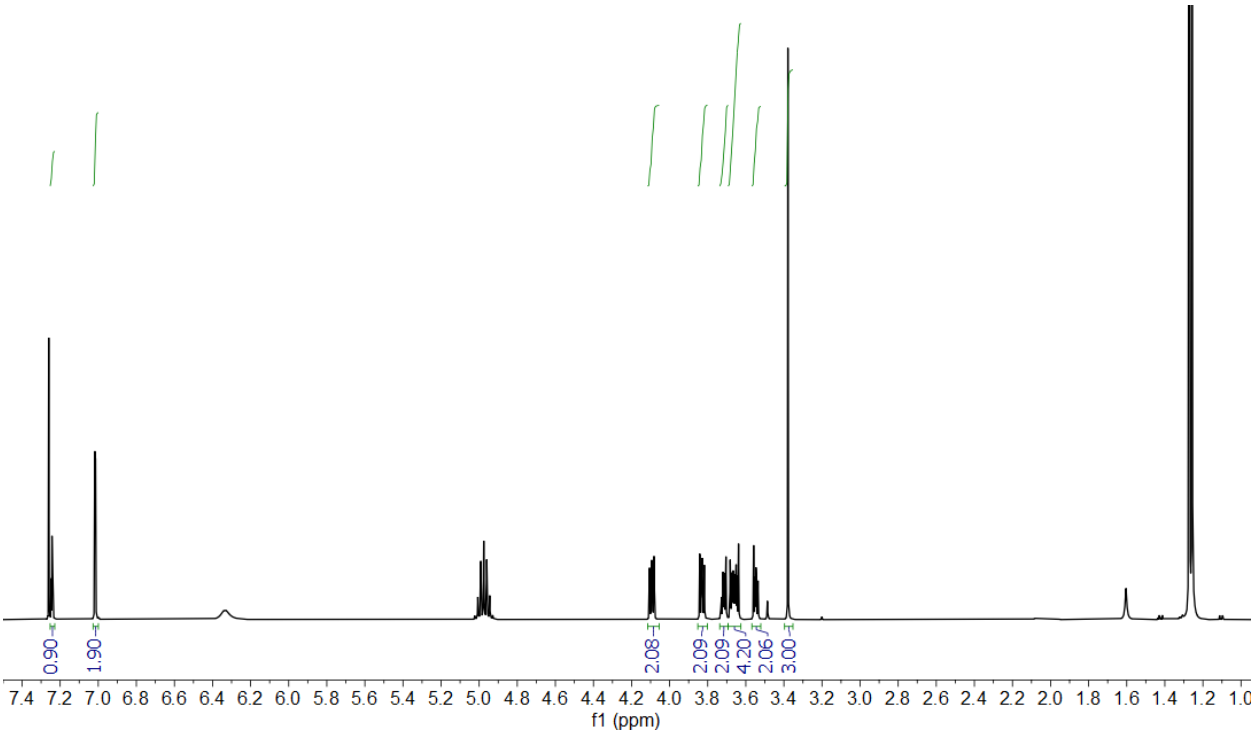

Figure S48. ^{1}H NMR (500 MHz, $CDCl_3$, 25 °C) spectrum of 1,3-dibromo-5-(2-(2-(2-methoxyethoxy)ethoxy)ethoxy)benzene [20] containing impurities. Quintet at 4.97ppm and doublet at 1.26 ppm were assigned to 2-propanol impurities.

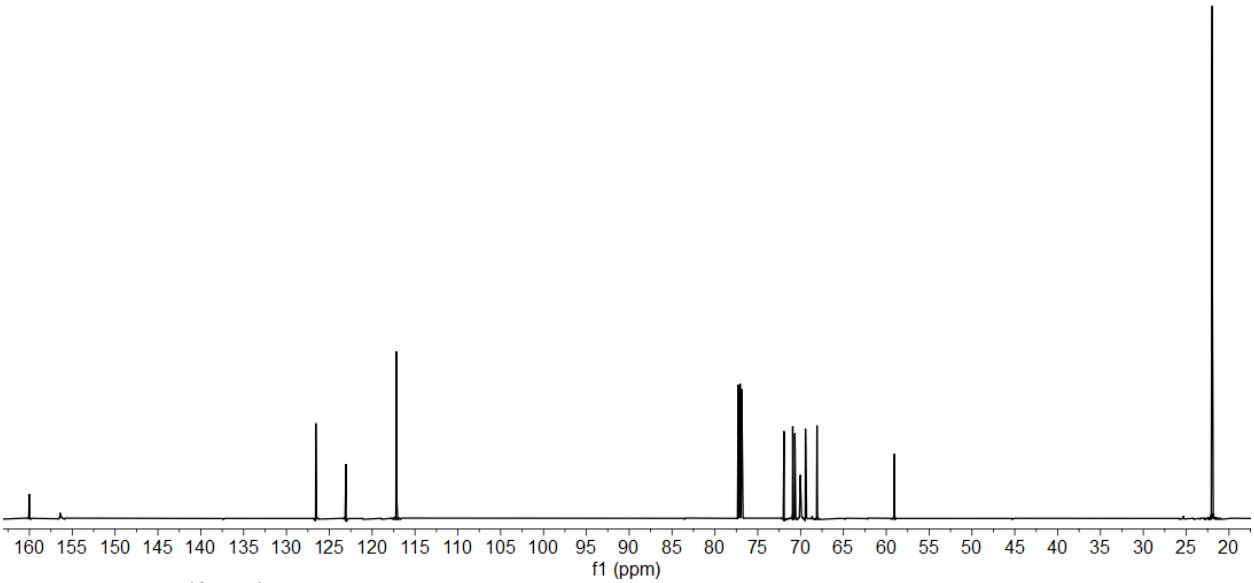

Figure S49. ^{13}C-{^{1}H} NMR (151 MHz, $CDCl_3$, 25 °C) spectrum of 1,3-dibromo-5-(2-(2-(2-methoxyethoxy)ethoxy)ethoxy)benzene [20] containing impurities.

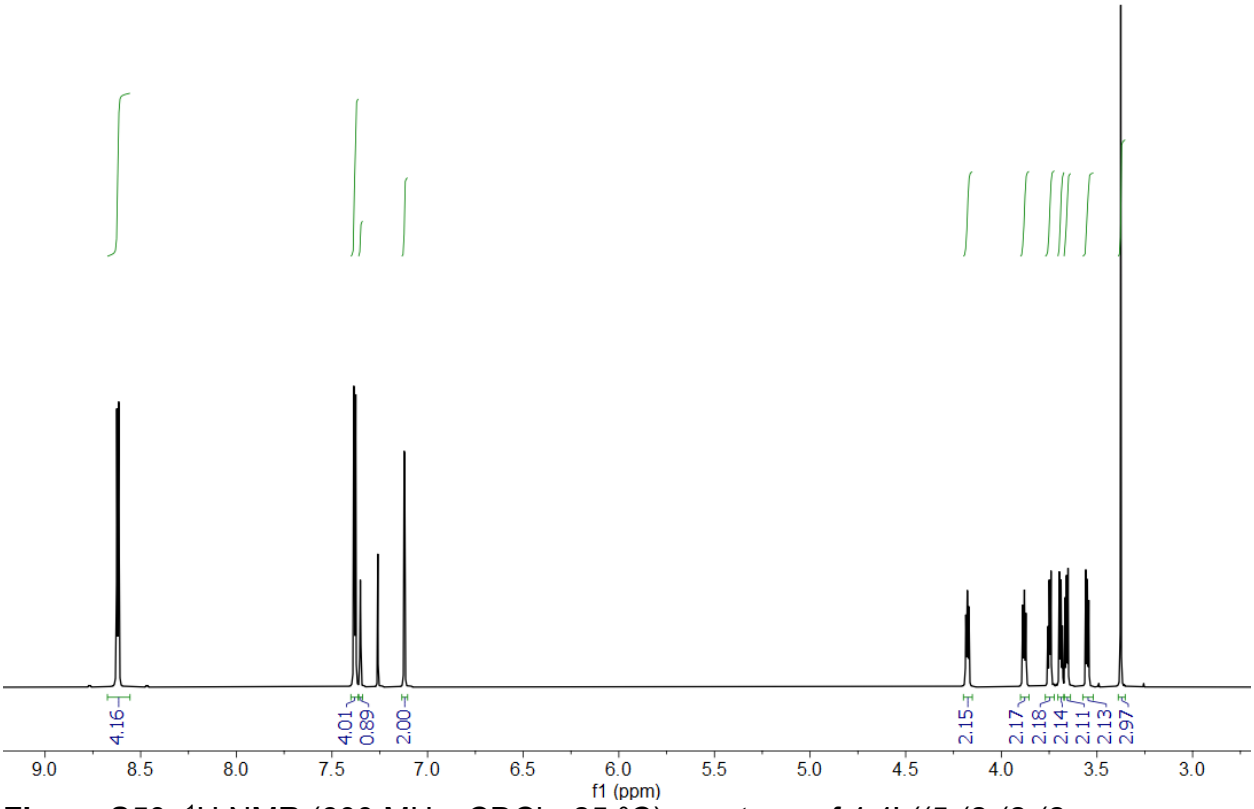

Figure S50. ^{1}H NMR (600 MHz, $CDCl_3$, 25 °C) spectrum of 4,4'-((5-(2-(2-(2-methoxyethoxy)ethoxy)ethoxy)-1,3-phenylene)bis(ethyne-2,1-diyl))dipyridine [21].

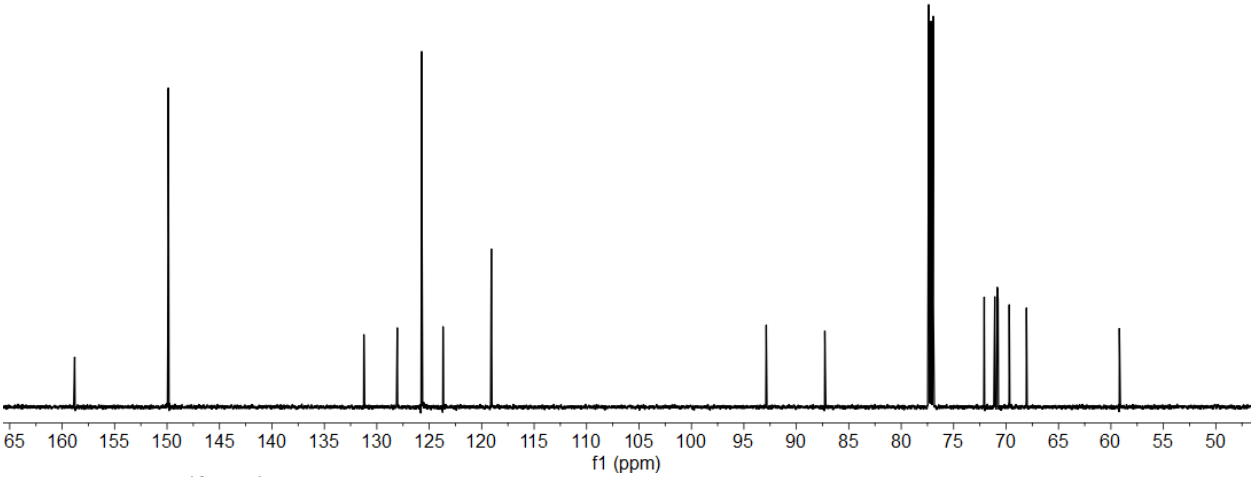

Figure S51. ^{13}C-{^{1}H} NMR (151 MHz, $CDCl_3$, 25 °C) spectrum of 4,4'-((5-(2-(2-(2-methoxyethoxy)ethoxy)ethoxy)-1,3-phenylene)bis(ethyne-2,1-diyl))dipyridine [21].

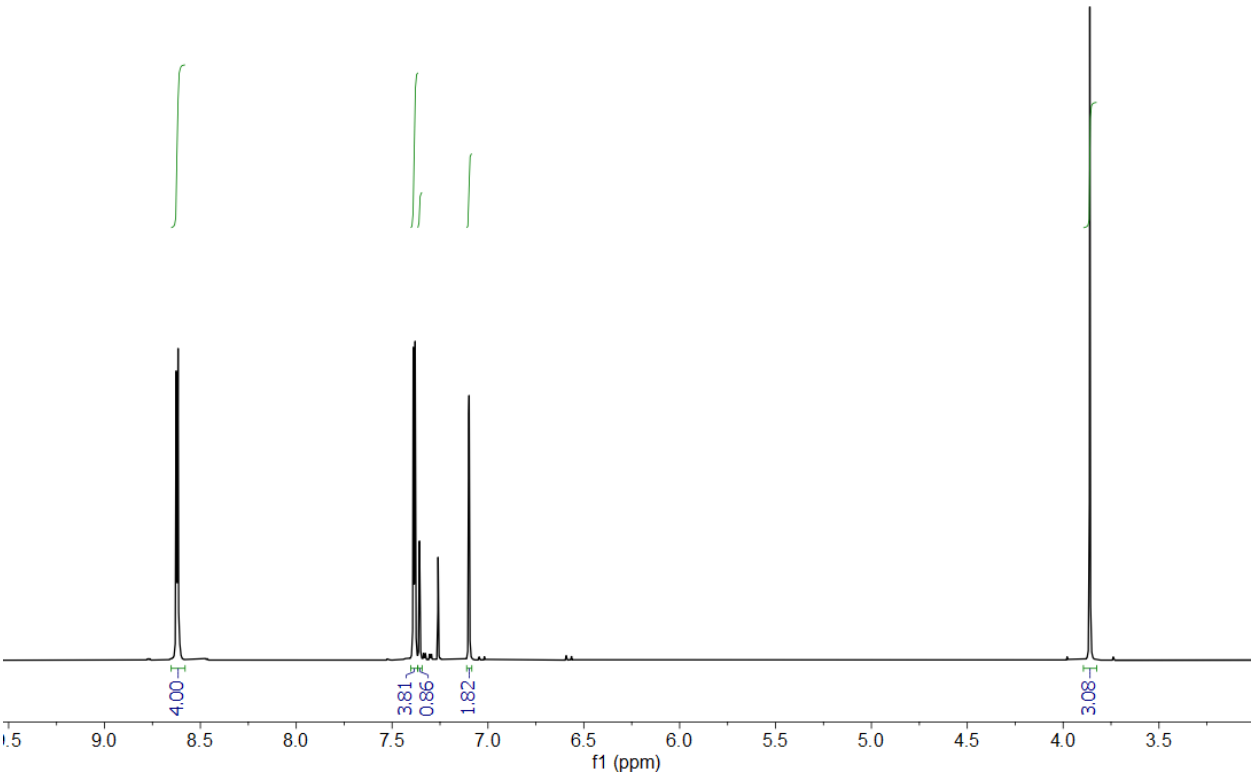

Figure S52. ^{1}H NMR (600 MHz, $CDCl_3$, 25 °C) spectrum of 4,4'-((5-methoxy-1,3-phenylene)bis(ethyne-2,1-diyl))dipyridine [22].

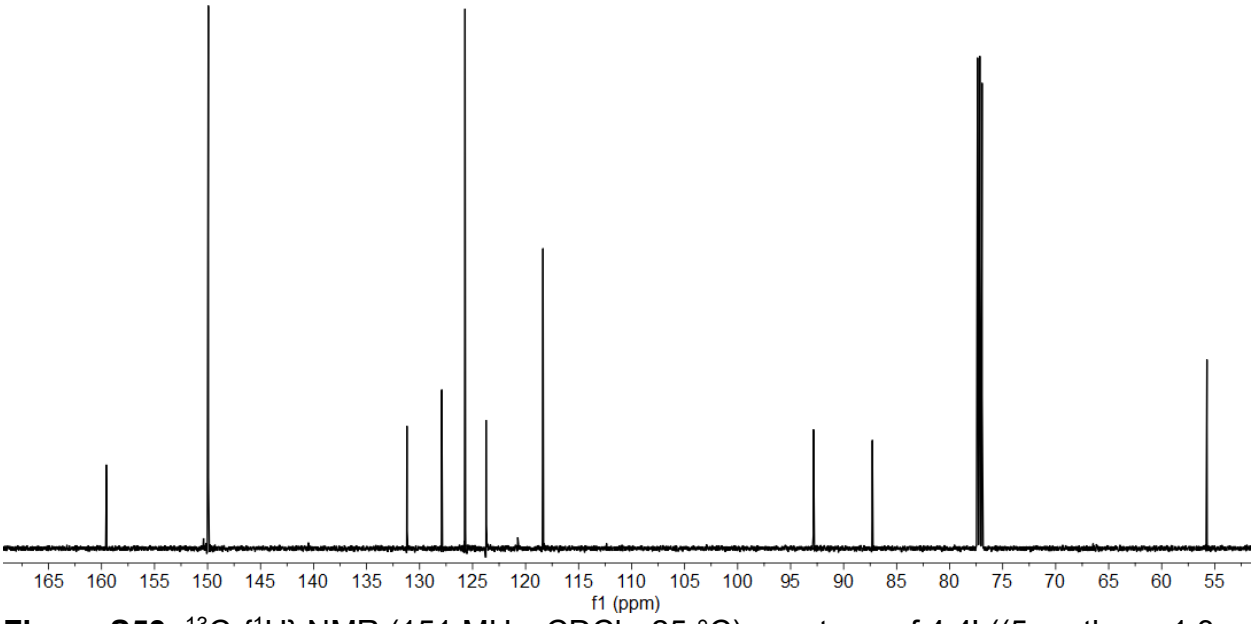

Figure S53. ^{13}C-{^{1}H} NMR (151 MHz, $CDCl_3$, 25 °C) spectrum of 4,4'-((5-methoxy-1,3-phenylene)bis(ethyne-2,1-diyl))dipyridine [22].

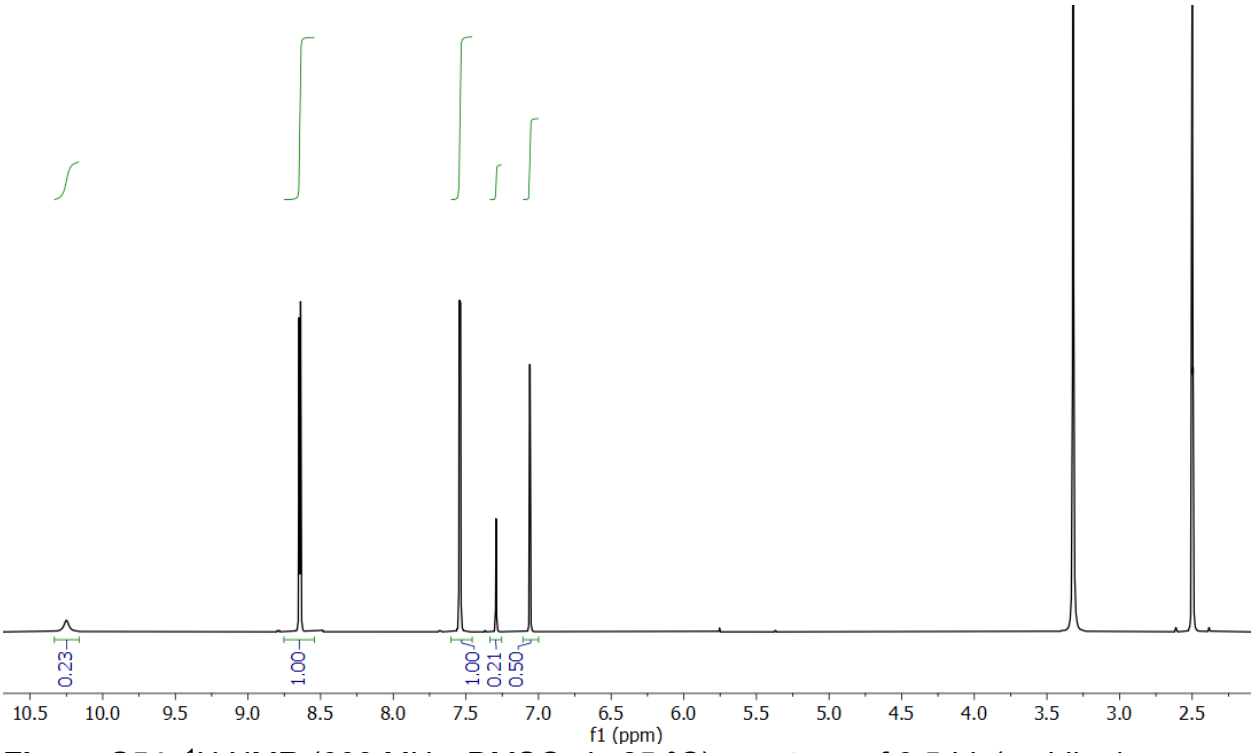

Figure S54. ^{1}H NMR (600 MHz, DMSO-d_6, 25 °C) spectrum of 3,5-bis(pyridin-4-ylethynyl)phenol [23].

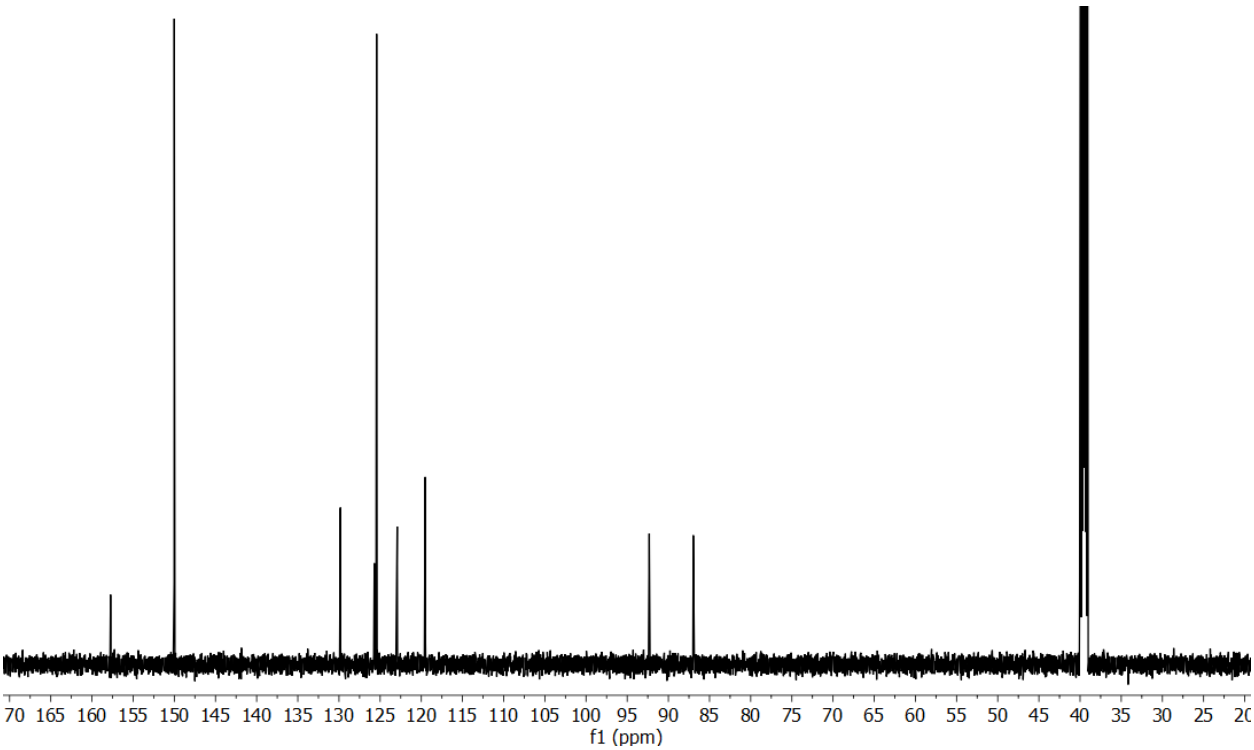

Figure S55. ^{13}C-{^{1}H} NMR (151 MHz, DMSO-d_6, 25 °C) spectrum of 3,5-bis(pyridin-4-ylethynyl)phenol [23].

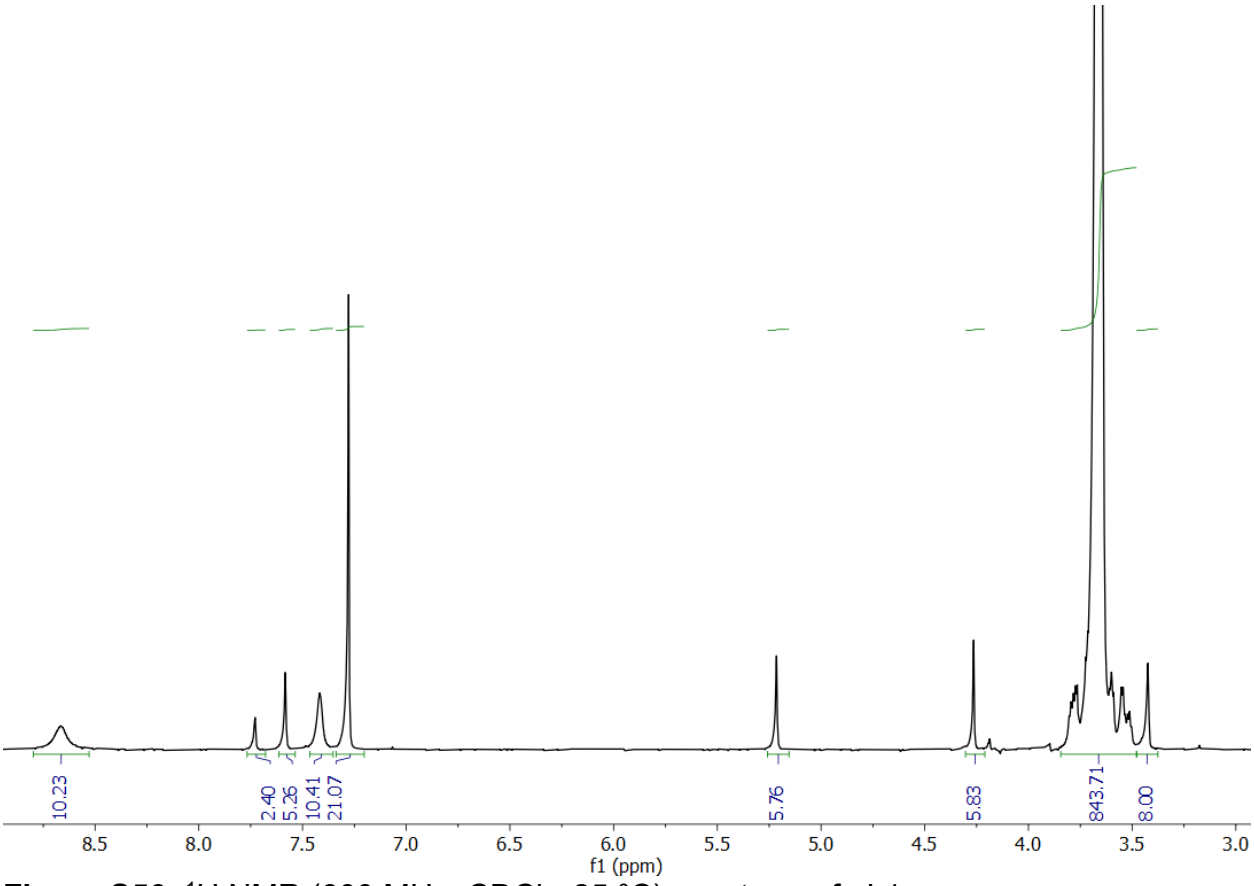

Figure S56. ^{1}H NMR (600 MHz, $CDCl_3$, 25 °C) spectrum of pL1.

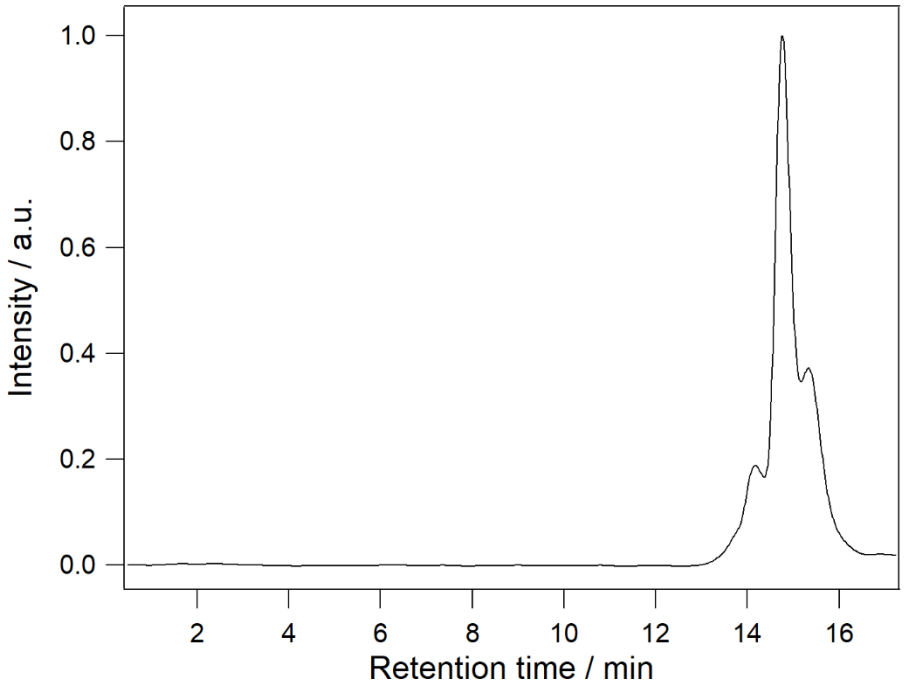

Figure S57. GPC (0.025 M LiBr in DMF, 25 °C) of pL1. Higher and lower molecular weight degradation byproducts are seen in this trace. A higher purity sample was not obtained due to Spring 2020 COVID-19 shutdown of MIT facilities.

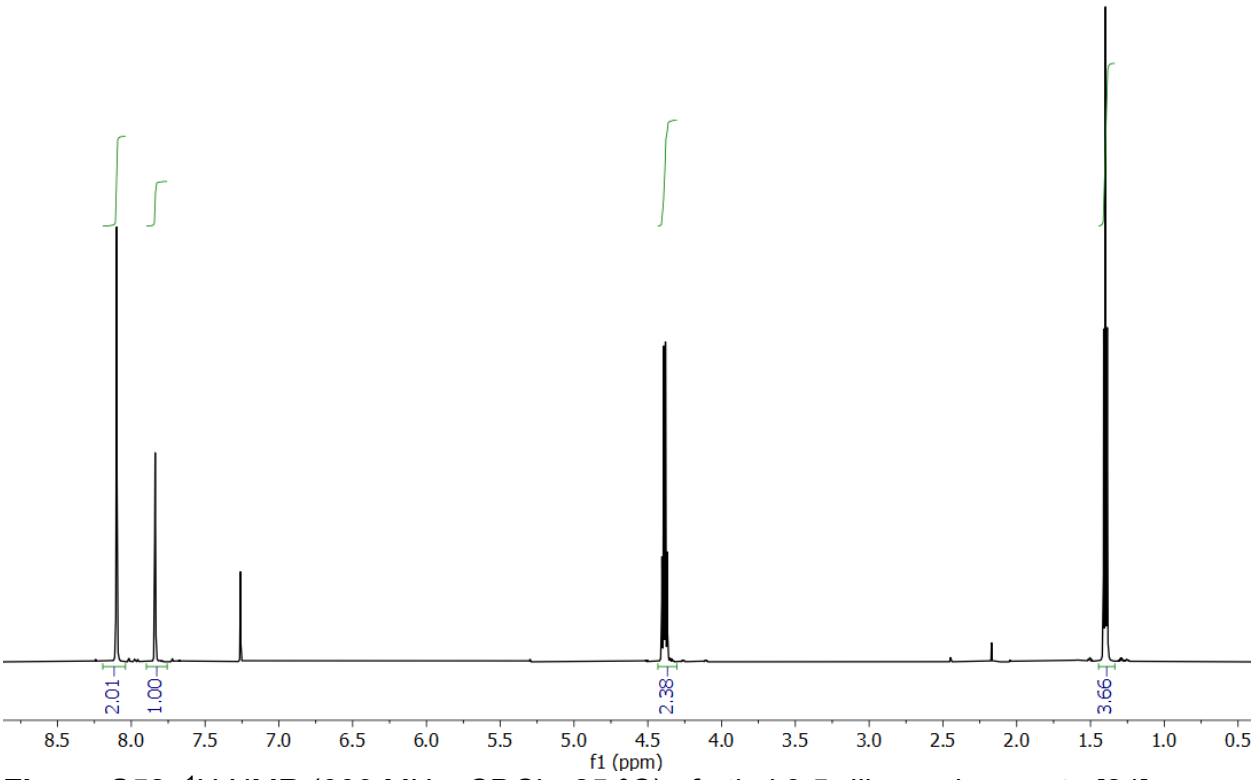

Figure S58. ^{1}H NMR (600 MHz, $CDCl_3$, 25 °C) of ethyl 3,5-dibromobenzoate [24]. Synthesized by David J. Lundberg.

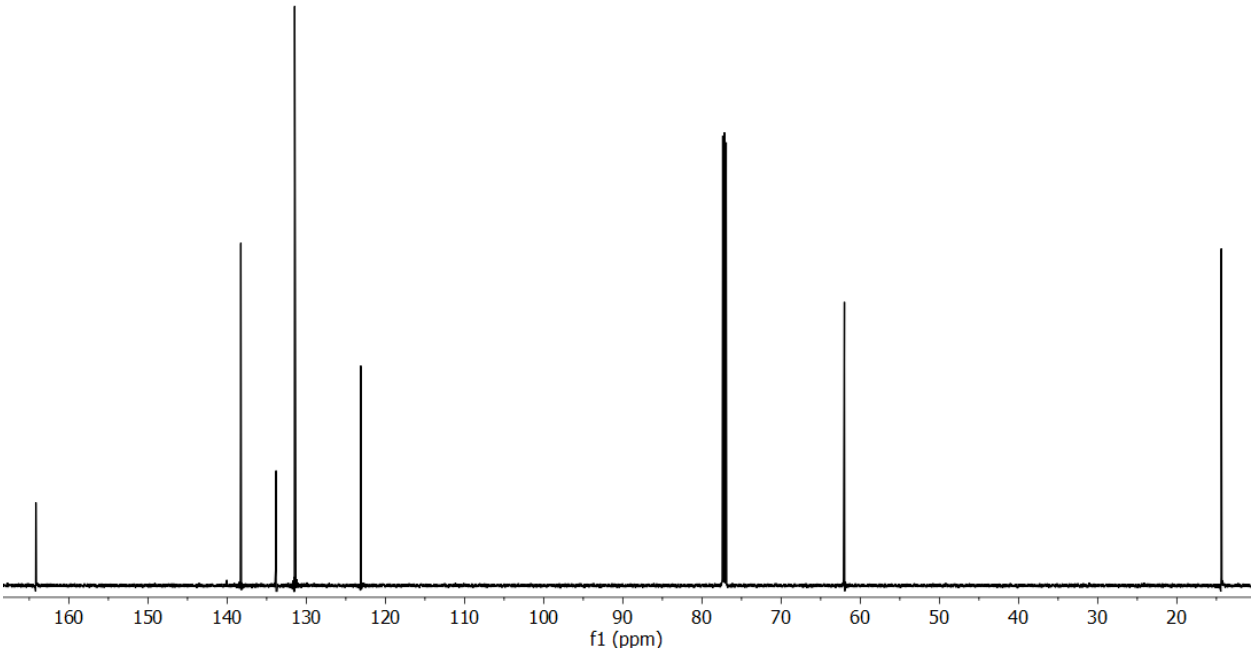

Figure S59. ^{13}C-{^{1}H} NMR (151 MHz, $CDCl_3$, 25 °C) of ethyl 3,5-dibromobenzoate [24]. Synthesized by David J. Lundberg.

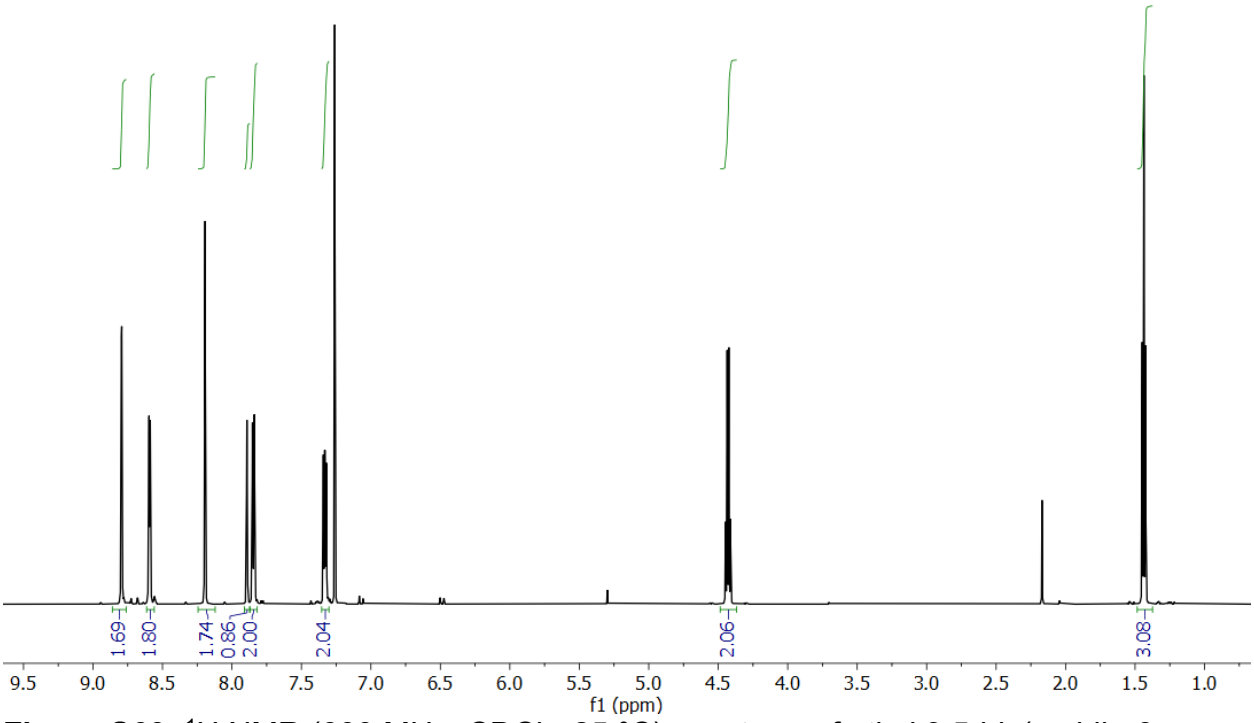

Figure S60. ^{1}H NMR (600 MHz, $CDCl_3$, 25 °C) spectrum of ethyl 3,5-bis(pyridin-3-ylethynyl)benzoate [25]. Synthesized by David J. Lundberg.

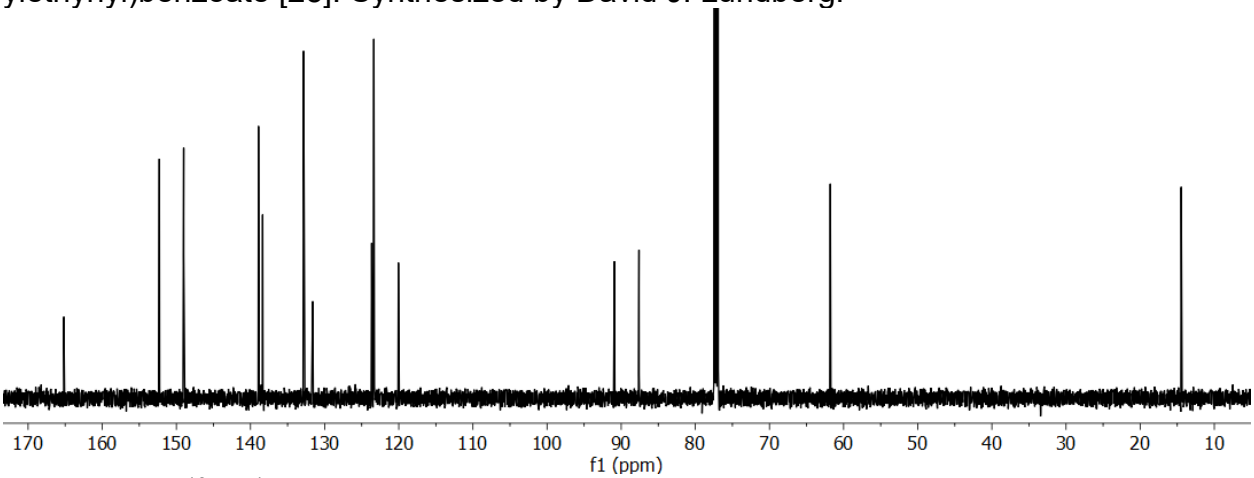

Figure S61. ^{13}C-{^{1}H} NMR (151 MHz, $CDCl_3$, 25 °C) spectrum of ethyl 3,5-bis(pyridin-3-ylethynyl)benzoate [25]. Synthesized by David J. Lundberg.

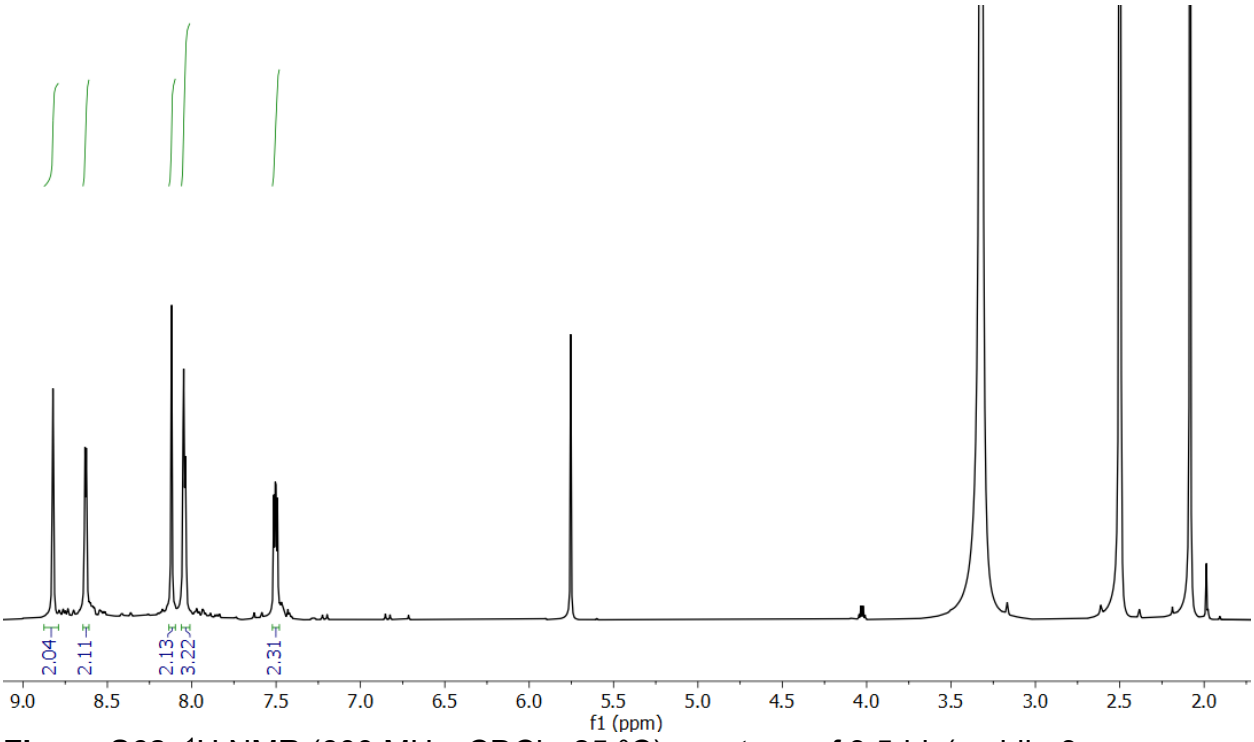

Figure S62. ^{1}H NMR (600 MHz, $CDCl_3$, 25 °C) spectrum of 3,5-bis(pyridin-3-ylethynyl)benzoic acid [26]. Synthesized by David J. Lundberg.

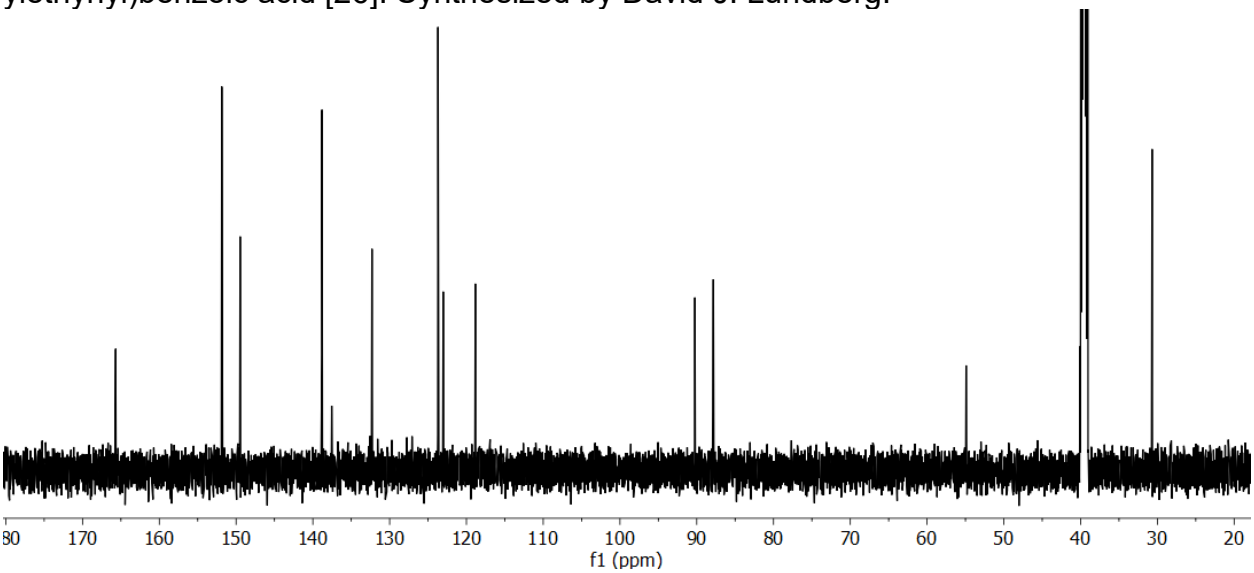

Figure S63. ^{13}C-{^{1}H} NMR (151 MHz, $CDCl_3$, 25 °C) spectrum of 3,5-bis(pyridin-3-ylethynyl)benzoic acid [26]. Synthesized by David J. Lundberg.

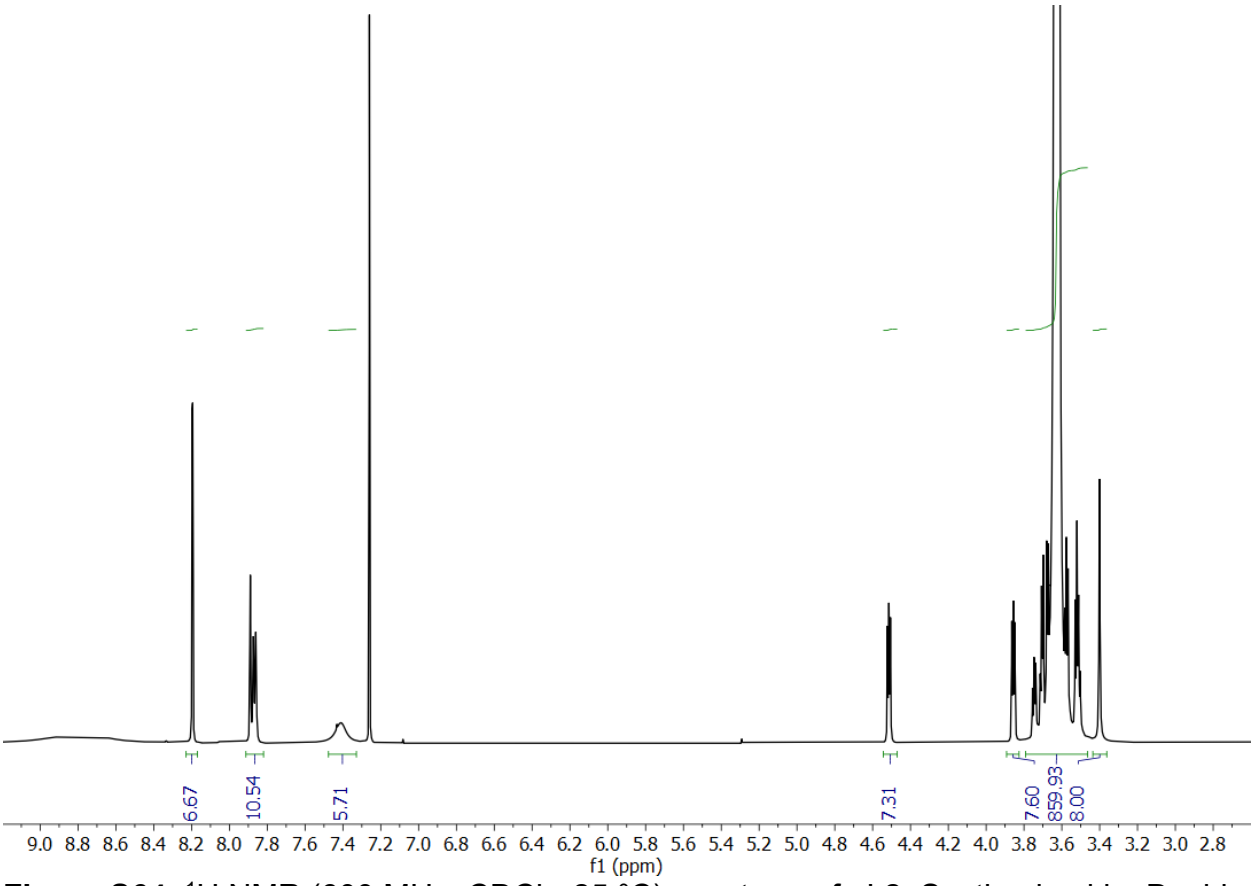

Figure S64. ^{1}H NMR (600 MHz, $CDCl_3$, 25 °C) spectrum of pL2. Synthesized by David J. Lundberg.

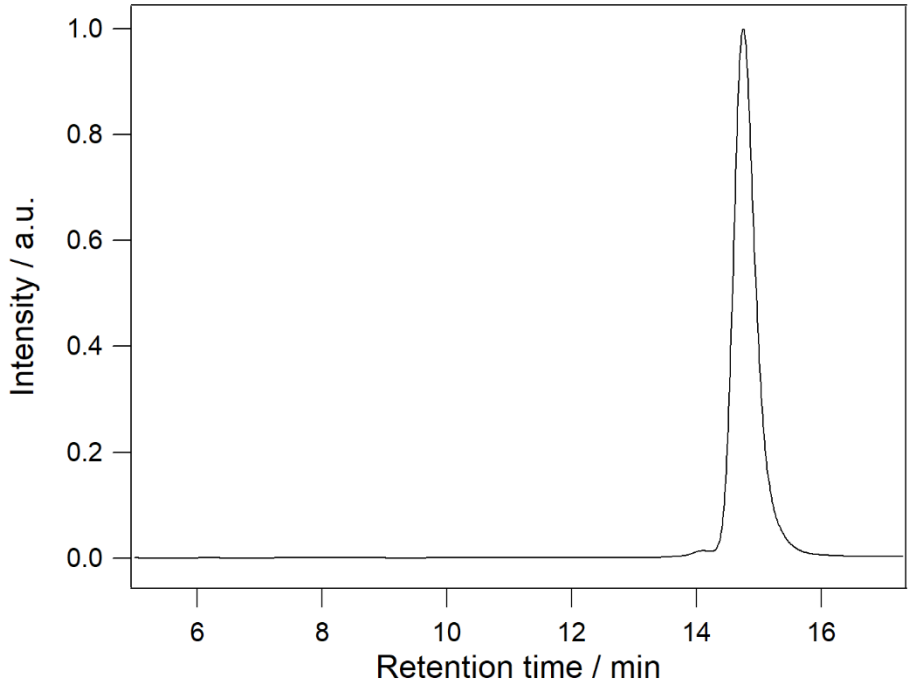

Figure S65. GPC (0.025 M LiBr in DMF, 25 °C) of pL2.

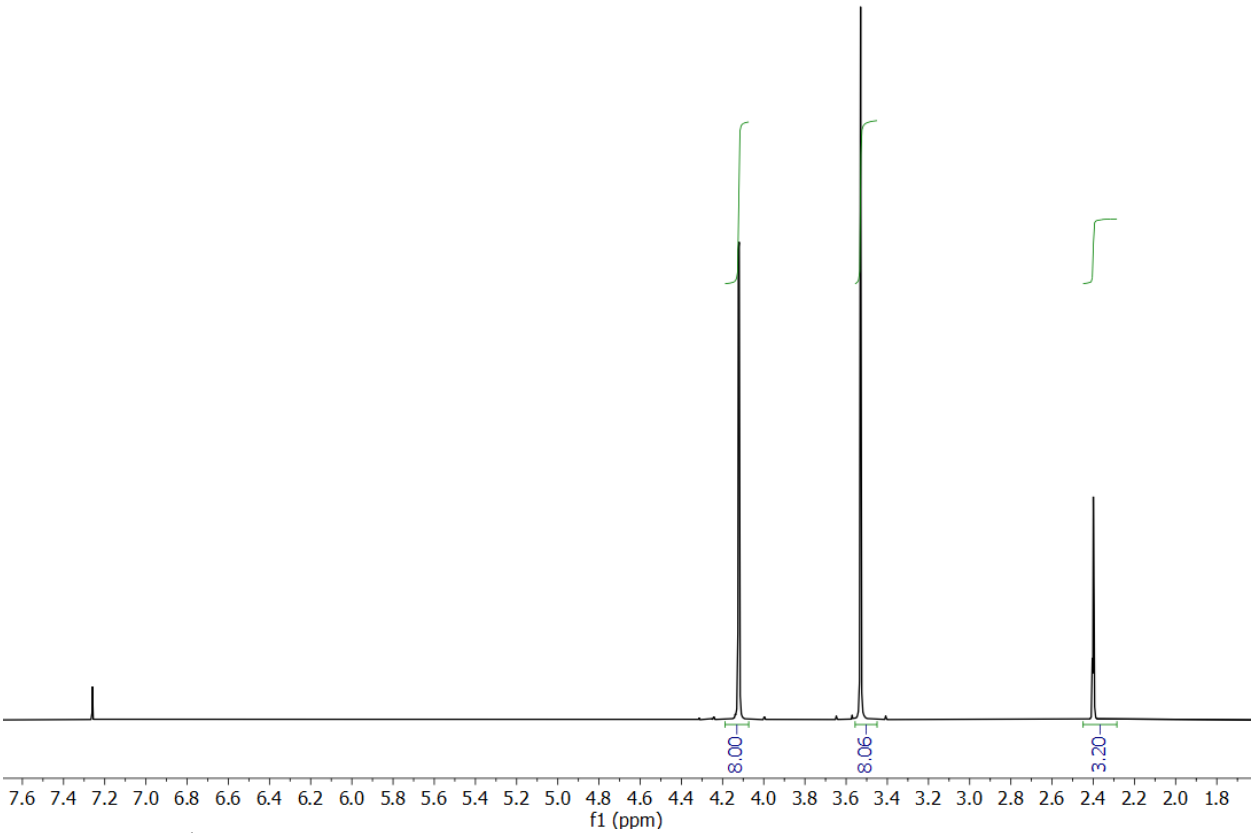

Figure S66. ^{1}H (600 MHz, $CDCl_3$, 25 °C) spectrum of 3-(3-(prop-2-yn-1-yloxy)-2,2-bis((prop-2-yn-1-yloxy)methyl)propoxy)prop-1-yne [27]. Synthesized by Dr. Nathan J. Oldenhuis.

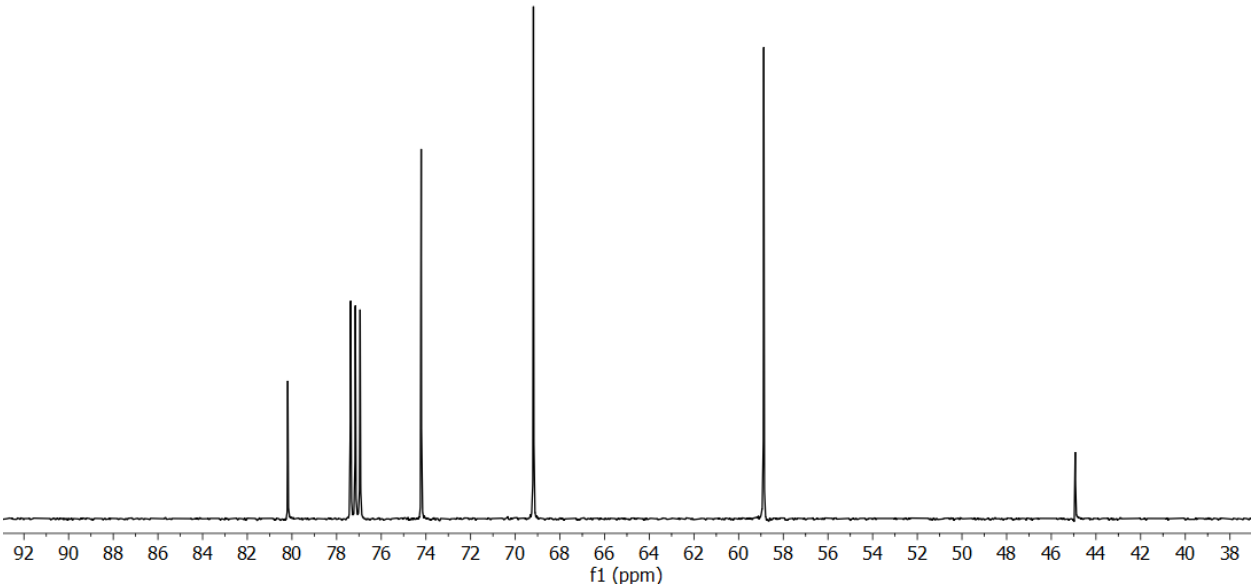

Figure S67. ^{13}C-{^{1}H} (600 MHz, $CDCl_3$, 25 °C) spectrum of 3-(3-(prop-2-yn-1-yloxy)-2,2-bis((prop-2-yn-1-yloxy)methyl)propoxy)prop-1-yne [27]. Synthesized by Dr. Nathan J. Oldenhuis.

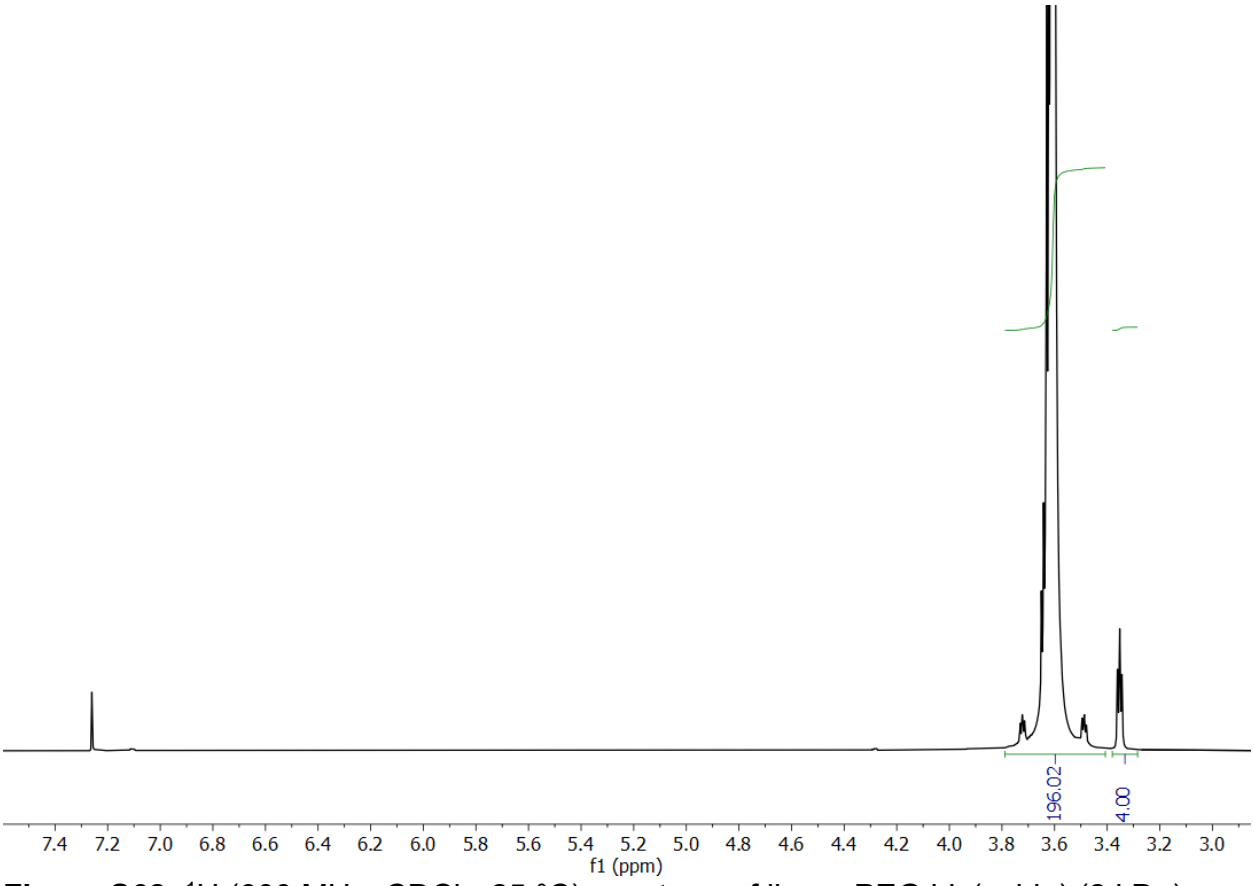

Figure S68. ^{1}H (600 MHz, $CDCl_3$, 25 °C) spectrum of linear PEG bis(azide) (2 kDa). Synthesized by Dr. Nathan J. Oldenhuis.

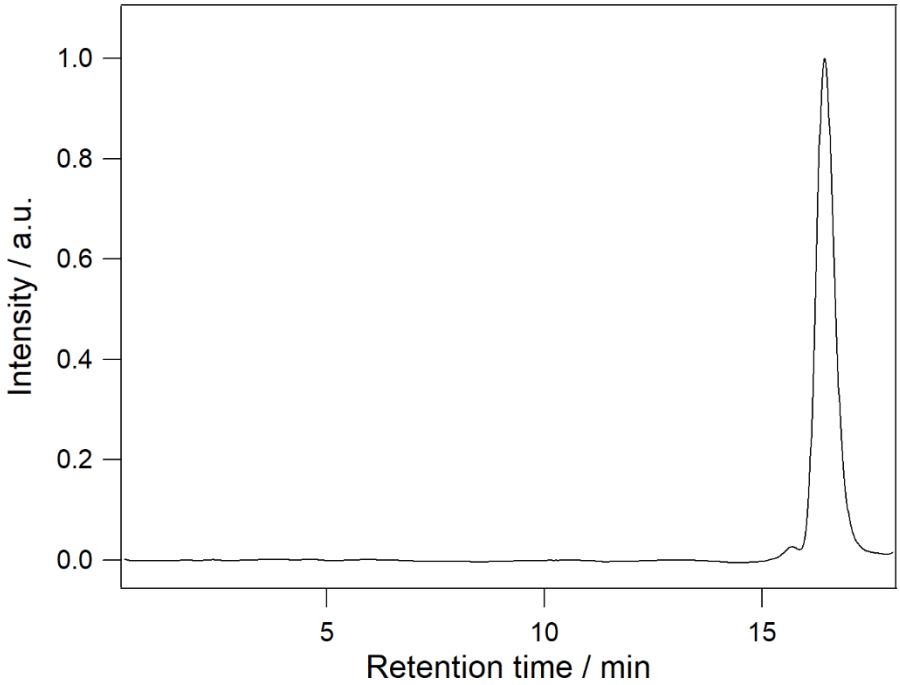

Figure S69. GPC (0.025 M LiBr in DMF, 25 °C) of linear PEG bis(azide) (2 kDa).

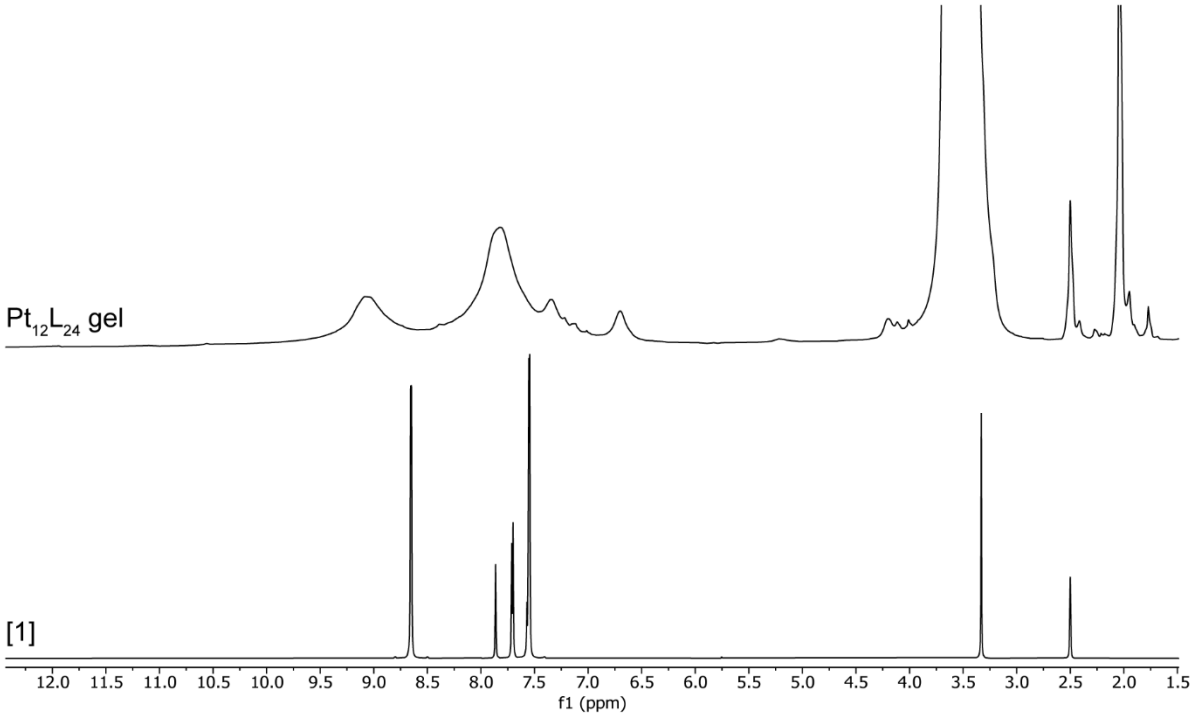

Figure S70. MAS ^{1}H solid-state NMR (500 MHz, 25 °C, 5 kHz spin rate) characterization of $Pt_{12}L_{24}$-based gel formed with pL1 and [1]. Compared with [1] in solution (600 MHz, DMSO-d_6, 25 °C). A spectrum of the $Pt_{12}L_{24}$ cage in solution for complete comparison was not obtained due to the Spring 2020 COVID-19 shutdown of MIT research facilities. Solid-state characterization by Dr. Nathan J. Oldenhuis.

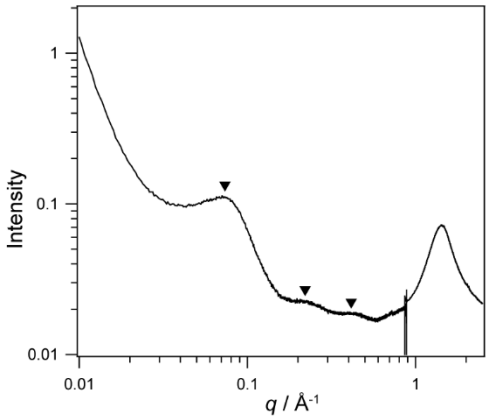

Figure S71. SAXS/WAXS characterization of $Pt_{12}L_{24}$-based polyMOC gels formed from pL1, [1], and $Pt(MeCN)_4(OTf)_2$. The leftmost peak at q = 0.0724 Å^{-1} corresponds to a d-spacing and interMOC distance of 8.7 nm, corresponding well to previously characterized 10 kDa star polyMOC gels.[10] The right peaks at q = 0.224, 0.430 Å^{-1} are attributed to a spherical form factor with radius ~2.5 nm, which agrees with the expected cage diameter.[14]

Figure S72. (L) Pt(II)-based and **(R)** Pd(II)-based polyMOC gels after five cycles of use.

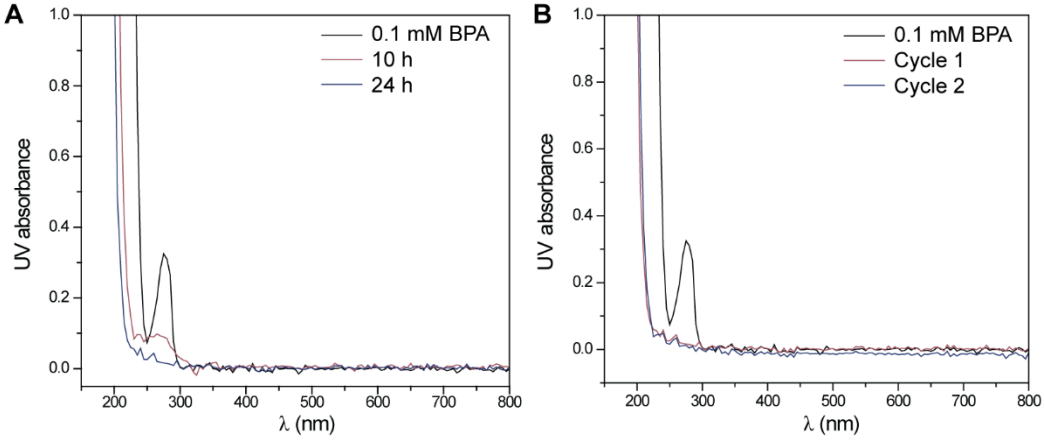

Figure S73. UV-Vis spectra of preliminary BPA absorption studies using Gel 2. (A) UV-Vis spectra of 0.1 mM BPA solution after 10 h and 24 h of absorption time. Experimental duration was set at 24 h to ensure maximum absorption. (B) UV-Vis spectra of 0.1 mM BPA solution following two cycles of absorption using the same Gel 2. Gels were washed through similar solvent exchange procedures detailed.

Table S1. Coumarin absorption performances of Gels 1–3.

Gel	Sample	Coumarin adsorbed (%)	Average (n = 2. %)*
1	A	60.5	60.2 ± 0.4
1	B	59.9	
2	A	58.4	57.8 ± 0.7
2	B	57.3	
3	A	50.0	59.2 ± 1.2
3	B	48.3	

* Additional replicates could not be collected due to the Spring 2020 COVID-19 shutdown of MIT research facilities.

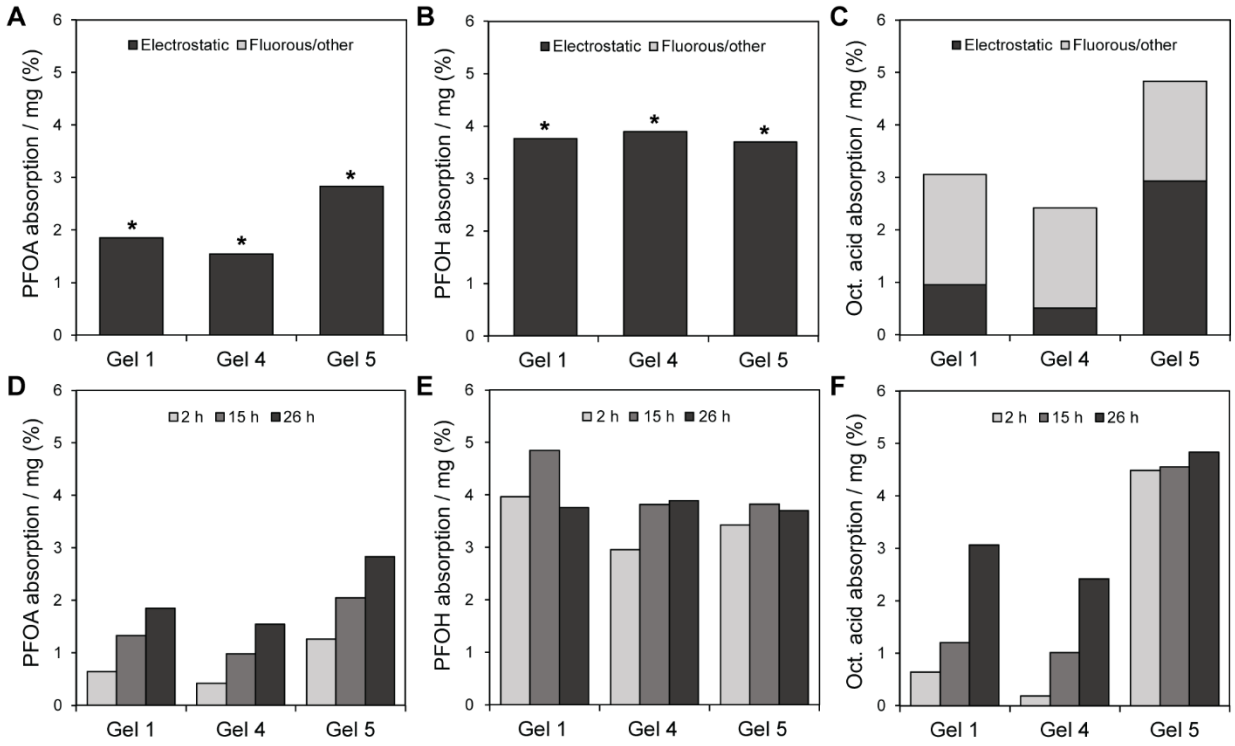

Figure S74. Quantitative NMR studies performed on the absorption of PFOA, PFOH, and octanoic acid using Gels 1, 4, and 5. (A) PFOA, (B) PFOH, and (C) octanoic acid absorption per mg gel, with calculated electrostatic and fluorous contributions in dark and light gray, respectively. Asterisk (*) represents instances where electrostatic contributions were calculated as > 100%. (D) PFOA, (E) PFOH, and (C) octanoic acid absorption of gels was monitored over time. These studies were ultimately inconclusive due to the inability to isolate electrostatic and fluorous contributions through control compounds, as well as the >100% electrostatic contributions calculated for PFOA and PFOH. Absorption percentages also varied dramatically between different NMR studies. These inconsistencies were attributed to the high concentrations of absorbates needed to perform NMR studies, which might have resulted in oversaturation of gels.

3.6 References

1. Hoslett, J.; Massara, T. M.; Malamis, S.; Ahmad, D.; van den Boogaert, I.; Katsou, E.; Ahmad, B.; Ghazal, H.; Simons, S.; Wrobel, L.; Jouhara, H. Surface water filtration using granular media and membranes: a review. *Sci. Total Environ*. **2018**, *639*, 1268–1282.
2. Pieper, K. J.; Martin, R.; Tang, M.; Walters, L.; Parks, J.; Roy, S.; Devine, C.; Edwards, M. A. Evaluating water lead levels during the Flint Water Crisis. *Environ. Sci. Technol.* **2018**, *52* (15), 8124–8132.
3. Strynar, M.; Dagnino, S.; McMahen, R.; Liang, S.; Lindstrom, A.; Andersen, E.; McMillan, L.; Thurman, M.; Ferrer, I.; Ball, C. Identification of novel perfluoroalkyl ether carboxylic acids (PFECAs) and sulfonic acids (PFESAs) in natural waters using accurate mass time-of-flight mass spectrometry (TOFMS). *Environ. Sci. Technol.* **2015**, *49* (19), 11622–11630.
4. Sonune, A.; Ghate, R. Developments in wastewater treatment methods. *Desalin.* **2004**, *167*, 55–63.
5. Wolfram, J.; Stehle, S.; Bub, S.; Petschick, L. L.; Schulz, R. Meta-analysis of insecticides in United States surface waters: status and future implications. *Environ. Sci. Technol.* **2018**, *52* (24), 14452–14460.
6. Hu, X. C.; Andrews, D. Q.; Lindstrom, A. B.; Bruton, T. A.; Schaider, L. A.; Grandjean, P.; Lohmann, R.; Carignan, C. C.; Blum, A.; Balan, S. A.; Higgins, C. P.; Sunderland, E. M. Detection of poly- and perfluoroalkyl substances (PFASs) in U.S. drinking water linked to industrial sites, military fire training areas, and wastewater treatment plants. *Environ. Sci. Technol. Lett.* **2016**, *3* (10), 344–350.
7. Boone, J. S.; Vigo, C.; Boone, T.; Byrne, C.; Ferrario, J.; Benson, R.; Donohue, J.; Simmons, J. E.; Kolpin, D. W.; Furlong, E. T.; Glassmeyer, S. T. Per- and polyfluoroalkyl substances in source and treated drinking waters of the United States. *Sci. Total Environ.* **2019**, *653*, 359–369.
8. Ross, I.; McDonough, J.; Miles, J.; Storch, P.; Thelakkat Kochunarayanan, P.; Kalve, E.; Hurst, J.; S. Dasgupta, S.; Burdick, J. A review of emerging technologies for remediation of PFASs. *Remediation* **2018**, *28* (2), 101–126.
9. Wilkinson, J.; Hooda, P. S.; Barker, J.; Barton, S.; Swinden, J. Occurrence, fate and transformation of emerging contaminants in water: an overarching review of the field. *Environ. Pollut*. **2017**, *231* (1), 954–970.
10. Zhukhovitskiy, A. V.; Zhao, J.; Zhong, M.; Keeler, E. G.; Alt, E. A.; Teichen, P.; Griffin, R. G.; Hore, M. J. A.; Willard, A. P.; Johnson, J. A. Polymer structure dependent hierarchy in polyMOC gels. *Macromolecules* **2016**, *49* (18), 6896–6902
11. Harris, K.; Fujita, D.; Fujita, M. Giant hollow M_nL_{2n} spherical complexes: structure, functionalisation and applications. *Chem. Commun.* **2013**, *49* (60), 6703–6712.
12. Sato, S.; Iida, J.; Suzuki, K.; Kawano, M.; Ozeki, T.; Fujita, M. Fluorous nanodroplets structurally confined in an organopalladium sphere. *Science* **2006**, *313* (5791), 1273–1276.
13. Suzuki, K.; Iida, J.; Sato, S.; Kawano, M.; Fujita, M. Discrete and well-defined hydrophobic phases confined in self-assembled spherical complexes. *Angew. Chemie Int. Ed.* **2008**, *47* (31), 5780–5782.
14. Tominaga, M.; Suzuki, K.; Murase, T.; Fujita, M. 24-fold endohedral functionalization of a self-assembled $M_{12}L_{24}$ coordination nanoball. *J. Am. Chem. Soc.* **2005**, *127* (34), 11950–11951.
15. Suzuki, K.; Takao, K.; Sato, S.; Fujita, M. Coronene nanophase within coordination spheres: increased solubility of C60. *J. Am. Chem. Soc.* **2010**, *132* (8), 2544–2545.
16. Sun, Q.-F.; Sato, S.; Fujita, M. Self-assembled inverse dendrimer. *Chem. Lett.* **2011**, *40* (7), 726–727.
17. Zhukhovitskiy, A. V.; Zhong, M.; Keeler, E. G.; Michaelis, V. K.; Sun, J. E. P.; Hore, M. J. A.; Pochan, D. J.; Griffin, R. G.; Willard, A. P.; Johnson, J. A. Highly branched and loop-rich gels via formation of metal–organic cages linked by polymers. *Nat. Chem.* **2016**, *8* (1), 33–41.
18. Wang, Y.; Gu, Y.; Keeler, E. G.; Park, J. V.; Griffin, R. G.; Johnson, J. A. Star polyMOCs with diverse structures, dynamics, and functions by three-component assembly. *Angew. Chem. Int. Ed.* **2017**, *56* (1), 188–192.
19. Wang, Y.; Zhong, M.; Park, J. V.; Zhukhovitskiy, A. V.; Shi, W.; Johnson, J. A. Block co-polyMOCs by stepwise self-assembly. *J. Am. Chem. Soc.* **2016**, *138* (33), 10708–10715.

20. Rubin, B. S. Bisphenol A: An endocrine disruptor with widespread exposure and multiple effects. *J. Steroid Biochem. Mol. Biol.* **2011**, *127* (1–2), 27–34.
21. Rochester, J. R. Bisphenol A and human health: a review of the literature. *Reprod. Toxicol.* **2013**, *42*, 132–155.
22. Tsai, W.-T. Human health risk on environmental exposure to bisphenol-A: a review. *J. Environ. Sci. Heal. C* **2006**, *24* (2), 225–255.
23. Rosenfeld, P. E.; Feng, L. G. H. Pesticides. In *Risks of Hazardous Wastes*; William Andrew Publishing, 2011; pp 127–154.
24. Chesters, G.; Simsiman, G. V.; Levy, J.; Alhajjar, B. J.; Fathulla, R. N.; Harkin, J. M. Environmental fate of alachlor and metolachlor. *Rev. Environ. Contam. Toxicol*. **1989**, *110*, 1–74.
25. Lake, B. G. Coumarin metabolism, toxicity and carcinogenicity: relevance for human risk assessment. *Food Chem. Toxicol*. **1999**, *37* (4), 423–453.
26. Lake B.G. Young Scientists Award Lecture 1983: Investigations into the Mechanism of Coumarin-Induced Hepatotoxicity in the Rat. In: Chambers P.L., Preziosi P., Chambers C.M. (eds) *Disease, Metabolism and Reproduction in the Toxic Response to Drugs and Other Chemicals*. Archives of Toxicology (Supplement), vol 7. Springer, Berlin, Heidelberg, 1984. Lake, B. G.
27. Basic information on PFAS: per- and polyfluoroalkyl Substances (PFAS). https://www.epa.gov/pfas/basic-information-pfas (accessed Apr 15, 2020).
28. Hekster, F. M.; Laane, R. W. P. M.; De Voogt, P. Environmental and toxicity effects of perfluoroalkylated substances. *Rev. Environ. Contam. Toxicol.* **2003**, *179*, 99–121.
29. Sunderland, E. M.; Hu, X. C.; Dassuncao, C.; Tokranov, A. K.; Wagner, C. C.; Allen, J. G. A Review of the pathways of human exposure to poly-and perfluoroalkyl substances (PFASs) and present understanding of health effects. *J Expo. Sci. Env. Epidemiol.* **2019**, *29* (2), 131–147.
30. Grandjean, P.; Clapp, R. Changing interpretation of human health risks from perfluorinated compounds. *Public Health Rep.* **2014**, *129* (6), 482–485.
31. US EPA - Office of Water. *Drinking Water Health Advisory for Perfluorooctanoic Acid (PFOA)- Drinking Water Health Advisory for Perfluorooctanoic Acid (PFOA)*; 2016.
32. Xiao, L.; Ling, Y.; Alsbaiee, A.; Li, C.; Helbling, D. E.; Dichtel, W. R. β-cyclodextrin polymer network sequesters perfluorooctanoic acid at environmentally relevant concentrations. *J. Am. Chem. Soc.* **2017**, *139* (23), 7689–7692.
33. Kumarasamy, E.; Manning, I. M.; Collins, L. B.; Coronell, O.; Leibfarth, F. A. Ionic fluorogels for remediation of per- and polyfluorinated alkyl substances from water. *ACS Cent. Sci.* **2020**, *6* (4), 487–492
34. Lindstrom, A. B.; Strynar, M. J.; Libelo, E. L. Polyfluorinated compounds: past, present, and future. *Environ. Sci. Technol.* **2011**, *45* (19), 7954–7961.
35. Burns, D. C.; Ellis, D. A.; Li, H.; McMurdo, C. J.; Webster, E. Experimental pK_a determination for perfluorooctanoic acid (PFOA) and the potential impact of pk a concentration dependence on laboratory-measured partitioning phenomena and environmental modeling. *Environ. Sci. Technol.* **2008**, *42* (24), 9283–9288
36. Huang, P. J.; Hwangbo, M.; Chen, Z.; Liu, Y.; Kameoka, J.; Chu, K. H. Reusable functionalized hydrogel sorbents for removing long- and short-chain perfluoroalkyl acids (PFAAs) and GenX from aqueous solution. *ACS Omega* **2018**, *3* (12), 17447–17455.
37. Koda, Y.; Terashima, T.; Takenaka, M.; Sawamoto, M. Star polymer gels with fluorinated microgels via star-star coupling and cross-linking for water purification. *ACS Macro. Lett.* **2015**, *4* (4), 377–380.
38. Koda, Y.; Terashima, T.; Sawamoto, M. Fluorous microgel star polymers: Selective recognition and separation of polyfluorinated surfactants and compounds in water. *J. Am. Chem. Soc.* **2014**, *136* (44), 15742–15748.
39. Klemes, M. J.; Ling, Y.; Ching, C.; Wu, C.; Xiao, L.; Helbling, D. E.; Dichtel, W. R. Reduction of a tetrafluoroterephthalonitrile-β-cyclodextrin polymer to remove anionic micropollutants and perfluorinated alkyl substances from water. *Angew. Chem. Int. Ed.* **2019**, *58* (35), 12049–12053.
40. Brenner, W.; Ronson, T. K.; Nitschke, J. R. Separation and selective formation of fullerene adducts within an $M^{II}_8L_6$ cage. *J. Am. Chem. Soc.* **2017**, *139* (1), 75–78.
41. Ueda, Y.; Ito, H.; Fujita, D.; Fujita, M. Permeable self-assembled molecular containers for catalyst isolation enabling two-step cascade reactions. *J. Am. Chem. Soc.* **2017**, *139* (17), 6090–6093.
42. Harris, J. M.; Kozlowski, A.; Guo, L. Method of preparing carboxylic acid functionalized polymers.

US 8067505 B2, 2011.
43. Kawamoto, K.; Zhong, M.; Wang, R.; Olsen, B. D.; Johnson, J. A. Loops versus branch functionality in model click hydrogels. *Macromolecules* **2015**, *48* (24), 8980–8988.
44. Oldenhuis, N. J.; Qin, K. P.; Wang, S.; Ye, H.; Alt, E. A.; Willard, A. P.; Van Voorhis, T.; Craig, S. L.; Johnson, J. A. Photoswitchable sol–gel transitions and catalysis mediated by polymer networks with coumarin‐decorated Cu_{24} L_{24} metal–organic cages as junctions. *Angew. Chem. Int. Ed.* **2020**, *59* (7), 2784–2792.
45. Wendt, O. F.; Kaiser, N.-F. K.; Elding, L. I. Acetonitrile and propionitrile exchange at palladium(II) and platinum(II). ***1997**, 24*, 4733–4738.